

von Karman Institute for Fluid Dynamics
Chaussée de Waterloo, 72
B - 1640 Rhode Saint Genèse - Belgium

CONTRACT REPORT 2003-08

December 2002

LES INVESTIGATION OF COHERENT STRUCTURES
IN BOUNDARY LAYERS AND WAKES
VOLUME I: INVESTIGATION OF COHERENT STRUCTURES
IN AN ATTACHED SHEAR LAYER

GRANT N00014-99-1-0834

R. Giammanco & C. Benocci

DISTRIBUTION STATEMENT A

Approved for Public Release
Distribution Unlimited

EAR9944

20030320 108

AQ F03-06-1406

Abstract

Purpose of the present investigation was to assess the feasibility of simulating and studying coherent structures in turbulent shear layers, making use of Large Eddy Simulations (LES).

The current investigation has been performed across a rather wide range of simulated flows and LES implementations, starting from an established and validated structured LES code based on finite differences and cartesian grids ending to an unstructured LES code under development. The use of the unstructured approach was considered necessary whenever complex geometries have to be analyzed, which cannot be handled by the structured code, regardless its advanced features (like multi-domain approach). The unstructured LES code was developed in the frame of current GRANT, and it has undergone validation. The structured LES code, which had already validated over a wide range of flow configurations, was used to analyze the wake behind an obstacle, attempt which was not made before. Extensive studies were needed in the attempt to validate to code for this case.

Given the wide scope of present report and the mass of data available from different LES codes, flows and structures, the work has been spit between two work groups, the one devoted to the structured LES and the one devoted to the unstructured LES. In this frame it was found more practical to sub-divide the full report in three volumes:

Volume I Investigation of Coherent Structures in an Attached Shear Layer

Volume II Wake around square Cylinder

Volume III Unstructured LES

The different volumes are not completely independent: Volume I, for example, in the description of the structured LES code, introduces concepts and algorithms which will be applied in computations that will be presented only in Volume II.

The subdivision of present report in different volumes was, indeed, adopted to simplify the organize and present the collected data, and also to take into account the fact that different groups worked on different aspects of the grant, and their respective work should be easily recognizable.

Volume I of present report has described the general background, the main development and the results obtained for wall bounded turbulent flow, particularly, for the case of turbulent plane channel flow at equilibrium.

Volume II is devoted to the study of the flow around an obstacle, specifically, a cylinder with square cross section and infinite length in span-wise direction. This test case belongs

to a completely different class of flows, respect to the one analyzed in Volume I, and it is a severe test case for the LES code.

Most of the advanced features of the code were exploited to achieve this task, different simulations were performed, in order to collect, whenever possible, sufficient data to draw conclusions and remarks.

Differently from the case of channel flow, where the code has been extensively validated and analyzed in detail, down to the level of turbulent kinetic energy budget, the present flow constitutes a still active area of basic research.

The higher complexity of the flow, the absence of a second direction of homogeneity, beside the span-wise direction, the existence of a dominant frequency in the flow, the necessity of employing upwinding discretization for advection terms and other numerical difficulties have led to such complexities of execution that only the very basic set of statistics (statistical moments of first and second order) were obtained. At the same time, limits and draw-backs for current LES code implementation have been outlined.

Most of the efforts were devoted to reach a sufficient similarity in behavior between LES simulation and reference experimental data; this attempt has led to build grids not perfectly suited to analyze structures applying the criteria introduced in Volume I, which are based on operators working on the tensor of gradient of velocity.

This fact, together with intrinsic difficulty of dealing with the presence of a wide range of structures of different sizes and shapes, has limited the possibility to obtain a thorough and complete description of vortical behavior for this class of flow.

However, it was possible to find useful global statistics for organized turbulence and to show that a very important part of the entire turbulent field lies within very active structures, which cover a very small part of the entire flow field. It can be moreover suggested that these characteristics of these structures are the ones which define and control the wake behavior, and their identification could be key of understand and possibly identify and recognize specific wakes.

Possible avenues for future investigations starting from present study are also suggested.

Acknowledgements

Present research has been funded by the by Office Naval Research under Grant N00014-99-1-0834, under supervision of Program Officers Dr. Candace Wark and Dr. Patrick Purtell.

Table of Contents

Abstract	ii
Acknowledgements	v
List of tables	viii
List of figures	ix
1. Introduction	1
2. Large-Eddy Simulation concept	5
2.1 Governing Equations	5
2.2 Principles of Direct and Large-Eddy Simulation	5
2.3 SGS Modeling	9
2.3.1 Fully dissipative SGS models	9
2.3.2 Self-similar SGS models	13
3. Numerical solution of LES equations	17
3.1 Time-Integration	17
3.2 Spatial Discretization	19
3.3 Multi-domain technique	23
4. Coherent structure concept	27
4.1 introduction	27
4.2 Deduction of coherent structures	29
4.2.1 Detection criterion	29
4.3 Detection procedure	32
4.4 Definition and classification procedure	38
4.4.1 Algorithm Description	38
4.5 Statistical tools	43
4.5.1 Geometry and distribution of structures	43
4.5.2 Dynamics of structures	43
4.5.3 Kinetic energy budget for structures	49
5. Simulation of coherent structures in attached wall shear layer	54
5.1 Investigation of organized structures for plane channel at $Re_\tau = 180$ (Case I)	55
5.1.1 Conclusion	81
5.2 Effect of grid resolution	83
5.2.1 Conclusion	97
5.3 Detection criterion	102
5.4 Effect of precision of LES numerical algorithm	118
5.5 Effect of choice of SGS model	120
5.6 Conclusions	123

6. Investigation of coherent structures at different Reynolds numbers	124
6.1 Test conditions and global results	124
6.2 Analysis of coherent structures at $Re_\tau = 395$	127
6.2.1 Conclusion	137
6.3 Analysis of coherent structures at $Re_\tau = 590$	142
6.4 Conclusion	149
7. Conclusions	157
APPENDIX	163
A. $Re_\tau = 180$ -CASE II	163
B. $Re_\tau = 180$ -CASE IV	166
C. $Re_\tau = 180$ -CASE IV-B	174
D. $Re_\tau = 180$ -CASE V-A	177
E. $Re_\tau = 180$ -CASE V-B	180
F. $Re_\tau = 180$ -CASE V-C	183
G. $Re_\tau = 180$ -CASE V	184
H. $Re_\tau = 395$	235
I. $Re_\tau = 590$	238

List of Tables

4.1	Structures statistics $Re_\tau = 180$ (Example): Trigger	34
4.2	Structures statistics $Re_\tau = 180$ (Example): Enstrophy comp	37
4.3	Structures statistics $Re_\tau = 180$ (Example): Enstrophy in Zone 2	37
4.4	Plane channel at equilibrium at $Re_\tau = 180$. (Example) Structures and Noise .	43
4.5	Structures statistics $Re_\tau = 180$ (Example): Volume percentage	47
5.1	Plane channel at equilibrium at $Re_\tau = 180$ (Case I). Geometrical Parameters	55
5.2	Plane channel at equilibrium at $Re_\tau = 180$ (Case I). Volume	59
5.3	Plane channel at equilibrium at $Re_\tau = 180$ (Case I). Enstrophy	59
5.4	Plane channel at equilibrium at $Re_\tau = 180$ (Case I). Summary zone by zone .	61
5.5	Plane channel at equilibrium at $Re_\tau = 180$ (Case I). Most common values for L_x , L_y and L_z in wall units (Zone 2)	65
5.6	Plane channel at equilibrium at $Re_\tau = 180$ (Case I). Most common values for joint L_x - L_y , L_x - L_z and L_y - L_z in wall units.	68
5.7	Plane channel at equilibrium at $Re_\tau = 180$, alternative grid tested (Case II). Geometrical Parameters	83
5.8	Plane channel at equilibrium at $Re_\tau = 180$ (Case II). Volume	84
5.9	Plane channel at equilibrium at $Re_\tau = 180$ (Case II). Total quantities	84
5.10	Plane channel at equilibrium at $Re_\tau = 180$ (Case II). Most common values for L_x , L_y and L_z in wall units for Zone 2	88
5.11	Plane channel at equilibrium at $Re_\tau = 180$ (Case II). Most probable structure values for L_x , L_y and L_z in wall units for Zone 2 based on the JPDFs	89
5.12	Plane channel at equilibrium at $Re_\tau = 180$ (Case III). Volume	103
5.13	Plane channel at equilibrium at $Re_\tau = 180$ (Case III). Most common values for L_x , L_y and L_z in wall units for Zone 2	105
5.14	Plane channel at equilibrium at $Re_\tau = 180$ (Case IV). Total quantities	118
5.15	Plane channel at equilibrium at $Re_\tau = 180$ (Case IV). Volume	118
5.16	Plane channel at equilibrium at $Re_\tau = 180$ (Case V). Global	121
5.17	Plane channel at equilibrium at $Re_\tau = 180$ (Case V). Volume	122
6.1	Reynolds effect study: Relevant parameters for computational field and grid sizes	124
6.2	Reynolds effect study: Trigger level for different Re_τ	125
6.3	Reynolds effect study: Volume	125

List of Figures

2.1	Typical spectrum of kinetic energy of turbulent flows	6
2.2	Separation of grid-scale and sub-grid scale turbulence	7
2.3	Kinetic energy exchange between grid-scales and sub-grid scales	10
2.4	Kinetic energy interchange between grid-scales and sub-grid scales. (P=turbulent production, E=turbulent dissipation, e=interchange)	14
2.5	Region of interaction between smallest resolved scales (1) and biggest unresolved scales (2)	15
3.1	Location of the velocity coordinates and pressure on a staggered grid	19
3.2	Cell and flux surfaces for velocity component \bar{u}_i	20
3.3	Small and large grid for 4 th order discretization	21
3.4	Spectral behavior of $G(r)$	23
3.5	Example of subdivision in 3 sub-domains $\Omega_1, \Omega_2, \Omega_3$ connected by interfaces Γ_1, Γ_2	24
3.6	Boundary points update at vertical interface between sub-domains Ω_i, Ω_j	24
4.1	Vortex structures in wake behind cylinder of square cross-section	28
4.2	Horse-shoe structure detected in DNS	29
4.3	Vortex structures detected in DNS	30
4.4	Iso-surfaces of $Q = 5$; plane channel	33
4.5	PDF of Q for plane channel at equilibrium	33
4.6	Iso-surfaces of $Tr = 91$, plane channel at equilibrium, $Re_\tau = 180$	34
4.7	Iso-surfaces of $Tr = 200$, plane channel at equilibrium, $Re_\tau = 180$	34
4.8	Structures statistics $Re_\tau = 180$ (Example): mass center distribution	36
4.9	Structures statistics $Re_\tau = 180$ (Example): specific enstrophy	36
4.10	Smallest Recognized Structure	38
4.11	Finding interior nodes	39
4.12	Vortex core identification and construction	39
4.13	Skin growth simplified description	40
4.14	Identification algorithm log: First Iteration	41
4.15	Identification algorithm log: Second Iteration	41
4.16	Detection mask M of plane channel $Re_\tau = 180$ (Example)	41
4.17	Identified structures at $Re_\tau = 180$ (Example)	42
4.18	Noise of plane channel at $Re_\tau = 180$ (Example)	42
4.19	Detected Mask (blue) and Identified Structures (red) at comparison (DNS)	44
4.20	Structures statistics $Re_\tau = 180$ (Example): Volume	45
4.21	Structures statistics $Re_\tau = 180$ (Example): Stream-wise extension	45
4.22	Structures statistics $Re_\tau = 180$ (Example): specific vorticity modulus	48
4.23	Structures statistics $Re_\tau = 180$ (Example): specific enstrophy	48
4.24	Structures statistics $Re_\tau = 180$ (Example): JPDP for structures length	49

4.25	Structures statistics $Re_\tau = 180$ (Example): JPDF for specific vorticity	49
4.26	Structures statistics $Re_\tau = 180$ (Example): Convection velocity	50
4.27	Resolved Turbulent Kinetic Energy Budget $Re_\tau = 180$ (Example)	52
4.28	Resolved Turbulent Kinetic Energy Pseudo Dissipation $Re_\tau = 180$ (Example) .	52
4.29	Resolved Turbulent Kinetic Energy Production $Re_\tau = 180$ (Example)	53
5.1	Plane channel geometry	54
5.2	Mean stream-wise velocity and rms of resolved turbulence of plane channel at $Re_\tau = 180$ (Case I)	56
5.3	Anisotropic part of the resolved Reynolds stress tensor of plane channel at $Re_\tau = 180$ and total shear stress (Case I)	57
5.4	Budget of resolved turbulent kinetic energy of plane channel at $Re_\tau = 180$ (Case I)	58
5.5	PDF of Q plane channel at $Re_\tau = 180$ (Case I)	59
5.6	Structures Volume of plane channel at $Re_\tau = 180$ (Case I)	60
5.7	Structures mass center of plane channel at $Re_\tau = 180$ (Case I)	60
5.8	Side view of the field of detected structures of plane channel at $Re_\tau = 180$ (Case I)	61
5.9	Stream-wise advection of structures center of mass of plane channel at $Re_\tau = 180$ (Case I)	62
5.10	3-D overview of the field of detected structures of plane channel at $Re_\tau = 180$ (Case I)	62
5.11	Typical structures elongated in stream-wise direction of plane channel at $Re_\tau = 180$ (Case I)	63
5.12	Example of complex structures of plane channel at $Re_\tau = 180$ (Case I).	64
5.13	Examples of elongated structures at $Re_\tau = 180$ (Case I)	65
5.14	Estimation of size of structures from their projections on coordinate axis . . .	65
5.15	Structures statistics at $Re_\tau = 180$ (Case I): length in wall units	66
5.16	Structures statistics: JPDF for structures extension. $Re_\tau = 180$ (Case I) . . .	67
5.17	Estimation of size of structures from their projections on coordinate axis could be problematic	68
5.18	Structures statistics, $Re_\tau = 180$ (Case I): spatial alignment	70
5.19	Structures statistics $Re_\tau = 180$ (Case I): Tilting angle	71
5.20	Structures statistics $Re_\tau = 180$ (Case I): Incidence angle	71
5.21	Structures statistics $Re_\tau = 180$ (Case I): Equivalent cylinder radius	72
5.22	Structures statistics $Re_\tau = 180$ (Case I): Equivalent cylinder length	72
5.23	Structures statistics $Re_\tau = 180$ (Case I): Equivalent cylinder volume deviation	73
5.24	Structures statistics $Re_\tau = 180$ (Case I): Equivalent ellipsoid minor semi-axis .	73
5.25	Structures statistics $Re_\tau = 180$ (Case I): Equivalent ellipsoid middle semi-axis	74
5.26	Structures statistics $Re_\tau = 180$ (Case I): Equivalent ellipsoid major semi-axis .	74
5.27	Structures statistics $Re_\tau = 180$ (Case I): Equivalent ellipsoid volume deviation	75

5.28	Structure statistics: Specific Vorticity and enstrophy; $Re_\tau = 180$ (Case I) . . .	76
5.29	Structure statistics: Specific Vorticity and enstrophy; local percentages, $Re_\tau = 180$ (Case I)	77
5.30	Structure statistics: Specific span-wise Vorticity for half a channel	78
5.31	Structures statistics, whole channel: JPDF for structures vorticity. $Re_\tau = 180$ (Case I)	79
5.32	Structures statistics, lower half-channel: JPDF for structures vorticity. $Re_\tau = 180$ (Case I)	80
5.33	3-D overview of the field of detected structures of plane channel at $Re_\tau = 180$ (Case II)	85
5.34	Lateral overview of the field of detected structures of plane channel at $Re_\tau = 180$ (Case II)	85
5.35	Increased resolution multiply the presence of identified structures of small dimensions for plane channel at $Re_\tau = 180$ (Case II)	86
5.36	Typical structures elongated in stream-wise direction of plane channel at $Re_\tau = 180$ (Case II)	87
5.37	Structures Volume of plane channel at $Re_\tau = 180$ (Case II)	88
5.38	Structures Volume of plane channel at $Re_\tau = 180$ (Case II), alternative PDF	88
5.39	Structures statistics at $Re_\tau = 180$ (Case II): length in wall units	89
5.40	Structures statistics: JPDF for structures extension. $Re_\tau = 180$ (Case II)	90
5.41	Structures statistics, $Re_\tau = 180$ (Case II): spatial alignment, Zones 1 and 2	91
5.42	Structures statistics, $Re_\tau = 180$ (Case II): spatial alignment, Zone 3	92
5.43	Structures statistics $Re_\tau = 180$ (Case II): Tilting angle	93
5.44	Structures statistics $Re_\tau = 180$ (Case II): Incidence angle	93
5.45	Structures statistics $Re_\tau = 180$ (Case II): Tilting angle, local percentages	94
5.46	Structures statistics $Re_\tau = 180$ (Case II): Incidence angle, local percentages	94
5.47	Structures statistics, $Re_\tau = 180$ (Case II): spatial alignment, alternative formulation	96
5.48	Structures statistics $Re_\tau = 180$ (Case II): Equivalent ellipsoid minor semi-axis	97
5.49	Structures statistics $Re_\tau = 180$ (Case II): Equivalent ellipsoid middle semi-axis	97
5.50	Structures statistics $Re_\tau = 180$ (Case II): Equivalent ellipsoid major semi-axis	98
5.51	Structures statistics $Re_\tau = 180$ (Case II): Equivalent ellipsoid volume deviation	98
5.52	Structure statistics: Specific Vorticity and enstrophy at $Re_\tau = 180$ (Case II)	99
5.53	Structures statistics, whole channel: JPDF for structures vorticity at $Re_\tau = 180$ (Case II)	100
5.54	Structures statistics, lower half-channel: JPDF for structures vorticity at $Re_\tau = 180$ (Case II)	101
5.55	PDF of D plane channel at $Re_\tau = 180$ (Case III)	102
5.56	3-D overview of the field of detected structures of plane channel at $Re_\tau = 180$ (Case III)	104

5.57	Lateral overview of the field of detected structures of plane channel at $Re_\tau = 180$ (Case III)	104
5.58	Structures Volume of plane channel at $Re_\tau = 180$ (Case III)	104
5.59	Structures mass center of plane channel at $Re_\tau = 180$ (Case III)	105
5.60	Stream-wise advection of structures center of mass of plane channel at $Re_\tau = 180$ (Case III)	105
5.61	Structures statistics at $Re_\tau = 180$ (Case III): length in wall units	106
5.62	Structures statistics: JPDF for structures extension. $Re_\tau = 180$ (Case III)	107
5.63	Structures statistics, $Re_\tau = 180$ (Case III): spatial alignment, Zones 1 and 2	108
5.64	Structures statistics, $Re_\tau = 180$ (Case III): spatial alignment, Zone 3	109
5.65	Structures statistics $Re_\tau = 180$ (Case III): Tilting angle	110
5.66	Structures statistics $Re_\tau = 180$ (Case III): Incidence angle	110
5.67	Structures statistics $Re_\tau = 180$ (Case III): Equivalent ellipsoid minor semi-axis	111
5.68	Structures statistics $Re_\tau = 180$ (Case III): Equivalent ellipsoid middle semi-axis	111
5.69	Structures statistics $Re_\tau = 180$ (Case III): Equivalent ellipsoid major semi-axis	112
5.70	Structures statistics $Re_\tau = 180$ (Case III): Equivalent ellipsoid volume deviation	112
5.71	Example of complex structures of plane channel at $Re_\tau = 180$ (Case III)	113
5.72	Typical structures elongated in stream-wise direction of plane channel at $Re_\tau = 180$ (Case III)	114
5.73	Equivalent ellipsoidal Structures Volume of plane channel at $Re_\tau = 180$ (Case III)	114
5.74	Structure statistics: Specific Vorticity and enstrophy; $Re_\tau = 180$ (Case III)	115
5.75	Structures statistics, lower half-channel: JPDF for structures vorticity. $Re_\tau = 180$ (Case III)	116
6.1	3-D overview of the field of detected structures of plane channel at $Re_\tau = 395$	127
6.2	Lateral overview of the field of detected structures of plane channel at $Re_\tau = 395$	127
6.3	Structures Volume of plane channel at $Re_\tau = 395$	128
6.4	Structures mass center of plane channel at $Re_\tau = 395$	128
6.5	Stream-wise advection of structures center of mass of plane channel at $Re_\tau = 395$	129
6.6	Structures statistics at $Re_\tau = 395$: length in wall units	130
6.7	Structures statistics: JPDF for structures extension, Zones 1 and 2. $Re_\tau = 395$	131
6.8	Structures statistics: JPDF for structures extension, Zone 3. $Re_\tau = 395$	132
6.9	Structures statistics, $Re_\tau = 395$: spatial alignment, Zones 1 and 2	133
6.10	Structures statistics, $Re_\tau = 395$: spatial alignment, Zone 3	134
6.11	Structures statistics $Re_\tau = 395$: Tilting angle	135
6.12	Structures statistics $Re_\tau = 395$: Incidence angle	135
6.13	Structures statistics $Re_\tau = 395$: Tilting angle, local percentages	136
6.14	Structures statistics $Re_\tau = 395$: Incidence angle, local percentages	136
6.15	Structures statistics $Re_\tau = 395$: Equivalent ellipsoid minor semi-axis.	137
6.16	Structures statistics $Re_\tau = 395$: Equivalent ellipsoid middle semi-axis.	137

6.17	Structures statistics $Re_\tau = 395$: Equivalent ellipsoid major semi-axis.	138
6.18	Structures statistics $Re_\tau = 395$: Equivalent ellipsoid volume deviation.	138
6.19	Structure statistics: Specific Vorticity and Enstrophy. $Re_\tau = 395$	139
6.20	Structures statistics lower half-channel: JPDF for structures vorticity, Zones 1 and 2	140
6.21	Structures statistics lower half-channel: JPDF for structures vorticity, Zone 3 .	141
6.22	3-D overview of the field of detected structures of plane channel at $Re_\tau = 590$	142
6.23	Lateral overview of the field of detected structures of plane channel at $Re_\tau = 590$	142
6.24	Structures Volume of plane channel at $Re_\tau = 590$	143
6.25	Structures mass center of plane channel at $Re_\tau = 590$	143
6.26	Stream-wise advection of structures center of mass of plane channel at $Re_\tau =$ 590. Number of bins 200, limits 3.71 . . . 22.11.	144
6.27	Structures statistics at $Re_\tau = 590$: length in wall units	145
6.28	Structures statistics: JPDF for structures extension. $Re_\tau = 590$, Zones 1 and 2	146
6.29	Structures statistics: JPDF for structures extension. $Re_\tau = 590$, Zone 3	147
6.30	Structures statistics, $Re_\tau = 590$: spatial alignment, Zones 1 and 2	148
6.31	Structures statistics, $Re_\tau = 590$: spatial alignment, Zone 3	149
6.32	Structures statistics $Re_\tau = 590$: Tilting angle	150
6.33	Structures statistics $Re_\tau = 590$: Incidence angle	150
6.34	Structures statistics $Re_\tau = 590$ (Case I): Tilting angle, local percentages	151
6.35	Structures statistics $Re_\tau = 590$: Incidence angle, local percentages	151
6.36	Structures statistics $Re_\tau = 590$: Equivalent ellipsoid minor semi-axis.	152
6.37	Structures statistics $Re_\tau = 590$: Equivalent ellipsoid middle semi-axis.	152
6.38	Structures statistics $Re_\tau = 590$: Equivalent ellipsoid major semi-axis.	153
6.39	Structures statistics $Re_\tau = 590$: Equivalent ellipsoid volume deviation.	153
6.40	Structure statistics: Specific Vorticity and Enstrophy, $Re_\tau = 590$	154
6.41	Structures statistics lower half-channel: JPDF for structures vorticity	155
6.42	Structures statistics lower half-channel: JPDF for structures vorticity	156
A.1	Anisotropic part of the resolved Reynolds stress tensor of plane channel at $Re_\tau = 180$ (Case II: refined grid) and total shear stress	163
A.2	Mean stream-wise velocity and rms of resolved turbulence of plane channel at $Re_\tau = 180$ (Case II: refined grid)	164
A.3	Budget of resolved turbulent kinetic energy of plane channel at $Re_\tau = 180$ (Case II: refined grid)	165
B.1	Anisotropic part of the resolved Reynolds stress tensor of plane channel at $Re_\tau = 180$ (Case IV: 4 th order) and total shear stress	166
B.2	Mean stream-wise velocity and rms of resolved turbulence of plane channel at $Re_\tau = 180$ (Case IV: 4 th order)	167
B.3	Budget of resolved turbulent kinetic energy of plane channel at $Re_\tau = 180$ (Case IV: 4 th order)	168

B.4	$Re_\tau = 180$ (Case IV: 4 th order), various plots	169
B.5	Structures statistics at $Re_\tau = 180$ (Case IV: 4 th order): length in wall units. .	170
B.6	Structures statistics: JPDF for structures extension. $Re_\tau = 180$ (Case IV: 4 th order). Left column zone 1, right column zone 2, xy -top, xz -middle and yz -bottom.	171
B.7	Structure statistics': Specific Vorticity (left) and enstrophy(right) for x (top), y (middle) and z (bottom). $Re_\tau = 180$ (Case IV: 4 th order).	172
B.8	Structures statistics, lower half-channel: JPDF for structures vorticity.Left zone 1, right zone 2, xy -top, xz -middle and yz -bottom. $Re_\tau = 180$ (Case IV: 4 th order)	173
C.1	Anisotropic part of the resolved Reynolds stress tensor of plane channel at $Re_\tau = 180$ (Case IV-B: 4 th order, $Css = 0.065$) and total shear stress	174
C.2	Mean stream-wise velocity and rms of resolved turbulence of plane channel at $Re_\tau = 180$ (Case IV-B: 4 th order, $Css = 0.065$)	175
C.3	Budget of resolved turbulent kinetic energy of plane channel at $Re_\tau = 180$ (Case IV-B: 4 th order, $Css = 0.065$)	176
D.1	Anisotropic part of the resolved Reynolds stress tensor of plane channel at $Re_\tau = 180$ (Case V-A: FSF) and total shear stress	177
D.2	Mean stream-wise velocity and rms of resolved turbulence of plane channel at $Re_\tau = 180$ (Case V-A: FSF)	178
D.3	Budget of resolved turbulent kinetic energy of plane channel at $Re_\tau = 180$ (Case V-A: FSF)	179
E.1	Anisotropic part of the resolved Reynolds stress tensor of plane channel at $Re_\tau = 180$ (Case V-A: NO) and total shear stress	180
E.2	Mean stream-wise velocity and rms of resolved turbulence of plane channel at $Re_\tau = 180$ (Case V-A: NO)	181
E.3	Budget of resolved turbulent kinetic energy of plane channel at $Re_\tau = 180$ (Case V-A: NO)	182
F.1	Mean stream-wise velocity and rms of resolved turbulence of plane channel at $Re_\tau = 180$ (Case V-A: NO)	183
G.1	Volume comparison between SGS models	184
G.2	JPF for structure extensions between SGS models: Zone 1, $L_x - L_y$ -I-	185
G.3	JPF for structure extensions between SGS models: Zone 1, $L_x - L_y$ -II-	186
G.4	JPF for structure extensions between SGS models: Zone 1, $L_x - L_z$ -I-	187
G.5	JPF for structure extensions between SGS models: Zone 1, $L_x - L_z$ -II-	188
G.6	JPF for structure extensions between SGS models: Zone 1, $L_y - L_z$ -I-	189
G.7	JPF for structure extensions between SGS models: Zone 1, $L_y - L_z$ -II-	190
G.8	JPF for structure extensions between SGS models: Zone 2, $L_x - L_y$ -I-	191

G.9 JPF for structure extensions between SGS models: Zone 2, $L_x - L_y$ -II-	192
G.10 JPF for structure extensions between SGS models: Zone 2, $L_x - L_z$ -I-	193
G.11 JPF for structure extensions between SGS models: Zone 2, $L_x - L_z$ -II-	194
G.12 JPF for structure extensions between SGS models: Zone 2, $L_y - L_z$ -I-	195
G.13 JPF for structure extensions between SGS models: Zone 2, $L_y - L_z$ -II-	196
G.14 JPF for structure extensions between SGS models: Zone 3, $L_x - L_y$ -I-	197
G.15 JPF for structure extensions between SGS models: Zone 3, $L_x - L_y$ -II-	198
G.16 JPF for structure extensions between SGS models: Zone 3, $L_x - L_z$ -I-	199
G.17 JPF for structure extensions between SGS models: Zone 3, $L_x - L_z$ -II-	200
G.18 JPF for structure extensions between SGS models: Zone 3, $L_y - L_z$ -I-	201
G.19 JPF for structure extensions between SGS models: Zone 3, $L_y - L_z$ -II-	202
G.20 JPF for vorticity components between SGS models: Zone 1, $\omega_x - \omega_y$ -I-	203
G.21 JPF for vorticity components between SGS models: Zone 1, $\omega_x - \omega_y$ -II-	204
G.22 JPF for vorticity components between SGS models: Zone 1, $\omega_x - \omega_z$ -I-	205
G.23 JPF for vorticity components between SGS models: Zone 1, $\omega_x - \omega_z$ -II-	206
G.24 JPF for vorticity components between SGS models: Zone 1, $\omega_y - \omega_z$ -I-	207
G.25 JPF for vorticity components between SGS models: Zone 1, $\omega_y - \omega_z$ -II-	208
G.26 JPF for vorticity components between SGS models: Zone 2, $\omega_x - \omega_y$ -I-	209
G.27 JPF for vorticity components between SGS models: Zone 2, $\omega_x - \omega_y$ -II-	210
G.28 JPF for vorticity components between SGS models: Zone 2, $\omega_x - \omega_z$ -I-	211
G.29 JPF for vorticity components between SGS models: Zone 2, $\omega_x - \omega_z$ -II-	212
G.30 JPF for vorticity components between SGS models: Zone 2, $\omega_y - \omega_z$ -I-	213
G.31 JPF for vorticity components between SGS models: Zone 2, $\omega_y - \omega_z$ -II-	214
G.32 JPF for vorticity components between SGS models: Zone 3, $\omega_x - \omega_y$ -I-	215
G.33 JPF for vorticity components between SGS models: Zone 3, $\omega_x - \omega_y$ -II-	216
G.34 JPF for vorticity components between SGS models: Zone 3, $\omega_x - \omega_z$ -I-	217
G.35 JPF for vorticity components between SGS models: Zone 3, $\omega_x - \omega_z$ -II-	218
G.36 JPF for vorticity components between SGS models: Zone 3, $\omega_y - \omega_z$ -I-	219
G.37 JPF for vorticity components between SGS models: Zone 3, $\omega_y - \omega_z$ -II-	220
G.38 Comparison for structures length in stream-wise between SGS models	221
G.39 Comparison for structures length in span-wise between SGS models	222
G.40 Comparison for structures length in wall-normal between SGS models plus position of mass center in wall-normal direction	223
G.41 Comparison for structures vorticity in stream-wise direction between SGS models	224
G.42 Comparison for structures vorticity in span-wise direction between SGS models	225
G.43 Comparison for structures vorticity in wall-normal direction between SGS models	226
G.44 Comparison for structures convection velocity in stream-wise direction between SGS models	227
G.45 Comparison for structures convection velocity in wall-normal direction between SGS models	228
G.46 Comparison for structures ΔV in stream-wise direction between SGS models	229

G.47	Comparison for structures ΔV in span-wise direction between SGS models . .	230
G.48	Comparison for structures ΔV in wall-normal direction between SGS models .	231
G.49	Comparison for structures enstrophy in stream-wise direction between SGS models	232
G.50	Comparison for structures enstrophy in span-wise direction between SGS models	233
G.51	Comparison for structures enstrophy in wall-normal direction between SGS models	234
H.1	Anisotropic part of the resolved Reynolds stress tensor of plane channel at $Re_\tau = 395$ and total shear stress	235
H.2	Mean stream-wise velocity and rms of resolved turbulence of plane channel at $Re_\tau = 395$	236
H.3	Budget of resolved turbulent kinetic energy of plane channel at $Re_\tau = 395$. .	237
I.1	Anisotropic part of the resolved Reynolds stress tensor of plane channel at $Re_\tau = 590$ and total shear stress	238
I.2	Mean stream-wise velocity and rms of resolved turbulence of plane channel at $Re_\tau = 590$	239
I.3	Budget of resolved turbulent kinetic energy of plane channel at $Re_\tau = 590$. .	240

1. INTRODUCTION

Since it was first recognized, turbulence has defied any complete definition:

Observe the motion of the water surface, which resembles that of hair, that has two motions: one due to the weight of the shaft, the other to the shape of the curls; thus, water has eddying motions, one part of which is due to the principal current, the other to the random and reverse motion. (Leonardo da Vinci 1510)

Under the practical point of view, the most visible and striking feature of turbulent flows would appear their exhibited unsteadiness and irregularity, leading to consider the details of their behavior random and unpredictable.

However, starting from the experiments of Brown and Roshko in 1975 (Brown and Roshko, 1975), the idea that there could be an underlying order in the chaos of the turbulence has gained momentum; the difficulty in the matter lying with its mix of deterministic organization together with chaotic features.

...frustration results largely from the mixture of chaos and order and the wide range of length and time scales that turbulent flows possess. (Moin and Mahesh, 1998)

The concept of an underlying deterministic structure of turbulent flow has been expressed by the definition of coherent structure, originally given by Hussain (Hussain, 1983, 1986):

A coherent structure is a connected turbulent fluid mass with instantaneously phase correlated vorticity over its spatial extend. ... We choose to designate the instantaneously space and phase-correlated vorticity as coherent vorticity. Thus, coherent vorticity is the primary identifier of coherent structures, which have distinct boundaries and independent territories.

Therefore, the understanding of the physics of the coherent structures and their interaction with the background motion is of paramount interest in turbulence research. Indeed, recently had been suggested by Farge (Farge et al., 1996) that separating and understanding the different physical behavior of coherent structures and un-coherent background might be the key to understand and predict the turbulence behavior.

Most previous studies on the topic followed the experimental approach: detection of coherent structures and deduction of their behavior alongside their physics are obtained by velocity measurements of the flow, applying point measurements as such Laser Doppler Velocimetry (LDV) (Lyn et al., 1995); multi-point point measurements such as a rack of Hot Wire (HW) probes (Hussain and Hayakawa, 1987); in plane measurements as such as Particle Image Velocimetry (PIV) (Scarano et al., 1999). Of course, in all the cases previously

considered, it is impossible to have simultaneous three-dimensional data to take into account the inherited three-dimensional nature of turbulent processes.

The fundamental advantage of the numerical approach, in the present case, is its capability to produce instantaneous, three-dimensional flow-fields. The tremendous potential of this approach was demonstrated by pioneering work of Robinson & al. (Robinson et al., 1990) who visualized the coherent structures in boundary layer flow over a flat plate.

This study was performed using flow-fields created by Direct Numerical Simulation (DNS) (Spalart, 1988) where all the turbulent scales down to the Kolmogorov scale are resolved.

While the advantages of DNS are evident and well known (Moin and Mahesh, 1998), its numerical costs are likely to confine its applications to Reynolds numbers (Re) and simple geometry for next future.

Simulation of flows at higher Re and complex geometry could be feasible applying Large Eddy Simulation (LES) (Rodi et al., 1997; Piomelli, 1997).

The basis of LES approach is the application of a filter operation to the Navier-Stokes equations to obtain the corresponding transport equation for filtered scales: scales larger than width of filter (grid scales) are resolved by numerical solution. Scales than smaller width of filter (sub-grid scales) are cut-off by filtering operation; effect sub-grid scales on the grid ones takes the form of stresses (sub grid stresses: SGS) and are modeled with an ad hoc model (sub-grid model). Under the physical point of view, the concept is to reproduce the different behavior of large eddies and small eddies in the transfer of turbulent kinetic energy (Tennekes and Lumley, 1983): assuming the spectrum of energy to have an equilibrium range, it can be supposed that smaller scales in this range are nearly isotropic in their behavior, and therefore easier to be modeled than the full turbulent field.

Available understanding of coherent structures shows that their size is considerably larger than the turbulent macro-scale, making permissible the application of LES to their simulation and study, with the advantage to be able to study their behaviour at higher Re and complex geometry.

Purpose of the present study is to validate the use of LES to the study of coherent structures in shear layer and apply it to different flow cases at high Re .

As previous studies have shown that structures characteristics are quite different for different classes of flow, notably between wall-bounded and free flows, three different cases will be considered, namely:

1. Attached wall-flows, for which plane channel at equilibrium will be adopted as test case
2. Free flows, for which case plane mixing layer will be studied

3. Separated flows; which will be represented by flow around a bluff body

All these three types of flow are investigated in order to find out the general and universal characteristics of the coherent structures.

The initial point of the present work is the Large Eddy Simulation code developed at the von Karman Institute (Simons, 2000).

Its fundamental features are:

- Finite differences
- Cartesian coordinates
- Staggered Grid Approach
- Second order accurate in space and time
- Filtering implicitly performed from finite differences
- Multi-Domain approach for not trivial geometries

In order to apply this code the study of the coherent structures the main task to be performed will be the development of:

- Algorithms for detection for the coherent structures in three-dimensional fields
- Statistical tool for analysis of the structures

These capabilities are implemented in a code treating structures defined on structured, Cartesian grids.

In order to assess the capability of LES to the study of coherent structures in general flows which cannot well be represented over Cartesian grids, a code which solves large-eddy equations in un-structured frame has been developed.

Present report is the subdivided in 3 volumes, each for the basic topics of the study.

Volume I Is devoted to the discussion of the structured code, the development of algorithm for detection and classification of the coherent structures and assess the result of its application to simulation of attached wall flow.

Volume II Covers the simulation of flow and coherent structures around the cylinder of square cross-section, and assess the performances of the present algorithms for wake flows.

Volume III Discusses the development and the performances of unstructured LES code.

Present Volume I, then, discusses basic elements of phomenology of coherent structures and all mathematical and statistical tools developed for they analysis. Performances of these algorithms, sensitivity of simulation to different physical and computational parameters and their influence on the definition the coherent structures are assessed in the case of plane turbulent channel at equilibrium.

The Volume is organized as:

- Theory of LES is briefly discussed in § 2
- Structured LES solver is presented in § 3
- Development of code for detection and analysis of coherent structures is presented in § 4
- Study of coherent structures in attached wall-flow is presented in § 5 and § 6
- Achieved conclusions are presented in § 7

2. LARGE-EDDY SIMULATION CONCEPT

2.1 Governing Equations

The Navier-Stokes equations provide a simplified, coarse-grained description of a Newtonian fluid flow and, despite the enormous simplification they represent respect of the molecular dynamics, contain all the relevant physics of the fluid at scales much larger than the mean free path of the molecules. As, *even the smaller scales occurring in a turbulent flow are ordinarily far larger than any molecular length scale* (Tennekes and Lumley, 1983) they allow to study and simulate and all the features of turbulent processes.

The present study is restricted to flows at low Mach numbers, where density and molecular viscosity can be assumed constant. In this case, the governing equations reduce to the well know incompressible Navier-Stokes equations for the conservation of mass and momentum, whose adimensional formulation is:

$$\frac{\partial u_i}{\partial x_i} = 0 \quad (2.1)$$

$$\frac{\partial u_i}{\partial t} + \frac{\partial u_i u_j}{\partial x_j} = -\frac{\partial P}{\partial x_i} + \frac{1}{Re} \frac{\partial^2 u_i}{\partial x_i \partial x_j} + f_i \quad (2.2)$$

where length: x_i , velocity: u_i and pressure: P are adimensionalized against a reference length δ_{ref} and velocity u_{ref} (superscript (*) denotes dimensional quantities):

$$x_i = \frac{x_i^*}{\delta_{ref}}; \quad u_i = \frac{u_i^*}{u_{ref}}; \quad t = \frac{t^* u_{ref}}{\delta_{ref}}; \quad P = \frac{P^*}{\rho u_{ref}^2} \quad (2.3)$$

and Re is the Reynolds number based on the above reference quantities.

$$Re = \frac{\delta_{ref} u_{ref}}{\nu} \quad (2.4)$$

2.2 Principles of Direct and Large-Eddy Simulation

Turbulence consists of a continuous spectrum of scales ranging in size from large scales of the same order of magnitude as the geometry of the flow to smallest scales whose corresponding Re is of the order of 1, which are also known as *Kolmogorov scale* (Tennekes and Lumley, 1983; Ferziger, 1997). Kolmogorov introduced the idea of an energy cascade (Fig. 2.1) which assumes that the turbulent energy produced by the largest turbulent structures is transferred, via the intermediate eddies, toward the smallest eddies where this it is dissipated by viscous effects.

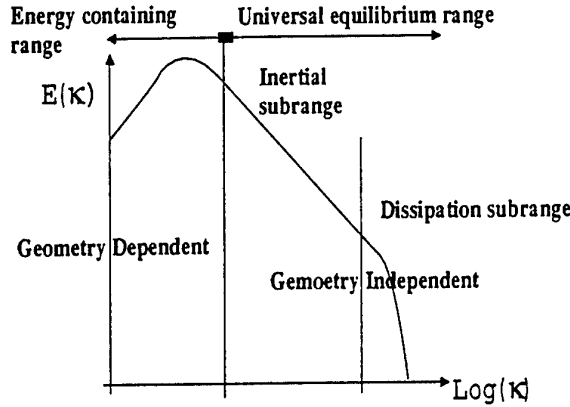


Fig. 2.1: Typical spectrum of kinetic energy of turbulent flows

Spectral analysis of kinetic energy associated with turbulent field E , versus wave-number k shows that, for flows characterized by developed turbulence, the length scales can be categorized into three distinct classes (Tennekes and Lumley, 1983; Ferziger, 1997):

1. **"Large" scales:** the integral length scales L in the flow are non-universal, highly anisotropic, due to the effect of the geometry on the flow. The wave numbers k are of the order of $2\pi/L$.
2. **"Medium" scales:** scales for which the energy spectrum $E(k)$ becomes more universal, moderately isotropic, and can be described by equation 2.5.

$$E(k) = C_K \bar{\epsilon}^{2/3} k^{-5/3} \quad (2.5)$$

where C_K is the Kolmogorov constant, ϵ is the dissipation rate.

3. **"Small" scales:** scales for which the energy spectrum $E(k)$ is universal, highly isotropic, and at which the energy is finally dissipated. The wave number is of the order $k = Re^{3/4} L^{-1}$.

Simulation of turbulence by numerical means then requires to solve the Navier-Stokes equations marching in time with a space discretization refined enough to resolve the smallest scales. Consequently Direct Numerical Simulation (DNS) is obviously the preferred tool for investigation of the physics of turbulence (Moin and Mahesh, 1998), and, in present case, for the study of the phenomenology of coherent structures.

However, its application is and is likely to remain, for some time, confined to flow at low Re and simple geometry, in view of the fact that the spatial resolution necessary for the

simulation of the smallest scales increases with $Re^{9/4}$ while the corresponding decreasing on the time scales leads the computer time of simulations to increase with a factor of Re^3 .

Simulations at higher Re (typically $Re > 10^4$, at present time) could be reasonably feasible only applying the Large Eddy Simulation (LES).

This modeling concept takes advantage of the different behavior of turbulence at largest and smallest scales (see above) to separate (Fig. 2.2) the large, highly anisotropic, energy carrying scales which are directly resolved from the small, nearly isotropic, energy dissipating scales which are modeled.

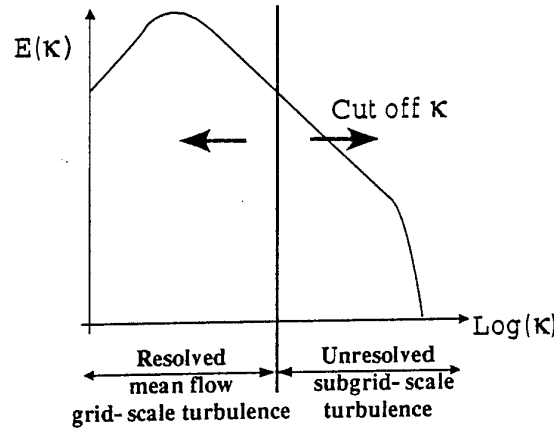


Fig. 2.2: Separation of grid-scale and sub-grid scale turbulence

Separation of the different scales is achieved applying a filtering operator, which takes the form a space filter expressed as a convolution integral (Germano, 1986, 1992).

$$\bar{u}_i(\vec{x}, t) = \iiint_V G(\vec{x} - \vec{\xi}, \Delta) u_i(\vec{\xi}, t) d^3\xi \quad (2.6)$$

In case of Finite Difference (FD) and Finite Volume discretization the well known "top hat" filter (Piomelli, 1997)

$$G(\vec{x} - \vec{\xi}, \Delta) = \begin{cases} 1/\Delta^3, & |\vec{x} - \vec{\xi}| \leq \Delta/2 \\ 0, & \text{otherwise} \end{cases} \quad (2.7)$$

is implicitly applied by the grid selected for the simulation, size of filter Δ corresponding to size of the grid Δx_i .

Concerning the formulation of spatial derivatives of filtered quantities it must remarked

that, on non-uniform grids, filtering and differentiation do commute only at a 2nd order commutative error (Ghosal and Moin, 1995), which should be taken in account, in case of application of discretization of order higher than 2.

Application of filtering operation to the incompressible Navier-Stokes equations, yields the LES equations:

$$\frac{\partial \bar{u}_i}{\partial x_i} = 0 \quad (2.8)$$

$$\frac{\partial \bar{u}_i}{\partial t} + \frac{\partial \bar{u}_i \bar{u}_j}{\partial x_j} = -\frac{\partial \bar{P}}{\partial x_i} + \frac{1}{Re} \frac{\partial^2 \bar{u}_i}{\partial x_j \partial x_j} + \bar{f}_i \quad (2.9)$$

where the over-bar denotes filtered (resolved) quantities. As resolved and un-resolved scales are defined by grid size, it is current to use the definition of “grid” and “sub-grid” scales for the two classes.

To express and solve the above equation in term of \bar{u}_i it is necessary to replace the term $\bar{u}_i \bar{u}_j$ by the one $\bar{u}_i \bar{u}_j$; the difference between the two terms takes the shape of a tensor

$$\tau_{ij} = \bar{u}_i \bar{u}_j - \bar{u}_i \bar{u}_j \quad (2.10)$$

which, by analogy with Reynolds tensor, is named “sub-grid stress” (SGS) tensor.

Equation 2.8 becomes

$$\frac{\partial \bar{u}_i}{\partial t} + \frac{\partial \bar{u}_i \bar{u}_j}{\partial x_j} = -\frac{\partial \bar{P}}{\partial x_i} + \frac{1}{Re} \frac{\partial^2 \bar{u}_i}{\partial x_j \partial x_j} - \frac{\partial \tau_{ij}}{\partial x_j} + \bar{f}_i \quad (2.11)$$

since each tensor can be decomposed in its isotropic and anisotropic components

$$\tau_{ij} = \tau_{ij}^{(a)} + \frac{1}{3} \tau_{kk} \delta_{ij} \quad (2.12)$$

and the isotropic part of the SGS tensor can be added to the pressure obtaining a *modified* pressure term

$$\bar{\varphi} = \bar{P} + \frac{1}{3} \tau_{kk} \quad (2.13)$$

Finally 2.8 becomes

$$\frac{\partial \bar{u}_i}{\partial x_i} = 0 \quad (2.14)$$

$$\frac{\partial \bar{u}_i}{\partial t} + \frac{\partial \bar{u}_i \bar{u}_j}{\partial x_j} = -\frac{\partial \bar{p}}{\partial x_i} + \frac{1}{Re} \frac{\partial^2 \bar{u}_i}{\partial x_j \partial x_j} - \frac{\partial \tau_{ij}^{(a)}}{\partial x_j} + \bar{f}_i \quad (2.15)$$

$$(2.16)$$

obviously, $\tau_{ij}^{(a)}$ must be modeled (SGS model) to close the problem.

The major advantage of LES concept with respect to Reynolds-averaged Navier-Stokes (RANS) approach lies on the fact that, while the latter attempts to model all turbulent scales, including the highly anisotropic scales of small wave-numbers, LES models only the effect, mostly dissipative, of smaller scales, which could be thought isotropic, at least in first approximation, and could, therefore, be expected to be easier to model.

It has to be remarked that, refining the grid (reducing filter size) size of $\tau_{ij}^{(a)}$ term reduces itself till all the relevant scales are captured and the DNS solution is recovered:

$$\bar{u}_i \cong u_i \quad (2.17)$$

2.3 SGS Modeling

As stated above, the τ_{ij} term, which must be somehow modeled, represents the interaction between the unresolved small scales and the resolved large scales. Different models are proposed by the current literature and is reviewed, among others, by Piomelli (1997); for the present study, the attention SGS model is justified by the need to verify to ensure that the simulated flow-field well reproduces the statistics of the turbulence and the need to assess the possible influence of SGS model on the simulation of structures themselves; therefore following discussion is confined with models actually applied in the frame.

SGS models can be sub-divided in two classes : fully dissipative and self-similar models.

2.3.1 Fully dissipative SGS models

Applying the classical concept of energy cascade, (Tennekes and Lumley, 1983), which assumes energy be transported from larger to smaller scales, energy transferred from grid scales to sub-grid scales could be considered a dissipation of energy; the task of a SGS model should be then to ensure the correct ratio of dissipation in the numerical solution of the transport equation of grid ones following the classical energy cascade concept (see Fig. 2.3).

Applying the classical concept of energy cascade, Tennekes and Lumley (1983), which assumes energy be transported from larger to smaller scales, energy transferred from grid scales

to sub-grid scales could be considered a dissipation of energy; the task of a SGS model should be then to ensure the correct ratio of dissipation in the numerical solution of equation 2.8. In this frame, the classical energy cascade concept would take form shown in Fig. 2.3.

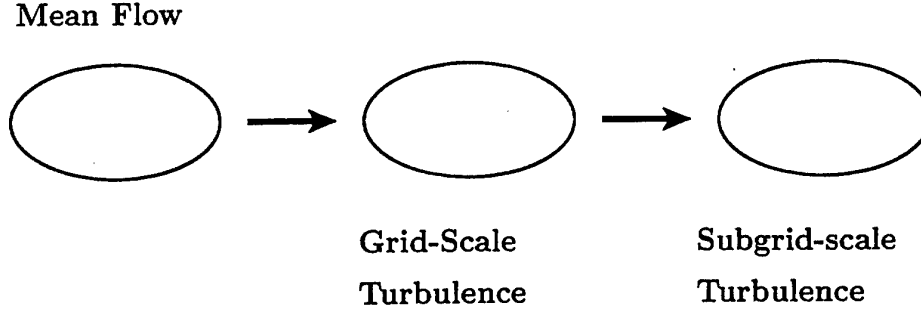


Fig. 2.3: Kinetic energy exchange between grid-scales and sub-grid scales

The simplest way to model a dissipation process is to consider it analogous to molecular one and model it through an Eddy viscosity concept (sub-grid viscosity):

$$\tau_{ij} = \frac{1}{3} \tau_{kk} \delta_{ij} - 2\nu_t \bar{S}_{ij} \quad (2.18)$$

It is to be noted that this modeling approach assumes *the turbulence to be in equilibrium*, i.e. production of turbulence locally balances its destruction. In other words, it is assumed the small scales of motion adjust instantaneously to the perturbations of the large scales implying the existence of an inertial sub-range.

2.3.1.1 Smagorinsky Model

By far, the most frequently applied SGS model is the one developed by Smagorinsky (1963). This model, based on dimensional arguments, assumes an Eddy viscosity based on local equilibrium. The model is based on the following quantities

$$\tau_{ij} = -2\nu_t \bar{S}_{ij} \quad (2.19)$$

$$\nu_t = C_s \bar{\Delta}^2 |S| \quad (2.20)$$

$$\bar{S}_{ij} = \frac{1}{2} \left(\frac{\partial \bar{u}_i}{\partial x_j} + \frac{\partial \bar{u}_j}{\partial x_i} \right) \quad (2.21)$$

$$|S| = \sqrt{2\bar{S}_{ij}\bar{S}_{ij}} \quad (2.22)$$

where \bar{S}_{ij} is the local strain rate tensor for the resolved scales velocity field, the filter size $\bar{\Delta}$ is taken to be proportional to the local grid spacing, and C_s is an empirical proportionality constant, which depends on the type of flow being modeled.

As it stands, it is evident that the Smagorinsky model suffers from two drawbacks.

First, the constant C_s is flow and grid dependent (Piomelli, 1997).

Second, the model does not account for the rapid decrease of length scales of turbulence approaching solid surfaces, and thus does not accurately represent the physics of the wall-layer. Therefore, a correction function must be added to account for the physical decrease of turbulence level nearing a solid boundary.

Wall correction usually takes the form of a van Driest damping function (eqn. 2.23).

$$\nu_t = C\bar{\Delta}^2 \left(1 - e^{-z^+/A^+}\right)^3 |\bar{S}| \quad (2.23)$$

where

$$z^+ = \frac{u_\tau z}{\nu}, \quad u_\tau = \sqrt{\frac{\tau_w}{\rho}}, \quad A^+ = 25 \quad (2.24)$$

2.3.1.2 Structure Function Model

Lesieur (1987) proposed a model of spectral turbulent viscosity. The idea is to find a relation between the length scale, ℓ , and the cutoff wave number, $k_c = (\pi/\Delta)$ as well as a relationship between the velocity, \vec{u} , with the cutoff kinetic energy, $E(k_c, t)$. A transformation from spectral space to physical space is achieved using the resolved second order Structure Function for the velocity vector \vec{u} , which can be expressed as

$$\bar{\mathfrak{S}}_2 = \langle \|u(x, t) - u(x + r, t)\|^2 \rangle \quad (2.25)$$

which could be related to local resolved strain rate and vorticity as

$$\bar{\mathfrak{S}}_2 = \Delta^2 \left(|\bar{S}|^2 + |\bar{\omega}|^2 \right) \quad (2.26)$$

$$\omega_{ij} = \frac{1}{2} \left(\frac{\partial \bar{u}_i}{\partial x_j} - \frac{\partial \bar{u}_j}{\partial x_i} \right) \quad (2.27)$$

$$|\bar{\omega}| = \sqrt{\bar{\omega}_{ij}\bar{\omega}_{ij}} \quad (2.28)$$

$$(2.29)$$

The corresponding SGS viscosity can be expressed as

$$\nu_{SGS} = C_{sf} \Delta \sqrt{\bar{\mathfrak{S}}_2}, \quad C_{sf} = 0.105 k_c^{-3/2} \quad (2.30)$$

Coefficient C_{sf} is obtained assuming a Kolmogorov cascade and is considered universal (Compte and Lesieur, 1998).

The resulting Structure function (FS) sub-grid model was shown (Compte and Lesieur, 1998) to be less dissipative than the Smagorinsky model.

An important improvement of this concept is the filtered structure function (FSF) (Compte and Lesieur, 1998) where a Laplacian filter Γ

$$\begin{aligned}\Gamma = & \\ & (f_{i+1,j,k} - 2f_{i,j,k} + f_{i-1,j,k}) + \\ & (f_{i,j+1,k} - 2f_{i,j,k} + f_{i,j-1,k}) + \\ & (f_{i,j,k+1} - 2f_{i,j,k} + f_{i,j,k-1})\end{aligned}\tag{2.31}$$

is thrice applied to the velocity field, to obtain the filtered structure function $\tilde{\mathfrak{S}}_2^{(3)}$ and its corresponding SGS viscosity

$$\nu_{SGS} = C_{FSF} \Delta \left[\tilde{\mathfrak{S}}_2^{(3)} \right]^{1/2}\tag{2.32}$$

The effect of the filtering is to enhance the contribution of the smallest resolved scales, which are known to be the most active in the interchange between resolved and unresolved fields. The coefficient C_{FSF} , which is again assumed universal, is optimized a priori, from benchmark numerical fields, to $C_{FSF} = 0.0084$.

Extensive in-house experience on FSF model (Hoffman, 1996) has shown it capable to yield quite satisfactory results and has been, therefore, applied in the present study.

2.3.1.3 Dynamic Model

A fundamental, inherent limitation of previous discussed SGS models lies with their dependence on a coefficient to be specified a priori, on the basis of type of flow and grid (Smagorinsky) or a priori optimization (structure function). This drawback could be overcome applying the dynamic procedure proposed by Germano et al. (1991) which allows to compute the model coefficient(s) dynamically in function of flow field, geometry and grid.

Dynamic procedure was, rightly, heralded as a major advance in theory and understanding SGS modeling, but extensive experience on different versions of dynamic Smagorinsky model have shown that, in application to wall-bounded flow it has yielded practical results which are not systematically better than ones yielded by basic Smagorinsky model (Akselvoll and Moin, 1995; Balaras, 1995; Cabot et al., 1999; Rodi et al., 1997). This finding was

confirmed by in-house experience (Laskowski, 1999; Simons, 2000), which led to avoid the application of this procedure for the present investigation.

2.3.1.4 Un-resolved DNS

It was often remarked in the literature that, in case of 2^{nd} order Finite Difference discretization LES equations, the contribution of SGS has the dimension of the leading term of the discretization error. Furthermore it was proposed (Ghosal, 1995) that this term is bigger than the one of model SGS.

If this is the case, it would be possible to perform LES without SGS model, solving eqn. 2.8 with

$$\tau_{ij}^{(a)} = 0 \quad (2.33)$$

and leaving the numerical error provides the necessary dissipation. Under the numerical point of view this simulation will correspond to a DNS over a grid too coarse to resolve the relevant scales, hence the naming for "un-resolved DNS" for this class of simulation.

It has to be stated that practical experience of present authors show LES to be sensible to effect of the SGS model, even for 2^{nd} order Finite Differencing, which will also be shown in § 5. On the other hand, it is actually possible to apply un-resolved DNS to flows close to equilibrium obtaining realization which are numerically stable and comparable with full LES (with SGS model). Therefore this approach represents an useful benchmark for the sensibility of results to the effect of SGS model and, for this reason, has been applied in present investigation.

2.3.2 Self-similar SGS models

It is well known (Härtel and Kleiser, 1998) that sub-grid viscosity cannot fully reproduce the actual behavior of sub-grid scales as put in evidence by DNS (Härtel and Kleiser, 1994), neither the effective process of energy transfer between the resolved and unresolved scales. This process can better understood considering the transport equation for the resolved turbulent kinetic energy:

$$\frac{\partial \bar{q}^2}{\partial t} + \frac{\partial \bar{q}^2 \bar{u}_j}{\partial x_j} = \frac{\partial}{\partial x_j} \left(-2\bar{p}\bar{u}_j - 2\tau_{ij}\bar{u}_i + \frac{1}{Re} \frac{\partial \bar{q}^2}{\partial x_j} \right) - \frac{2}{Re} \frac{\partial \bar{u}_i}{\partial x_j} \frac{\partial \bar{u}_i}{\partial x_j} + 2\tau_{ij}\bar{S}_{ij} \quad (2.34)$$

where the last two terms represent the production and destruction of resolved kinetic energy, whereas the other terms redistribute energy via advection and diffusion (Härtel and Kleiser, 1994). It is important to note that the last term can be positive, corresponding to a reverse

flow of energy from the small scales to the large scales, phenomenon commonly referred to as backscatter. It is found that, in case of wall-bounded flows, this process is primarily present and important in the buffer region of the wall layer, that is the region near a solid surface where $7 \leq z^+ \leq 20$. Therefore, sub-grid viscosity models will never be able to fully reproduce the behavior of sub-grid scales in wall layer (Härtel and Kleiser, 1994).

In this optic, a more physical model for interaction of grid and sub-grid scales could be the one proposed by Härtel and Kleiser (1994) and shown in Fig. 2.4.

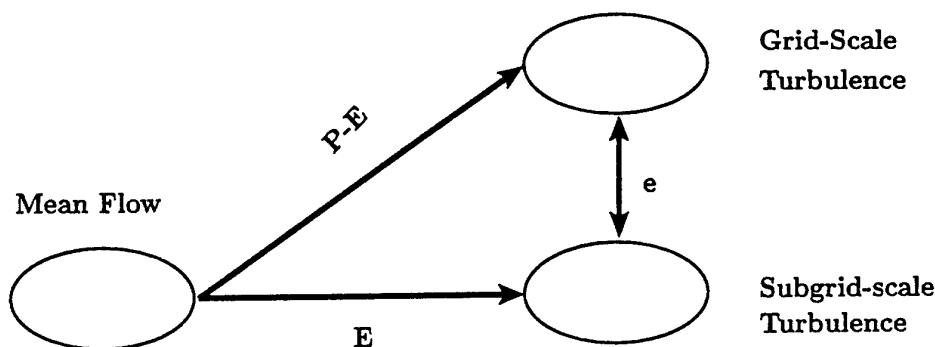


Fig. 2.4: Kinetic energy interchange between grid-scales and sub-grid scales. (P=turbulent production, E=turbulent dissipation, e=interchange)

where turbulent kinetic energy can flow from grid scales to sub-grid scales (forward scatter) and from sub-grid scales to grid scales (backward scatter).

This mechanism could be taken in account with applying self-similarity concept of SGS model (Meneveau and Katz, 2000).

This approach is based on the observation that most of the interchange between the resolved and unresolved scales happens between the smallest resolved scales and the biggest unresolved scales. Furthermore, these two families of scales exhibit similar behavior, due to the fact that the filter which artificially separate the inertial range (Fig. 2.2) and is the actual size of the filter which causes a scale belong to one of these two fields.

Self-similarity of smallest of the resolved scales and the biggest of unresolved scales could be in evidence with second filtering operation over the flow field (Fig. 2.5)

$$\overline{\overline{f}} \quad (2.35)$$

where f is a general operator.

Bardina's basic proposal (Bardina et al., 1984) is to filter the resolved field

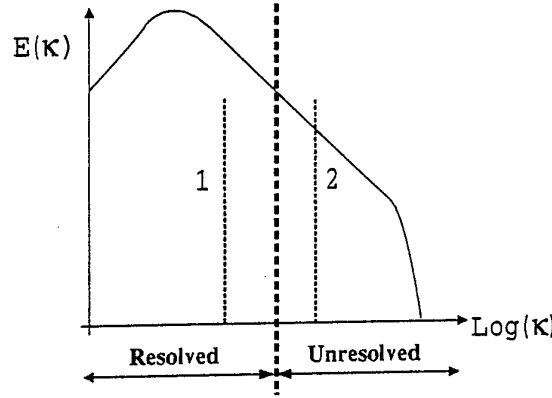


Fig. 2.5: Region of interaction between smallest resolved scales (1) and biggest unresolved scales (2)

$$\tau_{ij} = \overline{\overline{u_i u_j}} - \overline{u_i} \overline{u_j} \quad (2.36)$$

This approach has shown its capability to reproduce the physics sub-grid scales, but was found unable to create an adequate dissipation at the level of grid scales (Moin and Mahesh, 1998; Piomelli, 1997), and usually supplemented by dissipative term in form of sub-grid viscosity, to obtain the “Mixed model”

$$\tau_{ij} = \overline{\overline{u_i u_j}} - \overline{u_i} \overline{u_j} - \nu_{sgs} S_{ij} \quad (2.37)$$

$$(2.38)$$

where ν_{sgs} can be obtained with Smagorinsky model or through dynamic procedure Moin and Mahesh (1998).

Further analysis of filtering approach led the conclusion Domaradzki and Saiki (1997); Domaradzki and C. (1999); Moin and Mahesh (1998) that this operation should be, in principle, applied to the fully flow field u_i because main interactions are localized between the smallest resolved scales and the unresolved scales of sizes $\frac{\Delta}{2} < l < \Delta$.

In this optics Bardina’s model could be seen to approximate total u_i on the basis of $\overline{u_i}$

$$u_i \approx \overline{u_i} \quad (2.39)$$

Following this reasoning, different proposals Domaradzki and Saiki (1997); Domaradzki

and C. (1999); Shah and Ferziger (1995) have been made to obtain an estimation \tilde{u}_i of u_i from \overline{u}_i .

In particular, the proposition of Shah and Ferziger (1995) is to apply to a top-hat filter to \overline{u}_i to obtain a 3-diagonal systems in \tilde{u}_i

$$\overline{u}_i = a_{i-1}\tilde{u}_{i-1} + a_i\tilde{u}_i + a_{i+1}\tilde{u}_{i+1} \quad (2.40)$$

where \tilde{u}_i is an approximation to the FULL flow-field u_i .

It is stated (Shah and Ferziger, 1995) that this formulation produces enough dissipation to make unnecessary the SGS diffusivity term. This model was intensively tested in-house Louda (2001) and found to yield better representation of resolved scales than the one produced by sub-grid viscosity models at higher Reynolds number, although its computational cost makes it prohibitive for baseline SGS model for the complete study. It will be applied to assess the effect of sub-grid viscosity model on simulation of coherent structures.

3. NUMERICAL SOLUTION OF LES EQUATIONS

3.1 Time-Integration

Paramount influence of accuracy of discretization on LES (Ghosal, 1995) and, in consequence, on simulation of coherent structures, leads to the need of discussing in depth the numerical formulations applied in the present study.

As seen in 2.1 , transport equations for resolved scales take the form

$$\frac{\partial \bar{u}_i}{\partial x_i} = 0 \quad (3.1)$$

$$\frac{\partial \bar{u}_i}{\partial t} + \frac{\partial \bar{u}_i \bar{u}_j}{\partial x_j} = -\frac{\partial \bar{\rho}}{\partial x_i} + \frac{1}{Re} \frac{\partial^2 \bar{u}_i}{\partial x_j \partial x_j} - \frac{\partial \tau_{ij}^{(a)}}{\partial x_j} + \bar{f}_i \quad (3.2)$$

to be solved by numerical means.

The momentum equation can be re-written in functional form

$$\frac{\partial \bar{u}_i}{\partial t} = -\frac{\partial \bar{\rho}}{\partial x_i} + H(\bar{u}_i, \bar{u}_j) \quad (3.3)$$

where $H(\bar{u}_i, \bar{u}_j)$ contains the advective $C(\bar{u}_i, \bar{u}_j)$ and the diffusive $D(\bar{u}_i)$ operators

$$H(\bar{u}_i, \bar{u}_j) = -\frac{\partial \bar{u}_i \bar{u}_j}{\partial x_j} + \frac{\partial}{\partial x_j} \left(\frac{1}{Re} \frac{\partial \bar{u}_i}{\partial x_j} - \tau_{ij}^{(a)} \right) = C(\bar{u}_i, \bar{u}_j) + D(\bar{u}_i) \quad (3.4)$$

In the present code, the above equations are solved advancing in time, applying the second order accurate Adams-Bashforth algorithm (Balaras, 1995; Hoffman, 1996), which can be written as

$$\frac{\bar{u}_i^{n+1} - \bar{u}_i^n}{\Delta t} = \frac{3}{2} H(\bar{u}_i^n, \bar{u}_j^n) - \frac{1}{2} H(\bar{u}_i^{n-1}, \bar{u}_j^{n-1}) - \frac{\partial \bar{\rho}^{n+1}}{\partial x_i} \quad (3.5)$$

This formulation involves four unknowns at the time level $n+1$: u, v, w , and p , and only three transport equations for the three components for momentum. Matter of fact, in incompressible flows the unsteady Navier-Stokes equations involves temporal derivatives in the momentum equation but not in the mass equation. In consequence, the divergence of the velocity field appears only as a constraint on the solution of the momentum equations. This constraint is satisfied during time integration applying the fractional time step

approach (Chorin, 1968; Ferziger and Peric, 1997). This procedure consist of two successive steps: predictor and corrector step.

To estimate the velocity field at time-step $n + 1$, the predictor step computes an intermediate velocity field $\bar{u}_i^{n+\frac{1}{2}}$, applying the pressure field at time level n

$$\frac{\bar{u}_i^{n+frac{1}{2}} - \bar{u}_i^n}{\Delta t} = \frac{3}{2}H(\bar{u}_i^n, \bar{u}_j^n) - \frac{1}{2}H(\bar{u}_i^{n-1}, \bar{u}_j^{n-1}) - \frac{\partial \bar{\varphi}^n}{\partial x_i} \quad (3.6)$$

the resulting $\bar{u}_i^{n+frac{1}{2}}$ is not divergence-free.

The final, divergence free, solution is imposed in the corrector step, which is the difference of the two previous equations:

$$\frac{\bar{u}_i^{n+1} - \bar{u}_i^{n+\frac{1}{2}}}{\Delta t} = -\frac{\partial}{\partial x_i} (\bar{\varphi}^{n+1} - \bar{\varphi}^n) = -\frac{\partial \delta \bar{\varphi}}{\partial x_i} \quad (3.7)$$

while the divergence-free constraint is applied through a pressure Poisson equation whose the source term is supplied by the divergence operator for the intermediate velocity

$$\nabla \cdot \bar{u}_i^{n+1} = \nabla \cdot \bar{u}_i^{n+\frac{1}{2}} - \Delta t \nabla \cdot \left(\frac{\partial \delta \bar{\varphi}}{\partial x_i} \right) = 0 \quad (3.8)$$

Imposing the final solution to be divergence-free:

$$\nabla \cdot \bar{u}_i^{n+1} = 0 \quad (3.9)$$

the above can rewritten as

$$\frac{\partial^2 \delta \bar{\varphi}}{\partial x_i^2} = \frac{1}{\Delta t} \frac{\partial \bar{u}_i^{n+\frac{1}{2}}}{\partial x_i} \quad (3.10)$$

to find $\frac{\partial \delta \bar{\varphi}}{\partial x_i}$ and solve the corrector step.

Finally, the pressure field is updated

$$\bar{\varphi}^{n+1} = \bar{\varphi}^n + \delta \bar{\varphi} \quad (3.11)$$

In this form the velocity is explicitly solved whereas the pressure is solved implicitly. It should again be noted that, in this frame, $\bar{\varphi}$ is no more the adimensional form of the thermodynamic pressure, but a modified pressure containing the isotropic part of the SGS

stress tensor. Solving this modified pressure implicitly does not require the knowledge of the isotropic part of the SGS tensor but in the same time make more difficult compare results based on the pressure field. As the velocity is solved through a fully explicit algorithm (for viscous and advective terms), the permissible time step is limited by stability considerations based on both convection (C) and diffusion (D). Typical limits for Δt for Adams-Bashforth algorithm for present application are

$$\text{Convection} \rightarrow \Delta t_c \left(\frac{|\bar{u}_i|}{\Delta x_i} \right)_{\max} \leq 0.35 \quad (3.12)$$

$$\text{Diffusion} \rightarrow \nu_T \left(\frac{\Delta t_v}{\Delta x_i^2} \right)_{\max} \leq 0.1 \quad (3.13)$$

where ν_T is the sum of the molecular and SGS viscosity (obviously the SGS viscosity goes to zero for DNS simulations).

3.2 Spatial Discretization

In present investigation, LES equations are solved on stretched, orthogonal grids. Staggered grid is adopted to avoid the generation of spurious pressure oscillations associated with the solution of the incompressible Navier-Stokes equations on collocated grids (Ferziger and Peric, 1997). Fig. 3.1 shows the locations of u, v, w and p : pressure is located at the cell center and the velocity components are located at the corresponding flux surfaces.

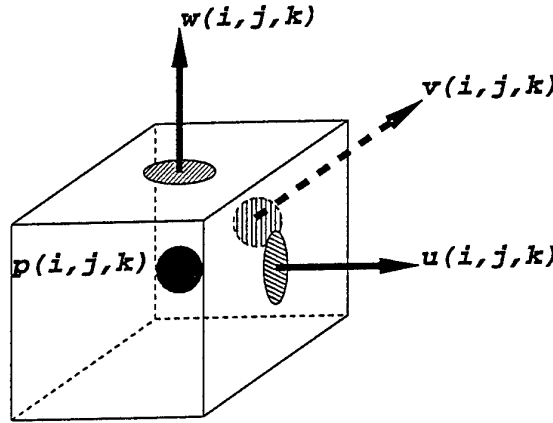


Fig. 3.1: Location of the velocity coordinates and pressure on a staggered grid

The Arakawa (1966) form of the advection term is adopted to minimize aliasing errors, which result from misrepresentation of shorter waves by the grid (Hoffman, 1996).

$$\frac{\partial \overline{u_i} \overline{u_j}}{\partial x_j} = \frac{1}{2} \left(\frac{\partial \overline{u_i} \overline{u_j}}{\partial x_j} + \overline{u_j} \frac{\partial \overline{u_i}}{\partial x_j} + \overline{u_i} \frac{\partial \overline{u_j}}{\partial x_j} \right) \quad (3.14)$$

This formulation imposes an integral constraint of mean kinetic energy by treating the advective terms as the average between the divergence and conservative form. In the most common approach, spatial derivatives are discretized applying 2nd order central finite differences. Staggered set-up needs the definition of velocities on the faces of cell velocity as shown in Fig. 3.2.

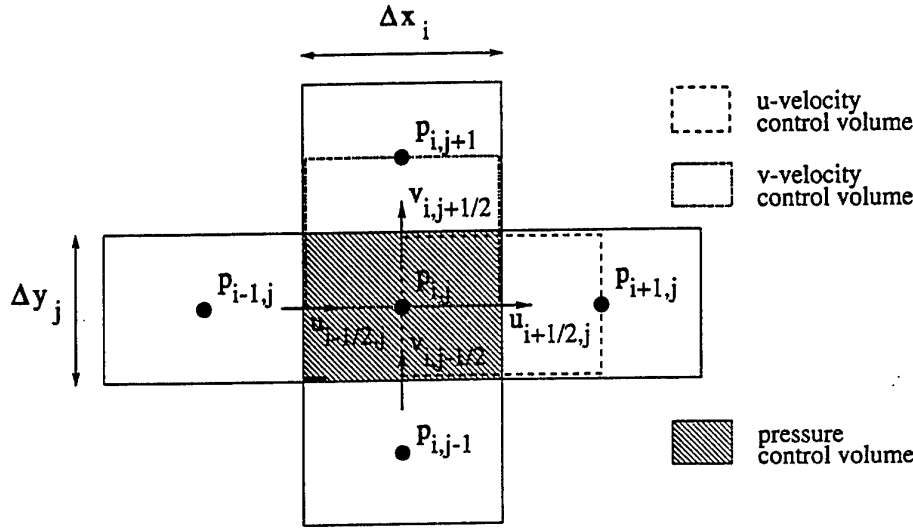


Fig. 3.2: Cell and flux surfaces for velocity component $\overline{u_i}$

The advective term is discretized as

$$\frac{\partial \overline{u_i} \overline{u_j}}{\partial x_j} = \frac{\overline{u_i}|_j^+ \overline{u_j}|_i^+ - \overline{u_i}|_j^- \overline{u_j}|_i^-}{\Delta x_j} \quad (3.15)$$

where $\overline{u_j}|_i^\pm$ denotes the interpolation of the j component of velocity in the i direction at the \pm flux surface. For the present investigation, linear interpolations are applied, to maintain 2nd order accuracy for the derivative at the velocity location.

Following the same approach, the molecular diffusive fluxes are discretized as

$$\frac{\partial^2 \overline{u_i}}{\partial x_j \partial x_j} = \frac{\partial}{\partial x_i} \left(\left. \frac{\partial \overline{u_i}}{\partial x_j} \right|_j^+ - \left. \frac{\partial \overline{u_i}}{\partial x_j} \right|_j^- \right) \quad (3.16)$$

where 2nd second order discretization is used for the first derivative $\frac{\partial \overline{u_i}}{\partial x_j}$ at flux surfaces.

Finally, the pressure gradient is discretized as:

$$\left. \frac{\partial \bar{\varphi}}{\partial x_i} \right|_{i+\frac{1}{2},j,k} = \frac{\bar{\varphi}_{i+1,j,k} - \bar{\varphi}_{i,j,k}}{x_{i+1,j,k} - x_{i,j,k}} \quad (3.17)$$

The limitations of second order discretization for LES are well known (Baggett et al., 1997). Therefore a fourth order discretization was also applied to assess the influence of numerical accuracy on simulation of coherent structures.

In present approach, fourth order accuracy is obtained applying the procedure proposed by Verstappen and Veldman (1997), where advective and diffusive flux are computed not only on the basic cell (Fig. 3.3), but also a superposed one, thrice bigger, one.



Fig. 3.3: Small and large grid for 4th order discretization

Linear interpolations are applied on both grids, corresponding to 2nd order accuracy on both grids.

$$\bar{u}_j^{\pm} = 0.5(\bar{u}_i + \bar{u}_{i\pm 2}) \quad (3.18)$$

Summing up the Right Sides calculated on the two grids, the final form is obtained

$$\frac{\partial \bar{u}_i}{\partial t} = \frac{9}{8} \left(-\frac{\partial \bar{\varphi}}{\partial x_i} + H(\bar{u}_i, \bar{u}_j) \right)_{smallgrid} - \frac{1}{8} \left(-\frac{\partial \bar{\varphi}}{\partial x_i} + H(\bar{u}_i, \bar{u}_j) \right)_{widegrid} \quad (3.19)$$

which yields, on weak stretched grids, fourth order accuracy for final solution.

The method proposed (Verstappen and Veldman, 1997) is based on the Richardson Extrapolation. Considering a second order central difference derivative on the usual stencil of 3 nodes

$$f'(x_i) = \frac{f(x_{i+1}) - f(x_{i-1}))}{2\Delta_x} + o1(\Delta_x^2) \quad (3.20)$$

and a generic stencil of $2 * j + 1$ nodes

$$f'(x_i) = \frac{f(x_{i+j}) - f(x_{i-j})}{2j\Delta_x} + o1(\Delta_x^2)j^2 \quad (3.21)$$

the Richardson extrapolation leads

$$f'(x_i) = \frac{j^2}{j^2 - 1} \frac{f(x_{i+1}) - f(x_{i-1})}{2\Delta_x} - \frac{1}{j^2 - 1} \frac{f(x_{i+j}) - f(x_{i-j})}{2j\Delta_x} + o2(\Delta_x^4) \quad (3.22)$$

Spectral behavior of the new formulation depends on the size of the new grid, its performances rapidly decaying with the increasing dimensions of the new grid. Remembering the implicit filtering performed from the finite differencing, eqn. 3.22 is equivalent to a new transfer function $G(r)$ (Fig. 3.4)

$$f'(x_i) = \frac{9}{8} \frac{f(x_{i+1}) - f(x_{i-1})}{2\Delta_x} - \frac{1}{8} \frac{f(x_{i+3}) - f(x_{i-3})}{6\Delta_x} \quad (3.23)$$

$$f'(x_i) = \frac{d}{dx} \int_{-\infty}^{\infty} G(y - x_i) f(y) dx \quad (3.24)$$

$$G(r) = -\frac{1}{8} \frac{1}{2\Delta_x} H(\Delta_x - |r|) + \frac{9}{8} \frac{1}{3(2\Delta_x)} H(3\Delta_x - |r|) \quad (3.25)$$

used to compute the filtered energy spectra

$$\overline{E_{11}}(k) = |G''(k)|^2 E_{11}(k) \quad (3.26)$$

where $G''(k)$ is the Fourier pair of $G(r)$.

This form of discretization has been intensively tested in house tests and improved simulation of resolved turbulence was found for the lower range of Re examined. At higher Re the velocity spectra present a deviation from the normal behavior that prevents its use.

Both 2^{nd} and 4^{th} central schemes do not satisfy the monotonic property (see Hirsh (1990) for a classical discussion of the matter) and may introduce spurious minima and maxima ("wiggles") in the solution when applied to flows at high Re . The phenomenon can be minimized, or avoided, implementing upwind or upwind-biased discretizations (Hirsh, 1990) where the computational pencil is weighted in upstream direction. In the application, an upwind-biased 3^{rd} order (Kawamura et al., 1984) scheme is introduced. This scheme is made of the sum of a 5 points 4^{th} order central discretization $C^{4th}(f_{i-2}, f_{i-1}, f_i, f_{i+1}, f_{i+2})$ and a 4^{th} order dissipation $D^{4th}(f_{i-2}, f_{i-1}, f_i, f_{i+1}, f_{i+2})$

$$\frac{\partial f}{\partial x} = C^{4th}(f_{i-2}, f_{i-1}, f_i, f_{i+1}, f_{i+2}) + \alpha D^{4th}(f_{i-2}, f_{i-1}, f_i, f_{i+1}, f_{i+2}) \quad (3.27)$$

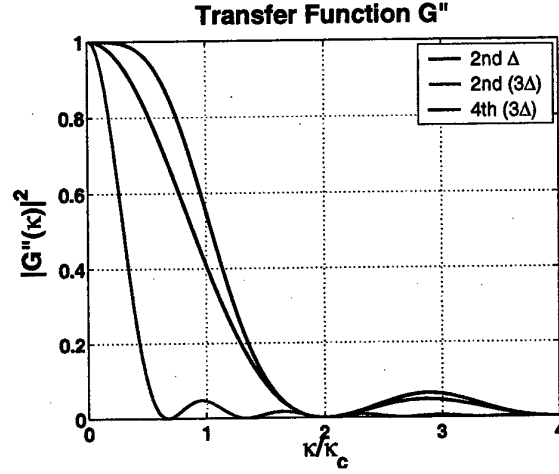


Fig. 3.4: Spectral behavior of $G(r)$

where $0 < \alpha < 1$ with $\alpha = 0$ yields central 4th order scheme and $\alpha = 1$ yields the full 3rd order up-wind scheme. While this scheme is not strictly monotonic, it was found adequate to control the formation of wiggles in present applications Hoffman (1996); Giammanco et al. (2001).

3.3 Multi-domain technique

Application of LES to flow around bodies, such as cylinder to be considered for the present study, poses challenging fundamental problems concerning the implementation of wall condition and economical solution of equation for the pressure.

In fact, Fast Poisson Solvers (FPS) (Schmidt et al., 1984) cannot directly be applied to this case and capacitance matrix technique, currently applied to extend FPS to complex geometries (Schmidt et al., 1984; Akselvoll and Moin, 1995), requires the solution of two Poisson problems over an enlarged domain including the actual computational field.

To overcome this problem, in present study, LES equations are solved applying the multi-domain (MD) technique. In MD approach, the computational field is sub-divided in a set of non-overlapping sub-domains and the original problem is decoupled in a set of two sub-problems: a sub-domain problem (consisting of a sub-set of decoupled problems, Fig. 3.5) and an interface condition (which ensures the appropriate coupling, Fig. 3.6).

The advantages of this procedure lie with the easiness of the description and discretization of complex geometries, good grid control, feasibility of parallel execution on multi-node computers (Simons, 2000), together with the possibility to work on simple sub-domains where Fast Poisson Solvers (FPS) could be applied.

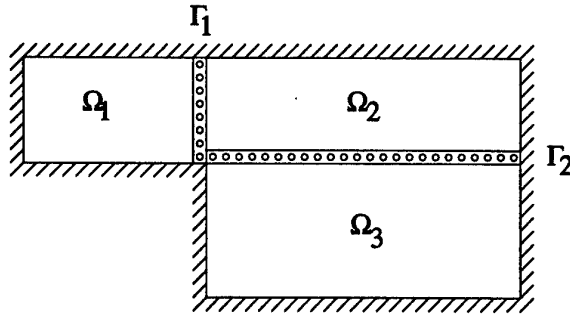


Fig. 3.5: Example of subdivision in 3 sub-domains $\Omega_1, \Omega_2, \Omega_3$ connected by interfaces Γ_1, Γ_2

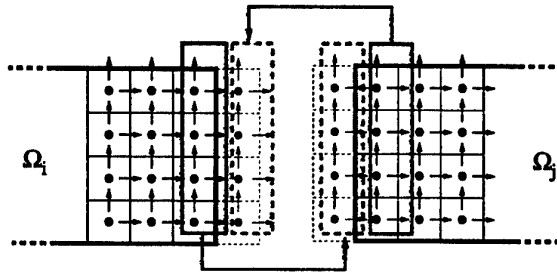


Fig. 3.6: Boundary points update at vertical interface between sub-domains Ω_i, Ω_j

The discretization of pressure in a multi-domain formulation is straightforward; it is nevertheless necessary to introduce some nomenclature: let x_Ω and x_Γ denote the solution vectors corresponding to the sub-domains and to the interfaces whose collection adds up to the original domain. In a collocated formulation the interface Γ is not well defined at discrete level (viz. there are no unknowns on the boundaries separating two sub-domains). Here Γ is defined as one (or more) layers of unknowns next to the boundary which are therefore eliminated from sub-domain count, where: $x = x_\Omega \cup x_\Gamma$.

Fourier expansion has been used for unknowns and right hand sides of the equations involved in the homogeneous span-wise direction y , so that the original three-dimensional Poisson problem is reduced to a set $N_{\frac{1}{2}}$ of two dimensional Helmholtz problems, which differ from each other exclusively for a parameter λ_m , which essentially depends on $m = 1, N_{\frac{1}{2}}$.

It must be noted that, because of the symmetry of the Fourier transformed equations, $N_{\frac{1}{2}}$ problems need to be solved. Ordering the unknowns in a domain wise fashion, followed by the inter-facial unknowns, and applying block Gaussian elimination to the original system of equations arising from the discretization, brings to the following system

$$\begin{pmatrix} a_{1,1} & \dots & 0 & a_{1,N} & \dots & a_{1,N+M} \\ \dots & \dots & \dots & \dots & \dots & \dots \\ 0 & \dots & a_{N,N} & a_{N,N+1} & \dots & a_{N,N+M} \\ 0 & 0 & 0 & s_{N+1,N+1} & \dots & s_{N+1,N+M} \\ 0 & 0 & 0 & \dots & \dots & \dots \\ 0 & 0 & 0 & s_{N+M,N+1} & \dots & s_{N+M,N+M} \end{pmatrix} \cdot \begin{pmatrix} x_{\Omega_1} \\ \dots \\ x_{\Omega_N} \\ x_{\Gamma_1} \\ \dots \\ x_{\Gamma_M} \end{pmatrix} = \begin{pmatrix} b_1 \\ \dots \\ b_N \\ \tilde{b}_{N+1} \\ \dots \\ \tilde{b}_{N+M} \end{pmatrix} \quad (3.28)$$

where $a_{i,i}$ is the matrix representing the discretization of the left sides of in Ω_i , N and M are, respectively, the number of sub-domains and interfaces number of unknowns, and $s_{i,i}$, $b_{i,i}$ are defined as

$$s_{ij} \equiv A_{ij} - \sum_{k=1}^N a_{ik} a_{kk}^{-1} a_{kj} \quad \forall i, j = N+1, N+M \quad (3.29)$$

$$\tilde{b}_j \equiv b_{ij} - \sum_{k=1}^N a_{jk} a_{kk}^{-1} b_k \quad \forall i, j = N+1, N+M \quad (3.30)$$

$$(3.31)$$

The interface unknowns can be determined from the lower right sub-block of

$$s \ x_{\Gamma} \equiv \begin{pmatrix} s_{N+1,N+1} & \dots & s_{N+1,N+M} \\ \dots & \dots & \dots \\ s_{N+M,N+1} & \dots & s_{N+M,N+M} \end{pmatrix} \cdot \begin{pmatrix} x_{\Gamma_1} \\ \dots \\ x_{\Gamma_M} \end{pmatrix} = \begin{pmatrix} \tilde{b}_{N+1} \\ \dots \\ \tilde{b}_{N+M} \end{pmatrix} \quad (3.32)$$

The sub-matrix s is generally referred to as the *Schur complement matrix*.

The connection between the sub-domain and interface unknowns, which is apparently lost, is now embedded in the right side of equation above.

To summarize, the solution algorithm reduces to the following a three-step procedure:

1. Separate solution of an elliptic problem in each of the sub-domains Ω_i , $i = 1, N$, using the original boundary conditions at the external boundaries, homogeneous Dirichlet boundary conditions at the internal boundaries and its original right sides.
2. Assembling of the right sides of the inter-facial problem using the previous step values, and solution of the Schur complement problem.
3. Separate solution of an additional elliptic problem in each of the sub-domains Ω_i , using the original boundary conditions at the external boundaries, original right sides b_i .

Although the overall cost of the elliptic kernel appears, at a first sight, more than doubled (two elliptic problems plus an interface problem of smaller size), this overhead is largely compensated by the fact that this approach not only allows to recover the use of fast Poisson solvers on rectangular domains (to tackle first and last step), but also opens the way to parallel execution.

Additionally, in an iterative solution context, it provides the opportunity of relaxing the stiffness of the full scale original problem (which is reduced to a set of smaller size, better conditioned sub-problems) and is intrinsically suited for zone approaches and heterogeneous problems.

For application of the LES, which effectively requires the solution of several elliptic equations with varying right sides for a large number of times steps, it can be argued that it is convenient and feasible to compute and store the inverse of the Schur matrix through a pivoted LU factorization procedure in a pre-processing step.

The overhead of the factorization will be quickly amortized over the large number of time steps necessary to build the statistics. It has to be underlined that, when the original problem is rank deficient, it will show up in step 2 of the MD algorithm and has therefore to be tackled. Present code keeps the capability to solve the discretized elliptic problems found in first and last step in a direct or iterative fashion (Simons, 2000).

Extensive previous testing on simulation of boundary layer (Schmidt et al., 1984) or flow over a backward looking step (Simons et al., 2001) has put in evidence the efficiency and accuracy of the procedure and it yielded satisfactory results in the present study (Giammanco et al., 2001).

4. COHERENT STRUCTURE CONCEPT

4.1 introduction

Introduction of coherent structure concept in the study of physics and phenomenology of turbulent flows was led by the observation (Brown and Roshko, 1975) that the ensemble of instantaneous, three-dimensional motions, which make turbulence (Tennekes and Lumley, 1983), contains events larger and longer lived than the scales of turbulent transport (Lesieur, 1987; Tennekes and Lumley, 1983).

These events were shown to have a level of internal organization much higher than turbulent background, leading to concept of *coherent structure*. Even if different definitions of coherent structure can be found in literature, the one proposed by Hussain (1986) and already cited in chapter 1 was found adequate for present purposes

A coherent structure is a connected turbulent fluid mass with instantaneously phase correlated vorticity over its spatial extend. ... We choose to designate the instantaneously space and phase-correlated vorticity as coherent vorticity. Thus, coherent vorticity is the primary identifier of coherent structures, which have distinct boundaries and independent territories.

As implied by the above definition, vorticity is considered the main physical parameter characterizing the phenomenon (Farge et al., 1996).

Paramount importance of coherent structures lies with the growing understanding of the existence of an underlying order in chaos-looking turbulence, the difficulty lying with identifying and assessing of respective effects of deterministic organization and chaos-like background and interaction.

...frustration results largely from the mixture of chaos and order and the wide range of length and time scales that turbulent flows possess. (Moin and Mahesh, 1998).

Coherent structures or *quasi-coherent* (this being the case for organization observed in space only (Robinson et al., 1990)) structures have been identified in a variety of turbulent shear layers. This type of organization is more evident in free layers, where most of flow activity re-organizes itself in very large, quasi-periodic, vortices such as those can be observed for mixing layers (Brown and Roshko, 1975), plane wakes (Hussain and Hayakawa, 1987), wakes behind a solid body (Lyn et al., 1995) and can be put in evidence by numerical simulation (Fig. 4.1).

Concerning wall layers, a variety of quasi-coherent structures was put in evidence for the case of attached boundary layer (Robinson et al., 1990; Spalart, 1988), and, in particular, the well known horse-shoe or hair-pin (depending on Reynolds number of flow) vortex has

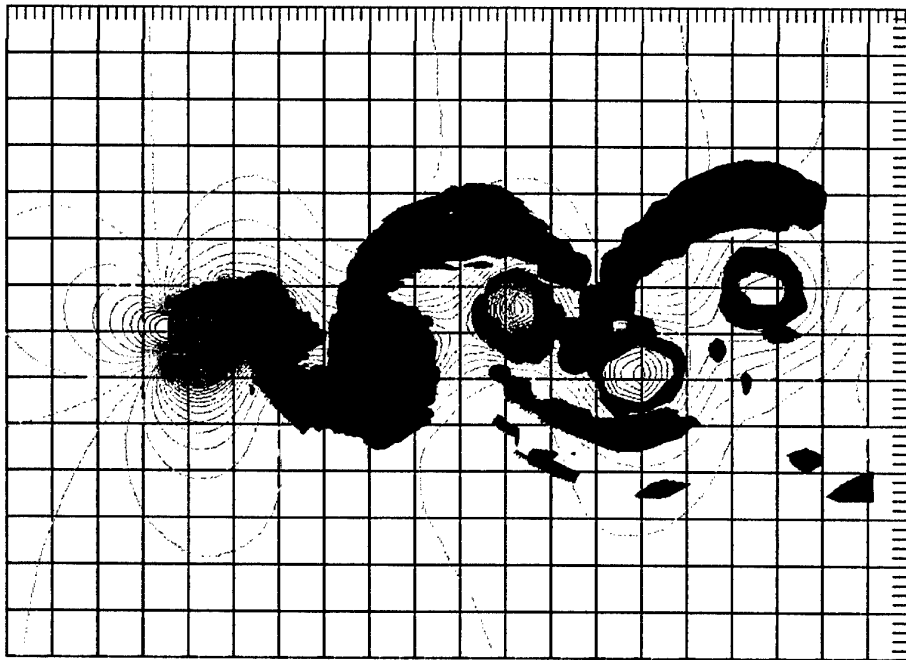


Fig. 4.1: Vortex structures in wake behind cylinder of square cross-section, $Re_H=22,000$. LES

drawn attention of researchers, being considered the typical structure associated to turbulence production in buffer layer (Fig. 4.2)

However, recent DNS(s) tend to indicate that the preferred organization in buffer and inertial layer consists of structures elongated in stream-wise direction (Chong et al., 1998; Jeong et al., 1997). This conclusion seem to be confirmed by recent in-house DNS (Rambaud, 2000) for plane channel at equilibrium, where “true” horse-shoe vortex seem to be relatively scarce (Fig. 4.3)

In case of separate wall flows, quasi-coherent structures have been put in evidence in case of backward facing step (Scarano et al., 1999).

Overall, the need to understand the physics of coherent structures and their influence on the average behavior of the flow is evident for all classes of flows.

To quote two opposite views of the matter: Hussain (1986) concludes that, in case of developed turbulence, behavior of coherent and un-coherent fields is similar, while Farge et al. (1996) takes the opposite view and proposes that understanding and, possibly, modeling the different physical behavior of coherent structures and un-coherent background might be the key to understanding and successful prediction of turbulence. In particular, Farge considers, on the basis of behavior of two-dimensional turbulence, that turbulent flow could be sub-

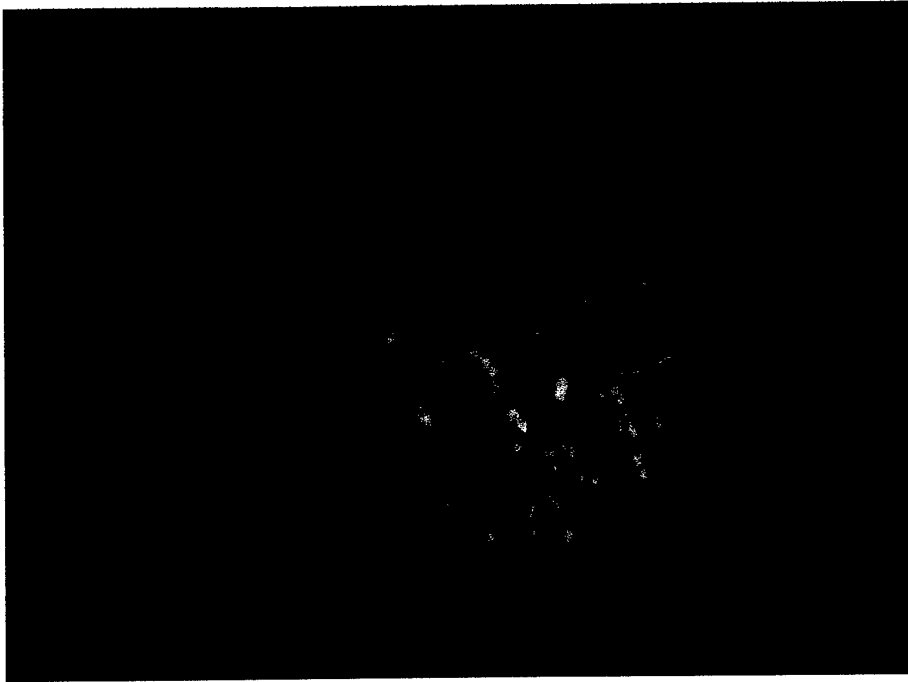


Fig. 4.2: Horse-shoe structure detected in plane channel at $Re_\tau=180$. DNS (Rambaud, 2001)

divided in *vorticity-dominated* regions, *strongly sheared* regions and *weakly sheared* regions, each of them characterized by different energy spectra, whose different characteristics are masked by statistical approach embodied by classical Kolmogorov spectrum (Tennekes and Lumley, 1983).

The considerations lead to the need to understand, not only shape and dynamics of typical structure, but also the quantitative effect of coherent structures on the overall behavior of turbulent field.

This being the case, it would appear that the numerical simulation would be, the most appropriate approach to this task, because it offers the possibility to access, identify and study all structures which might be present within flow-field under study.

4.2 Deduction of coherent structures

4.2.1 Detection criterion

Following the arguments presented in the previous paragraph, the basic problem would be to detect organized structures within three-dimensional instantaneous flow-fields produced by DNS and LES. It is clear, from the previous discussion, that any possible detection criterion would involve the gradients of velocity vector u_i . Therefore, the starting point should be the

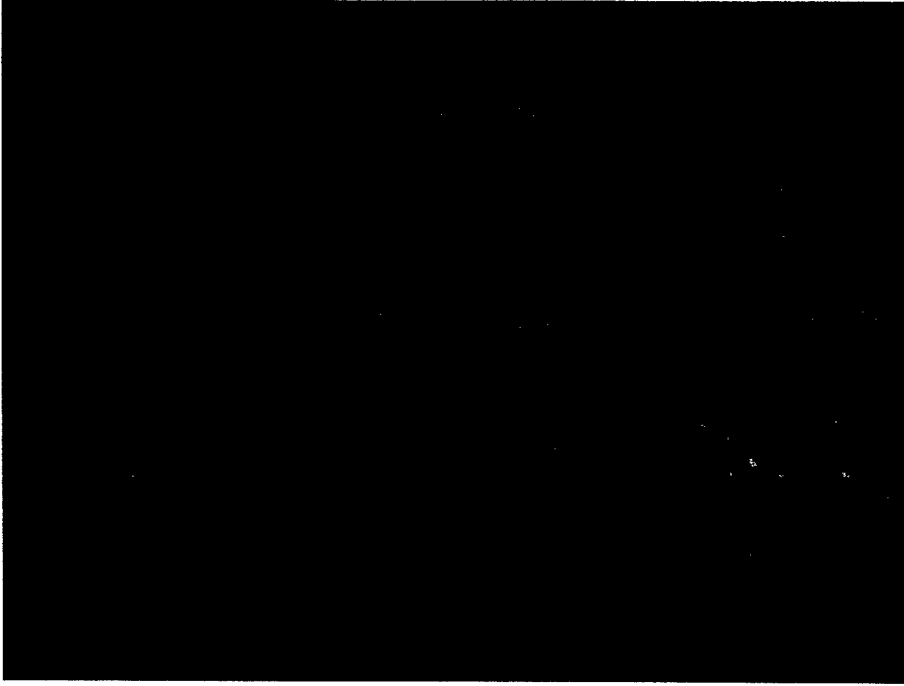


Fig. 4.3: Vortex structures detected in plane channel at $Re_\tau = 180$; Top view. DNS (Rambaud, 2000).

gradient tensor A of u_i .

Applying analysis and nomenclature proposed by Cantwell (1992) for A the basic operator to be considered would be

$$A = \nabla u_i; \quad A_{ij} = \frac{\partial u_i}{\partial x_j} \quad (4.1)$$

which can, obviously, be decomposed in symmetric rate strain tensor S

$$S_{ij} = \frac{1}{2} (A_{ij} + A_{ji}) \quad (4.2)$$

and anti-symmetric rate of rotation Ω

$$\Omega_{ij} = \frac{1}{2} (A_{ij} - A_{ji}) \quad (4.3)$$

The eigenvalues Λ of A are solution of the characteristic equation

$$\Lambda^3 + P\Lambda^2 + Q\Lambda + R = 0 \quad (4.4)$$

where

$$P = -S_{ii} \quad (4.5)$$

$$Q = \frac{1}{2}(P^2 - S_{ij}S_{ji} - \Omega_{ij}\Omega_{ji}) \quad (4.6)$$

$$R = \frac{1}{3}(-P^3 + 3PQ - S_{ij}S_{jk}S_{ki} - \Omega_{ij}\Omega_{jk}\Omega_{ki}) \quad (4.7)$$

Within this frame, three different detection algorithms can be found in present literature

1. “D” (Cantwell, 1992) criterion : in this case the discriminant D

$$D = \frac{27}{4}R^2 + Q^3 \quad (4.8)$$

of the above characteristic equation is tested. The region where D is strictly positive is supposed to contain the coherent structures.

2. “Q” (Hunt et al., 1988) criterion: in this case, the region where the second invariant of ∇u_i

$$Q = 1/2(\|S\|^2 - \|\Omega\|^2)^{1/2} \quad (4.9)$$

is positive.

3. λ_2 criterion (Jeong et al., 1997): in this case, a connected region where two of the three eigenvalues λ of the operator $S^2 + \Omega^2$ are negative is defined as “vortex core”; assuming $\lambda_1 > \lambda_2 > \lambda_3$, this definition leads to the criterion

$$\lambda_2 < 0 \quad (4.10)$$

for the detection of a “vortex core”. Focusing on the “vortex core” allows to separate true coherent vortices from other possible (incoherent) regions of high Ω .

It was pointed out by a very recent analysis (Rambaud, 2000), the three previous criteria correspond to three different concepts of organized vorticity

- D detects the regions where stream-lines are helicoidal

- Q detects the region where local vorticity are stronger than local shear
- λ_2 detects the regions of minimum pressure within the body of structure.

As found in (Rambaud, 2000) and in present study, these criteria do not necessarily yield coinciding results, as it will be discussed in Chapter 5.

4.3 Detection procedure

Under theoretical point, all the above-introduced criteria take the form of a test on the sign (positive or negative, depending on particular criterion selected) of a testing quantity, function of velocity gradients of the flow. This theoretical criterion must be integrated into a general procedure for detection and definition of organized structures in three-dimensional numerical flow-fields. Development and inner working of the resulting algorithm are presented and exemplified for the case of LES of plane channel at equilibrium, at $Re_\tau = 180$, discretized over a grid of $96 \times 128 \times 64$ points (Annex A); Q criterion is applied for purpose of presentation, but present processing and arguments lead to similar results applying λ_2 criterion, while D criterion yields remarkable different results, as it will be shown in Chapter 5.

The actual construction of structures in the simulated flow-field depends of discretization employed for the resolution the flow-field. In the case of present code (chapter 3), this is performed by finite differencing over staggered grid where the three components of velocity and the pressure are evaluated at different positions in the space (Fig. 3.1 in 3.2).

Since the pressure node is located at the center of the computational cell, it is natural to apply the detection algorithm at the pressure node and evaluate at this location the velocity derivatives used by the detection algorithm. Therefore, the initial result is a three-dimensional matrix $Q(x, y, z)$ located at the pressure nodes.

Theoretically, all the grid points where $Q > 0$ should be considered part of a coherent structure, but, under the practical point view, strict application of this criterion yields noisy fields, where it is impossible resolve the individual structures, as it can be seen in Fig. 4.4.

In order to avoid numerical noise created by values close to 0 it is necessary, as attested by current literature (Baggett et al., 1997), to introduce a threshold value ("trigger level", Tr), sufficiently higher than 0, above which the criterion is considered satisfied.

Choice of a trigger level, obviously, retains a degree of arbitrariness, but a sound criterion could be deduced from the analysis of the probability function (PDF) of Q (Fig. 4.5).

It can be observed from Fig. 4.5 that positive values of Q for global PDF span from 0 to 4000 (in wall units), while the region $Q < 10$ can be interpreted as a region of "white noise" which is strongly affected by precision of the simulation. Therefore, an useful trigger level

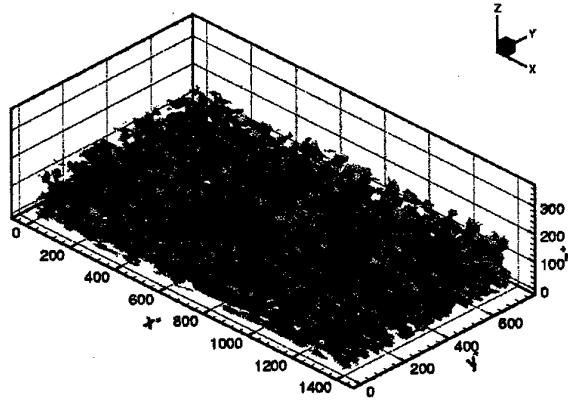


Fig. 4.4: Iso-surfaces of $Q = 5$; plane channel at equilibrium, at $Re_\tau = 180$; lower half channel.

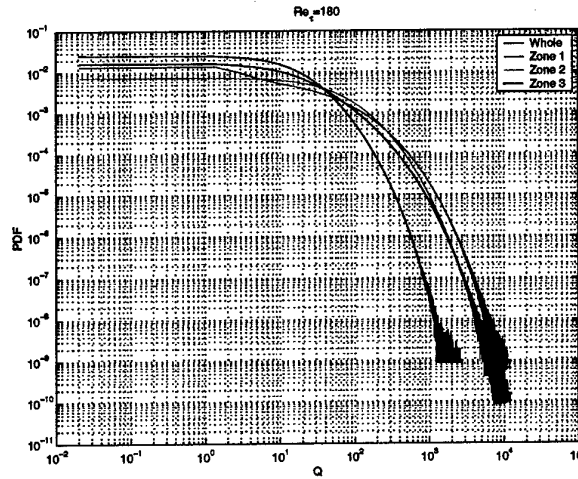


Fig. 4.5: PDF of Q for plane channel at equilibrium, at $Re_\tau = 180$. Zone 1: $0 < z^+ < 30$; Zone 2: $30 < z^+ < 100$; Zone 3: $z^+ > 100$

should be chosen above this range. As title of example, the effect of trigger levels $Tr = 91$ (Fig. 4.6) and (Fig. 4.7) $Tr = 200$ are presented and it can be remarked that this choice has paramount effect on the final result

It can be remarked that introduction of a trigger produces distinct and separate structures which could be identified and defined by an appropriate algorithm.

Further, the drastic decrease of population of structures with increasing Tr is evident. This effect can be appreciated applying the statistical tools to be presented in next paragraph: the percentage of volume of computational field where $Q > Tr$ for the two cases is summarized in Tab. 4.1, where a dramatic change of detected structures is evident.

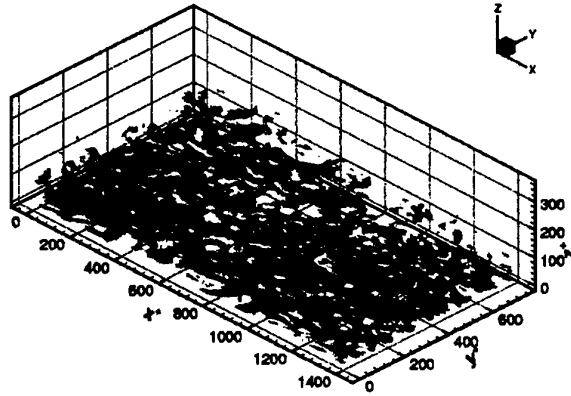


Fig. 4.6: Iso-surfaces of $Tr = 91$, plane channel at equilibrium, at $Re_\tau = 180$; lower half channel.

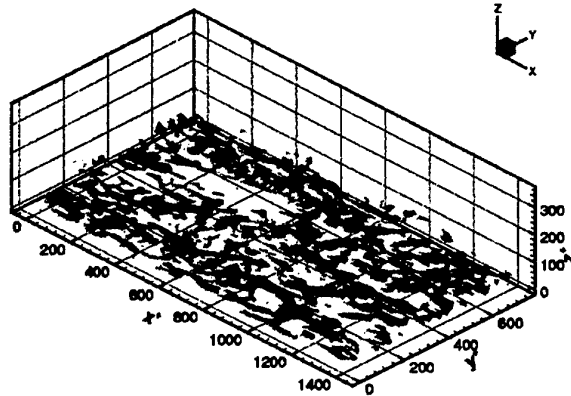


Fig. 4.7: Iso-surfaces of $Tr = 200$, plane channel at equilibrium, at $Re_\tau = 180$; lower half channel.

Table 4.1: Plane channel at equilibrium at $Re_\tau = 180$ (Example). Nominal structures percentage in volume

Trigger level Tr	Volume $Q > Tr$
91	11.33
200	5.1376

It has to be remarked that values quoted in Tab. 4.1 correspond to the volume having $Q > Tr$ without discerning whether this volume is made of only true structures or numerical noise as well; this matter will be discussed in next section.

The conclusion to be drawn is: selecting the lower value of trigger level, it is possible to find most of the structures possibly present in the field, while, applying the higher level only

the ones corresponding to strongest activities turbulent motions are retained.

In the second case, a sub-set of vortex structures is identified, whose characteristics are different of the overall average. Structures of this last family are mostly located in inner wall-layer ($z^+ \leq 50$), as it can be seen comparing the distribution of structures across the height of the channel for $Tr = 91$ and $Tr = 200$ (see Fig. 4.8).

It is important at this point, to stress the following concept: all the following plots, which show statistical properties such as single PDF, joint PDF are based on histograms. An histogram can be defined in different ways but the simplest one consists in choosing a series of equal-spaced data defining an interval called sampling bin. Considering a fixed interval to cover, higher is the number of points chosen to represent it, smaller is the size of the bin and smaller is the number of points that fell into this interval.

Using an histogram is nothing else than smoothing the raw data; this concept must be kept present, when examining, for example, at Fig. 4.8, where the number of points chosen and the interval to cover are clearly mentioned. The bin size is easily extrapolated from these two data.

At title of example, in aforementioned figure, ordinate axis represents a percentage. It represents, in detail, the percentage of structures which, in average, have their barycenter within the limits identified by the corresponding abscissa and the bin width. Decreasing the number of points would have meant increasing the bin width and therefore increasing the percentage associated to the same abscissa.

In any case, the discrete sum of the ordinates of the nodes it will always be 100, unless the plot is showing a zoom of a region of interest, which is usually the case for plot of vorticity, enstrophy and other dynamic quantities.

In the present investigation, the number of points has been chosen high enough to mimic the real behavior of the data, but with a bin size high enough to perform some smoothing of the results.

In the following, the number of bins taken and the interval they represent will be quoted in all plots, except when such information is not necessary.

Coming back to the examination of the two families of structures defined by the two different trigger levels, it can be observed that they have different physical properties, which is shown, for example, by the distribution of specific enstrophy (enstrophy of structure divided by the volume of the structure) over the population (Fig. 4.9).

Specific Enstrophy

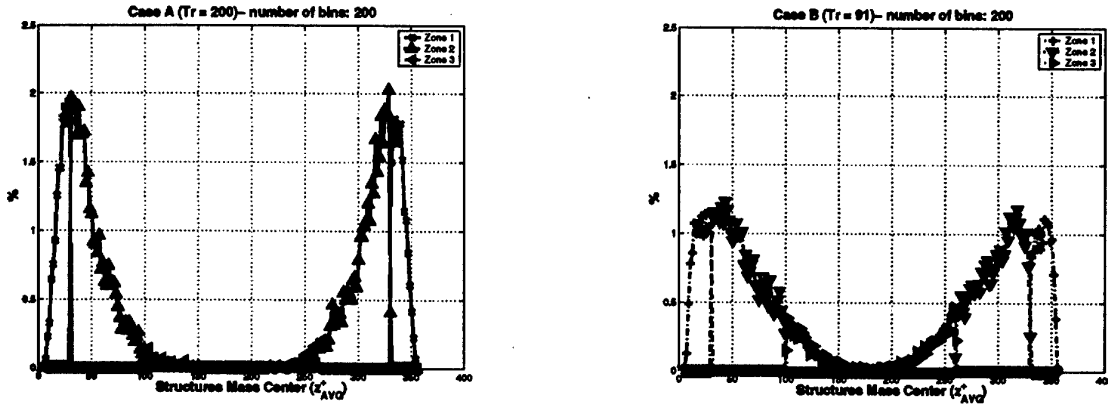


Fig. 4.8: Distribution of structures across the height of the channel at $Re_\tau = 180$ (Limits of histograms: 0 – 360). Left, $Tr = 200$. Right, $Tr = 91$

$$\frac{\iiint_{STR} \frac{1}{2} |\nabla \wedge \vec{V}|^2 dx dy dx}{\iiint_{STR} dx dy dx} \quad (4.11)$$

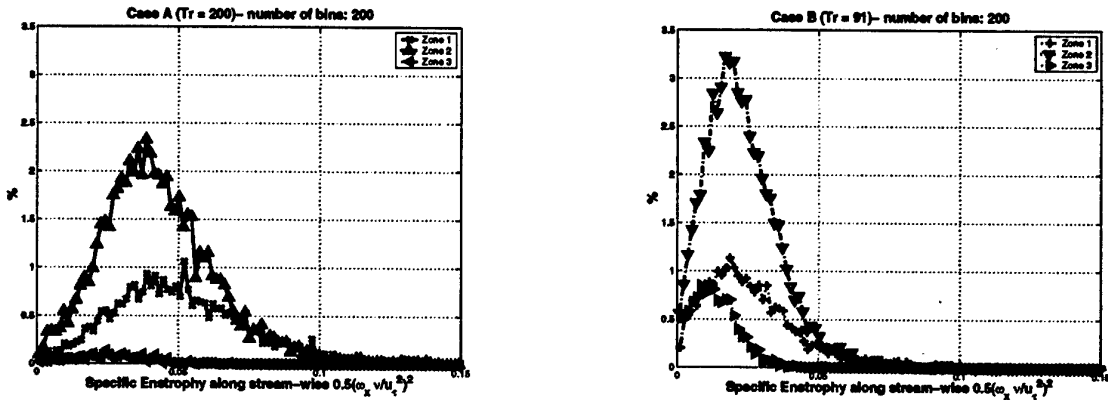


Fig. 4.9: Distribution of specific enstrophy of structures of a plane channel at equilibrium at $Re_\tau = 180$ (Limits of histograms: 0 – 0.3). Left, $Tr = 200$. Right, $Tr = 91$

It is possible to remarked the much higher of preferred level for distribution corresponding to $Tr=200$ (Fig. 4.9 left) compared with the one corresponding to $Tr=91$ (Fig. 4.9 right).

It can be concluded that choice of trigger level will always retain a certain level of user-choice, while it is feasible, and it might be useful, to separate a sub-set of structures and study them in comparison with the overall averages of the whole flow- field.

It is then evident that choice of trigger level will depend of the flow to be studied and the phenomenology to be put in evidence. In the case of attached wall layer, a strategy would

be to take in account the different behavior which are encountered in the 3 layers which can be identified moving away of the wall

Zone 1 Inner (Viscous-buffer) layer: $0 < z^+ < 30$

Zone 2 Inertial layer: $30 < z^+ < 100$

Zone 3 Wake region: $z^+ > 100$

As most of turbulent production is concentrated in the inertial layer, physics suggests that trigger level should be chosen to capture most of it process; concentration of structures of high specific enstrophy (Fig. 4.9) confirms this point. Therefore, a general procedure could be to start from the PDF for Zone 2 (Fig. 4.5) and choose a value Tr corresponding to a decrease of value of PDF by a decade. This choice is found to eliminate numerical noise due of the LES algorithm and yet retain the maximum of useful information. However, since the choice of this region retains somewhat arbitrary arbitrariness, it was thought safer to apply this criterion to the global PDF of the whole channel, and this procedure was scrupulously followed whenever possible, in the following.

In present case, this criterion would will produce a value $Tr = 91$, which is the one used for the left sides of Figs 4.8 and 4.9.

Structures found applying this trigger level have a content of enstrophy which is can be seen in Tab. 4.2 for the overall channel:

<i>Enstrophy_x</i>	<i>Enstrophy_y</i>	<i>Enstrophy_z</i>	<i>Enstrophy</i>
47.168	16.436	31.859	27.273

Table 4.2: Plane channel at equilibrium at $Re_\tau = 180$ (Example). Overall structures percentage in enstrophy

while, detail of Zone 2, which contains most of the activity, is presented in Tab. 4.3.

<i>Enstrophy_x</i>	<i>Enstrophy_y</i>	<i>Enstrophy_z</i>	<i>Enstrophy</i>
82.882	63.080	64.252	69.812

Table 4.3: Plane channel at equilibrium at $Re_\tau = 180$. (Example) Zone 2 structures percentage in enstrophy

showing the capability this procedure to isolate the relevant physical quantities for further investigation.

To conclude, a general procedure to select a suitable trigger level for a specific flow could be

1. Select the region of interest in computational field, such as: inner layer for attached wall-layer; separate region or re-attachment region in wall-layers with detachment; wake region for flow around a body in free flow; or, like in present study, the overall computational field.
2. Find the PDF for Q (or for λ_2, D)
3. Fix as Tr an a value of Q one order magnitude lower than the one corresponding to numerical noise of LES

This process has been followed in the following investigation.

4.4 Definition and classification procedure

Once applied the trigger to the test variable (be it Q, λ_2, D), the further step is to identify and classify the actual structures.

The final product of the detection algorithm is a "mask" ($M(i, j, k)$), indicating whether a node ($M(i, j, k) = 1$) satisfies the chosen criterion and is, potentially, part of a vortex structure. All the grid points where $M(i, j, k) = 1$ are tested to assess whether they are truly part of a structure. Basic principle of acceptance criterion is that the node should be part of a connected region larger than a single cell, and the actual minimum accepted size is an octahedron whose vertices are pressure nodes (Fig 4.10). All nodes found within such structure or connected to it by a connectivity are tentatively added to it.

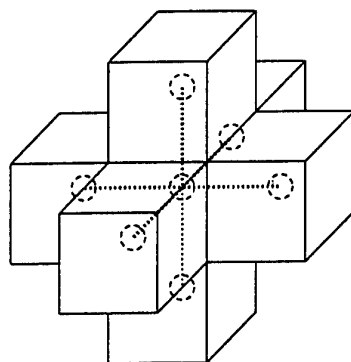


Fig. 4.10: Smallest Recognized Structure

4.4.1 Algorithm Description

Once the trigger level has been chosen, it is possible to produce the mask $M(i, j, k)$; this mask is processed looking for all the possible nodes that could be at the earth of an octahedron (Fig. 4.10). At this point, the flag of interior nodes is attributed to these nodes

(Fig. 4.11). The next logical step would be to look around each of these interior nodes to see whether the neighboring nodes are interior as well.

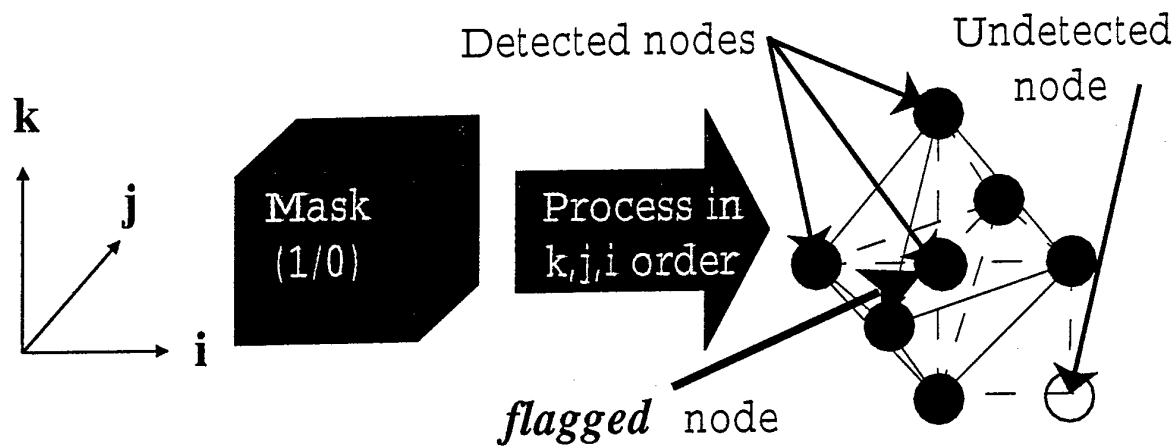


Fig. 4.11: Finding interior nodes

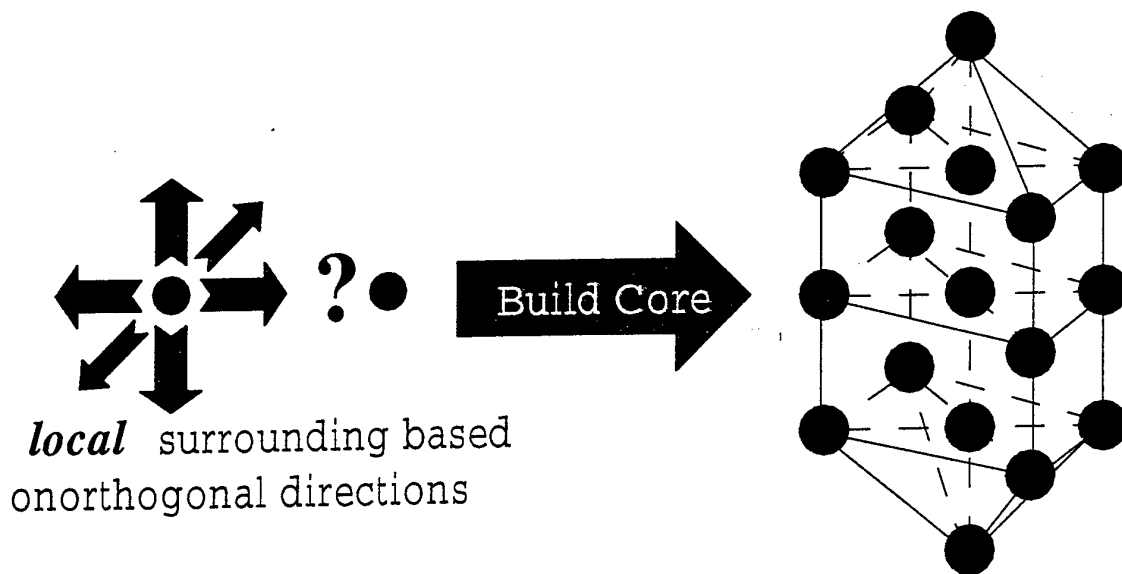


Fig. 4.12: Vortex core identification and construction

If this is the case, and they are strongly connected, they are assembled together giving birth to what will be hereafter called vortex core (Fig. 4.12).

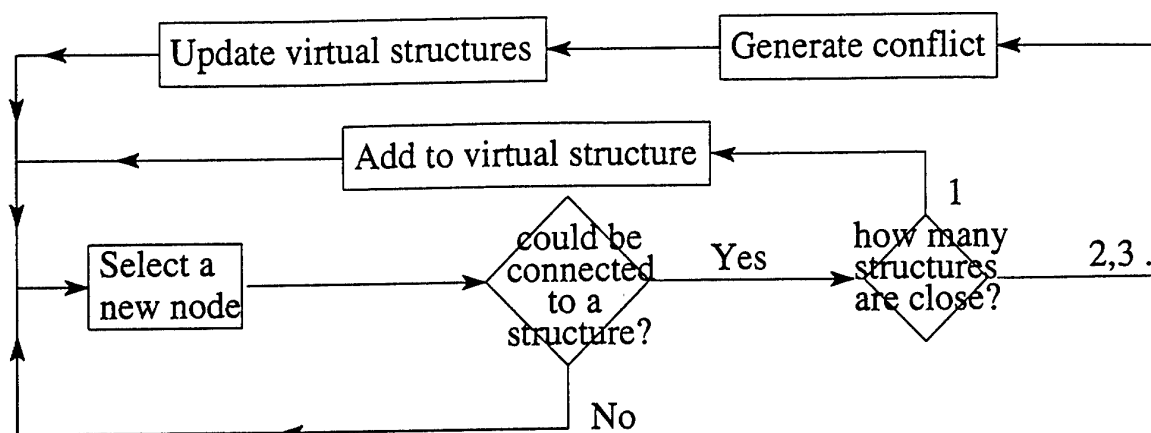


Fig. 4.13: Skin growth simplified description

Once the different vortex cores have been identified, the next step is to find their outer skin. In this phase, adjacent nodes are checked and their connectivity tested together with neighboring cores in order to identify if they belong to one, two or more structures. In this phase conflicts could arise, since the procedure is typically iterative, meaning only one node is examined at a time, and it is impossible to foresee whether this node will finally belong to only one structure that is made of two vortex cores connected by a thin membrane or is a point common to two otherwise distinct structures.

In summary, it was found that the procedure to add to vortex cores a growing skin layer is not enough to define the structures in an unequivocal way because, sweeping the field in sequence, a node could be assigned to different successive ones.

Therefore, it was found necessary to iterate over the flow-field, building a virtual list of associations in order to detect all the conflicts of attribution and solve them. In a simplified way, the procedure of skin reconstruction can be resumed with the scheme proposed in Fig. 4.13.

Since the procedure so outlined is iterative in a k, j, i fashion, once iterated on the flow field, a list of possible conflicts is outlined, and virtual structures grown on around the vortex cores are considered. However, due to the iterative procedure, a point that was considered only adjacent to a structure but not belonging to it when it was first tested, could, at the end of the whole scan of the interested volume, be indeed found part of a structure or part of a filament connecting two structures. This shortcoming of the procedure is inherited from the procedural language used to develop the algorithm, FORTRAN90, in the present case. It is not difficult to imagine, considering the entities we are dealing with, that an object oriented language could manage this phase in a more efficient and reasonable way. At the moment, the limit of the procedural language requires to reiterate the whole procedure, building a library of virtual structures until all the possibilities are examined. In other terms, a further step is computed to check whether no new conflicts are added to the previously discovered

in the first sweep of the volume (see Fig. 4.14).

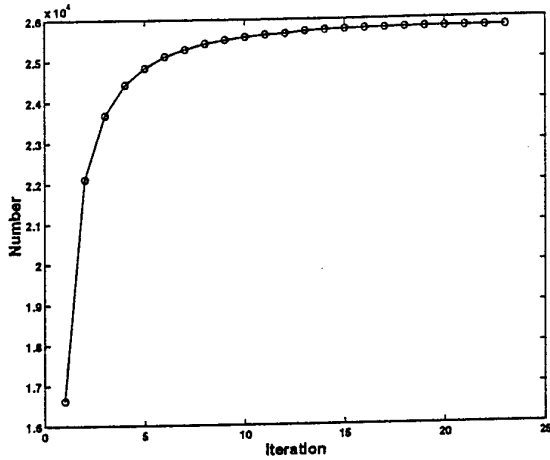


Fig. 4.14: Identification algorithm log: First Iteration

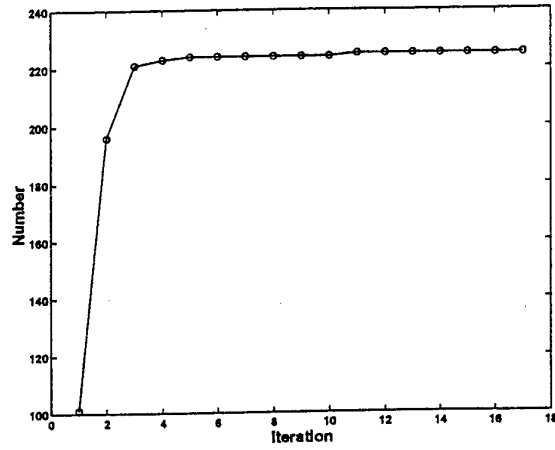


Fig. 4.15: Identification algorithm log: Second Iteration

At this point the conflicts are analyzed. Typical outcome of a conflict analysis would be to merge two or different structures, while it is possible that other conflicts will not solved since they consist of two structures briefly touching along their external surfaces. Once the structures database is updated, the procedure starts again, looking for new conflicts. Usually, at the second sub step the number of conflicts is dramatically reduced (see Fig. 4.15). The procedure continue until all the structures are finalized.

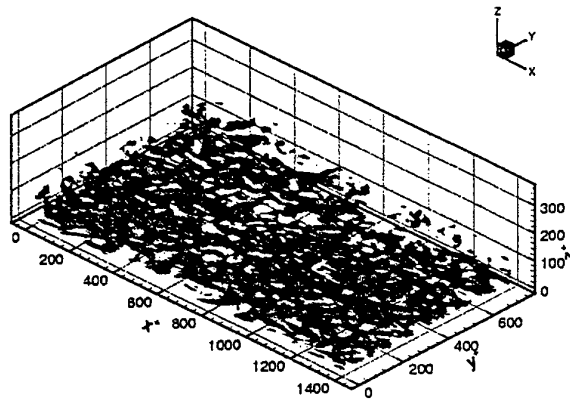


Fig. 4.16: Detection mask M of plane channel at equilibrium, at $Re_\tau = 180$; lower half channel.

The result of present procedure can be observed comparing Fig. 4.16, which is the initial field $M(i, j, k)$, with Fig. 4.17 which presents the structures accepted at end of the process,

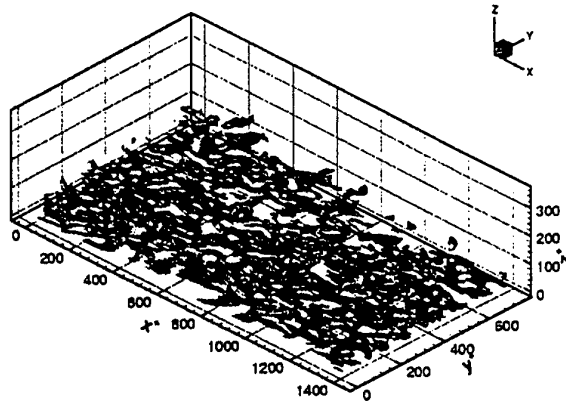


Fig. 4.17: Identified structures of plane channel at equilibrium, at $Re_\tau = 180$; lower half channel

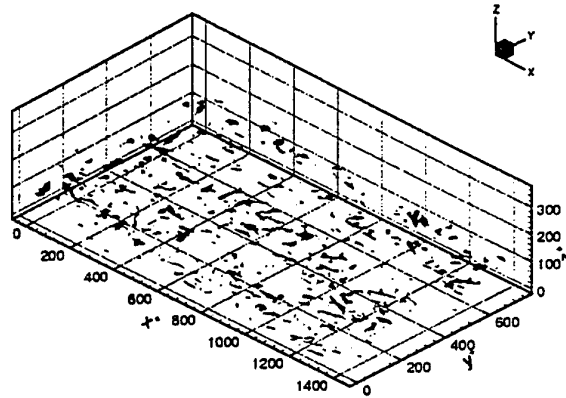


Fig. 4.18: Noise of plane channel at equilibrium, at $Re_\tau = 180$; lower half channel

while Fig. 4.18 shows the nodes accepted from the detection algorithm and rejected from the identification algorithm, or, in other terms, the difference between Fig. 4.17 and Fig. 4.16.

For an acceptable result, the ensemble of grid cells so rejected should, ideally, be far smaller than the final retained one; for the current case the corresponding values are presented in Tab. 4.4 and show that this requirement is satisfied.

The ratio structures versus noise could, of course, be improved fitting trigger level case by case, but at the cost the generality of the procedure; the present result shows that application of a method fixed a priori produces satisfactory filtering of M and definition of organized structures in flow-field. Therefore, it will be applied in the following investigation and is recommended for future applications.

As a last example, Fig. 4.19 shows two rendering of the same data-field (from flow

Table 4.4: Plane channel at equilibrium at $Re_\tau = 180$. (Example) Percentage of Volume, Enstrophy, Enstrophy_x found in noise and structures versus total quantities; entire computational field

	<i>Volume</i>	<i>Enstrophy</i>	<i>Enstrophy_x</i>
Noise	1.4360	2.1259	2.5761
Structures	9.8888	27.273	47.168

realization different of the one presented in the previous pages). On the upper figure a particular visualization technique has been used instead of the usual iso-surface procedure: since to each node we consider is associated a volume, and in a staggered grid this volume is a parallelepiped, where the mask M is equal to 1, there is a parallelepiped in blue, that is transparent, so it is possible to see through them to see the identified structures in red. The upper image is less clear than the lower one, where mask and detected structures are way more simpler to see, but offers a glimpse to the data the identification algorithm has to deal with.

4.5 Statistical tools

It was anticipated that field M , identified by the detection algorithm, is treated to extract the relevant statistics of the coherent field. Statistical tools developed for the task already been applied to produce the data presented in previous section, but are fully described and shown in this section, using, as example, results for the afore-discussed case of plane channel at $Re_\tau = 180$.

4.5.1 Geometry and distribution of structures

Besides overall volume occupied by the structures (as given in Tab. 4.3), the distribution of volume of individual structures can be found (Fig. 4.20).

Distribution of size of structures, projected on the axis x, y, z, L_x, L_y, L_z can also be extracted; at title of example, length in x direction is presented (Fig. 4.21).

This information is completed with the position of the center of mass of the structure (as already seen in Fig. 4.8), which allows to localize the regions of highest activity.

4.5.2 Dynamics of structures

Dynamics of structures and their interaction with background are described by

- Kinetic Energy

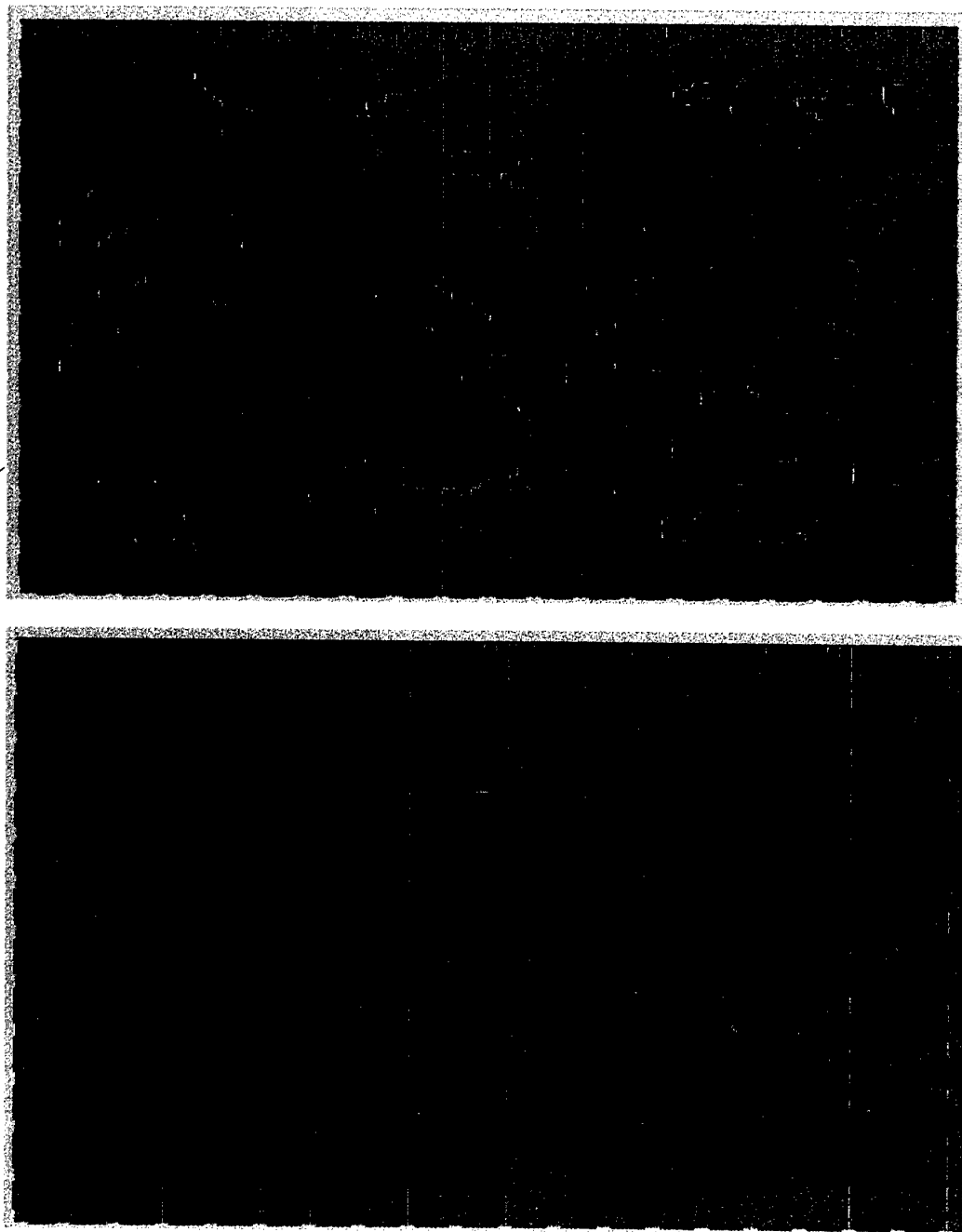


Fig. 4.19: Detected Mask (blue) and Identified Structures (red) at comparison. Lower half of the plane channel at $Re_\tau = 180$. View from top.

$$KE = \iiint_D \frac{1}{2} |V|^2 dx dy dz$$

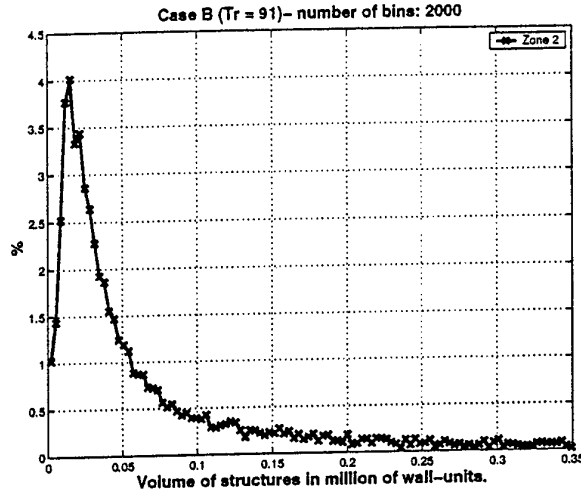


Fig. 4.20: Structures statistics: volume in wall units Re_τ (Example); inertial layer ($30 < z^+ < 100$). (Limits of histograms: 0 – 7)

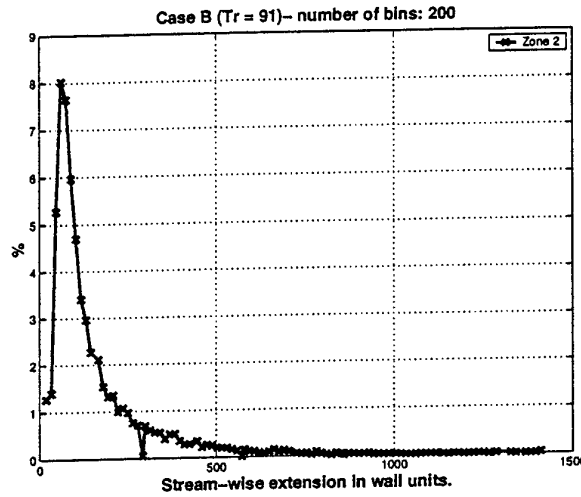


Fig. 4.21: Structures statistics: Stream-wise extension at Re_τ (Example) in wall units; inertial layer ($30 < z^+ < 100$). (Limits of histograms: 0 – 1500)

- Turbulent Kinetic Energy

$$TKE = \iiint_{\Omega} \frac{1}{2} |V'|^2 dx dy dz$$

- Vorticity, component per component, here shown for stream-wise direction

$$\omega_x = \iiint_{\Omega} (\nabla \wedge \vec{v})_x dx dy dz$$

- Vorticity, modulus

$$\omega = \iiint_{\Omega} |\nabla \wedge \vec{v}| dx dy dz$$

- Enstrophy

$$ens = \iiint_{\Omega} \frac{1}{2} (\nabla \wedge \vec{v})^2 dx dy dz$$

- Enstrophy, component per component, here shown for stream-wise direction

$$ens_x = \iiint_{\Omega} \frac{1}{2} (\nabla \wedge \vec{v})_x^2 dx dy dz$$

where the Ω represents the whole computational domain; to all respects, these are global quantities.

The quantitative importance of structures on overall flow is expressed as the ratio of structure content versus entire flow, which, for general scalar quantity F , is expressed in eqn. 4.12.

$$\frac{\iiint_{STRS} F dx dy dz}{\iiint_{\Omega} F dx dy dz} \quad (4.12)$$

where $STRS$ represents the portion of the domain occupied from the various structures and as before Ω is the whole computational domain.

For example, the ratios for module vorticity and enstrophy are represented in eqn. 4.13 and 4.14.

$$\frac{\iiint_{STRS} |\nabla \wedge \vec{V}| dx dy dz}{\iiint_{\Omega} |\nabla \wedge \vec{V}| dx dy dz} \quad (4.13)$$

$$\frac{\iiint_{STRS} |\nabla \wedge \vec{V}|^2 dx dy dz}{\iiint_{\Omega} |\nabla \wedge \vec{V}|^2 dx dy dz} \quad (4.14)$$

It has to be remarked that individual components of vorticity and enstrophy vectors are also examined, to take in account the anisotropic nature of turbulence in shear layer.

Table 4.5: Plane channel at equilibrium at $Re_\tau = 180$. Percentage of Volume, K.E., T.K.E. and Enstrophy found in structures versus total quantities; entire computational field

	Structures
<i>Volume</i>	9.8888
<i>K.E.</i>	8.0895
<i>T.K.E.</i>	14.280
<i>VorticityModule</i>	20.850
<i>Enstrophy_x</i>	47.168
<i>Enstrophy_y</i>	16.436
<i>Enstrophy_z</i>	31.859
<i>Enstrophy</i>	27.273

As already shown in previous section, percentage of overall contribution of structures to entire flow-field is available. To complete the example presented in previous section, corresponding data is presented in Tab. 4.5.

While this information defines the overall behavior of structures, the details of the this population is better captured introducing the definition of specific vorticity and specific enstrophy, as shown in eqn. 4.15.

$$\frac{\iiint_{STR} |\nabla \wedge \vec{V}|^2 dx dy dz}{\iiint_{STR} dx dy dz} \quad (4.15)$$

This definition allow associate vorticity components, enstrophy or other quantities of the structure to its volume.

This presentation allows to put in evidence the existence of preferential states for vorticity and enstrophy associated with the structures; for example, specific vorticity and specific enstrophy of x axis are presented in Fig. 4.22 and 4.23

In previous figures, histograms have been applied in order to approximate numerically PDFs. In the same way is possible to approximate a joint PDF, which, assuming the phenomenon to obey to the ergodic principle, expresses the probability for two variables x, y of falling in a certain interval centered around two values X and Y ; calling $P(X, Y, dx, dy)$ the aforementioned probability, we find the *JPDF* defined in eqn. 4.16.

$$P(X, Y, dx, dy) = \int_{X-\frac{1}{2}dx}^{X+\frac{1}{2}dx} \int_{Y-\frac{1}{2}dy}^{Y+\frac{1}{2}dy} JPDF(x_1, x_2) dx_1 dx_2 \quad (4.16)$$

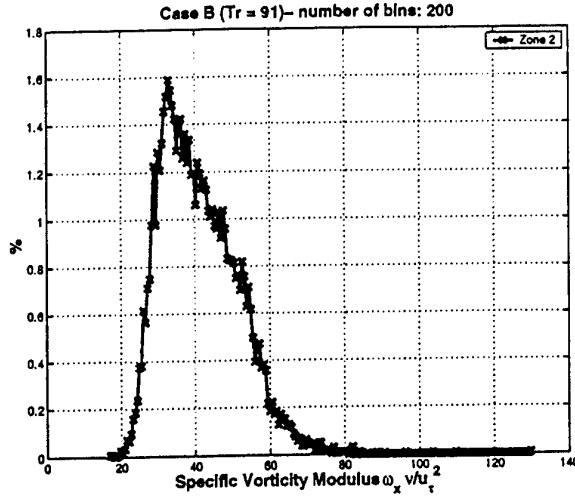


Fig. 4.22: Structures statistics at Re_τ (Example): specific vorticity modulus (non-dimensional); inertial layer ($30 < z^+ < 100$) (Limits of histograms: 16 – 130).

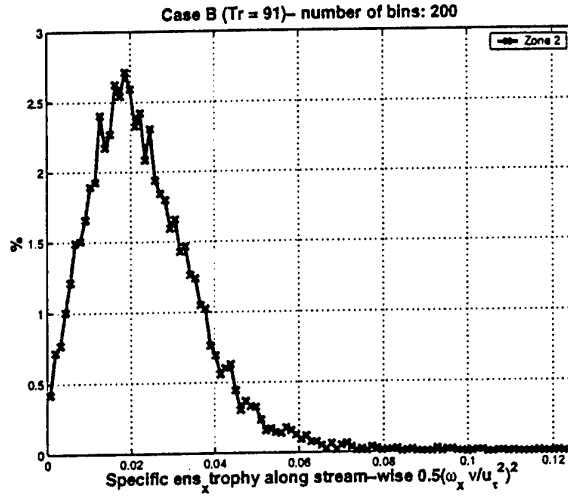


Fig. 4.23: Structures statistics at Re_τ (Example): specific enstrophy in stream-wise (non-dimensional); inertial layer ($30 < z^+ < 100$). (Limits of histograms: 0 – 0.24)

JPDFs can be used to put in evidence preferred states in the present distribution, in terms of structure geometry (Fig. 4.24), or vorticity (Fig. 4.25). For the latter, it is useful to note that, for the study of channel flow, a proper choice of the post-processing procedure will be able to extract from the whole channel the behavior of a simple half channel. This capability will be used following analysis.

A last quantity of fundamental interest to understand the present phenomenology is the convection velocity of the centroid of the structures, defined in eqn. 4.17.

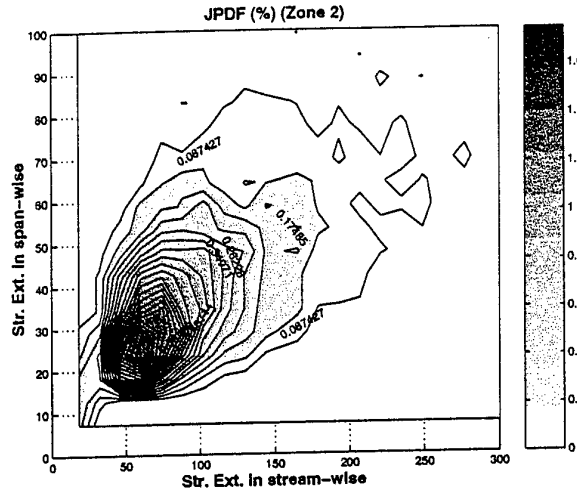


Fig. 4.24: Structures statistics $Re_\tau = 180$ (Example): JPDF for structures length in x and y in wall-units; inertial layer ($30 < z^+ < 100$). (Limits of histograms: 18 – 1400, 6 – 550, 200×200 bins)

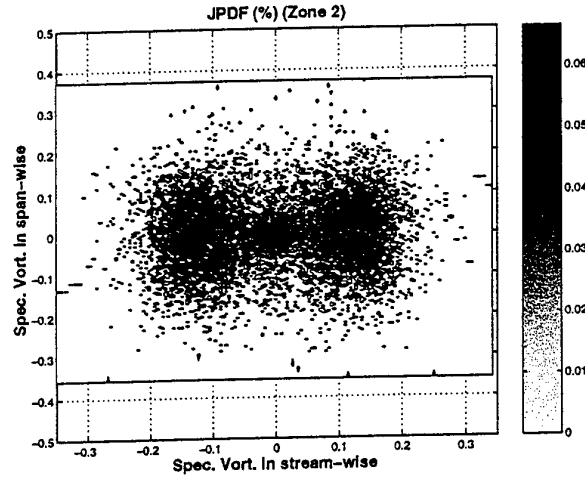


Fig. 4.25: Structures statistics: JPDF for specific vorticity in x and y (non-dimensional); inertial layer ($30 < z^+ < 100$). (Limits of histograms: 18 – 1400, 6 – 550, 200×200 bins)

$$\frac{\iiint_{STR} U dx dy dz}{\iiint_{STR} dx dy dz} \quad (4.17)$$

which would allow to track structures in time and assess how they follow the average flow.

The above presented tools allow to study in depth the phenomenology of organized structures and will be applied in next Chapters.

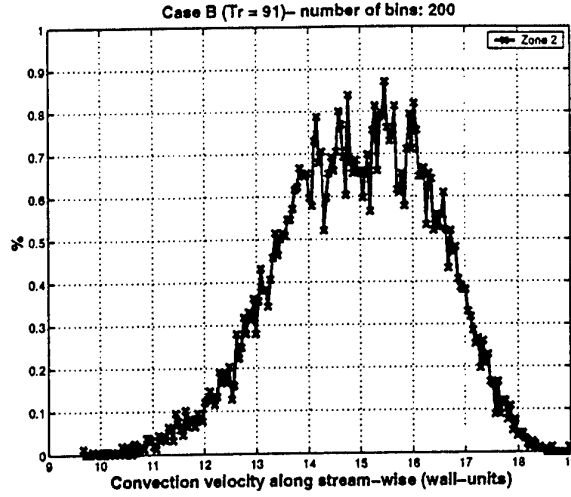


Fig. 4.26: Structures statistics $Re_\tau = 180$ (Example): Convection velocity (non-dimensional); inertial layer ($30 < z^+ < 100$). (Limits of histograms: 9.5 – 19)

4.5.3 Kinetic energy budget for structures

To complete the study of coherent structures, it is necessary to examine their contributions to the different processes involved in the transport of kinetic energy.

Matter of fact, as it was pointed out in paragraph 4.1, it is of fundamental interest to find out whether turbulent statistics are different of organized field and un-coherent background. For this purpose the budget of resolved kinetic energy is computed; the definitions to be applied are

$$U_i(\vec{x}, t) = \overline{U}_i(\vec{x}, t) + v^{SGS}_i(\vec{x}, t) \quad (4.18)$$

$$\overline{u}_i(\vec{x}, t) = (\overline{U}_i(\vec{x}, t) - \langle \overline{U}_i(\vec{x}, t) \rangle) \quad (4.19)$$

$$\overline{k} = \frac{1}{2} \overline{u}_i \overline{u}_i \quad (4.20)$$

$$(4.21)$$

The basics of transport equation for kinetic energy in LES have been presented in Chapter 2; in the following, resolved turbulent kinetic energy (*r.t.k.e.*) (which is indicated as: \overline{k}) will be considered.

For a statistically stationary flow and applying the Reynolds decomposition, it is possible to identify the fluctuating component of the resolved velocity field and from it compute the instantaneous *r.t.k.e.*

Manipulating the filtered dimensional Navier Stokes equations and averaging in time,

the corresponding budget of the resolved turbulent kinetic energy (*r.t.k.e.b.*) is defined

$$\frac{\partial \langle \bar{k} \rangle}{\partial t} = \quad (4.22)$$

$$- \langle \bar{u}_i \bar{u}_j \rangle \frac{\partial \langle \bar{U}_i \rangle}{\partial x_j} - \langle \bar{U}_j \rangle \frac{\partial \langle \bar{k} \rangle}{\partial x_j} - \frac{\partial \langle \bar{k} \bar{u}_j \rangle}{\partial x_j} + \dots \quad (4.23)$$

$$\dots - \left\langle \frac{\partial p'_{\text{mod}}}{\partial x_i} \right\rangle + \nu \Delta \langle \bar{k} \rangle - \nu \left\langle \frac{\partial \bar{U}_i}{\partial x_j} \frac{\partial \bar{U}_i}{\partial x_j} \right\rangle - \frac{\partial \langle \bar{u}_i \tau'_{ij}{}^a \rangle}{\partial x_j} + \left\langle \tau'_{ij}{}^a \frac{\partial \bar{u}_i}{\partial x_j} \right\rangle \quad (4.24)$$

$$(4.25)$$

Where

$$p_{\text{mod}} = \frac{\bar{p}}{\rho} + \frac{\tau_{kk}}{3} \quad (4.26)$$

$$p'_{\text{mod}} = p_{\text{mod}} - \langle p_{\text{mod}} \rangle \quad (4.27)$$

$$\tau'_{ij}{}^a = \tau_{ij}^a - \langle \tau_{ij}^a \rangle \quad (4.28)$$

For the present purpose, a conditional averaging must be performed over population of coherent structures and incoherent turbulence. This conditional sampling would provide a physical understanding of behavior of the two different states for the different terms of the turbulent kinetic energy budget.

The application of this algorithm to the present case of plane channel at equilibrium of $Re_\tau = 180$ is here shown; DNS data taken from AGARD (1998) are given as reference.

The complete budget is presented in Fig. 4.27 with an example of conditional averaging: LES_{in} represents the conditional averaging performed inside the coherent structures, while LES_{out} on the incoherent turbulence.

In Fig. 4.29 and 4.28 a comparison of the production and of the dissipation of the resolved turbulent kinetic energy together with corresponding DNS data.

It can be remarked that the behavior and value for the different terms of the TKE budget obtained by present simulation are practically identical to the DNS ones except for the inner wall layer of distance from the wall smaller than 20 wall units. The peak in the turbulent production is not captured exactly, but, in the LES framework, the comparison can be assessed satisfactory.

Considering the turbulent dissipation, the SGS contribution, which represents the effects of the sub-grid scale motions to this process, coincides with the DNS dissipation above the

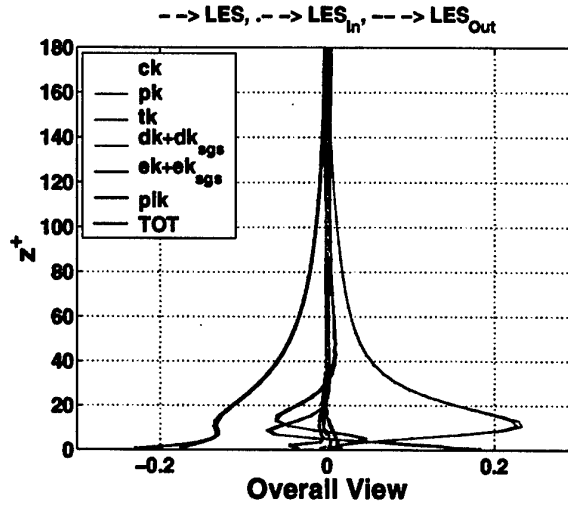


Fig. 4.27: Resolved Turbulent Kinetic Energy Budget $Re_\tau = 180$ (Example)

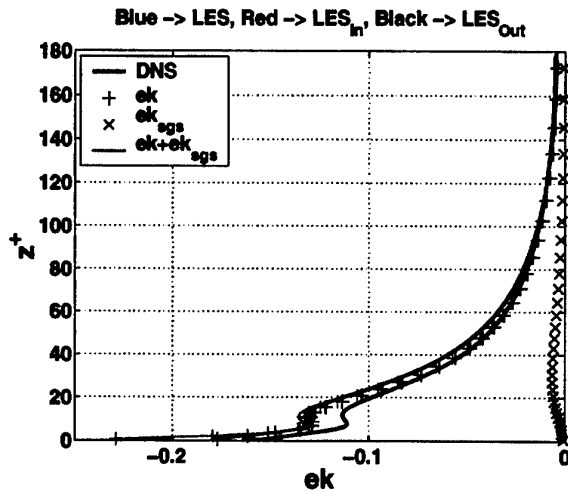


Fig. 4.28: Resolved Turbulent Kinetic Energy Pseudo Dissipation $Re_\tau = 180$ (Example)

20 wall units limit. Even closer to the wall the DNS behavior is correctly reproduced. Note that the lower production predicted by LES with respect to LES is also compensated by a lower dissipation, ensuring a correct overall budget.

Concerning the conditional averaging presented in Fig. 4.27, 4.28 and 4.29, the results seem suggest, that for this particular simulation flow, the overall behavior of the conditional averages converges to the classical one in the long term, consistent with Hussain (1983) interpretation. Further tests, performed in this frame, confirmed this interpretation

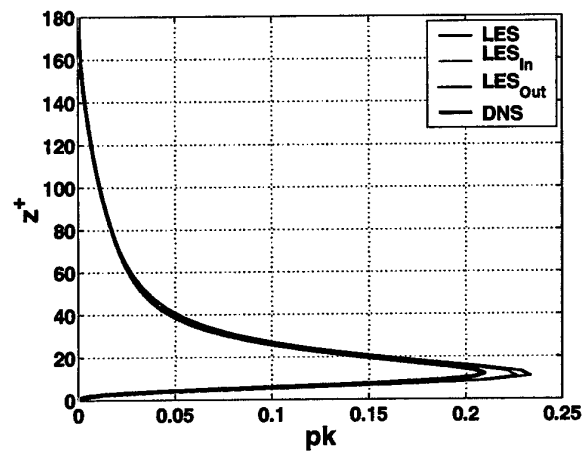


Fig. 4.29: Resolved Turbulent Kinetic Energy Production $Re_\tau = 180$ (Example)

5. SIMULATION OF COHERENT STRUCTURES IN ATTACHED WALL SHEAR LAYER

As announced in Introduction, the turbulent plane channel at equilibrium (Fig 5.1) is chosen as test case for the study of coherent structures in wall shear layers.

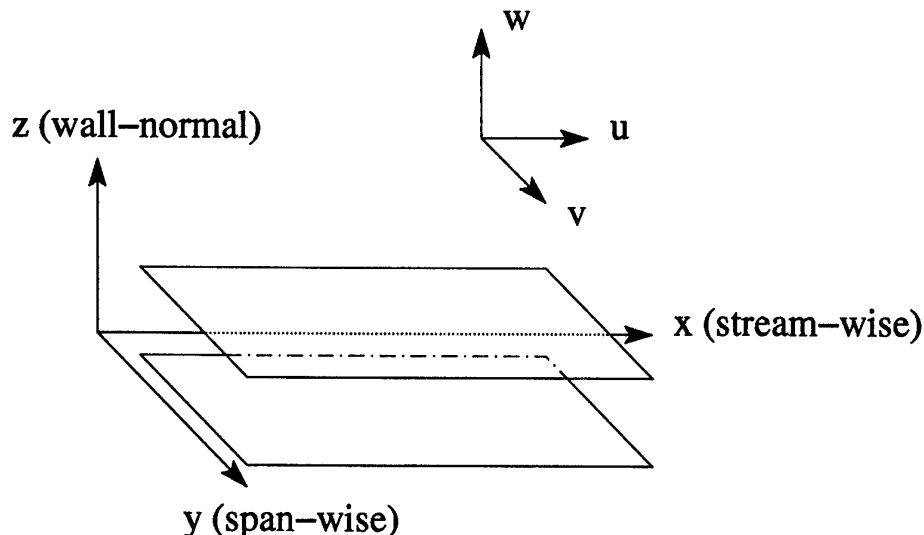


Fig. 5.1: Plane channel geometry

The turbulent flow in a plane channel is a well studied case and accurate DNS results at Reynolds $Re_\tau = 180, 395$ and 590 are available (AGARD, 1998) in literature for validation. The advantage of focusing on this case lies with its geometrical simplicity, which makes it feasible to simulate the full phenomenology of wall-bounded flows and to perform accurate simulations with relative limited computer power. At the same time, previous studies (Blackburn et al., 1996; Jeong et al., 1997) have shown the coherent structures found in this flow to be fully representative of general behavior to be encountered in this class of flows (Chacin and Cantwell, 2000; Chong et al., 1998).

Some results for the case of $Re_\tau = 180$ have already been presented in Chapter 4, as title of example, to demonstrate capability and working of present algorithm, but without detailed description of this simulation and its results, which will now be discussed in present chapter.

However, it can be at once remarked that this first calculation puts in evidence the existence of organized structures, elongated in stream-wise direction and characterized by clockwise and counter-clockwise rotation, as will be shown in the following pages.

Aim of present Chapter is to evaluate the procedure outlined in Chapter 4, study its sensibility to modeling and computational parameters, and, as well, to attain a satisfactory

understanding of physics of organized turbulence for this particular flow.

5.1 Investigation of organized structures for plane channel at $Re_\tau = 180$ (Case I)

Our analysis starts from the study of a channel flow at friction Reynolds number equal to 180 ($Re_\tau = 180$). The LES results can be compared with (AGARD, 1998). The basic parameters for this first simulation are resumed in Tab. 5.1; in wall normal direction a power stretching (its coefficient being equal to 1.08) has been employed.

Table 5.1: Plane channel at equilibrium at $Re_\tau = 180$ (Case I). Geometrical Parameters

Geometry & Grid			Test Bed		
L_x	L_y	L_z	$\frac{5}{2}\pi$	$\frac{4}{3}\pi$	2
N_x	N_y	N_z	64	96	64
Δx^+	Δy^+	Δz^+	22	7.85	$1.5 < \Delta z^+ < 16$

Smagorinsky SGS model with $C_s = 0.10$ and 2nd order accurate discretization in space and time are used for this analysis; comparison with reference DNS data shows that low order statistical moments (Fig. 5.2 and 5.3) and budget of turbulent kinetic energy of resolved turbulence (Fig. 5.4) show that the parameters chosen for this simulation lead to a satisfactory simulation of the flow.

Between the different detection criteria discussed in Chapter 4, the Q criterion has been chosen for detection of organized structures in view of its computational simplicity and clear-cut definition of trigger level, as it can be obtained from PDF of Q (Fig. 5.5) applying the criterion discussed in Chapter 4

Application of this procedure to present case yields value $Tr = 72$, for trigger level, expressed in wall units non-dimensionalization.

Statistical information on structures is obtained performing ensemble average over results from successive instantaneous flow-fields, separated by a 1/6 flow-through (flow-through = Length of domain/Bulk velocity). Experience has shown that an ensemble of more than 10,000 structures are necessary to ensure reliable statistics.

The overall importance of organized turbulence respect to total flow can be assessed in Tab. 5.2, where percentage of its contribution to global quantities of the turbulent field are presented.

It is to be remarked that contribution of organized turbulence to turbulent kinetic energy and vorticity is much higher than the volume occupied by the structures themselves,

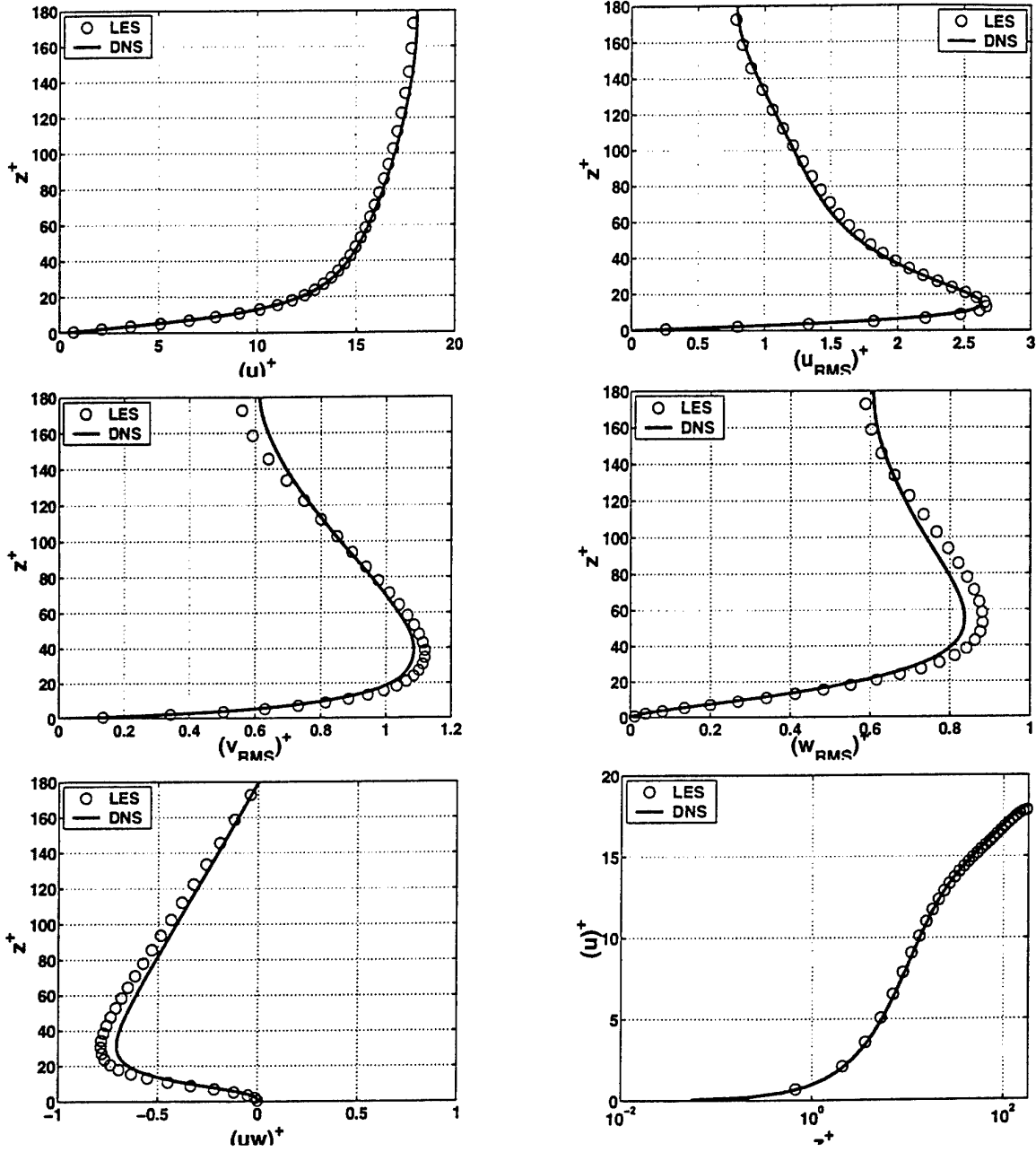


Fig. 5.2: Mean stream-wise velocity and rms of resolved turbulence of plane channel at $Re_\tau = 180$ (Case I)

confirming they correspond to the most active regions of the flow.

Distribution of enstrophy along the three axis (Tab. 5.3) confirms the existence of preferential pattern of rotation of around x axis, which was already visible in Fig. 4.19 in § 4.

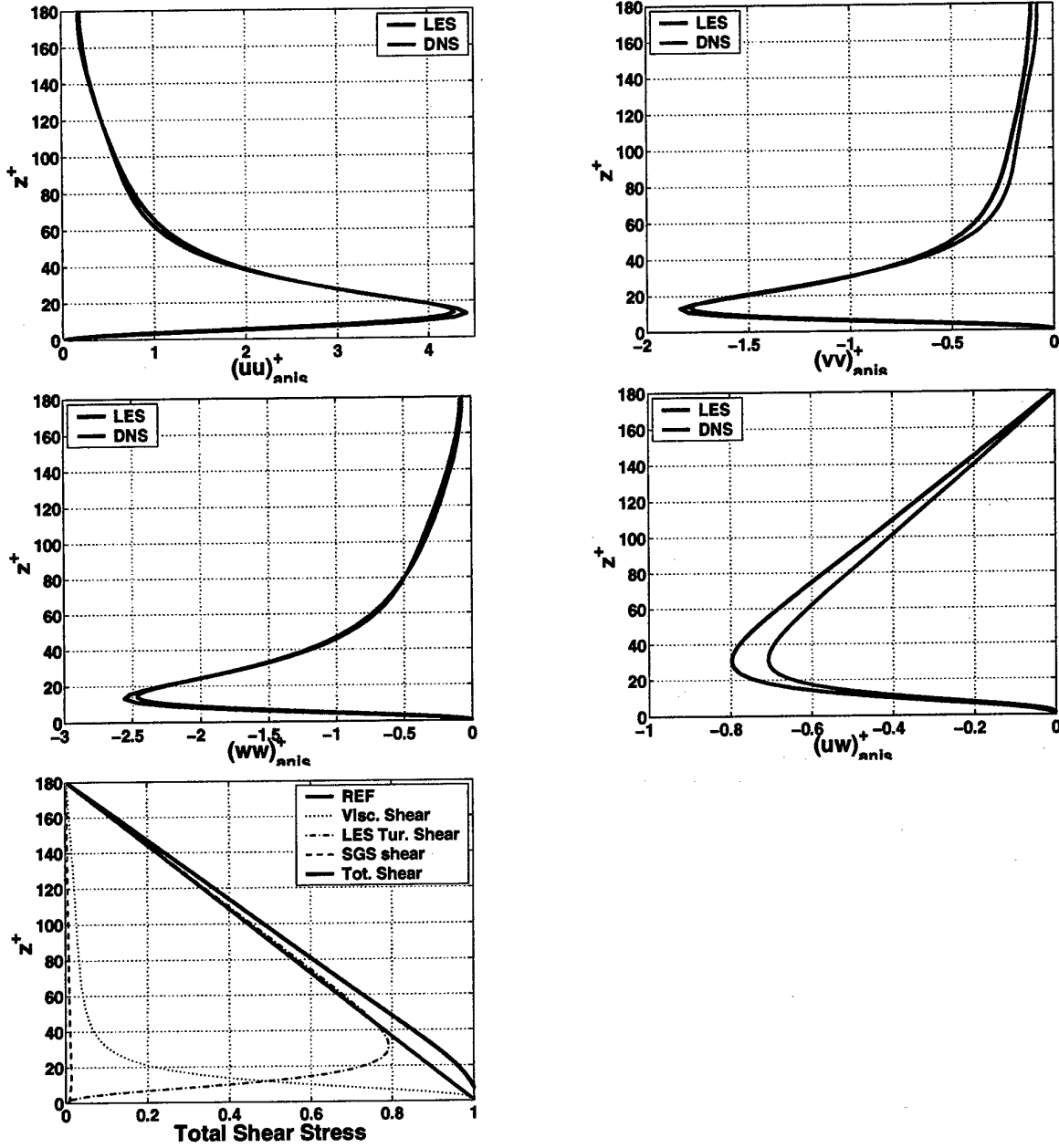


Fig. 5.3: Anisotropic part of the resolved Reynolds stress tensor of plane channel at $Re_\tau = 180$ and total shear stress (Case I)

These already interesting results can be enriched by a detailed analysis of the statistics of structures population, which can be obtained following the procedure established in Chapter 4. As there indicated, the computational field is sub-divided, for analysis purpose, in 3 layers in order of increasing distance z from the nearer wall.

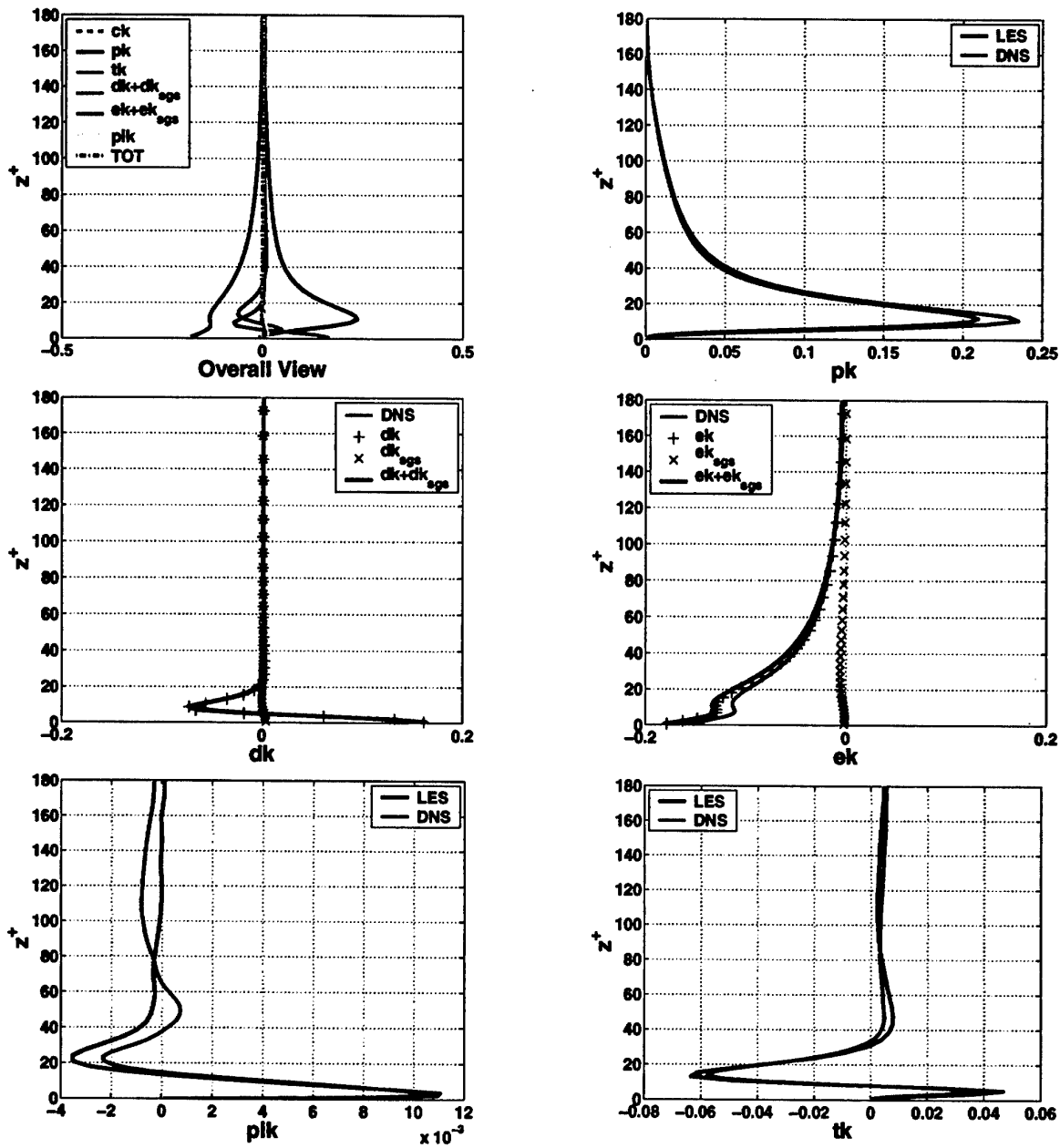


Fig. 5.4: Budget of resolved turbulent kinetic energy of plane channel at $Re_\tau = 180$ (Case I)

Zone 1 Inner (Viscous-buffer) layer: $0 < z^+ < 30$

Zone 2 Inertial layer: $30 < z^+ < 100$

Zone 3 Wake region: $z^+ > 100$

This procedure allows to put in evidence different importance of organized turbulence

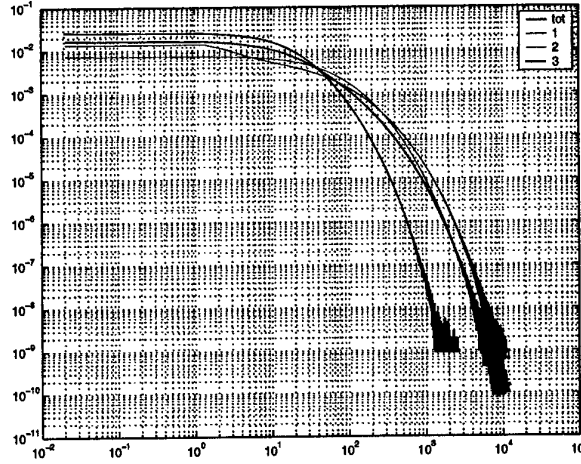


Fig. 5.5: PDF of Q plane channel at $Re_\tau = 180$ (Case I)

Table 5.2: Plane channel at equilibrium at $Re_\tau = 180$ (Case I). Volume, turbulent kinetic energy, module of vorticity and enstrophy within structures versus corresponding quantities contained within the full computational field

<i>Volume</i>	9.661 %
<i>TKE</i>	14.075 %
<i>VorticityModulus</i>	19.893 %
<i>Enstrophy</i>	25.058 %

Table 5.3: Plane channel at equilibrium at $Re_\tau = 180$ (Case I). Enstrophy within structures versus corresponding quantities with the full computational field

<i>Enstrophy_x</i>	45.9 %
<i>Enstrophy_y</i>	14.8 %
<i>Enstrophy_z</i>	29.4 %

in different regions of wall layers.

The average population is in the order of 250 structures for flow field. The distribution of volumes of structures is presented in Fig. 5.6, showing values in the range $1.68e^{+03}$ to $4.8e^{+06}$ units in wall non-dimensionalization, for an average value $Vol_{mean} = 1.48e^{+05}$ wall units. In this figure the usual distinction introduced above about distance from the wall is used in order to empathize a possible difference in behavior between the different zones.

The knowledge of structures volume is possibly not interesting in itself, but, when used in conjunction with data retrieved for the structures moment of inertia, could give interesting

insights on the structures dimensions and orientations, more interesting ground-work.

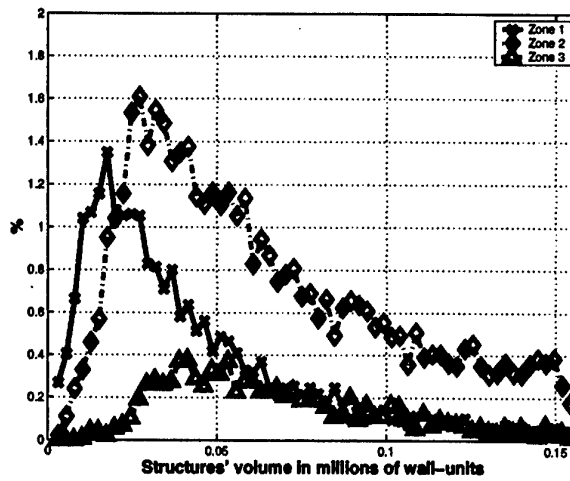


Fig. 5.6: Structures Volume of plane channel at $Re_\tau = 180$ with usual zone distinction (Case I). (Number of bins 1000; limits of histogram: 0.0017 ... 4.8)

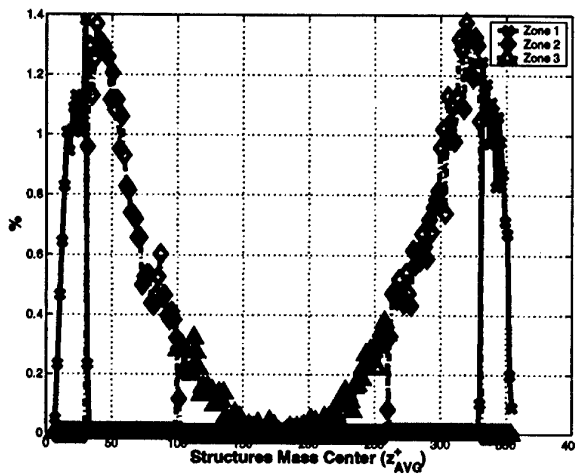


Fig. 5.7: Structures mass center of plane channel at $Re_\tau = 180$ with usual zone distinction (Case I). (Number of bins 200; limits of histogram: 5.27 ... 354.57)

The distribution of structures mass center across the height of the channel (Fig 5.7) shows that a large fraction of structures is located within the inertial layer with a maximum around top of the buffer layer, while structures are relatively rare within the wake region (Zone 3). This behavior is also shown by a side view of the field of detected structures (Fig 5.8), where for clarity only the structures of the lower half of the channel are shown (as will be for Fig 5.10).

Contribution of organized turbulence for the different zones is resumed in Tab. 5.4.

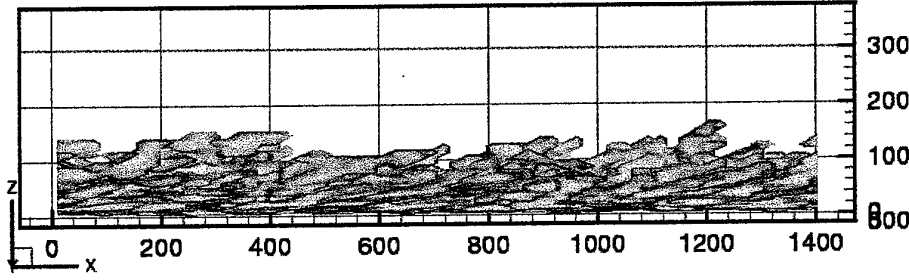


Fig. 5.8: Side view of the field of detected structures of plane channel at $Re_\tau = 180$ (Case I)

Table 5.4: Plane channel at equilibrium at $Re_\tau = 180$ (Case I). Volume, turbulent kinetic energy, module of vorticity and enstrophy within structures versus corresponding quantities computed zone by zone

Zone	Zone 1	Zone 2	Zone 3
<i>Volume</i>	4.858 %	21.571 %	1.233 %
<i>TKE</i>	4.156 %	25.825 %	1.107 %
<i>VorticityModulus</i>	5.551 %	41.167 %	3.236 %
<i>Enstrophy</i>	4.965 %	66.443 %	6.645 %

The collected data confirm patterns which might be assumed from Fig. 5.7: most of the activity resides in the inertial layer and the contribution of the wake region is negligible and can be, partly, neglected, as it will be done in following analysis.

Advection velocity of structures mass center (Fig. 5.9) indicates they follow average flow, without noticeable lag¹.

Visualization of whole field of detected structures for present simulation (Fig. 5.10), confirms the tendency of structures to be elongated in stream-wise direction.

Visualization of individual structures also puts in evidence the large spread of possible sizes within this class (Fig. 5.11).

However, structures of much more complex geometry can be encountered (and most importantly, the algorithm is 'able' to recognize them), as shown in (Fig. 5.12); if those structures truly exist or the present trigger level allows different structures merge, it is a point which needs to be assessed.

Influence of grid resolution on the definition of the individual structures will be addressed in a following section; it can, however, be remarked that horseshoe vortex are extremely rare

¹This comparing the velocities corresponding to the peaks of the PDF in the figure to an average velocity for the corresponding Zone.

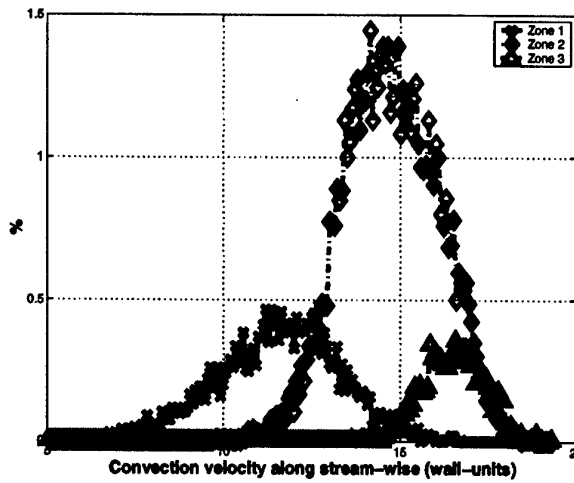


Fig. 5.9: Stream-wise advection of structures center of mass of plane channel at $Re_\tau = 180$ (Case I). (Number of bins 200; limits of histogram: 4.98 ... 19.33)

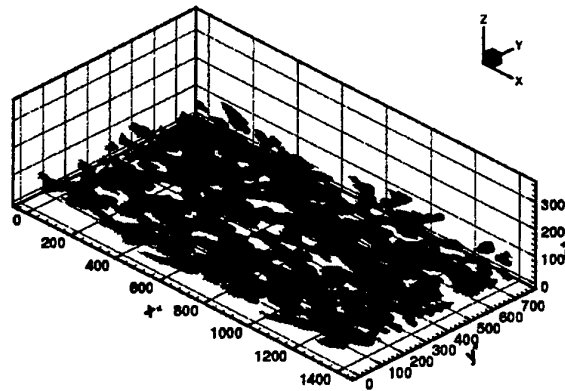


Fig. 5.10: 3-D overview of the field of detected structures of plane channel at $Re_\tau = 180$ (Case I)

with current resolution, and a clear sample was not possible to extract.

The statistical analysis of population of structures shows as well the occasional existence of relatively long structures, comparable in their size to dimension of the computational domain. Possibly these occurrences are linked to the complex structures shown in Fig. 5.12, however genuinely-looking long structures can be identified as well (Fig. 5.13).

The possible complexity of structures makes it very difficult to assess their dimensions and orientation for the whole population; relevant statistics can be gathered from the analysis of projection the structure: L_x , L_y and L_z on x , y , z axis respectively (Fig. 5.14), which bound the cartesian box containing the actual structure.

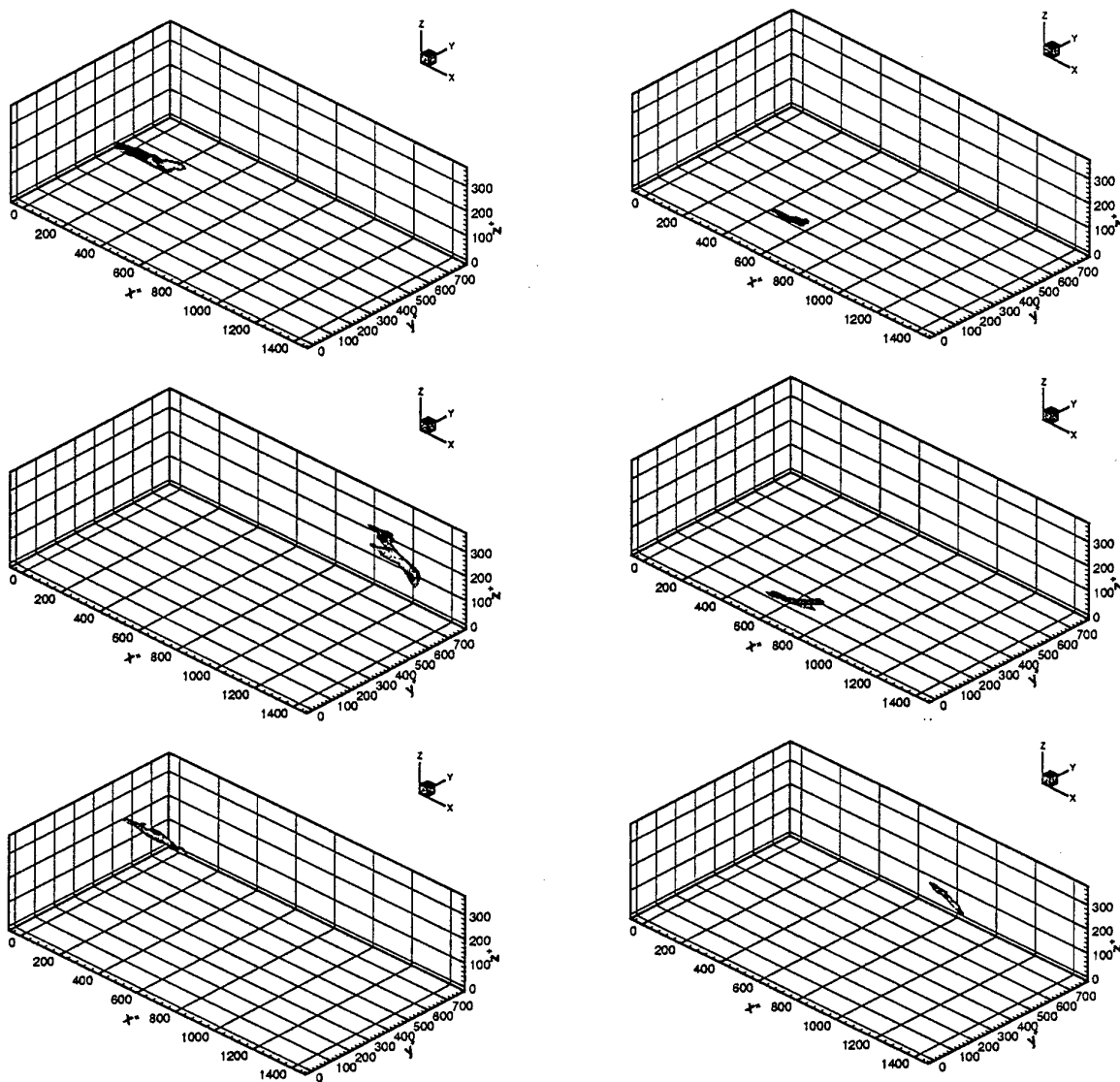


Fig. 5.11: Typical structures elongated in stream-wise direction of plane channel at $Re_\tau = 180$ (Case I)

It is clear from Fig. 5.14 that even with knowledge of L_x , L_y , L_z an important uncertainty remains concerning their actual size and orientation of the individual structure (see Fig. 5.17 below).

Actual distribution of L_x , L_y and L_z for present case is presented in Fig. 5.15.

The distribution of L_z in Fig. 5.15 needs some further comment: present grid is stretched in the wall normal direction, while it is uniform in the remaining directions. Non uniformity of grid increases the dispersion of the data relative to the size of the structures in wall-normal

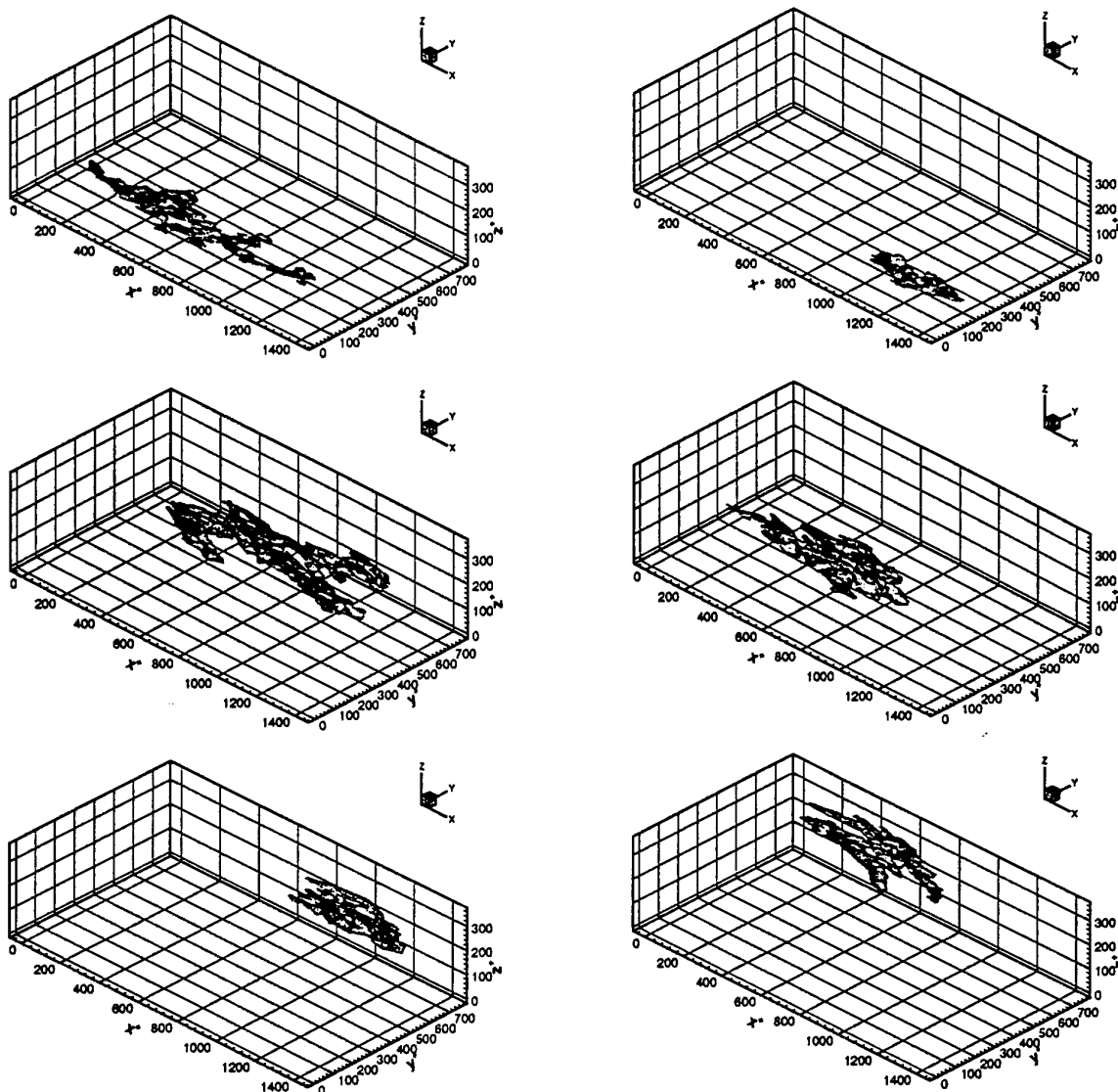


Fig. 5.12: Example of complex structures of plane channel at $Re_\tau = 180$ (Case I).

direction. To give an idea of better overall trend, the lines which bound the region where the data are collected are superposed.

Observing Fig. 5.15, it can be remarked that the distributions of L_x , L_y and L_z are relatively similar for Zones 1 and 2, which apparently indicates that structures in the two layers could belong to a same phenomenology, the most common values for Zone 2 are indicated in Tab. 5.5.

It has already been remarked that the distribution of L_z appears very noisy, in Fig. 5.15, compared to the ones for L_x , L_y : this behavior is due to much refined grid in z direction and

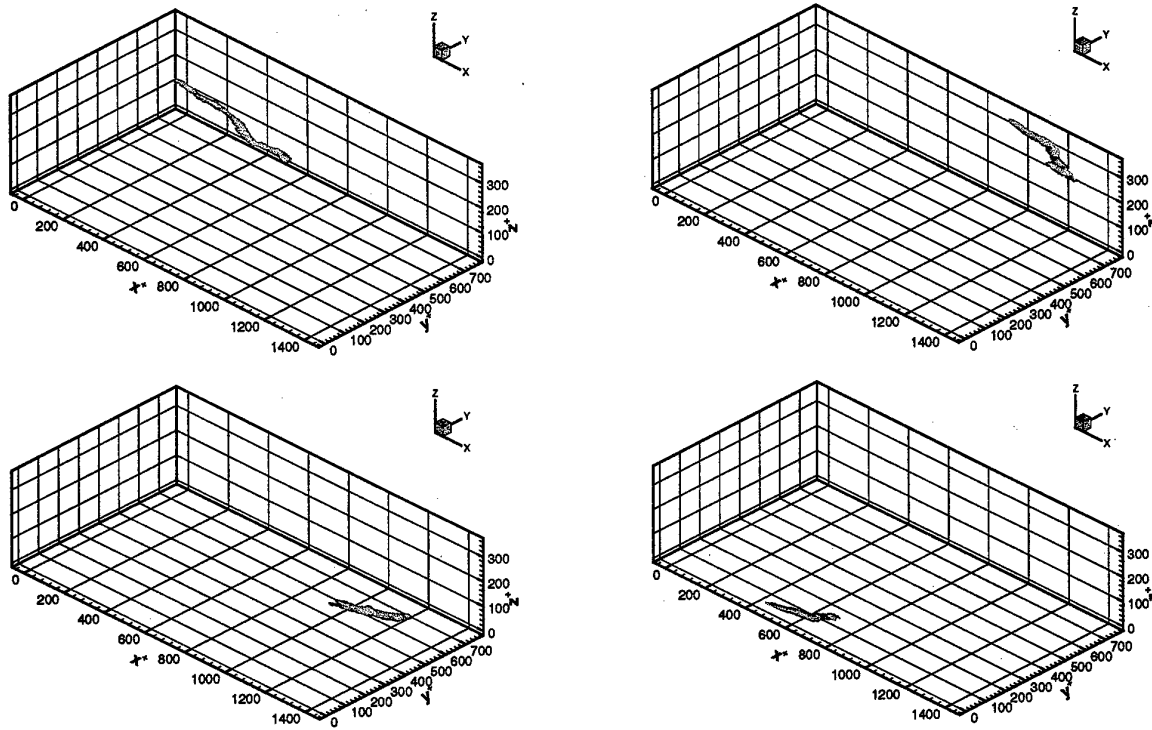


Fig. 5.13: Examples of elongated structures at $Re_\tau = 180$ (Case I)

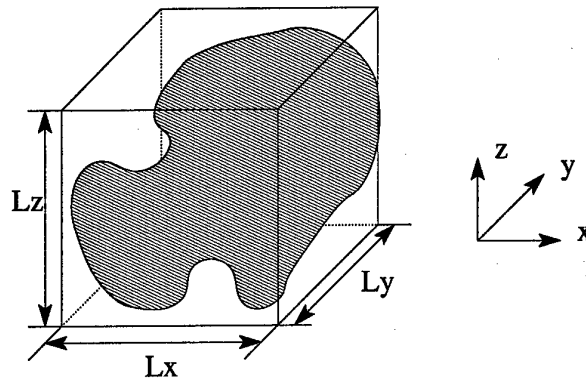


Fig. 5.14: Estimation of size of structures from their projections on coordinate axis

Table 5.5: Plane channel at equilibrium at $Re_\tau = 180$ (Case I). Most common values for L_x , L_y and L_z in wall units (Zone 2)

L_x	L_y	L_z
80 – 90	30 – 40	30 – 40

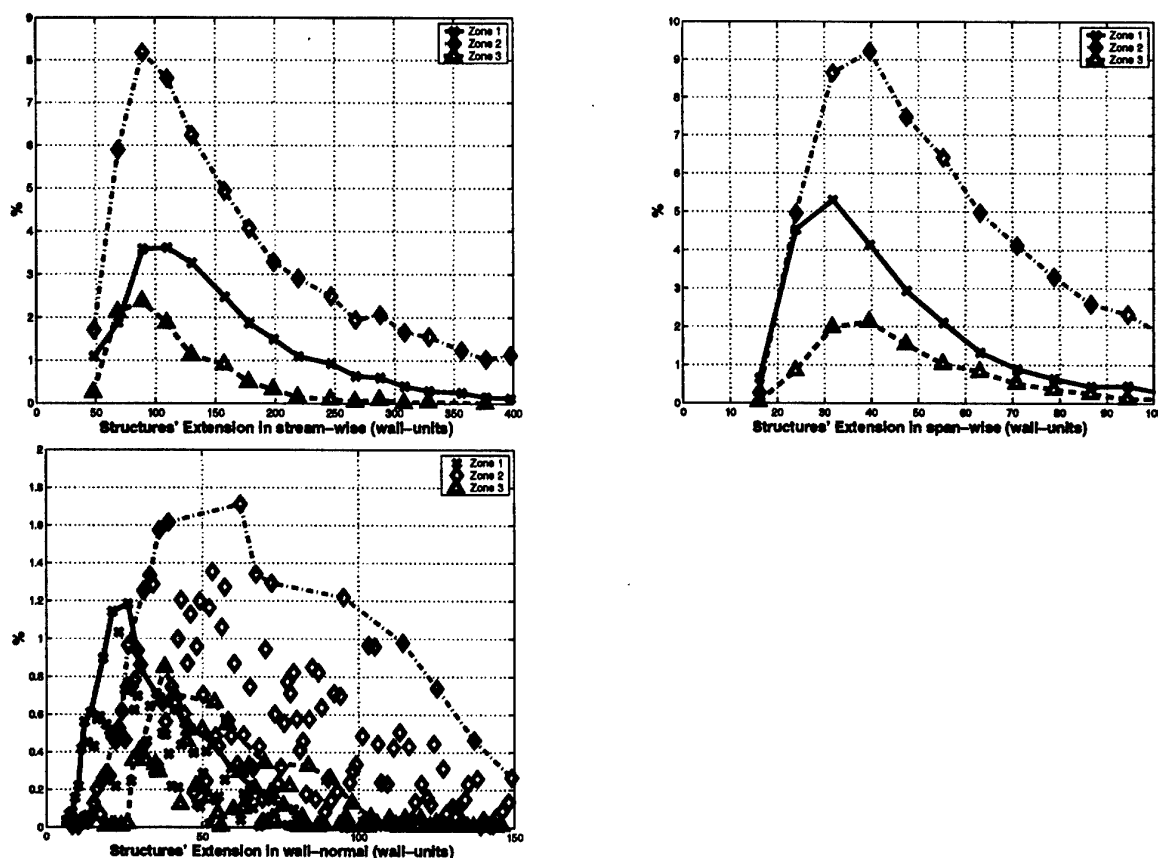


Fig. 5.15: Structures statistics at $Re_\tau = 180$ (Case I): length in wall units. (From top left to bottom right: Number of bins, 2000, 8000, 2000; limits of histograms: 44.17 ... 1413.7, 15.7 ... 463.38, 5.48 ... 205.28)

to its stretching; however the primary trend can still be detected, and it will be further put in evidence applying the joint probability function (JPDF) approach introduced in § 4.5.2.

In this case, L_x , L_y and L_z values are coupled two by two, to obtain the joint probability function for the couple of variables $L_x - L_y$, $L_x - L_z$ and $L_y - L_z$.

Corresponding distributions for Zones 1 and 2 are presented in Fig. 5.16; following previous remarks, Zone 3 has been neglected. Since we are interested mainly in finding the most probable couple of values from a JPDF, this value is loosely dependent from the number of bins and the limits of the histograms used to build the JPDF; so, in order not to clutter furthermore the information provided, the relative parameters are not included in the figure.

It can be again remarked that the main trends are qualitatively similar for the first two layers (see Tab. 5.6).

More probable value L_z is higher in Zone 2 than one for Zone 1 could be thought of an

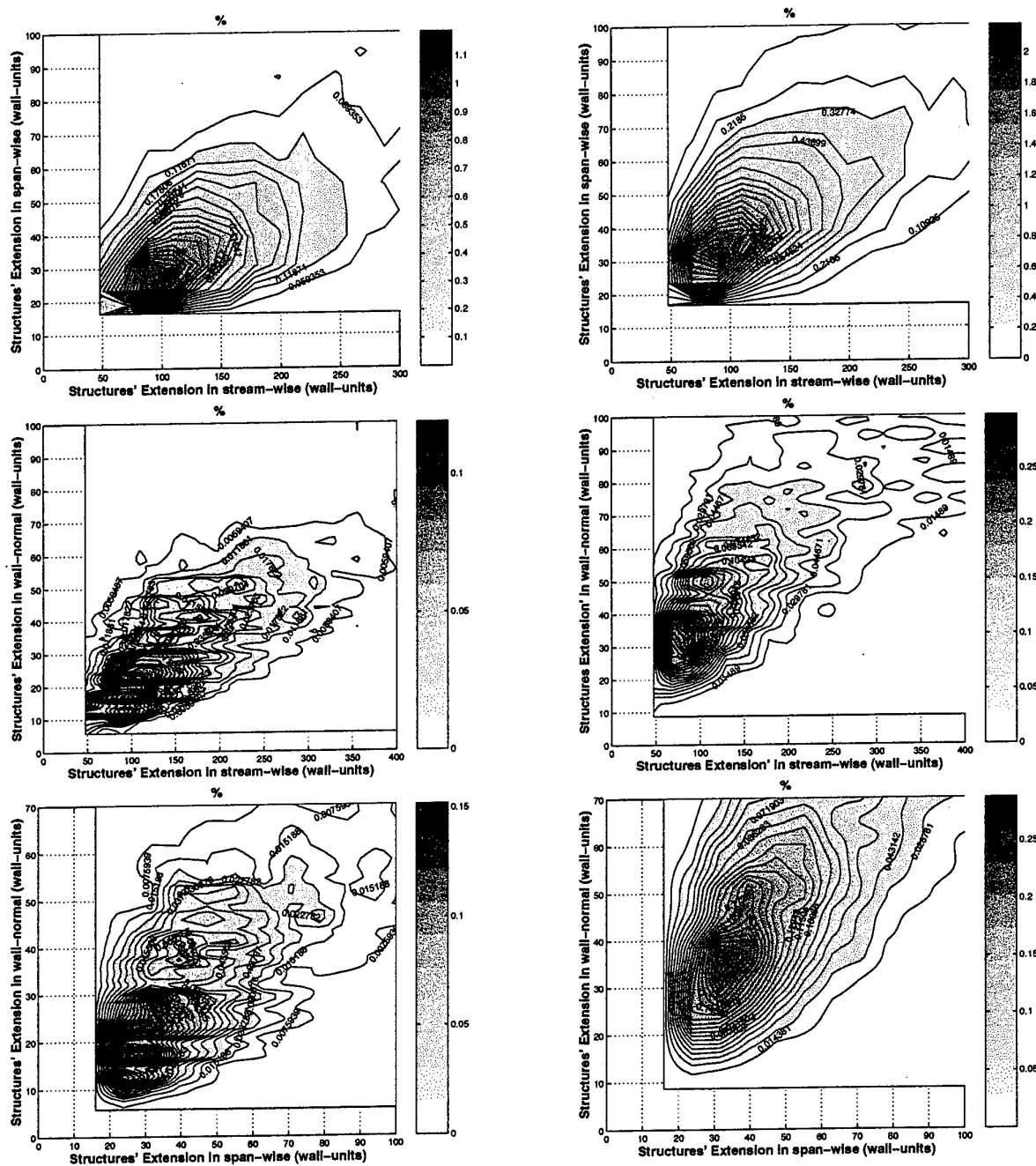


Fig. 5.16: Structures statistics: JPDF for structures extension. $Re_\tau = 180$ (Case I). Left column Zone 1, right column Zone 2, xy -top, xz -middle and yz -bottom

indication of tilting of the structures away the from $x-y$ plane with increasing distance from the wall, or of an effect of grid stretching.

The information from JPDF could be applied to build a model of typical structures:

Table 5.6: Plane channel at equilibrium at $Re_\tau = 180$ (Case I). Most common values for joint L_x-L_y , L_x-L_z and L_y-L_z in wall units.

Zone	$L_x - L_y$	$L_x - L_z$	$L_y - L_z$
1	88-33	88-20	33-25
2	88-33	88-45	38-44

JPDF L_x-L_y could be thought as indication of tilt angle in span-wise direction and JPDF L_x-L_z as an incidence angle in wall-normal direction. However, this information might be untrustworthy, considering Fig. 5.17, and a better approach to the problem will be proposed in the following.

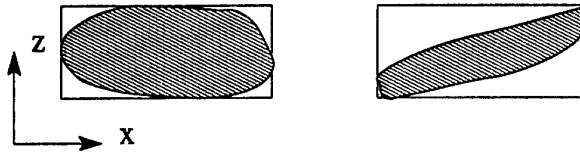


Fig. 5.17: Estimation of size of structures from their projections on coordinate axis could be problematic

A better estimation of size and orientation of a structure can be obtained from its principal inertial moments. These quantities are computed as an eigenvalues problem posed by the inertial tensor of the structure, where axial, centrifugal and tensor of moment of inertia are presented in eqn. 5.1.

$$\begin{aligned}
 I_x &= \int_{STR} \sqrt{y^2 + z^2} \rho \, dx \, dy \, dz \\
 I_{xy} &= \int_{STR} xy \rho \, dx \, dy \, dz \\
 \underline{\underline{I}} &= \begin{pmatrix} I_x & -I_{xy} & -I_{xz} \\ -I_{yx} & I_y & -I_{yz} \\ -I_{zx} & -I_{zy} & I_z \end{pmatrix}
 \end{aligned} \tag{5.1}$$

In first instance, the problem is to find the eigenvalues and eigenvectors of the inertial tensor, or, rather, the directions associated to them. Assuming the structures to have, in general, a preferential direction (and Fig. 4.19, 5.8, 5.10 etc. seem to confirm that), and considering the eigenvector associated with the smallest eigenvalue (or, in other words, the axis roughly in line with the structure), then it is possible to have an estimation of the orientation of the structures with better accuracy than the one yielded by other methods.

Fig. 5.18 produces a comprehensive visual representation of the alignment in space for the structures; for each structure the three directions associated to the inertial tensor intersect a sphere of radius one in 2 points each, an entrance point and an exit point; in color code, black corresponds to the the direction of highest interest, or the main direction of the structure. In present representation, 6 symbols correspond to each structure, but, in spite of this apparent complexity, this was found to be the best visual representation of the problem at hand.

To help to better visualize the spatial alignment of the structures, the sphere has been presented under three points of view. On the figure's left column there are the views relatives to Zone 1, while the ones for Zone 2 are on the right column. Zone 3 has been omitted altogether, and a particular handling of the data (see Chapter 4) has been performed in order to represent in Fig. 5.18 the behavior of one single half-channel, namely the lower half channel. It is understandable, indeed, that for the whole channel the main alignment of the structures should be, on average, in the stream-wise direction.

Processing the data in a this way would be indeed this result: no preferential direction in the $x-y$ plane, nor in the $x-z$. While this is unavoidable for the $x-y$ plane, considering only the data from the lower half channel, or manipulating in a proper way the data from the whole channel, it is still possible to obtain the preferential alignment for the structures in $x-z$ plane, which will be discussed further on (see. Fig. 5.20).

It is necessary to mention that to obtain Fig. 5.18 it is necessary to process a relatively high number of structures, which are obtained lumping together information from more than one flow realization; for the left side (or Zone 1) data from an average of 30 instantaneous flow-fields is used, while for the right (or Zone 2) only 6 fields are used. The reason of this difference lies within the different number of structures which are present in the two zones; as shown by previous results, Zone 2 contains, by far, the largest part of the population for the case under examination. Fig. 5.18 has exclusively an illustrative aim, and where not properly generated can be misleading, as will be seen in § 5.2. Here it is sufficient to confirm the main stream-wise orientation of the structures.

Extracting in a quantitative way the tilt and incidence angle for the population from these data yields the results presented in Fig. 5.19 and 5.20.

Fig. 5.19 indicates that most of the structures in the different zones have a tilt angle of less than 10 degrees, and predominant tendency is for the structure to lie on the x axis.

On the other side, Fig. 5.20, shows average incidence angle of about 7 degrees for Zone 1 and Zone 2. However, while for Zone 1 the peak is clearly defined, for Zone 2 the next possible angle considered from the histogram is of 14 degrees and corresponds to 88% of the value of the peak for 7 degrees. It will not come as a surprise then that in S 5.2 the peak will be indeed for 14 degrees. Similar behavior has already been remarked in different study (Chacin and Cantwell, 2000).

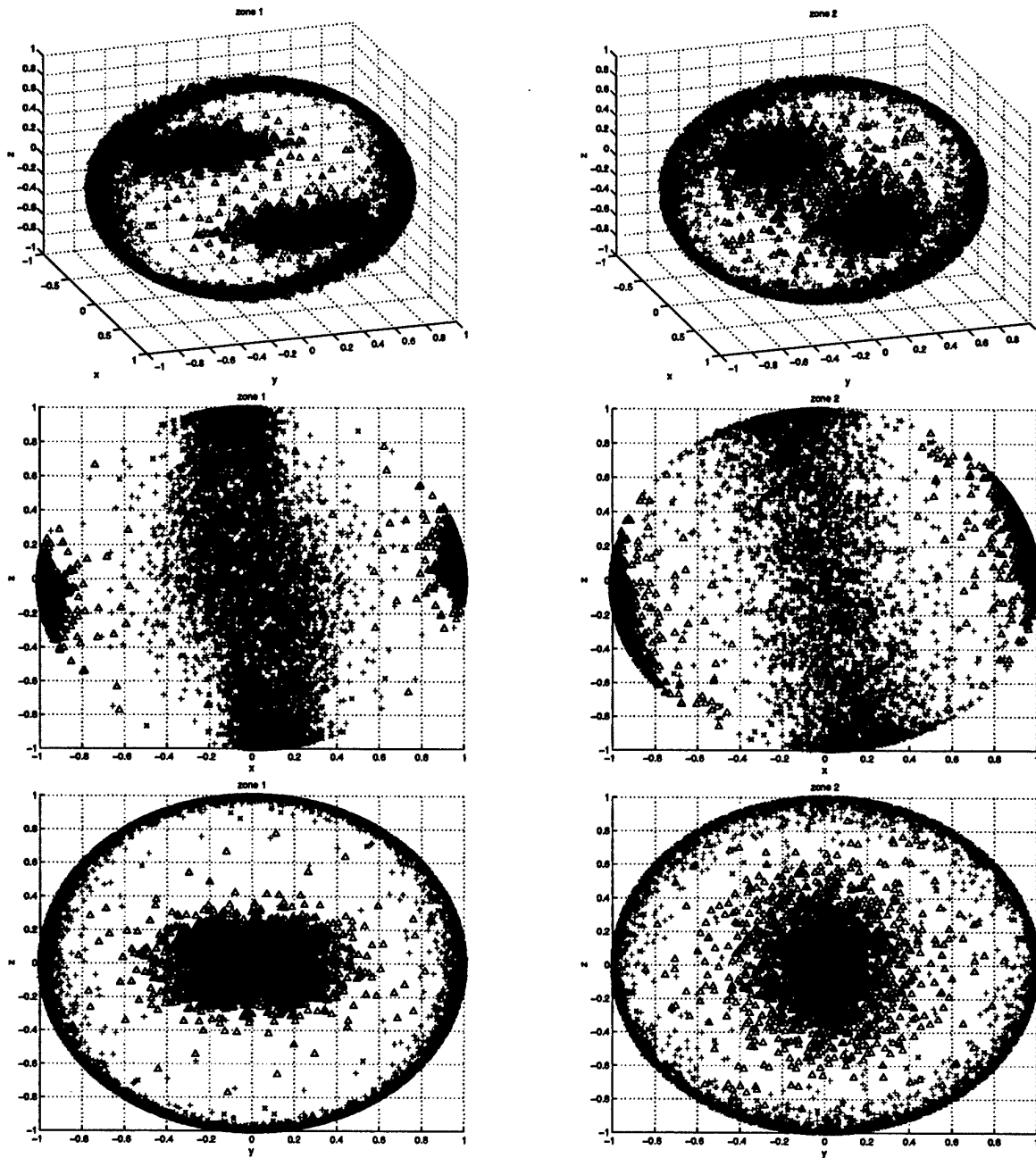


Fig. 5.18: Structures statistics, $Re_\tau = 180$ (Case I): spatial alignment, different pov. Δ Structure mean alignment. Zone 1 left column, Zone 2 right column

The inertial tensor \underline{I} is useful not only to provide an estimation of the orientation of the structures through its eigenvectors, but through its eigenvalues, it can be made to yield further information.

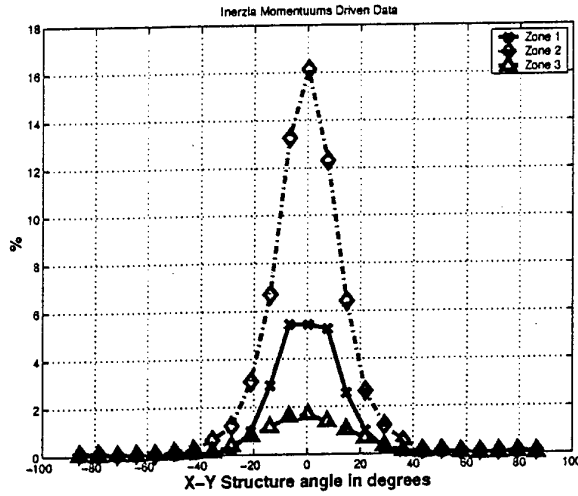


Fig. 5.19: Structures statistics $Re_\tau = 180$ (Case I): Tilting angle extracted from inertial tensor. (Number of bins: 25; limits of histograms: $-90 \dots 90$)

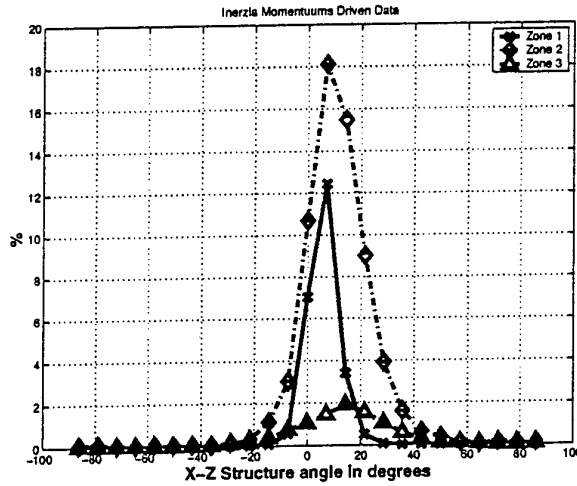


Fig. 5.20: Structures statistics $Re_\tau = 180$ (Case I): Incidence angle extracted from inertial tensor. (Number of bins: 25; limits of histograms: $-90 \dots 90$)

In fact, it is possible to associate to a structure an equivalent cylinder of length l and radius r , having the same principal inertial moments.

Calling I_i the i^{th} principal inertial moment in i direction and assuming $I_1 \leq I_2 \leq I_3$, it is found that, in general, $I_2 \approx I_3 \gg I_1$, so from an average of the two biggest moments of inertia and the volume of the structure is possible to compute the dimensions of an equivalent cylinder.

According to Fig. 5.21 and 5.22, the most probable values would be of 90 wall-units for

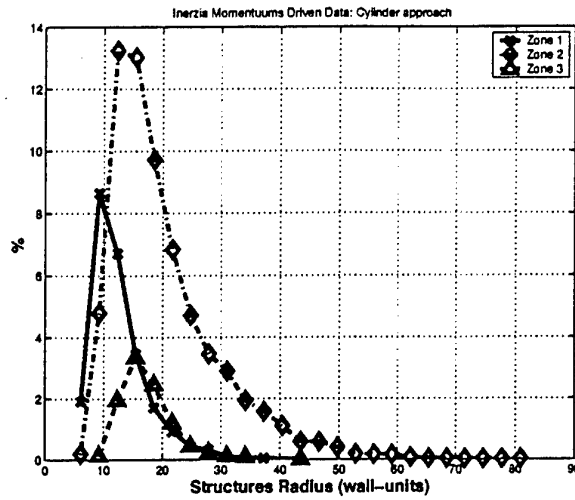


Fig. 5.21: Structures statistics $Re_\tau = 180$ (Case I): Equivalent cylinder radius. (Number of bins: 25; limits of histograms: 4.5 ... 82.4)

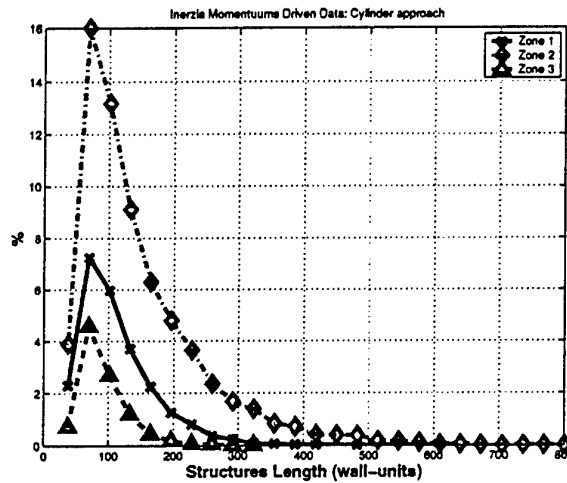


Fig. 5.22: Structures statistics $Re_\tau = 180$ (Case I): Equivalent cylinder length. (Number of bins: 25; limits of histograms: 21 ... 815)

the height of the cylinder and 16 wall-units for its radius. Computing the equivalent volume $\pi r^2 l$ and comparing it with volume obtained from Fig. 5.6 it can be seen in Fig. 5.23, that this model yields volumes 20 – 30 % lower than the original ones.

The sensibility of the result to the choice of the equivalent geometrical model for the structure can be appreciated comparing the previous result to the one which could be obtained assuming the typical structure to have the shape of an ellipsoid of volume $\frac{4}{3}\pi abc$, where $a \geq b \geq c$ are the semi-length on the 3 axis of the ellipsoid or length of the three semi-axes.

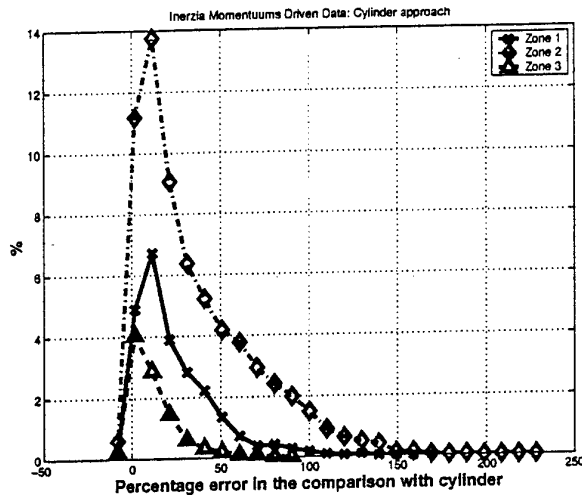


Fig. 5.23: Structures statistics $Re_\tau = 180$ (Case I): Equivalent cylinder volume deviation

An advantage of this second model is that, being the three semi-axes distinct, it is no more necessary to average I_2 and I_3 , decreasing the level of arbitrariness of the procedure.

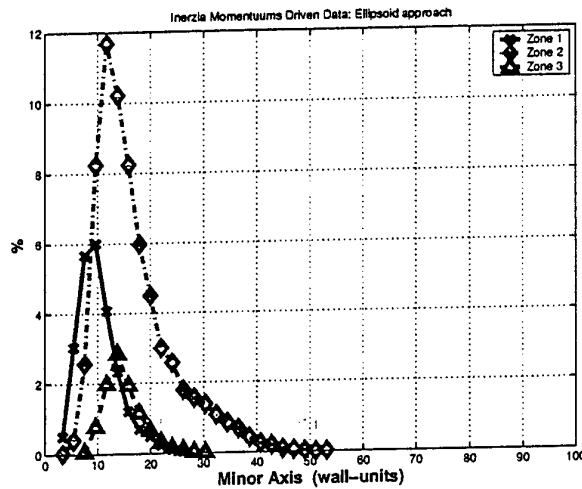


Fig. 5.24: Structures statistics $Re_\tau = 180$ (Case I): Equivalent ellipsoid minor semi-axis

According to Fig. 5.24 to 5.26, the most probable state, for Zone 2, would be an ellipsoid having $a \cong 45$, $b \cong 17$ and $c \cong 12$ in wall units. It is possible to compare the volume of the ellipsoid with the volume of the corresponding structure, being able finally to retrieve Fig. 5.27.

The differences between the two models can be appreciated from Fig. 5.23 and 5.27.

The difference is in order of 20%, which shows the difficulty to fit in a single model shape all present structures, some examples of which have previously shown. It has to be remarked

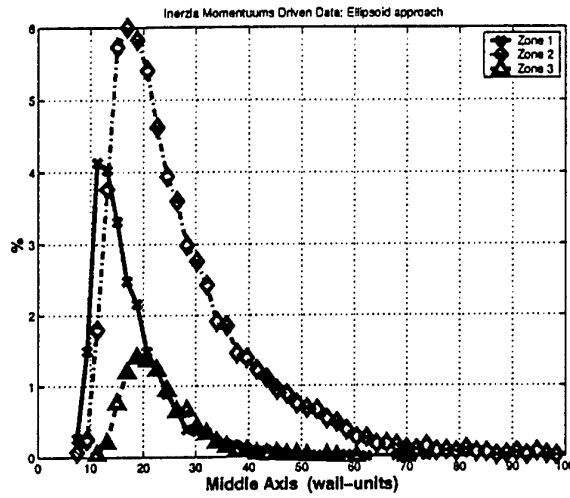


Fig. 5.25: Structures statistics $Re_\tau = 180$ (Case I): Equivalent ellipsoid middle semi-axis

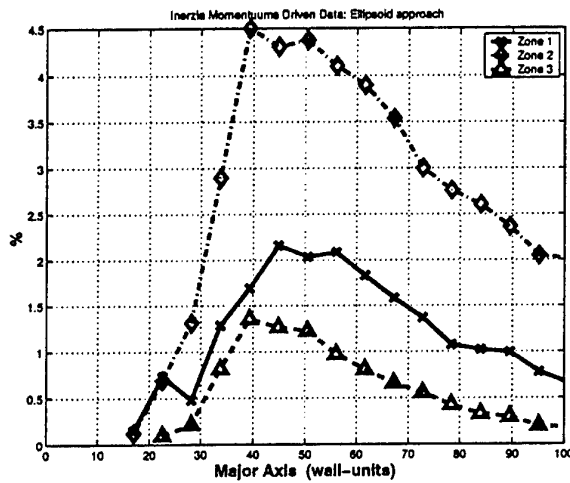


Fig. 5.26: Structures statistics $Re_\tau = 180$ (Case I): Equivalent ellipsoid major semi-axis

that the result can be influenced by anomalous structures of very big size, such as the ones presented in Fig. 5.12.

This behavior could be due to the conjunct effect of insufficient resolution of the grid and the choice of a too low Tr , which make impossible for the present algorithm to separate nearby structures; to address this problem the effect of grid resolution will be discussed in next section.

It can, however, be concluded that it is possible to produce a model of typical structure which fits, with reasonable accuracy, the present data and could be used as model of interpretation of the physics. Examination of actual structures (Fig. 5.11 and 5.12) and the lesser

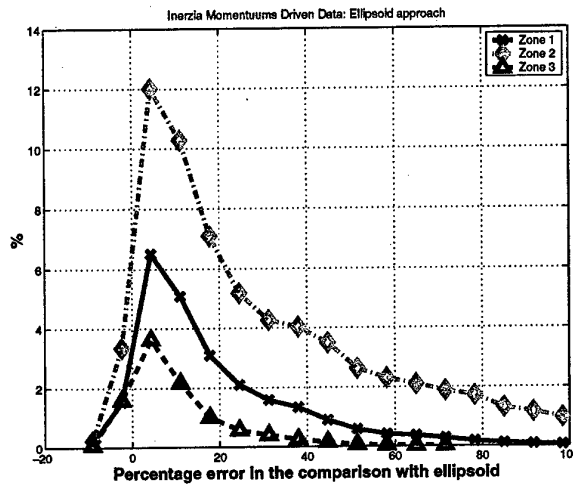


Fig. 5.27: Structures statistics $Re_\tau = 180$ (Case I): Equivalent ellipsoid volume deviation

arbitrariness of the model (see above) brought the present authors to the conclusion that the 3D elliptic shape is the most realistic model for typical structure and it was, therefore, retained for further study.

Dynamic of organized vorticity is assessed in Fig. 5.28, where specific vorticity and enstrophy (§4.5.2) are presented component per component. In this figure the percentages are computed considering the total number of structures, while in Fig. 5.29, the percentages are computed relatively to the local number of structures present in the current zone. This figure does not have all the curves collapsing the ones over the others, however it shows a similarity in the behavior of Zone 1 and Zone 2, especially regarding the vorticity and enstrophy along the stream-wise direction.

Regarding the vorticity components (Fig. 5.28 left column), predominant clockwise and counter-clockwise rotation around the stream-wise axis can be observed: relatively few structures have no or low stream-wise specific vorticity; corresponding behavior can be seen for wall-normal specific vorticity (although a loss of modulation is evident for Zone 2) indicating structures are rotating around an axis in $x-z$ plane. It should be noted that structures with a specific vorticity equal to zero could be complex structures as the ones depicted in Fig. 5.12, where counter rotating structures are merged together.

Regarding the specific vorticity in span-wise direction, it is necessary to keep in mind that, in the present analysis, the mean vorticity is subtracted from the instantaneous vorticity, in the tentative of removing the influence of the shear of the mean flow. On the data collected under such conditions, gaussian behavior of specific vorticity in span-wise direction (from middle left of Fig. 5.28 and 5.29) *apparently* puts in evidence the lack of preferred rotation around this axis; in reality, in the two aforementioned figures the average is performed on the whole channel. It does not come as a surprise the fact that the peak of vorticity is at zero,

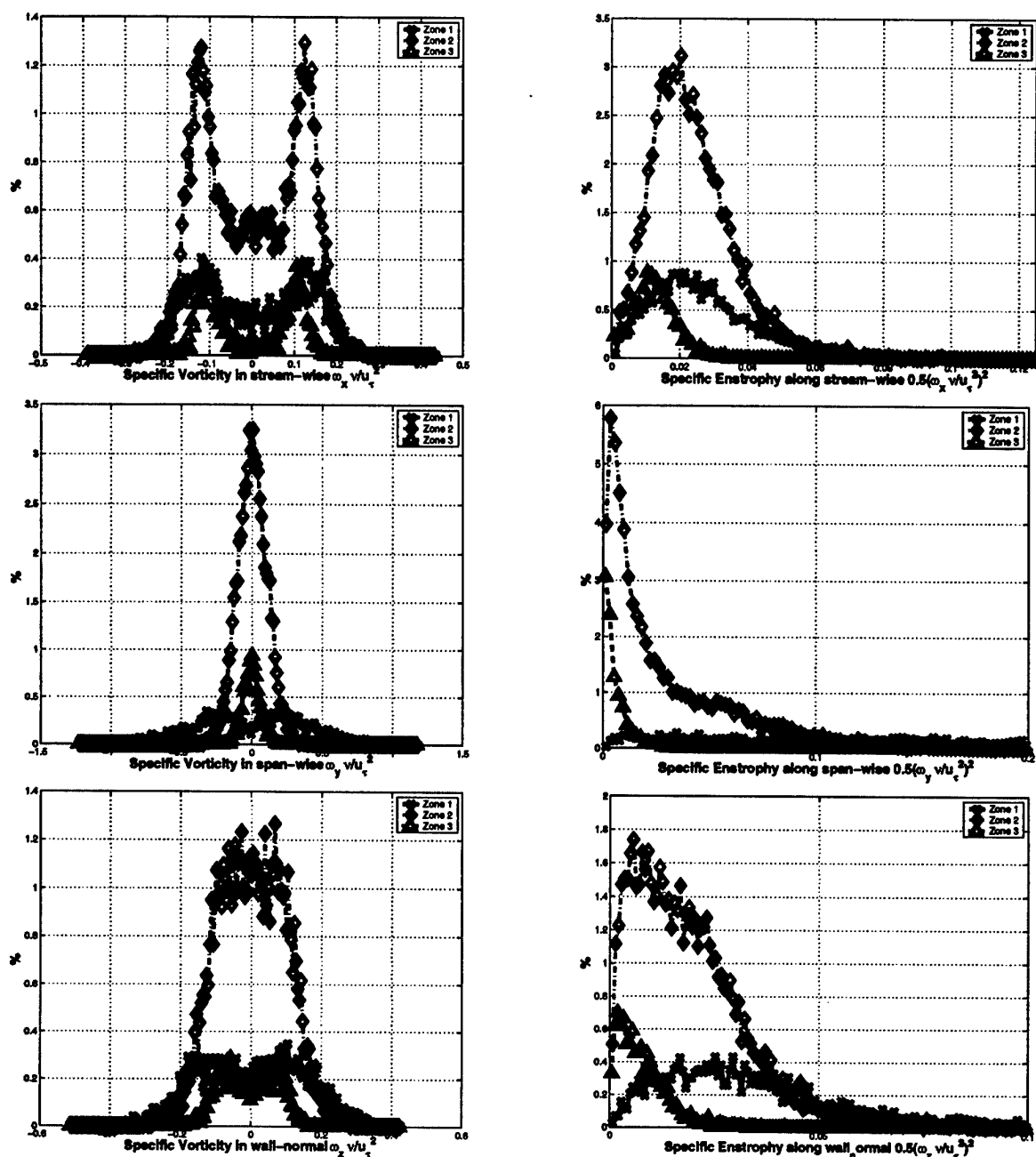


Fig. 5.28: Structure statistics: Specific Vorticity (left) and enstrophy (right) for x (top), y (middle) and z (bottom). $Re_\tau = 180$ (Case I). Percentage computed for total number of structures. (Number of bins: 200; limits of histograms (from top to bottom), vorticity: $-0.39 \dots 0.43$, $-1.23 \dots 1.18$, $-0.42 \dots 0.51$; enstrophy: $0 \dots 0.24$, $0 \dots 1.66$, $0 \dots 0.28$)

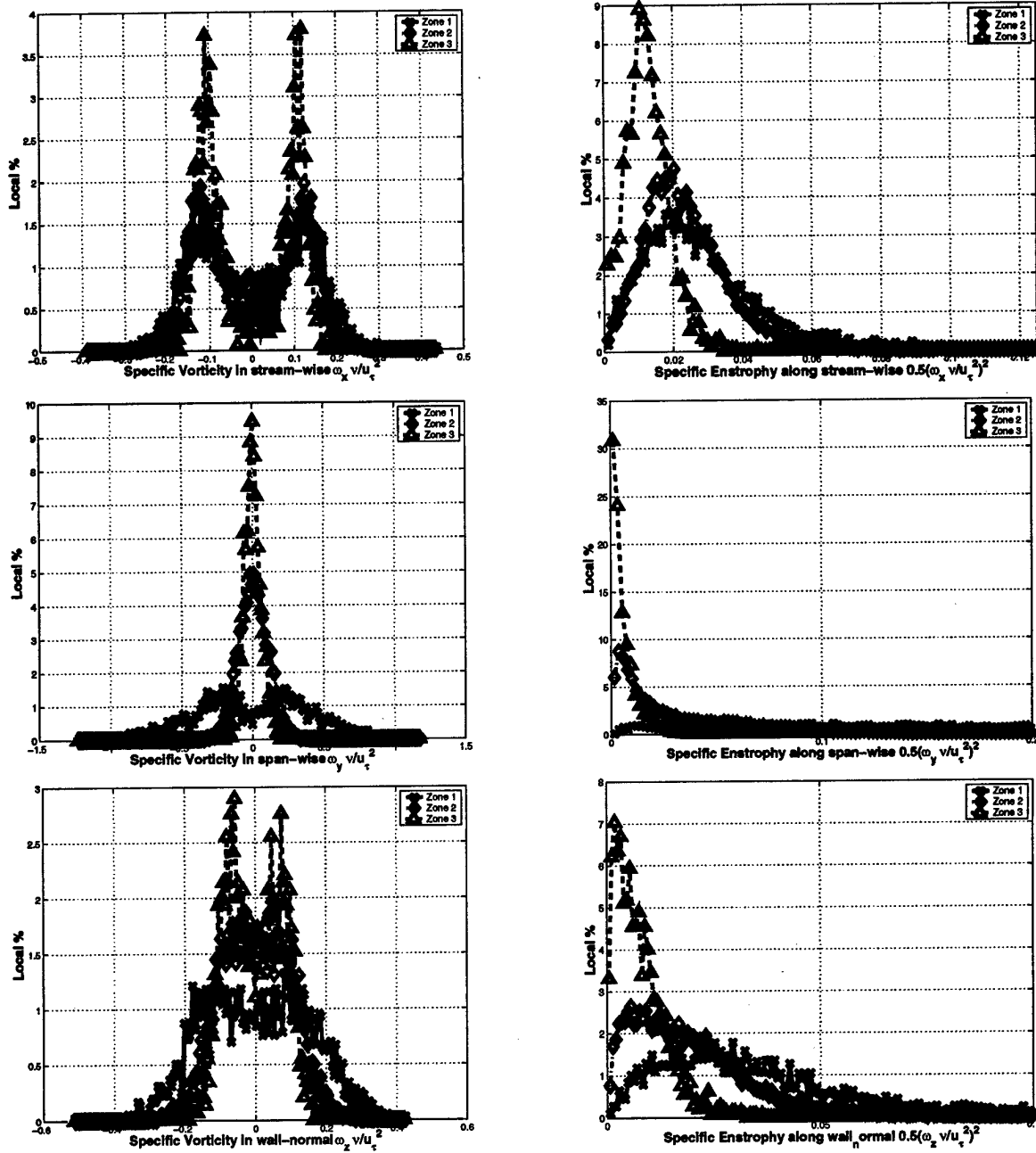


Fig. 5.29: Structure statistics: Specific Vorticity (left) and enstrophy (right) for x (top), y (middle) and z (bottom). $Re_\tau = 180$ (Case I). Percentage computed zone by zone. (Number of bins: 200; limits of histograms (from top to bottom), vorticity: $-0.39 \dots 0.43$, $-1.23 \dots 1.18$, $-0.42 \dots 0.51$; enstrophy: $0 \dots 0.24$, $0 \dots 1.66$, $0 \dots 0.28$)

and it is hard to imagine that the subtraction of mean vorticity could have a similar effect.

Indeed, considering only half a channel, the specific vorticity presents a bias consistent with the mean shear, see Fig. 5.30.

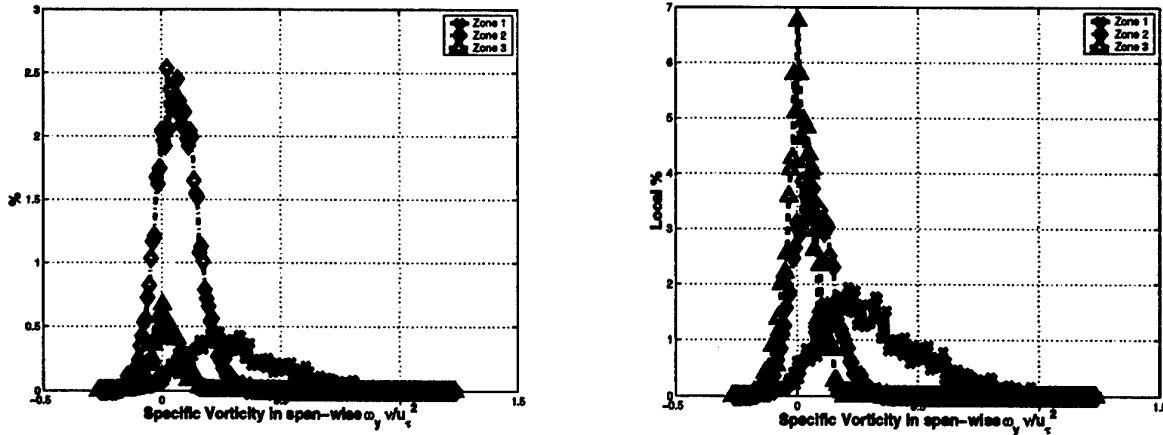


Fig. 5.30: Structure statistics: Specific span-wise Vorticity for half a channel; left, percentage compute respect the whole channel, right, percentage computed zone by zone

Regarding the enstrophy components (Fig. 5.28 right column), specific enstrophy confirms the tendency of the structures in Zone 2 to be more dense around a well defined value; this pattern is specially evident for stream-wise component: this behavior underlines the well defined rotation around this axis. The wide spread of values for span-wise and wall-normal component in Zone 1 puts in evidence the transition from longitudinal streaks to more complex and three-dimensional organization.

The JPDF of specific vorticity can be used to obtain a more complete understanding of the organization of vorticity field; similarly to what done for Fig. 5.20, it is possible to observe the behavior of the whole channel or only one half.

For the whole channel, an averaging is performed between the upper half and the lower one, and is shown in Fig. 5.31, while in Fig. 5.32 the data from both lower and upper halves are rearranged in order to represent exclusively the behavior of one half-channel, namely the lower one.

JPDF of specific vorticity in x and y direction for Zone 1 (top left of Fig. 5.31 or Fig. 5.32) extends the conclusions drawn from top left Fig. 5.28, showing the low probability of existence of structures with no rotation axis in $x-y$ plane (or, in other words, not rotating at all or only rotating along the wall-normal direction), especially for Zone 1; for structures with rotation around x values of stream-wise vorticity are clustered around ± 0.15 (Fig. 5.31, in units of present non-dimensionalization, namely $\omega_y \nu / u_\tau^2$). Corresponding plot for Zone 2 (top right of Fig. 5.32 or Fig. 5.31) shows a similar behavior, with a slightly higher probability of having structures not rotating in the $x-y$ plane ².

²Always keeping in mind that the number of structures belonging to Zone 2 is far greater of the one for

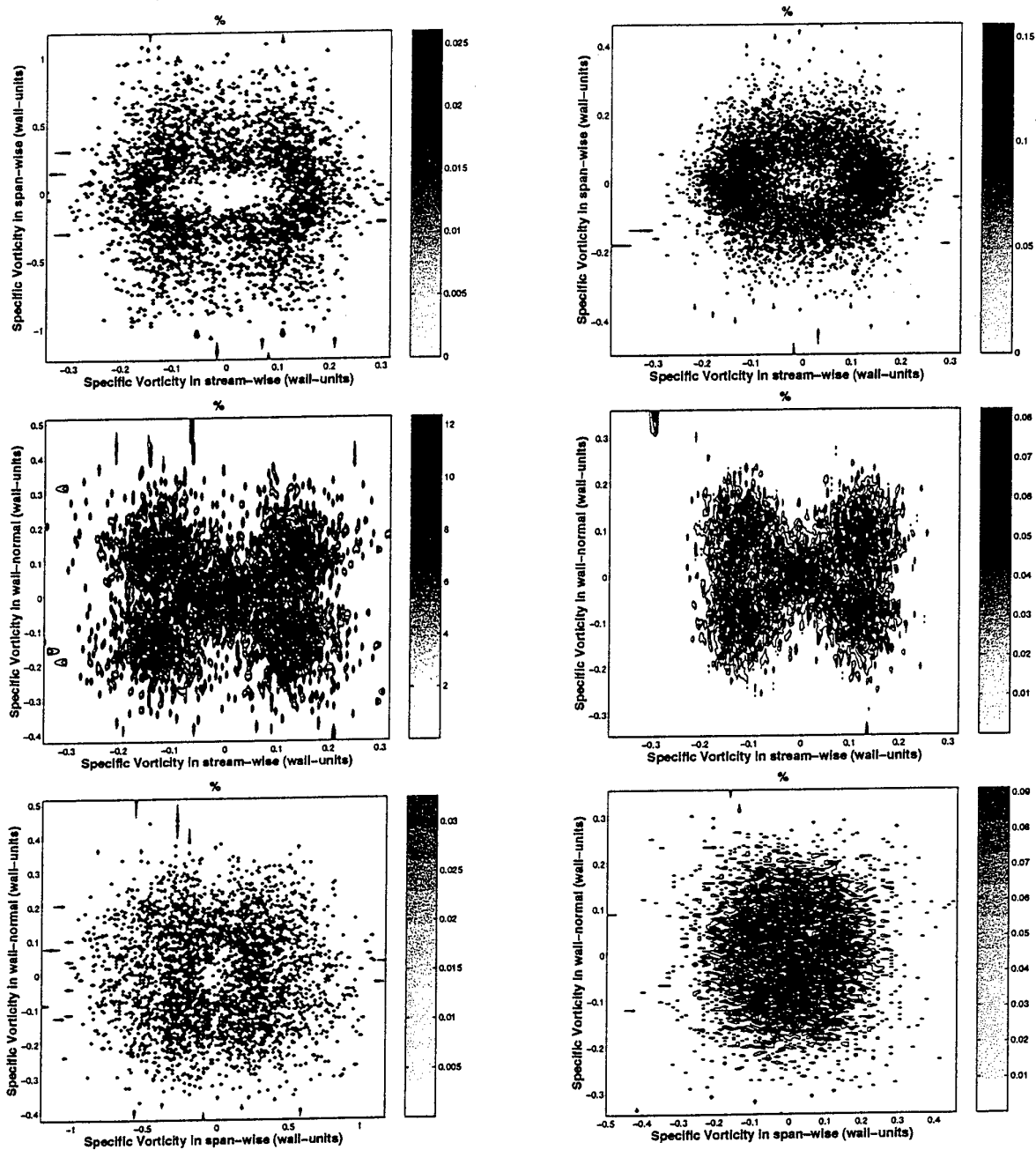


Fig. 5.31: Structures statistics, whole channel: JPDF for structures vorticity. Left Zone 1, right Zone 2, xy -top, xz -middle and yz -bottom. $Re_\tau = 180$ (Case I)

Different behavior can be noted examining JPDF of specific vorticity in x and z directions. Considering both Zones (central drawing on the left of Fig. 5.31), they have a clustering of points around $(0, 0)$; this is not a characteristics of the flow (having structures

Zone 1.

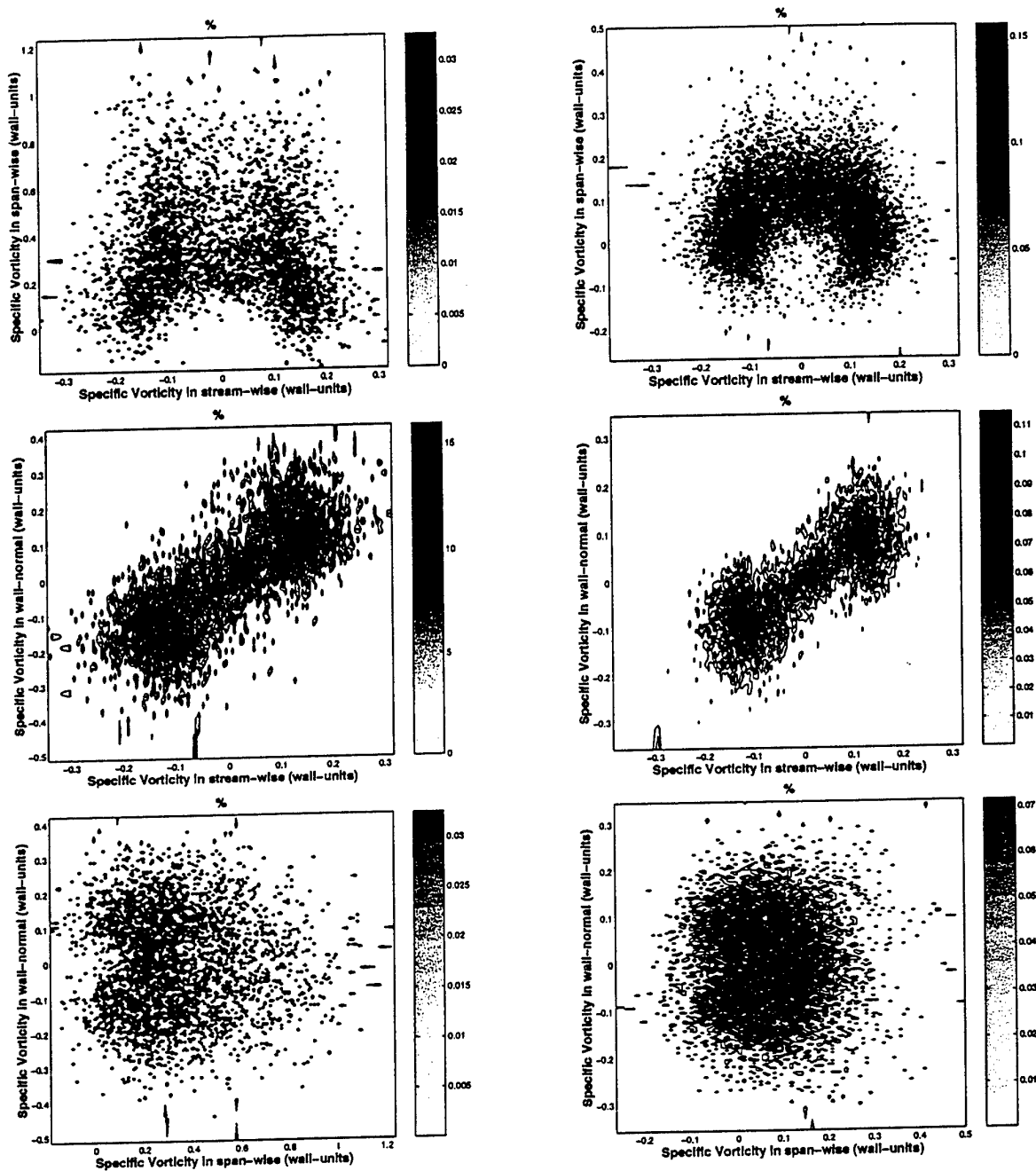


Fig. 5.32: Structures statistics, lower half-channel: JPDF for structures vorticity. Left Zone 1, right Zone 2, xy -top, xz -middle and yz -bottom. $Re_\tau = 180$ (Case I)

not rotating at all or simply rotating along span-wise direction), rather a consequence of the two lobes distribution of structures clearly evident in the center of Fig. 5.32: $(0, 0)$ connects the two region of higher density of structures and consequently inherits a certain number of structures around it.

Remember that in Fig. 5.31, where the behavior of the whole channel is considered, the four-lobe distribution is due to the symmetry of the channel and rotating and counter-rotating motions in the two wall layers.

Considering again the behavior of the single (lower) half channel (middle left of Fig. 5.32), the joint PDF clearly identifies the preferred vorticity orientation for the structures: vortical structures are usually streamlined entities developing close to the wall; due to vortex dynamics and interaction with the other structures, rotation in stream-wise induces a well defined evolution the other vorticity components, which is opposite for the two halves of the channel.

Pattern of behavior in Zone 2 consistent of this interpretation can be observed in central drawing on the right of Fig. 5.32: in this case it is clear that most of the structures are provided of rotation around the x and z axis.

Most probable values of specific vorticity are respectively $\pm 0.12 \dots 0.15$ and $\pm 0.08 \dots 0.1$ for x and z .

Regarding the JPDF of specific vorticity in y and z direction (bottom of Fig. 5.31 or Fig. 5.32), the first remark to do is the low probability, especially in Zone 1, of structures having only rotation along the stream-wise direction, or no rotation at all, meaning that the structures are characterized by off-axes rotations. The results are characterized by symmetry respect the wall normal direction, as it is to be expected, and while in the averaging in the whole channel produces an additional symmetry along the other axis in Fig. 5.31, from Fig. 5.32 it is clear that values for specific vorticity in y are higher than the corresponding ones for specific vorticity in z , even with subtracted the mean shear, confirming the tendency of structures to tilt away of the $x - y$ plane.

5.1.1 Conclusion

To conclude the present analysis, it can be stated that the present data show the presence of population of organized structures, mostly located within the inertial layer. Tab. 5.4 indicates the concentration of vorticity and enstrophy with these structures suggesting the inevitable conclusion that they must play a fundamental role in formation of turbulence. Analysis indicates the predominant existence of structures elongated in stream-wise direction.

Most probable size seems to be in the order of 100 wall-units for the structures main axis and 20 – 40 wall-units for the two other axis.

The second value is in the same order of the wall-normal macro-scale, as obtained from DNS data, while the first one is considerably lower than the stream-wise macro-scale (180 wall units) extracted from DNS data.

Fig. 5.11 allows to conclude that larger structures are present but would be a small minority of the overall population: structures with $L_x \cong 180$ correspond to 4% of the popu-

lation in Zone 1, and 2% in Zone 2. JPDF (Fig. 5.16) for $L_x - L_z$ for Zone 2 shows that all structures where $150 < L_x < 200$ fall in region of joint probability less than 0.1. Estimated tilting angle for these structures lies between 10 and 20 degrees.

Validity and consistence of present results and conclusions must be verified assessing the influence of basic parameters of simulation, namely:

- Grid resolution
- Detection criterion
- Numerical accuracy of the solver
- SGS model

This task will be addressed in the next sections.

5.2 Effect of grid resolution

Effect of size of LES grid on simulation of structures is assessed in first instance comparing the results presented in § 5.1 with the ones obtained on different grids as summarized in Tab. 5.7.

Table 5.7: Plane channel at equilibrium at $Re_\tau = 180$, alternative grid tested (Case II). Geometrical Parameters

Geometry & Grid			Alt. Grid (Case II)		
L_x	L_y	L_z	$\frac{5}{2}\pi$	$\frac{4}{3}\pi$	2
N_x	N_y	N_z	96	128	64
Δx^+	Δy^+	Δz^+	14.72	5.89	$1.5 < \Delta z^+ < 16$

It is to be remarked that the present grid has been refined both in stream-wise and span-wise directions, while the wall normal resolution has not been altered, since it was observed that the grid is already sufficiently small, compared to the typical size of the expected structures; all the test parameters are identical to the previous one (conf. § 5.1).

Detailed results of the LES computations are presented in Annex A, while present discussion focus on differences between the two simulations.

Applying established criterion (§ 4) for setting trigger level yields the value $Tr = 91$.

Global values for the two populations of structures are compared in Tab. 5.8 together with their relative deviation (f_{dev} given f_i variable of interest) respect to the algebraic averaged value (f_{mean}) defined in eqn. 5.2. Since only two sets of data have to be compared, in present case, the relative deviations are equal and opposite and we represent in Tab. 5.8 only the absolute percentage value.

$$f_{mean} = \frac{1}{n} \sum_{i=1}^n f_i \quad ; \quad f_{dev} = \frac{f_i - f_{mean}}{f_{mean}} \quad (5.2)$$

In Tab. 5.8 the comparison between the different quantities has been made in the following fashion: consider the structures volume; the volume in average occupied from the structures has been divided by the total volume of the computational field; the percentage presence in volume of the structures has been obtained for the two grids and the two results then compared. Another possibility could be the direct comparison of the raw value of the quantity between to two grids. Possibly this comparison is stricter than the former one, since the filtering produced by the division for the total value of the quantity under exam (ad example TKE) might somehow smooth the grid effect; however comparison of eulerian quantities (see Tab. 5.9) shows them to be close enough to neglect this point.

Table 5.8: Plane channel at equilibrium at $Re_\tau = 180$. Volume, turbulent kinetic energy, module of vorticity and enstrophy within structures versus corresponding quantities within the full computational field. Comparison between Case I and Case II

	Grid 1	Grid 2	Deviation
<i>Volume</i>	9.661 %	9.888 %	1.2 %
<i>TKE</i>	14.075 %	14.280 %	0.7 %
<i>VorticityModulus</i>	19.893 %	20.850 %	2.3 %
<i>Enstrophy</i>	25.058 %	27.273 %	4.2 %
<i>Num.ofStructures</i>	247	358	18.0 %

Table 5.9: Plane channel at equilibrium at $Re_\tau = 180$. Total, turbulent kinetic energy, vorticity and enstrophy in present non-dimensional units. Comparison between Case I and Case II

	Grid 1	Grid 2	Deviation
<i>TKE</i>	115.25	111.67	1.6 %
<i>VorticityModulus</i>	1457.0	1489.4	1.1 %
<i>Enstrophy</i>	63603.0	64868.0	1.0 %

The deviation is the order of 1%, indicating that eulerian field is sufficiently well converged.

Concerning the simulation of the structures, Tab. 5.8 shows values for global quantities to be very similar for the two cases, apart for a bigger difference about the number of detected structures; regarding the second, more resolved, grid, the flow field seems to be characterized by more numerous and smaller structures.

This effect can be observed, with some difficulties, in an overall visualization of the field, Fig. 5.33 and Fig. 5.34.

With respect to the structures detected on previous grid (see Fig. 5.11, Fig. 5.12 or Fig. 5.13), the number of detected structures increases, and most of the new ones have smaller size in longitudinal direction and are relatively quasi-isotropic ones; an example of this type of structures is shown in Fig. 5.35. This effect should not be surprising: it was stated in Chapter 4 that there is a minimal dimension for a structure to be detected and defined. Increasing the resolution, necessarily, leads to the increase in the number of the small structures considered.

Structures of topology comparable to ones found in the previous case (Fig. 5.11) are present, as it should be expected (see Fig. 5.36).

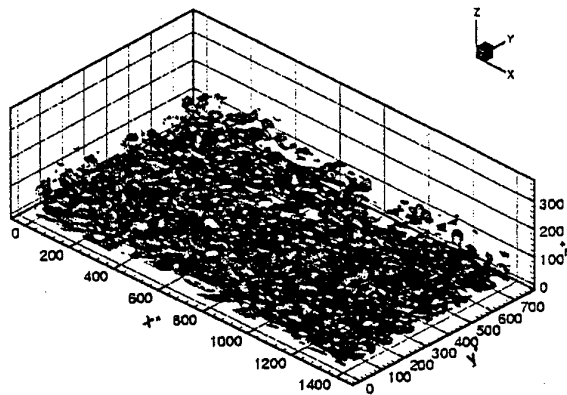


Fig. 5.33: 3-D overview of the field of detected structures of plane channel at $Re_\tau = 180$ (Case II)

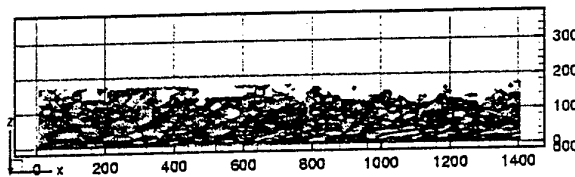


Fig. 5.34: Lateral overview of the field of detected structures of plane channel at $Re_\tau = 180$ (Case II)

The statistical importance of small structures can be seen by the distribution of volume of the population (Fig. 5.37).

Comparison of Fig. 5.6 and Fig. 5.37 offers a practical example of the way the PDF here presented should be considered. Considering Zone 2, the PDF has a peak of 4.68% for structures having a volume of roughly $1.3576e^{+04}$ wall units. Considering the limits of the PDF and the number of bins, remembering what explained in § 4.5.2, the bin extension is approximately of 3840 wall units. Then, since in Tab. 5.8 the average number of structures for field has been quantified in 358 structures, this means that there are $\frac{4.68 \cdot 358}{100} \approx 9$ structures having a volume oscillating between $1.3576e^{+04} - 3840 \approx 9735$ and $1.3576e^{+04} + 3840 \approx 17416$.

Now consider Fig. 5.38. In this figure the limits of the histograms are obviously the same, because the data analyzed does not change, but the number of bins has been halved. The peak is of 8.38% for a volume of $1.1656e^{+04}$ wall units. Now the bin size is 7680, exactly the double of previous case. Now there are 30 structures having volumes oscillating between $1.1656e^{+04} - 7680 \approx 3976$ and $1.1656e^{+04} + 7680 \approx 19336$.

Now the interval considered is twice wider than the previous one, but the number of structures included is three times bigger. It is easy to understand how to properly compare

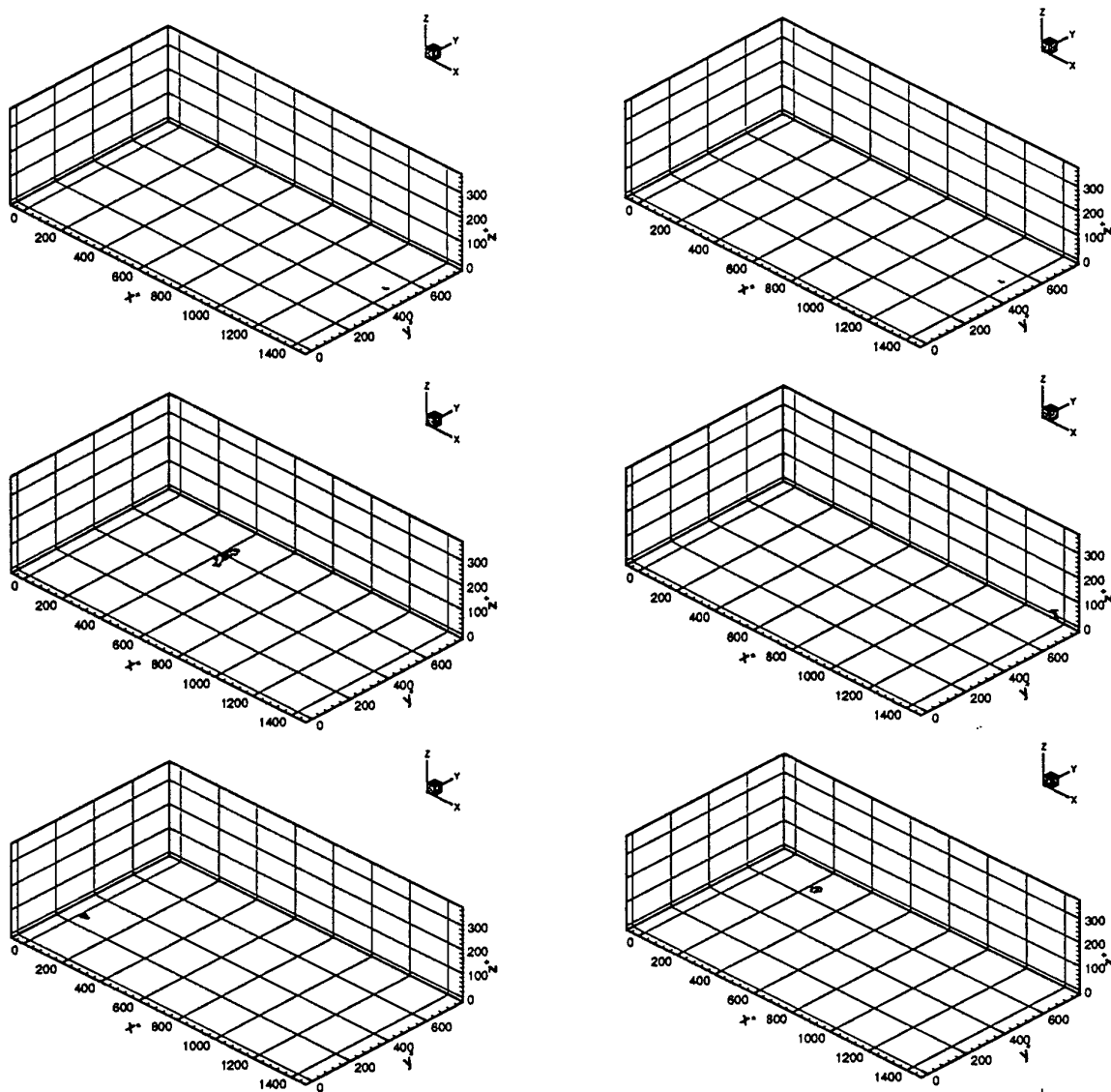


Fig. 5.35: Increased resolution multiply the presence of identified structures of small dimensions for plane channel at $Re_\tau = 180$ (Case II)

different results between them appropriate precautions should be taken³.

If, however, the main objective of the analysis is only to find the most probable dimension of structures for two different flow realizations and then compare them, most of the restrictions briefly stated can be disregarded and a simpler and faster analysis can be performed.

³This being the case for the results presented in Annex G, where the data handling took particular attention in order to keep the comparison consistent. See § 5.5 for the meaning of the Annex

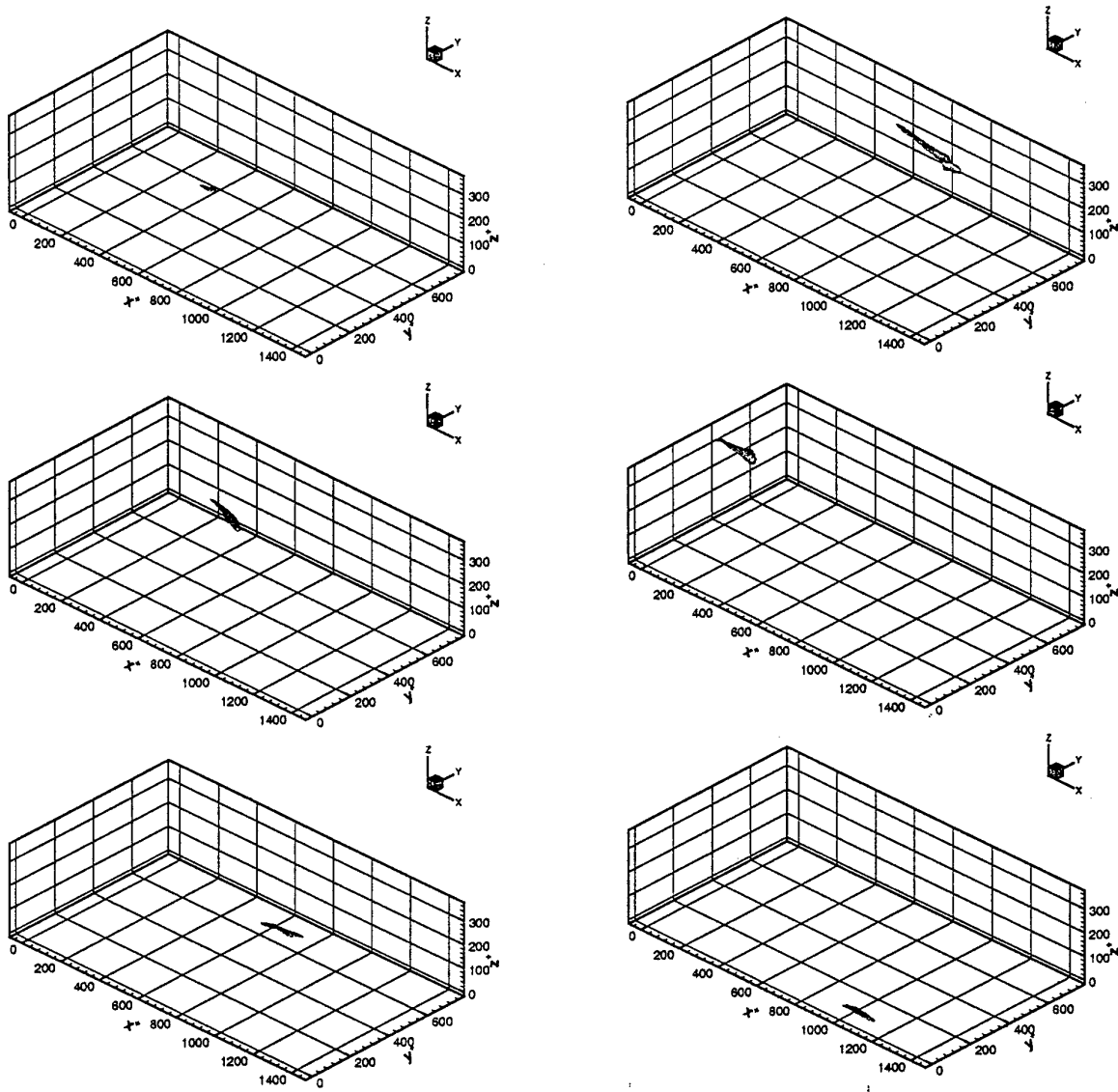


Fig. 5.36: Typical structures elongated in stream-wise direction of plane channel at $Re_\tau = 180$ (Case II)

The average volume (in an algebraic sense) is now of $Vol_{mean} = 1.06e^{+05}$, roughly 50% smaller than for previous simulation.

This effect can be assessed looking to the distribution of L_x , L_y and L_z for this new grid (Fig. 5.39 and Fig. 5.40).

It must be remarked that structures with L_x in the order macro-scale (namely the half-width of the channel) are still present (Fig. 5.36): Fig. 5.39 top left shows, on average, around 5 structures close to this value; comparing with the result of around 9 structures for the first

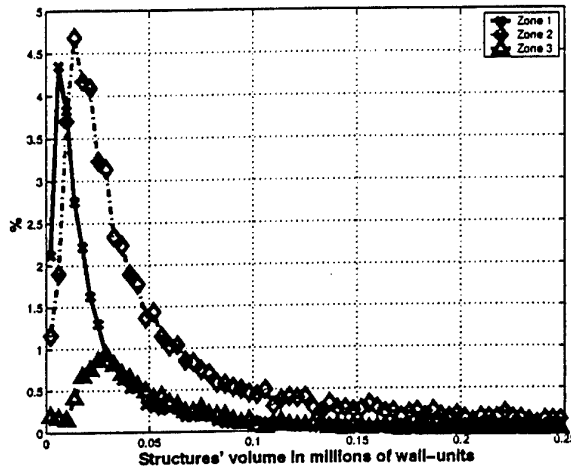


Fig. 5.37: Structures Volume of plane channel at $Re_\tau = 180$ (Case II) with usual zone distinction. (Number of bins 2000; limits of histogram: $135.7 \dots 7.68e^{+06}$)

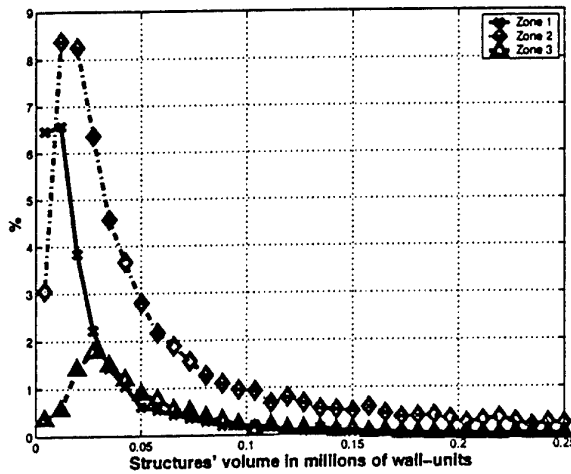


Fig. 5.38: Structures Volume of plane channel at $Re_\tau = 180$ (Case II) with usual zone distinction. (Number of bins 1000; limits of histogram: $135.7 \dots 7.68e^{+06}$)

Table 5.10: Plane channel at equilibrium at $Re_\tau = 180$ (Case II). Most common values for L_x , L_y and L_z in wall units for Zone 2

L_x	L_y	L_z
70 – 60	30 – 40	30 – 40

grid, the difference should not be statistically important, but the larger population of smaller structures accounts for an important change in relative percentages.

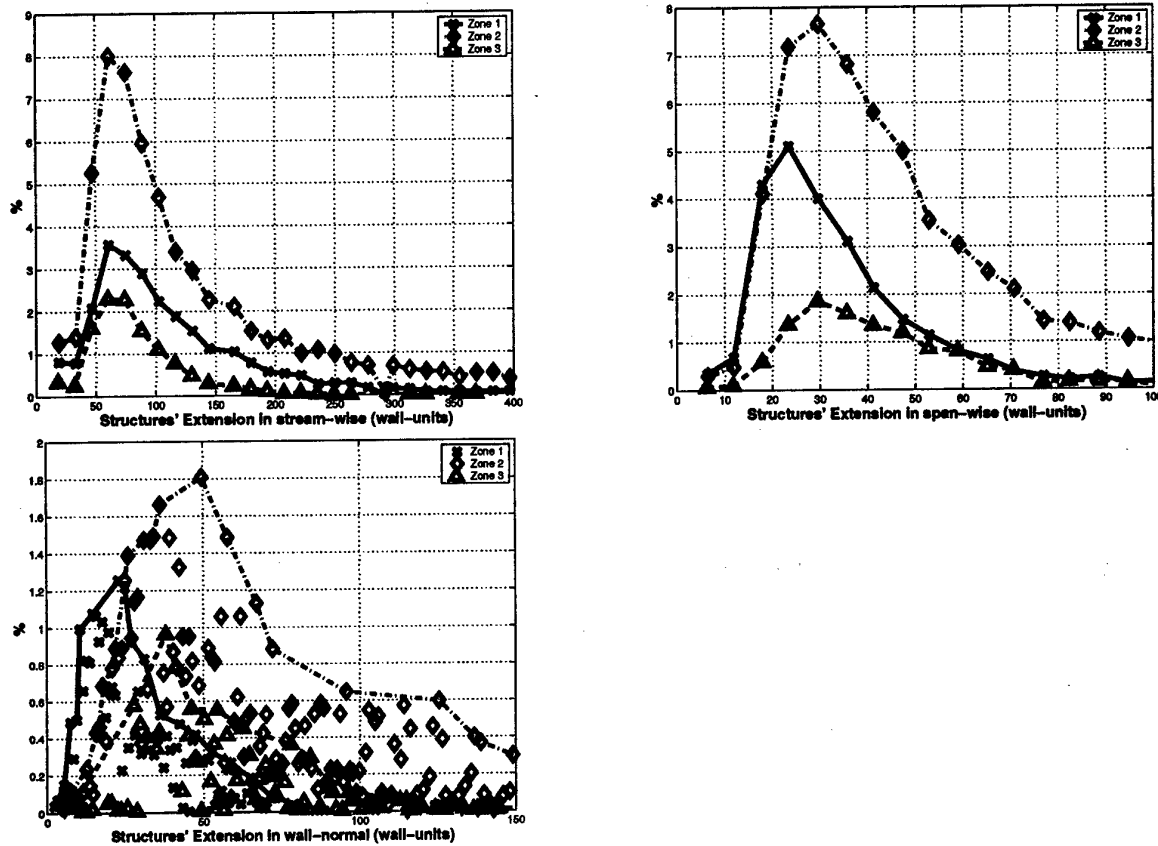


Fig. 5.39: Structures statistics at $Re_\tau = 180$ (Case II): length in wall units. (From top left to bottom right: Number of bins, 2000, 8000, 2000; limits of histograms: 14.72 ... 1413.7, 5.89 ... 553.70, 1.56 ... 206.72)

The data outlined above can be obtained computing the histograms in terms of number of structures or can be retrieved from the histograms expressed in percentage multiplying for the appropriate average number of structures for field.

Focusing on zone 2, and repeating the analysis performed in § 5.1, JPDF for $L_x - L_y$ and $L_x - L_z$ (Fig. 5.40) are examined to obtain a better estimation of typical structure.

Table 5.11: Plane channel at equilibrium at $Re_\tau = 180$ (Case II). Most probable structure values for L_x , L_y and L_z in wall units for Zone 2 based on the JPDFs

L_x	L_y	L_z
60	25	25 – 35

As shown in § 5.1, this has to be compared to estimation of size and orientation of the structures as can be obtained from their inertial moments.

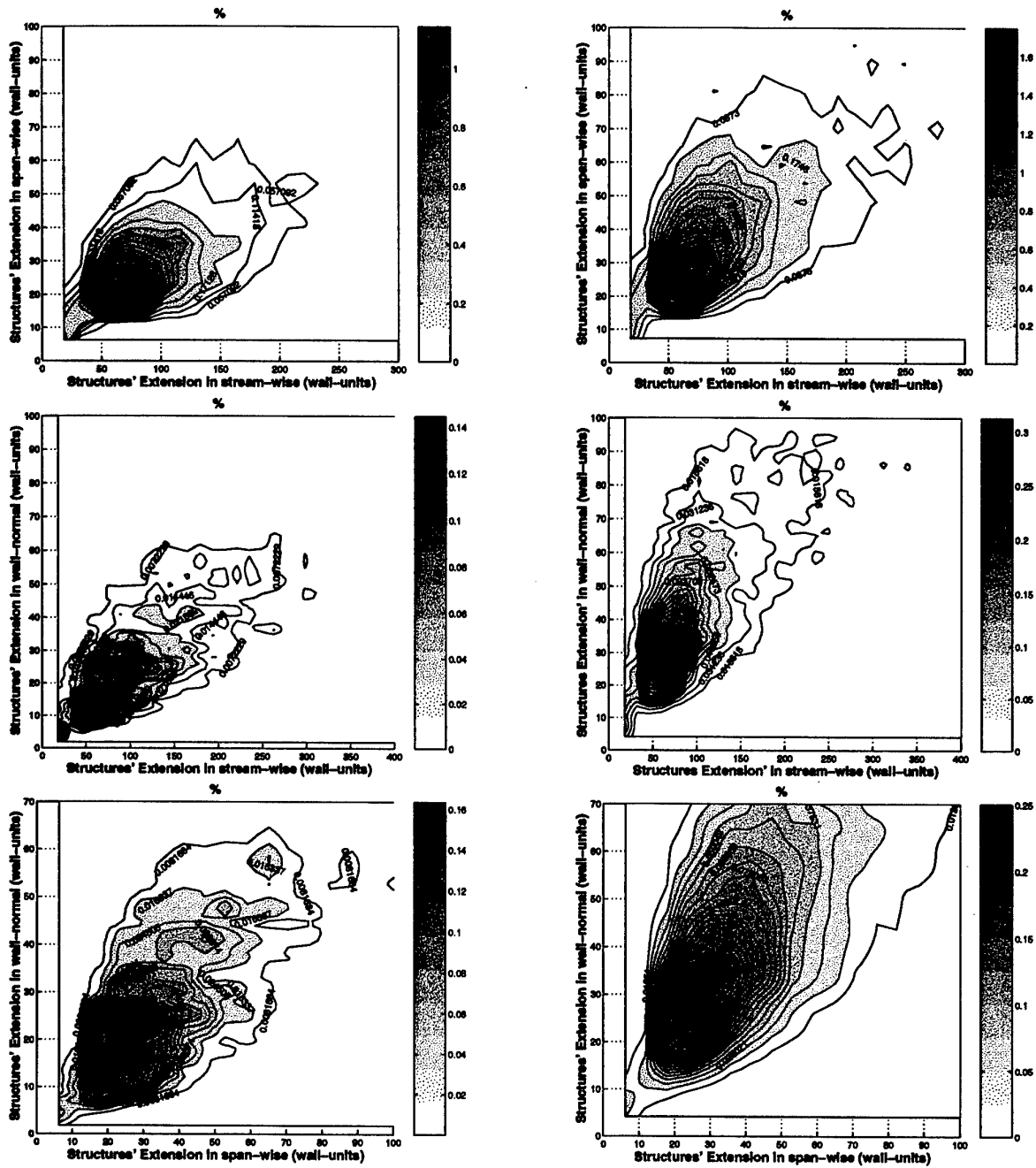


Fig. 5.40: Structures statistics: JPDF for structures extension. $Re_\tau = 180$ (Case II). Left column Zone 1, right column Zone 2, xy -top, xz -middle and yz -bottom

Inertial moments of present population for Zone 1 and 2 are presented in Fig. 5.41. It was considered interesting enough to present, in Fig. 5.42 the alignment for the structures in the third zone, close the channel centerline. In this region the structures are sufficiently far

away from the wall for its influence beginning to become negligible, starting a slow return to isotropy, as it clear to the more random distribution of the structures.

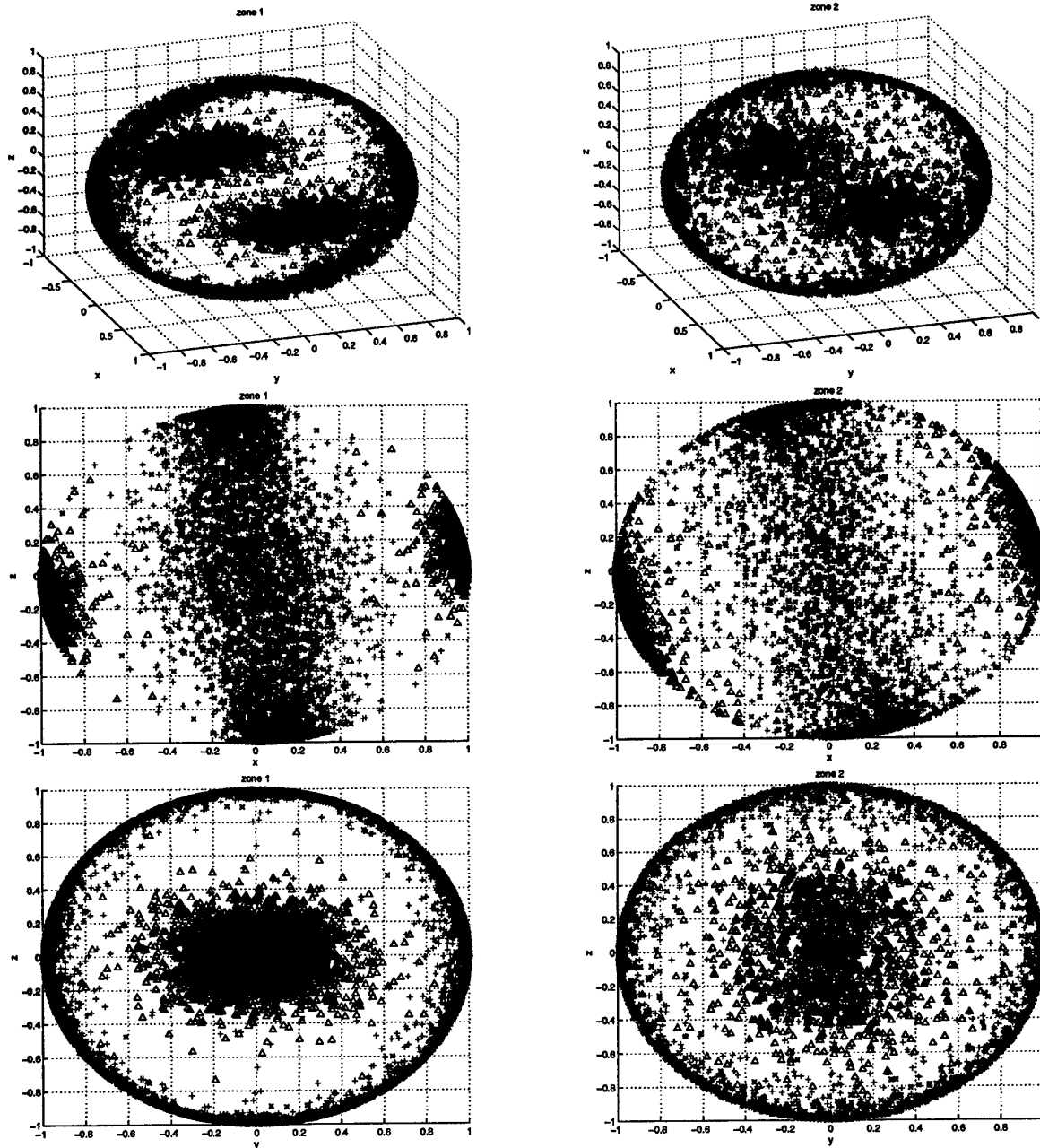


Fig. 5.41: Structures statistics, $Re_\tau = 180$ (Case II): spatial alignment, different pov. Δ Structure mean alignment. Zone 1 left column, Zone 2 right column

Present results show patterns very similar to the ones remarked for Grid 1. Beside the graphical representation of the structures depicted in Fig. 5.41 and Fig. 5.42, the statistics

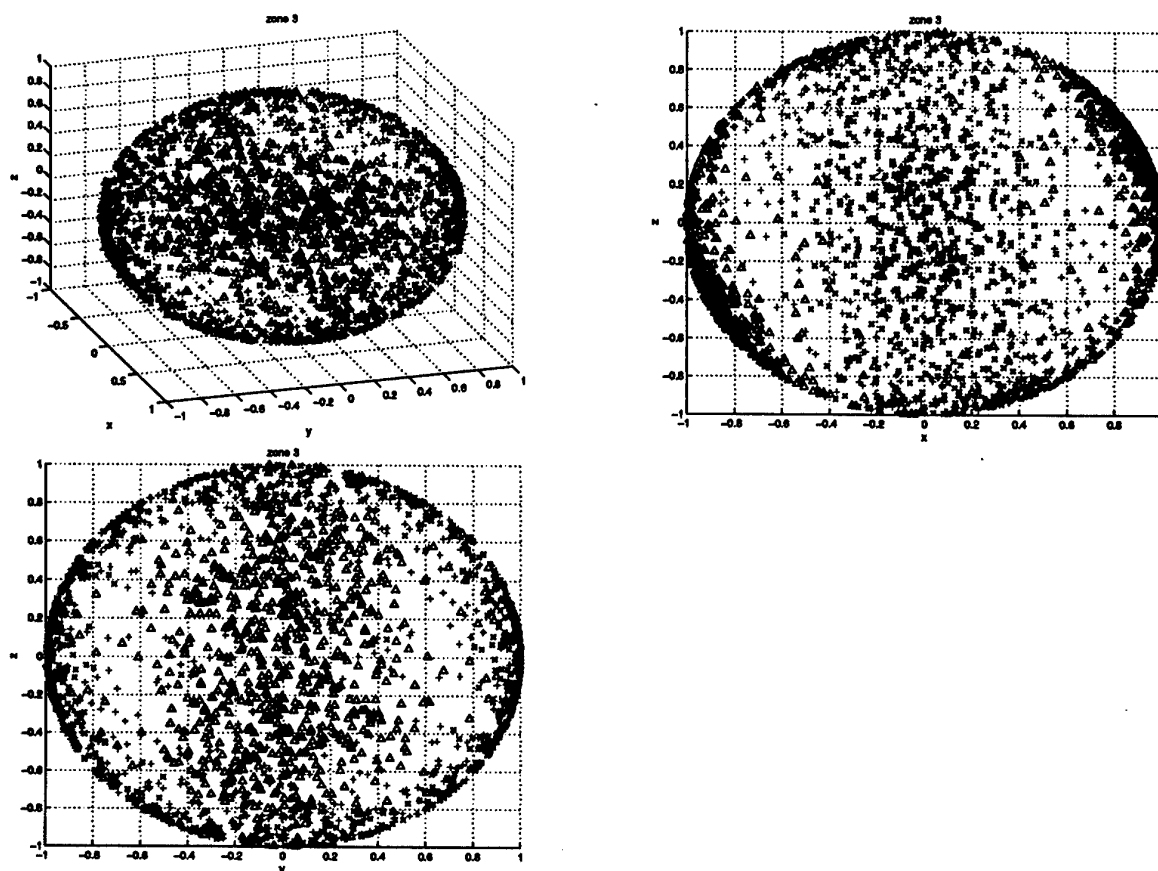


Fig. 5.42: Structures statistics, $Re_\tau = 180$ (Case II): spatial alignment, different pov. Δ Structure mean alignment. Zone 3

gathered on the structures lead to Fig. 5.43 and Fig. 5.44.

Comparing the two set of information, a possible incongruence appears, that has not been addressed in § 5.1 for simplicity, delaying its study to now.

From the graphical representation of the structures inclination, Fig. 5.41 top and bottom, it is clear how in Zone 1 most of the structures are oriented along the stream-wise direction; in Zone 2, with increasing distance of the structures from the wall, their range of possible $x - z$ angles increases, while conversely the one for the $x - y$ apparently decreases.

The observation concerning the $x - z$ inclination is confirmed from the PDF presented in Fig. 5.44 while Fig. 5.43 does not indicate a narrowing of the range of the tilting angle.

The reason of this apparent incongruity lies in what already said about Fig. 5.18. Matter of fact, the population of structures is different in number in Zone 2 and Zone 1, with a much bigger number of structures lying in Zone 2. Showing in the left and right columns the structures corresponding to the same number of flow fields would have resulted in a much

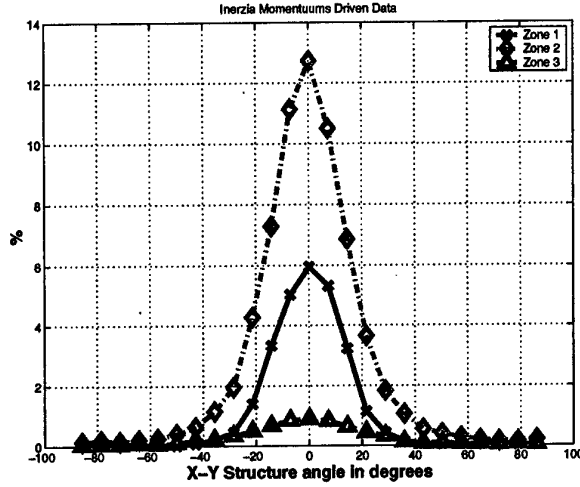


Fig. 5.43: Structures statistics $Re_\tau = 180$ (Case II): Tilting angle extracted from inertial tensor. (Number of bins: 25; limits of histograms: $-90 \dots 90$)

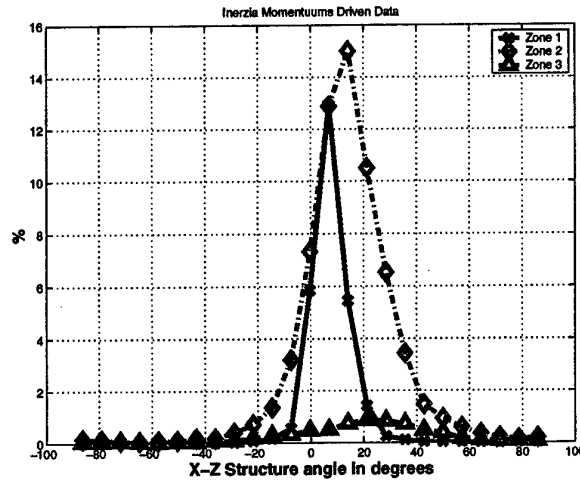


Fig. 5.44: Structures statistics $Re_\tau = 180$ (Case II): Incidence angle extracted from inertial tensor. (Number of bins: 25; limits of histograms: $-90 \dots 90$)

higher number of structures represented in the right column affecting the readability of the data. It was chosen, as a rule of thumb, to roughly show the same number of structures on left and right column, so that the left column of Fig. 5.41 corresponds to roughly five times the realizations (namely flow-fields) sampled for its right column.

This means that Zone 1 has higher probability to show, in Fig. 5.41, events of low probability (or structures with high tilting angle) rather than Zone 2, leading to the apparent incongruence between Fig. 5.41 and Fig. 5.43: the former suggests more structures with high tilting angle for the first zone, the second seems indicating the opposite.

To try to remedy this possible source of confusion, a revised-normalized version of Fig. 5.41 and Fig. 5.43 can be produced.

In this case, the first step is to present the PDF relative to the structure angles in terms of the percentage computed relatively to the number of structures present in the relative zone, and not to the total.

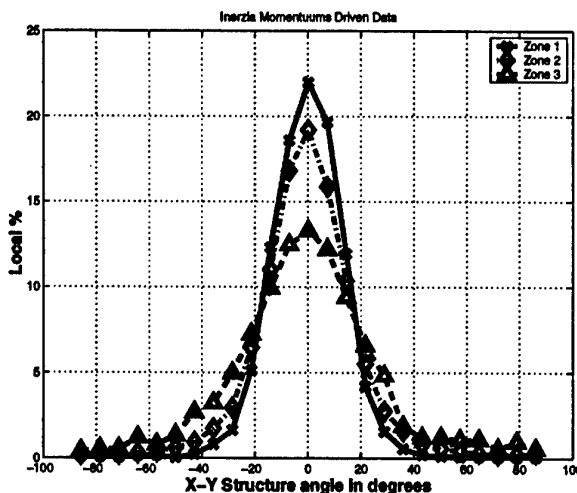


Fig. 5.45: Structures statistics $Re_\tau = 180$ (Case II): Tilting angle extracted from inertial tensor, local percentages. (Number of bins: 25; limits of histograms: $-90 \dots 90$)

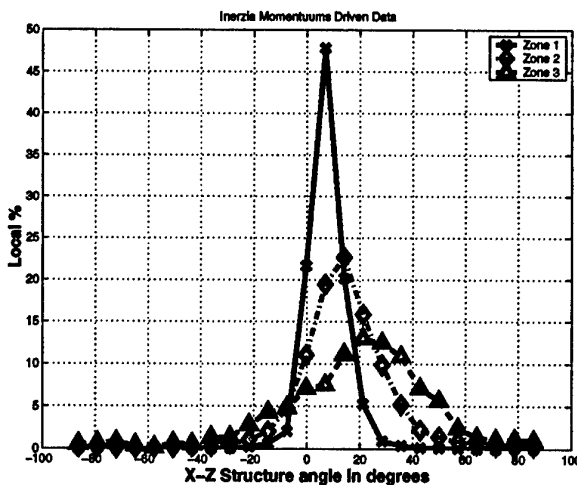


Fig. 5.46: Structures statistics $Re_\tau = 180$ (Case II): Incidence angle extracted from inertial tensor. (Number of bins: 25; limits of histograms: $-90 \dots 90$)

In this way, an interesting trend can be remarked, namely the fact Zone 1 and Zone 2 are extremely similar in the distribution of the tilting angle (Fig. 5.45), while for the incidence

angle (Fig. 5.46) it is clear that structures of Zone 1 appear to have the sharpest defined preferential angle.

In second place, it can be concluded that, the number of structures used in Fig. 5.41 being different (the left column -Zone 1- and the right one -Zone 2-) they can be useful for illustrative reasons only. Indeed, looking back to § 5.1, no conclusion were drawn from this corresponding figure, only from the relative PDF.

To correct this, in Fig. 5.47 the same number of structures has been used, and then there is no incongruence with Fig. 5.45.

Regarding the comparison with the previous grid, Fig. 5.43 or Fig. 5.45 confirms that there is no preferred tilt angle. Existence of an average incidence angle (Fig. 5.44 and Fig. 5.46) shows the tendency of structures to rotate away from the $x - y$ plane: incidence angle increases from Zone 1 (7 degrees) to Zone 2 to reach a most probable state of 14 degrees; it will increase further in Zone 3 where it reaches value 21 degrees. Again, it has to be remarked that difference with results for Grid 1 does not change substantially the structures behavior.

Following conclusions derived at the end of § 5.1, the typical shape of the structure is assumed to be an ellipsoid of volume $\frac{4}{3}\pi abc$, where $a \geq b \geq c$ are the semi-length on the 3 axis, whose values are presented in Fig. 5.48 to Fig. 5.50. It is possible to compare the volume of the ellipsoid with the volume of the corresponding structure, being able finally to retrieve Fig. 5.51.

According to Fig. 5.48 to 5.50, the most probable state, for Zone 2, would be an ellipsoid having $a \cong 42$, $b \cong 14$, $c \cong 9$ wall units.

From comparison with corresponding results for Grid 1, these values confirm the trend of more refined grid to yield a population with smaller most probable sizes. It is to be remarked that the values $2 \times a$, $2 \times b$ are in acceptable agreement with the most probable state yielded by the JPDF of $L_x - L_y - L_z$ (60 - 25 - 30) for Zone 2 (Tab. 5.11); obviously, a perfect agreement cannot be achieved, since in Tab. 5.11 the quantities shown in Fig. 5.14 are considered, and not the real dimensions of the structures.

Dynamic of organized vorticity can be assessed in Fig. 5.52.

Distribution of stream-wise component of vorticity (Fig. 5.52 top) shows a majority of structures to have a clockwise or counter-clockwise rotation around x axis in Zone 1 and 2. Again, the distribution is equivalent to one yielded by simulation on Grid 1.

Wall-normal specific vorticity (Fig. 5.52 bottom) shows a corresponding behavior and agreement, while gaussian-like behavior of specific vorticity in span-wise direction (middle) puts in evidence the lack of preferential rotation around this axis; it must again be remember that for Fig. 5.52 the average on the whole channel has been used.

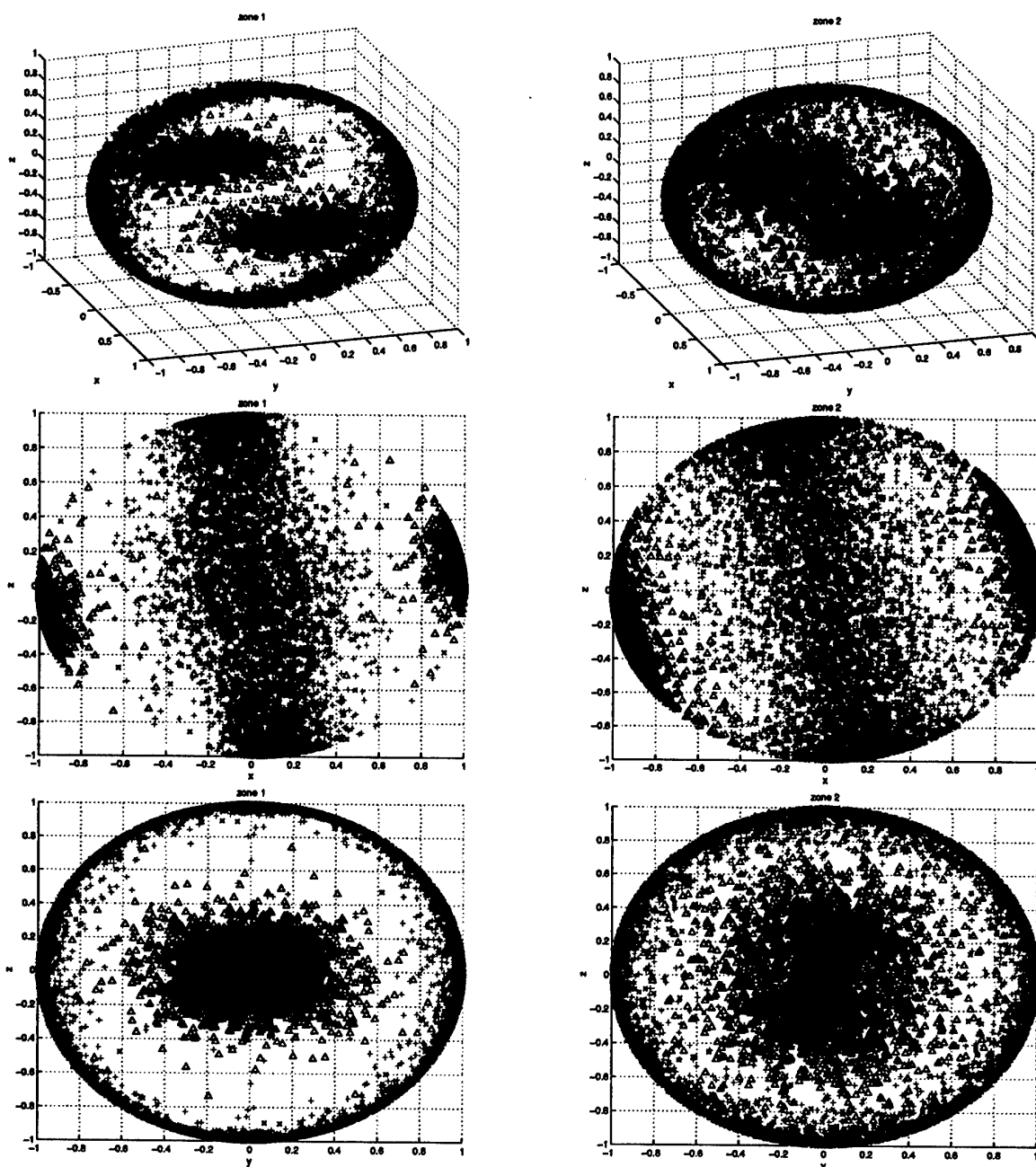


Fig. 5.47: Structures statistics, $Re_\tau = 180$ (Case II): spatial alignment, different pov. Δ Structure mean alignment. Same number of structures (1500) for Zone 1 left column, Zone 2 right column

The JPFD of specific vorticity for Zone 1 and 2 are presented in Fig. 5.53 and Fig. 5.54.

These distributions and most probable states are very similar to ones presented in § 5.1.

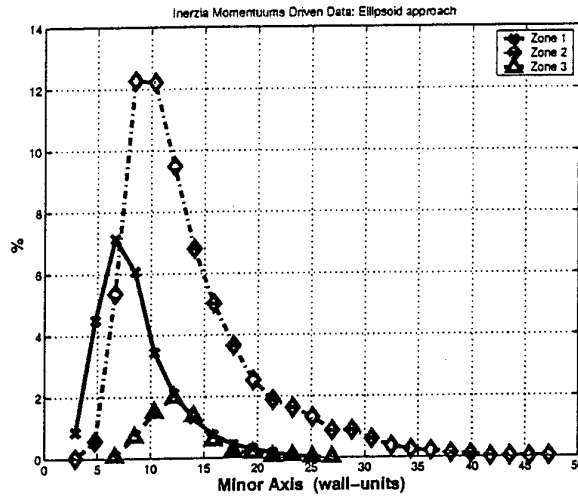


Fig. 5.48: Structures statistics $Re_\tau = 180$ (Case II): Equivalent ellipsoid minor semi-axis

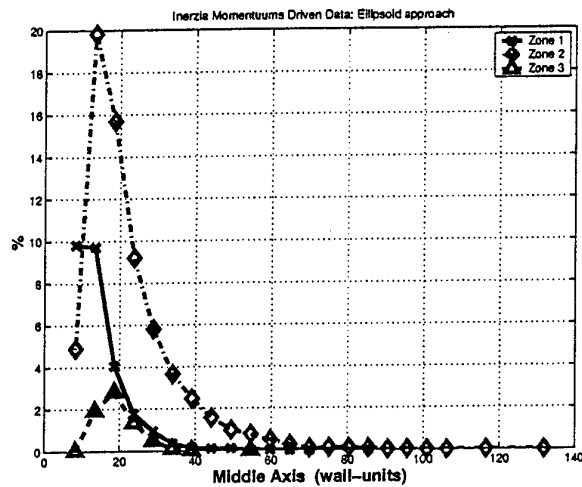


Fig. 5.49: Structures statistics $Re_\tau = 180$ (Case II): Equivalent ellipsoid middle semi-axis

The only remarkable difference concerns the $x - y$ JPDF in the proximity of the wall (Zone 1); comparison with corresponding results on Grid 1 shows that the "dough-nut" distribution where no points are found in $(0,0)$ region (Fig. 5.31), is replaced by a wider dispersion of points and, among the new structures put in evidence by the more refined grid, no-rotating states are more probable.

5.2.1 Conclusion

In conclusion, it can be estimated that results shown in the present § 5.2 lead to fact that the global statistics associated with organized turbulence are practically identical for

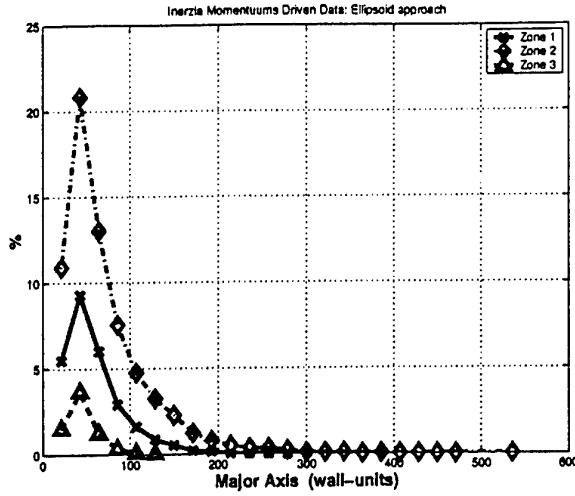


Fig. 5.50: Structures statistics $Re_\tau = 180$ (Case II): Equivalent ellipsoid major semi-axis

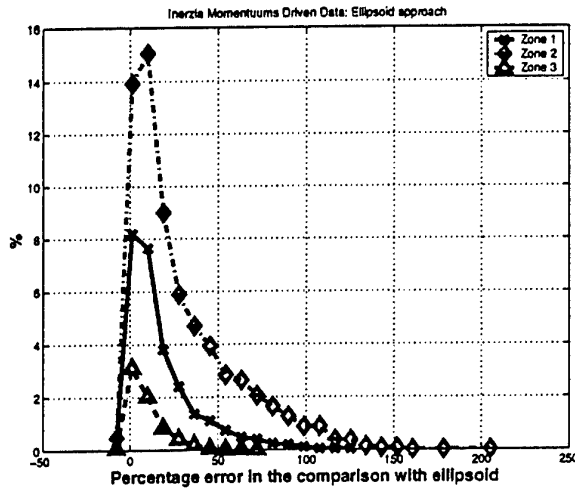


Fig. 5.51: Structures statistics $Re_\tau = 180$ (Case II): Equivalent ellipsoid volume deviation

Grid 1 and 2, which is also the case for the distribution of vorticity within the population. The main difference between the two simulations concerns the size of structures: grid refining leads the zones retained by Q criterion to become separated in smaller entities by the detection and classification algorithm. It can be suspected that this element is critically affected by the inner working and assumptions of present algorithm; therefore this argument could only be set by direct simulations.

However, the level of grid refinement associated with wall-resolved LES is sufficient to find quantitative information of the fields and its inner organization and could be retained as guideline for further investigations.

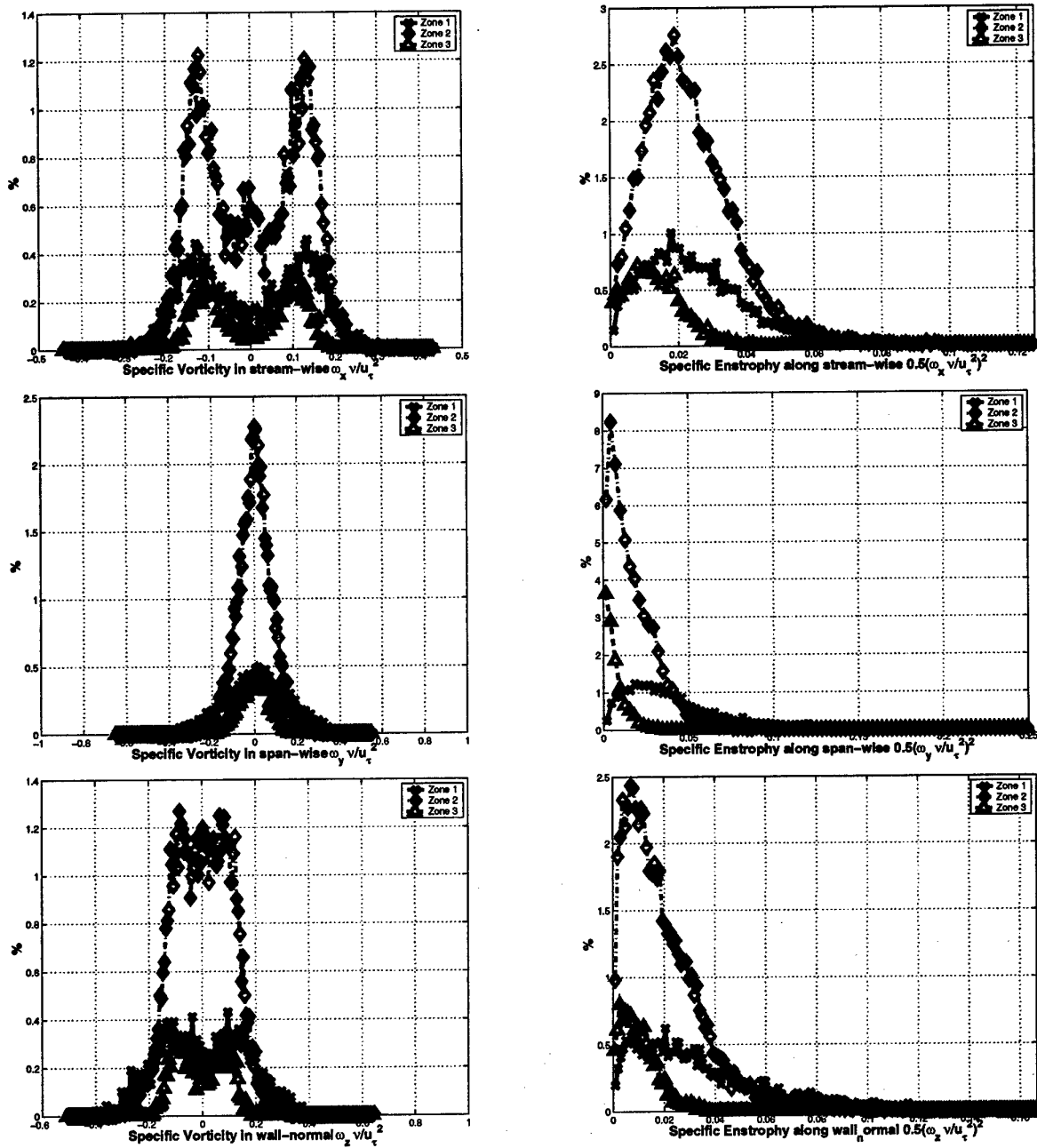


Fig. 5.52: Structure statistics: Specific Vorticity (left) and enstrophy (right) for x (top), y (middle) and z (bottom). $Re_\tau = 180$ (Case II). (Number of bins: 200; limits of histograms (from top to bottom), vorticity: $-0.44 \dots 0.43$, $-0.65 \dots 0.55$, $-0.51 \dots 0.64$; enstrophy: $0 \dots 0.24$, $0 \dots 2.2$, $0 \dots 0.41$)

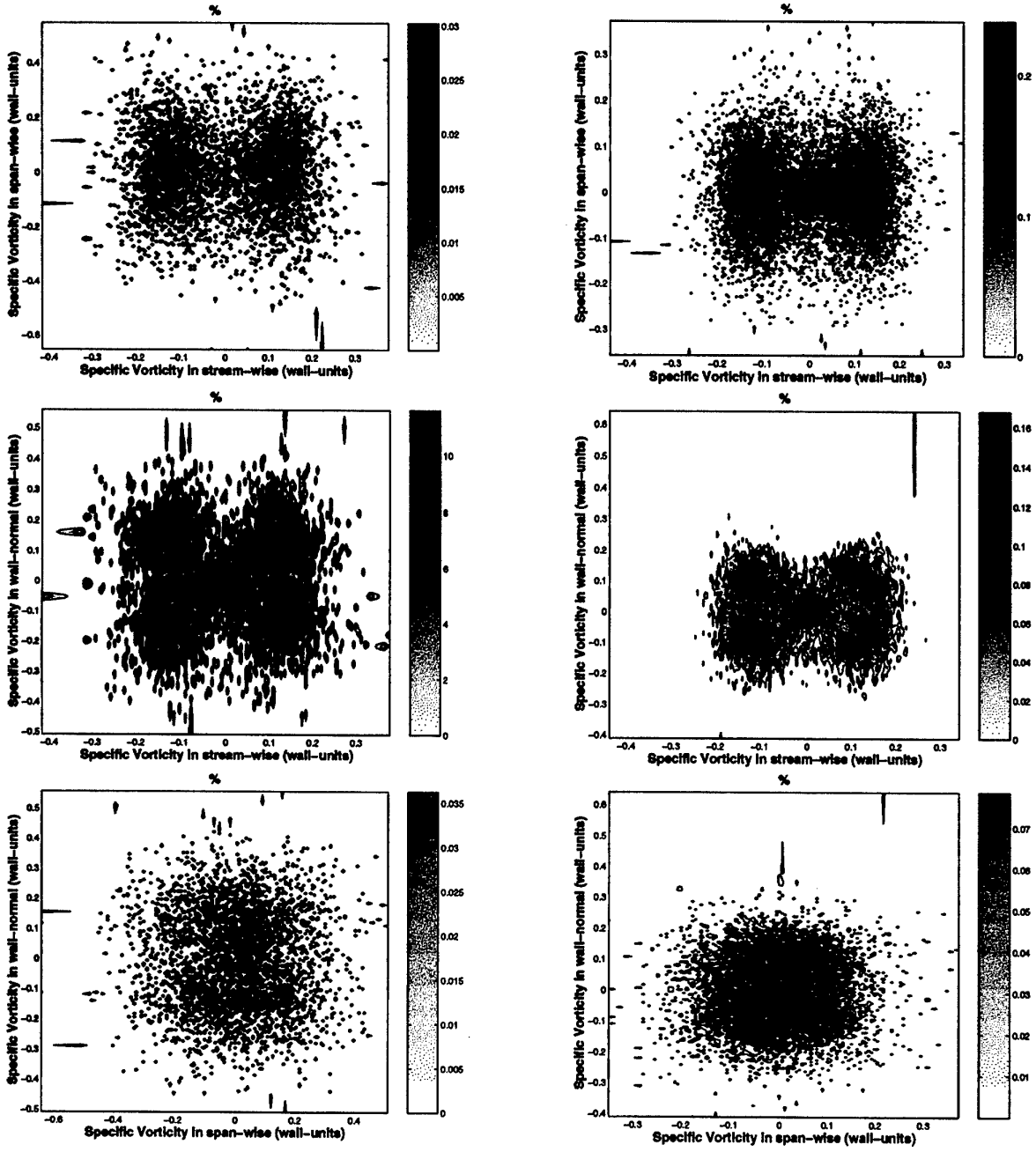


Fig. 5.53: Structures statistics, whole channel: JPDF for structures vorticity. Left Zone 1, right Zone 2, xy -top, xz -middle and yz -bottom. $Re_\tau = 180$ (Case II)

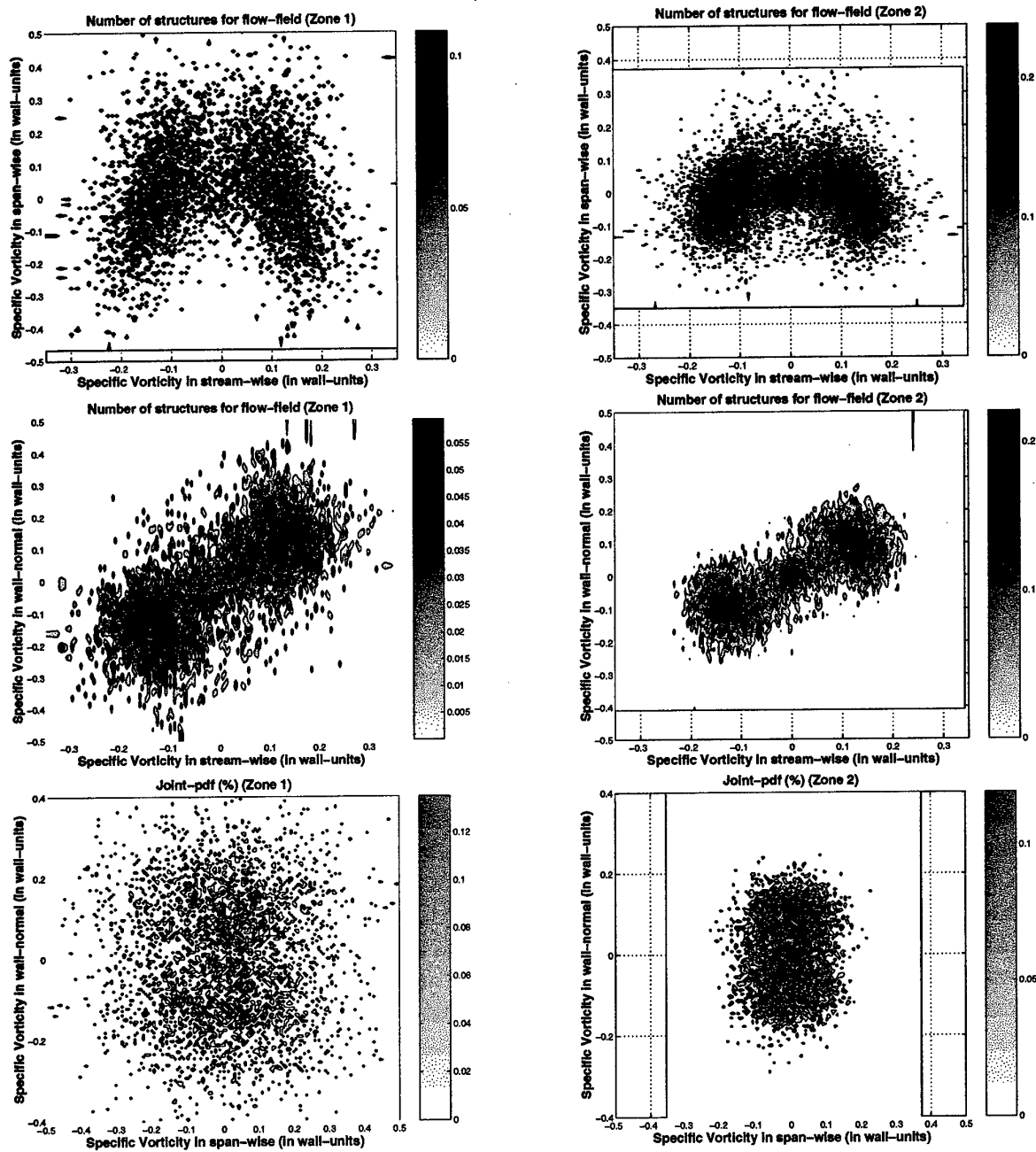


Fig. 5.54: Structures statistics, lower half-channel: JPDP for structures vorticity. Left Zone 1, right Zone 2, xy -top, xz -middle and yz -bottom. $Re_\tau = 180$ (Case II)

5.3 Detection criterion

Assessment of the sensibility of present simulation to the choice of criterion applied for the detection of organized structures is, evidently, of paramount importance to evaluate its results.

This point is investigated comparing results presented in § 5.1 and § 5.2 with ones obtained applying criterion D (see § 4); previous experiences (Giammanco, 2000) and literature (Chacin and Cantwell, 2000) have shown its results might be sensibly different of the ones obtained applying Q criterion. On contrary, better agreement was previously found between Q and λ_2 criteria (Giammanco, 2000), leading to the decision to neglect further testing on λ_2 .

In view of the sensibility of the results to grid refinement (§ 5.2), D criterion is applied on Grid 2; all the other test parameter being the same as stated in § 5.2.

A main problem encountered applying of D criterion lies with the shape of its PDF (Fig. 5.55): the lack of evident plateau of noise makes it difficult to apply the procedure proposed in § 4 to choice the trigger level. Examination of Fig. 5.55 brought, tentatively, to select the following trigger: $Tr = 9.6e^{+06}$ in current adimensionalization; this value has been chosen in order to have a similar percentage of volume occupied from the structures to one obtained in § 5.2.

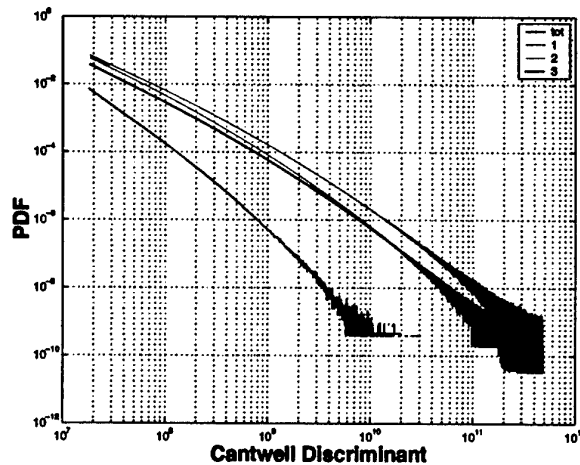


Fig. 5.55: PDF of D plane channel at $Re_\tau = 180$ (Case III)

Comparison which Tr values for Q criterion, obtained applying the same adimensionalization, puts in evidence the different numerical working of the criteria and the difficulty to choice a satisfactory Tr for D (Cantwell). Global values for the population of structures are presented in Tab. 5.12 together with deviation respect to the corresponding results for Q criterion as explained in § 5.2.

Table 5.12: Plane channel at equilibrium at $Re_\tau = 180$ (Case III). Volume, turbulent kinetic energy, module of vorticity and enstrophy within structures versus corresponding quantities within the full computational field. Comparison between D and Q

Grid 2	D	Q	Deviation	
<i>Volume</i>	8.646 %	9.888 %	6.7	%
<i>TKE</i>	15.599 %	14.280 %	3.6	%
<i>Vorticity Modulus</i>	20.335 %	20.850 %	1.5	%
<i>Enstrophy</i>	29.414 %	27.273 %	3.8	%
<i>Number of Structures</i>	190	358	30.0	%

Good agreement between D and Q , concerning for global quantities, can be remarked, it should however be remembered that the similarity in percentage in volume is a direct consequence of the choice of the trigger; what it is interesting instead is the fact that a similar percentage in volume lead to a similar percentage in the other quantities recalled in Tab. 5.12, meaning that similar fluid events are captured from the two detection criteria.

What stands out from the table as a major difference lies with the number of detected structures: the number of distinct structures separated by D criterion is lower, with a deviation from the average close to 30% (using eqn. 5.2), for an average volume of $Vol_{mean} = 1.74712e^{+05}$ wall units for the former and one of $Vol_{mean} = 1.0596e^{+05}$ wall units for the latter. This difference could be due to the difficulty to tune the trigger level for D and to the inherent difference of the two procedures.

Since the grid used is the same as one employed in § 5.2, the eulerian statistics are the same, indeed the same case has been processed looking for structures twice, first for § 5.2 and now; this means some more time steps have added to the averaging procedure, but since already in § 5.2 previous statistics were already fully converged, eulerian statistics presented in Annex A are also valid for the present discussion.

Shape of distribution of the population is qualitatively similar to one obtained applying Q criterion (§ 5.2), as shown in Fig. 5.56 and Fig. 5.57.

The distribution of structures mass center across the height of the channel (Fig. 5.59) again shows the structures to be mostly present within the inertial layer, with a maximum around top of the buffer layer, while they are relatively rare within the wake region (Zone 3). Zone 2 contains in average, around 67% of the total number of structures contained in this field and is, therefore, the main focus of the current investigation.

Advection velocity of centroid of the structures (Fig. 5.60) confirms they follow the average flow, without important lag⁴.

⁴Remember what said in § 5.1

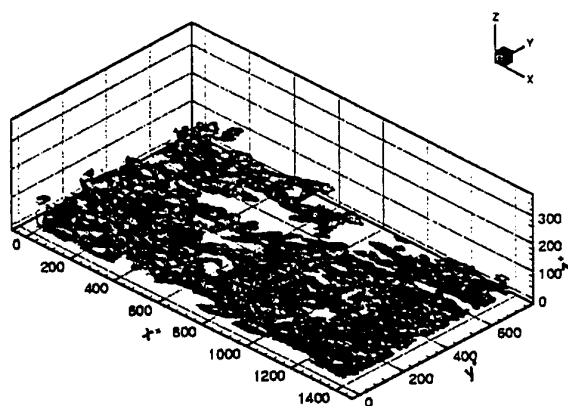


Fig. 5.56: 3-D overview of the field of detected structures of plane channel at $Re_\tau = 180$ (Case III)

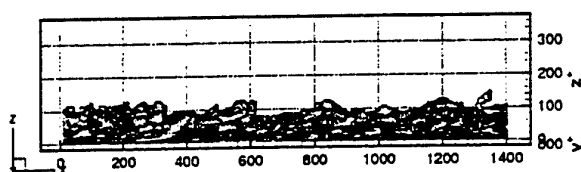


Fig. 5.57: Lateral overview of the field of detected structures of plane channel at $Re_\tau = 180$ (Case III)

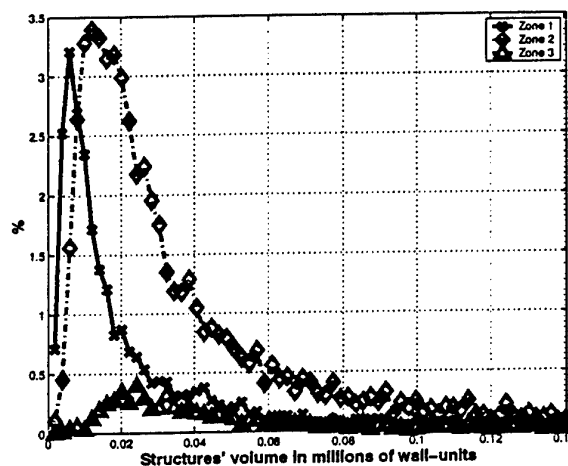


Fig. 5.58: Structures Volume of plane channel at $Re_\tau = 180$ (Case III) with usual zone distinction. (Number of bins: 8000; limits of histogram: 711 ... 16303)

On the basis of results of § 5.1 and § 5.2, information on size and orientation of structures is extracted from JPDF and inertial moments, even if, for clarity's sake, we also present in

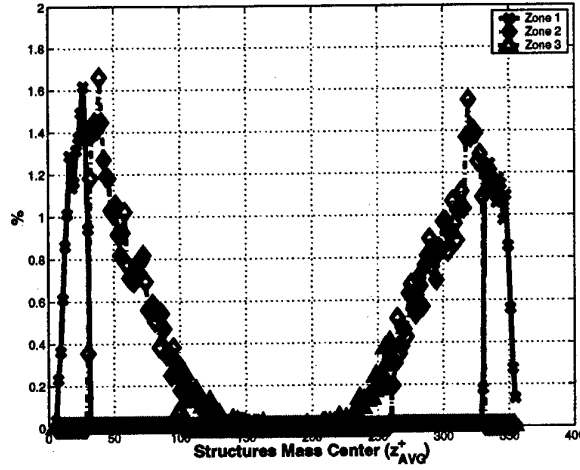


Fig. 5.59: Structures mass center of plane channel at $Re_\tau = 180$ (Case III) with usual zone distinction. (Number of bins: 200; limits of histogram: 4.15 ... 354.77)

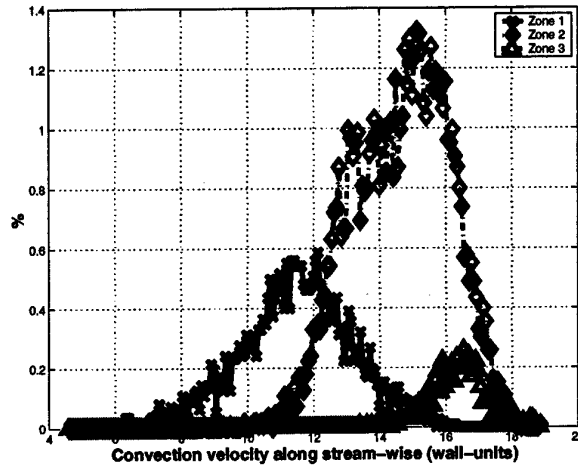


Fig. 5.60: Stream-wise advection of structures center of mass of plane channel at $Re_\tau = 180$ (Case III). (Number of bins: 200; limits of histogram: 4.54 ... 18.86)

Fig. 5.61 the distribution of L_x , L_y and L_z .

Table 5.13: Plane channel at equilibrium at $Re_\tau = 180$ (Case III). Most common values for L_x , L_y and L_z in wall units for Zone 2

L_x	L_y	L_z
60 – 74	23 – 29	45 – 47

Inertial moments of present population for Zones 1 and 2 are presented in Fig. 5.63. It

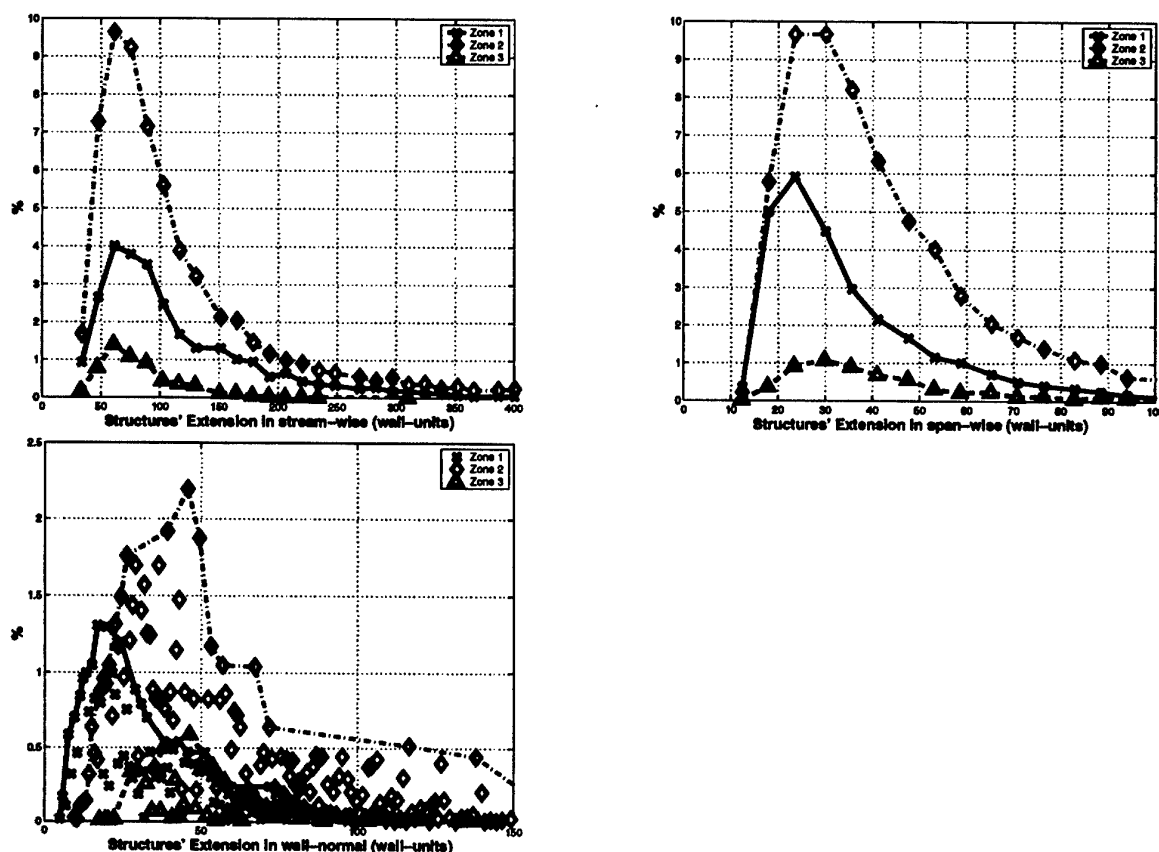


Fig. 5.61: Structures statistics at $Re_\tau = 180$ (Case III): length in wall units. (From top left to bottom right: number of bins: 2000, 8000, 2000; limits of histograms: 29.45 ... 1413, 11.78 ... 753, 4 ... 190)

was considered interesting enough to present, in Fig. 5.64, the corresponding results for Zone 3, close the channel centerline. In this region the structures are sufficiently far away from the wall for this influence beginning to become negligible, so starting a slow return to isotropy, as it is clear to the more random distribution of the structures.

Beside the graphical representation of the structures depicted in Fig. 5.63 and Fig. 5.64, the statistics gathered on the structures allow to define the distribution of tilt angle (Fig. 5.65) and of incidence angle (Fig. 5.66) for present population.

Fig. 5.65 confirms that there is no preferred tilt angle; variance of distribution increases moving from Zone 1 to Zone 2, while the sample data for Zone 3 is too small to allow firm conclusions. Existence of an average incidence angle (Fig. 5.66) shows the tendency of structures to rotate away from the $x - y$ plane: incidence angle slightly increases from $\cong 7 - 14$ degrees in Zone 1 to $\cong 14 - 21$ degrees for Zone 2; agreement with corresponding results for Q criterion (§ 5.2) is satisfactory.

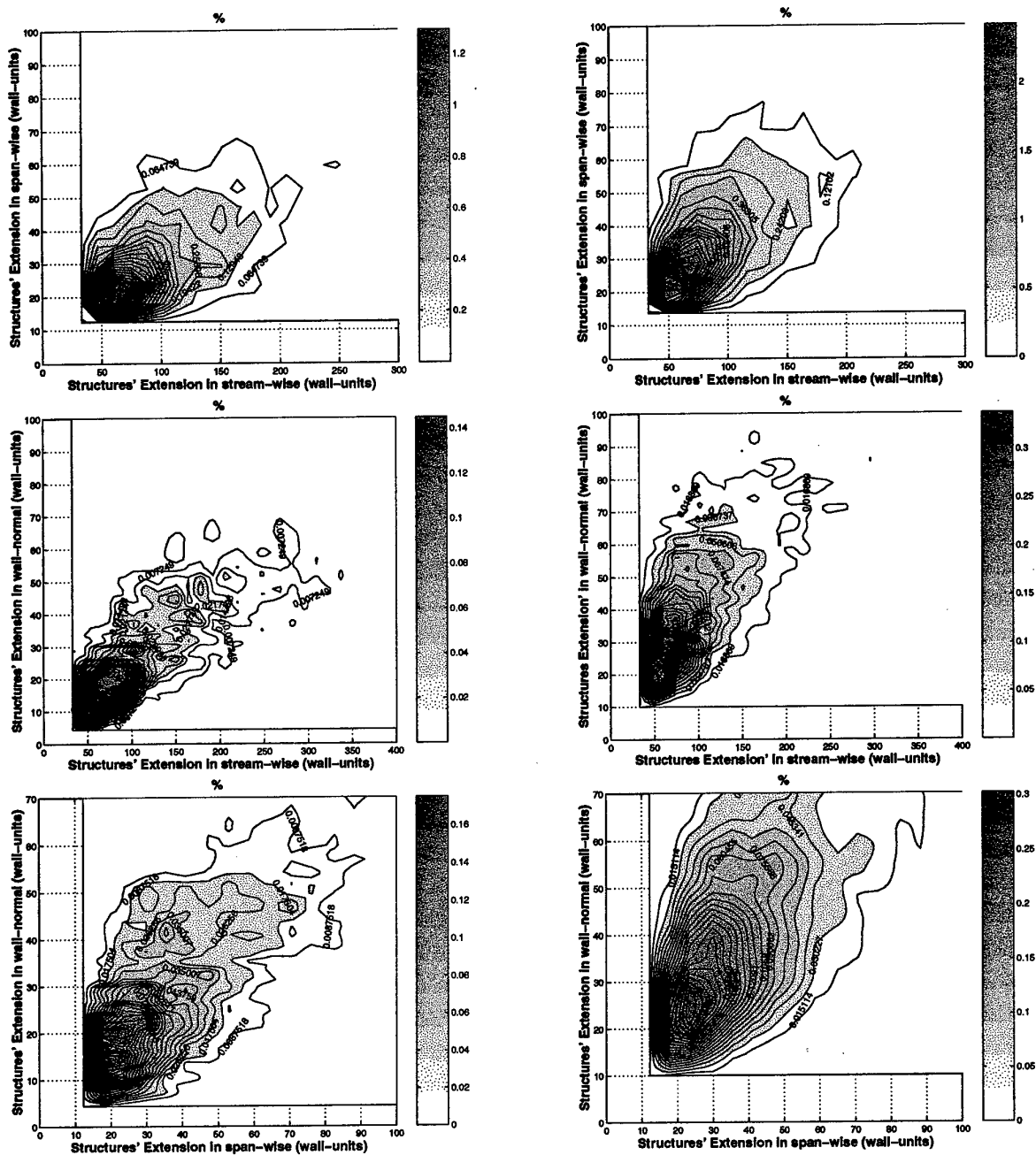


Fig. 5.62: Structures statistics: JPDF for structures extension. $Re_\tau = 180$ (Case III). Left column Zone 1, right column Zone 2, xy -top, xz -middle and yz -bottom

The typical shape of the structure is, again, assumed to be an ellipsoid of volume $\frac{4}{3}\pi abc$, where $a \geq b \geq c$ are the semi-length on the 3 axis, whose values are presented in Fig. 5.67 to Fig. 5.69. It is possible to compare the volume of the ellipsoid with the volume of the

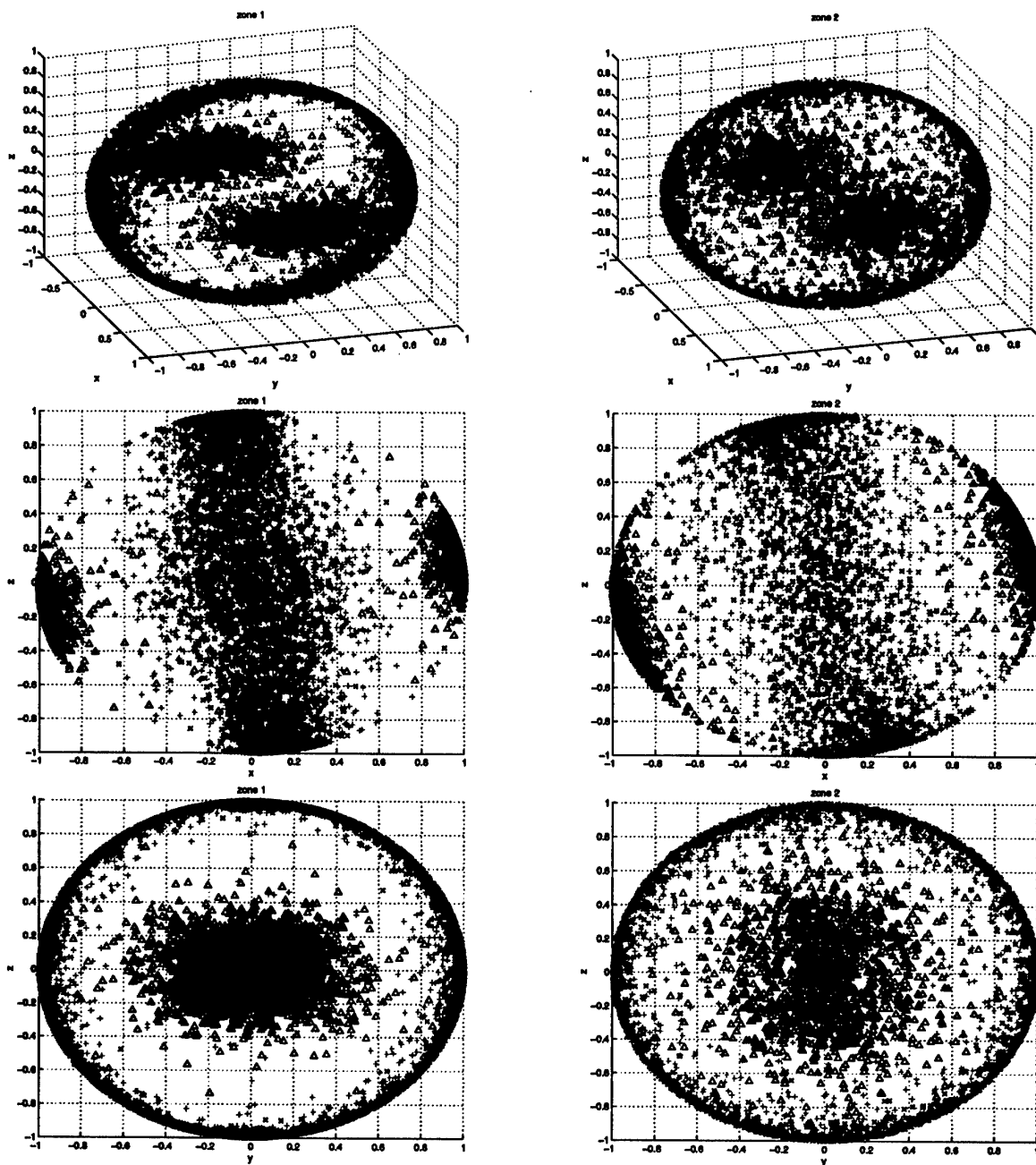


Fig. 5.63: Structures statistics, $Re_\tau = 180$ (Case III): spatial alignment, different pov. Δ Structure mean alignment. Zone 1 left column, Zone 2 right column

corresponding structure, being able finally to retrieve Fig. 5.70.

According to Fig. 5.67 to 5.69, the most probable state for Zone 2 would be an ellipsoid having sizes of: $a \cong 35 - 42$, $b \cong 13$, $c \cong 9$ wall units.

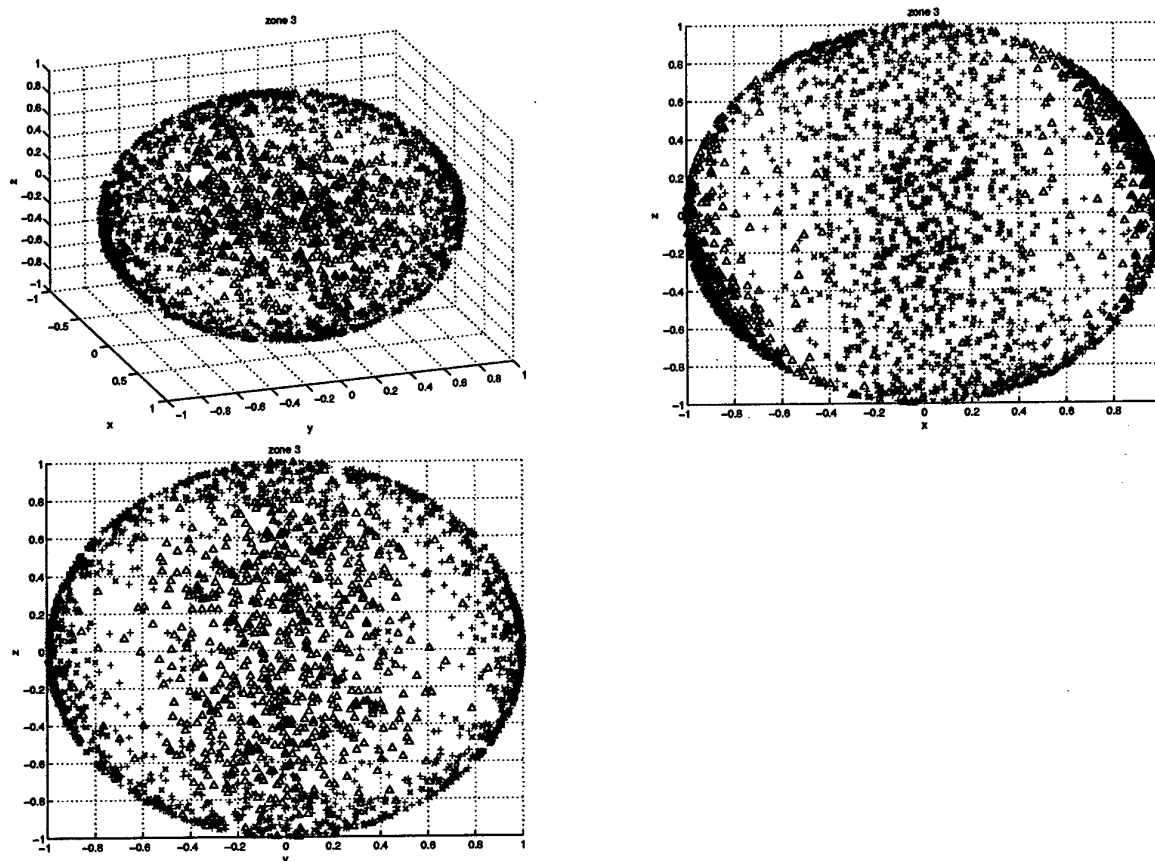


Fig. 5.64: Structures statistics, $Re_\tau = 180$ (Case III): spatial alignment, different pov. Δ Structure mean alignment. Zone 3

Values, which are, again, comparable to the ones yielded by Q criterion, even if present a is slightly shorter than the one found in previous case. It must be remarked that the values $2 \times a$, $2 \times b$ are close to the most probable state yielded by the JPDF $L_x - L_z$ for Zone 2: $L_x - L_z = 60 - 30$ (Fig. 5.62); this result confirms the capability of present approach to identify the dimensions of the representative structure, in the limits of the current implementation of detection and identification algorithms.

At this point in the analysis, an apparent contradiction is evident: information of Tab. 5.12 and Fig. 5.58 suggest that typical structure defined by D criterion should be much bigger than the ones defined by Q criterion (Tab. 5.2); on the contrary, examination of corresponding JPDF (Fig. 5.62) and data from inertial moments (Fig. 5.67 to 5.69) yield a typical structure much smaller, notably equivalent to the one extracted by application of Q criterion (§ 5.2).

Reason of this result lies with the nature of the detection criterion and the structures so defined: it has already been remarked, in § 5.1, the presence of abnormal structures of very

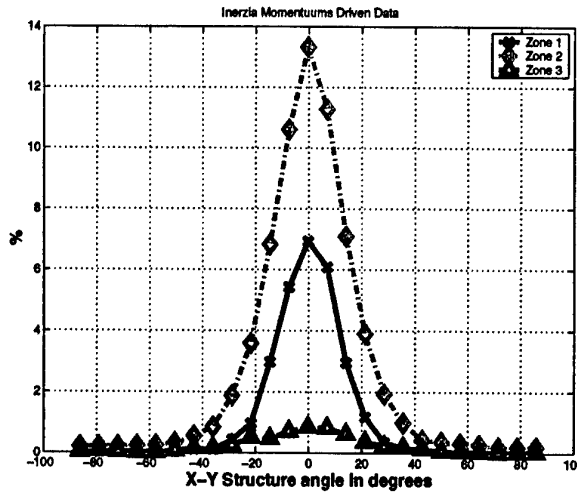


Fig. 5.65: Structures statistics $Re_\tau = 180$ (Case III): Tilting angle extracted from inertial tensor. (Number of bins: 25; limits of histograms: $-90 \dots 90$)

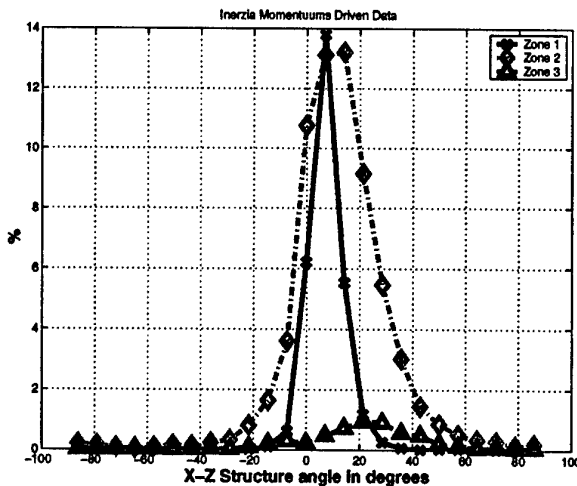


Fig. 5.66: Structures statistics $Re_\tau = 180$ (Case III): Incidence angle extracted from inertial tensor. (Number of bins: 25; limits of histograms: $-90 \dots 90$)

large sizes (Fig. 5.12) which could skew the interpretation of estimation of average volume of population. Examination of present population shows, at same level of grid refining, this behavior is much more common among structures defined by D criterion than among ones yielded by Q criterion.

Examples of this effect can be seen in Fig. 5.71.

However, the most common state remains made of structures, of different sizes (Fig. 5.72), elongated in x direction, similar to the ones presented in § 5.1 and § 5.2.

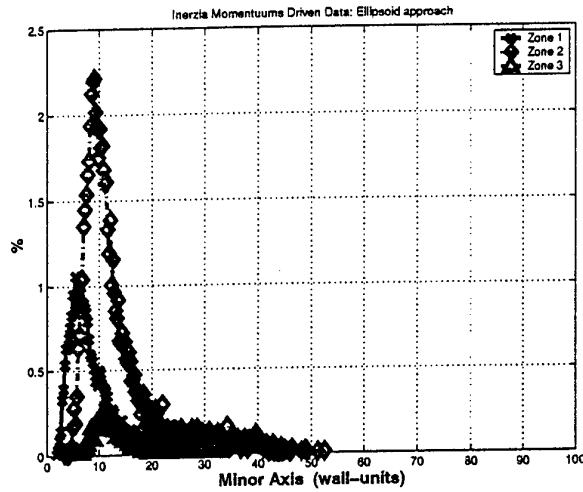


Fig. 5.67: Structures statistics $Re_\tau = 180$ (Case III): Equivalent ellipsoid minor semi-axis

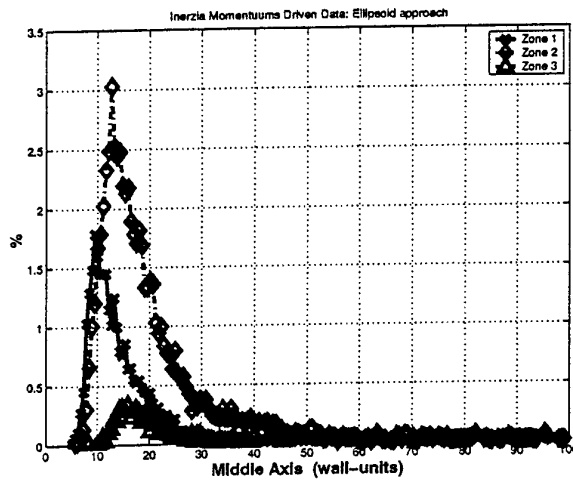


Fig. 5.68: Structures statistics $Re_\tau = 180$ (Case III): Equivalent ellipsoid middle semi-axis

It can be concluded that the presence of structures of abnormal sizes is a common problem, related not only to the nature of the algorithm, but, mostly, to the result of the detection criterion and the refinement of the grid. In other words, the algorithm has been thought in order to classify connected region of space as structures, and, to be applicable to LES resolution (against DNS resolution), it has been designed in order not to be extremely strict, leaving open the possibility of connectivity in off-cardinal directions. Nevertheless, from Fig. 5.72, it is clear that the algorithm identifies the structures in a logical way, in all the cases the present mask allows it to do so.

Therefore, definition and analysis of a typical structures must be performed considering the most probable state; evaluating a ' Vol_{mean} ' of structures by dividing the detected volume

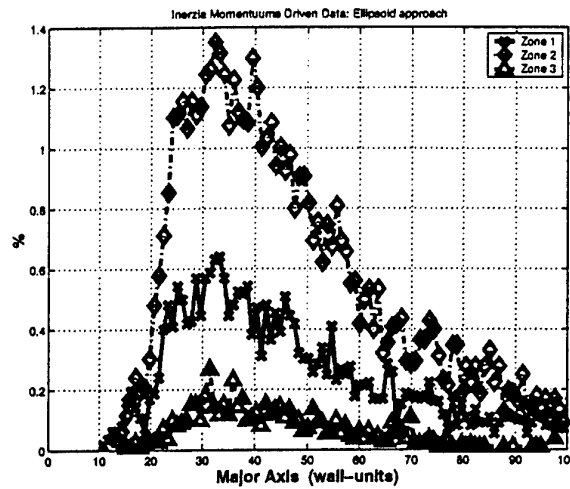


Fig. 5.69: Structures statistics $Re_\tau = 180$ (Case III): Equivalent ellipsoid major semi-axis

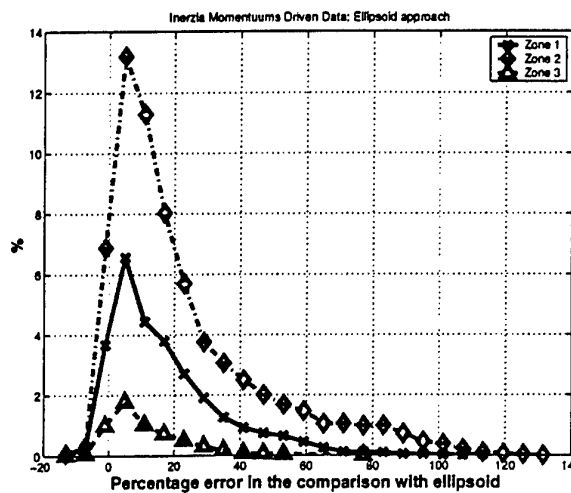


Fig. 5.70: Structures statistics $Re_\tau = 180$ (Case III): Equivalent ellipsoid volume deviation

by the number of structures found is proved a far too crude approximation. Taking the data of Fig. 5.58 and considering Zone 2, the peak of the PDF corresponds, roughly, to a $Vol = 1.1919e^{+04}$ in wall-units; comparing this value to the most probable one yielded applying the ellipsoid model (in Fig. 5.73) the corresponding value for of Zone 2 is, roughly, $1.0552e^{+04}$ in wall units, with a reasonable agreement (relative error 6%) between the two estimations.

Furthermore, these values are very close to the ones found applying Q criterion over the same grid; matter of fact, $Vol = 1.4739e^{+04}$ wall units is found from Fig. 5.37, while from an equivalent set of data for § 5.2 (not presented in present text) a value of $1.3432e^{+04}$ wall units is recovered.

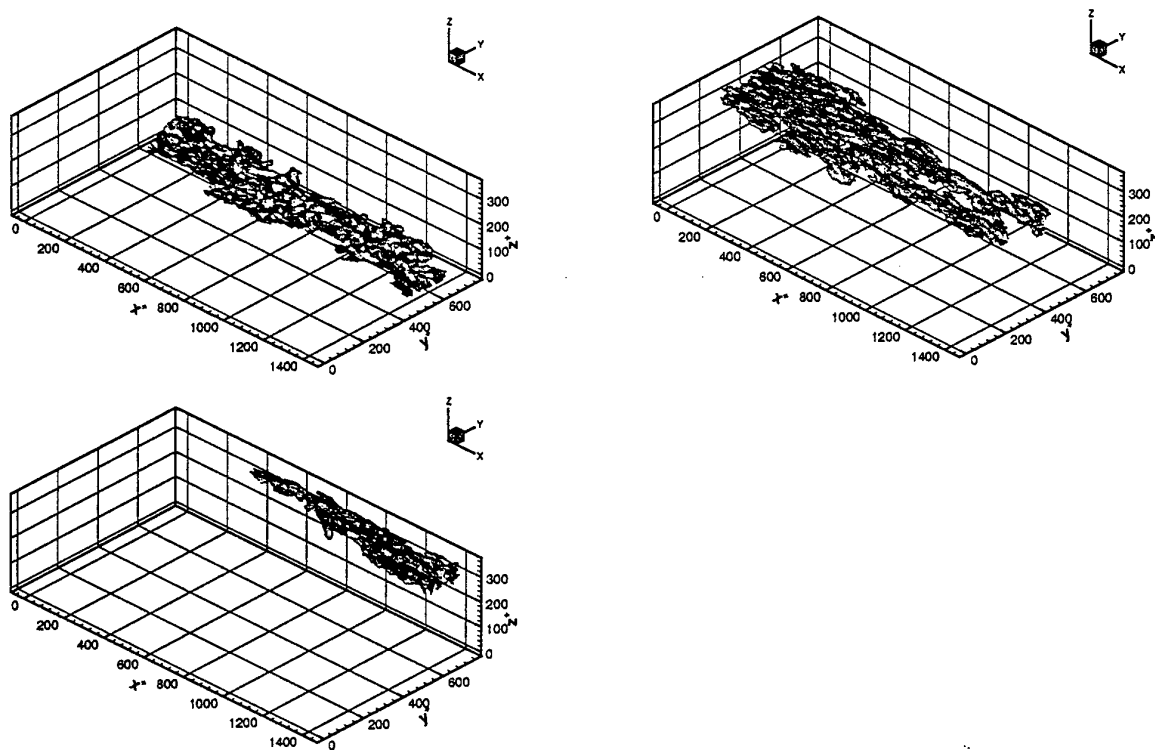


Fig. 5.71: Example of complex structures of plane channel at $Re_\tau = 180$ (Case III)

It can be concluded that reliable estimation of size of typical structure can be obtained from inertial moments of the population, and, within these terms, the two models show an acceptable agreement.

Dynamic of organized vorticity can be assessed in Fig. 5.74, where specific vorticity is presented component per component.

Distribution of stream-wise component (Fig. 5.74 top left) shows a majority of structures having clockwise or counter-clockwise rotation around x axis in Zone 1 and 2. A major difference versus results of Q (§ 5.2), lies with the existence, in Zone 2, of an important number of structures having negligible rotation around the x axis. This results underlines the different working of D and Q criteria and, in consequence, the different definition of structure.

Negligible importance of Zone 3 is, again, put in evidence by the results. Wall-normal specific vorticity (same figure bottom left) shows a corresponding behavior, while Gaussian behavior of specific vorticity in span-wise direction (middle left) puts in evidence the lack of preferential rotation around this axis (again, it must be considered that the average as been performed on the whole channel).

The JPDF of specific vorticity for Zone 1 and 2 are presented in Fig. 5.75.

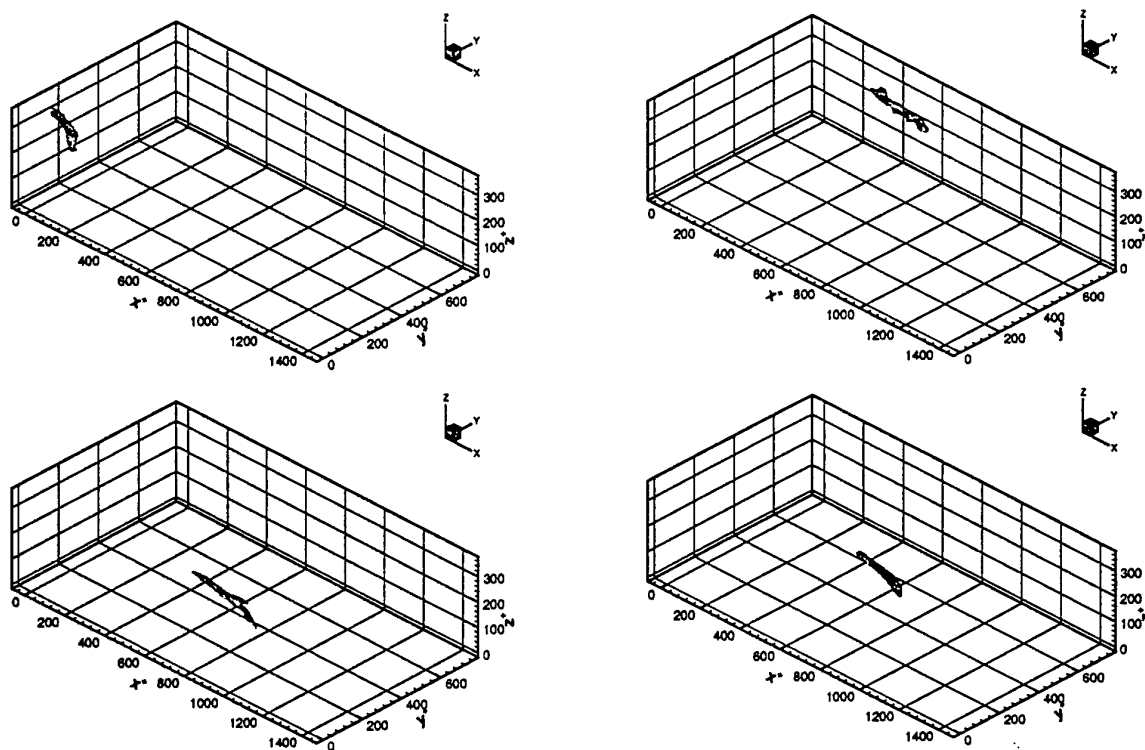


Fig. 5.72: Typical structures elongated in stream-wise direction of plane channel at $Re_\tau = 180$ (Case III)

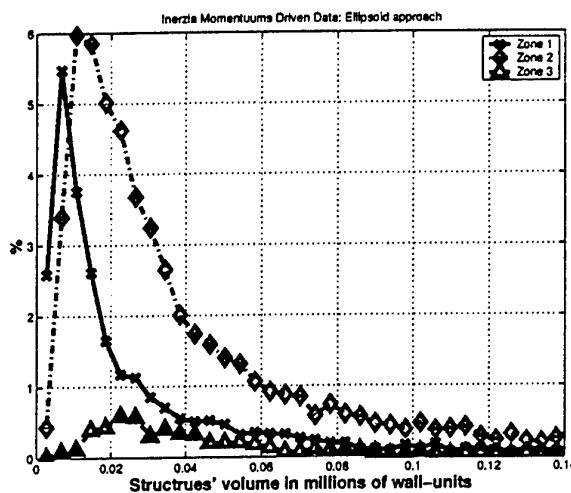


Fig. 5.73: Equivalent ellipsoidal Structures Volume of plane channel at $Re_\tau = 180$ (Case III) with usual zone distinction. (Number of bins: 8000; limits of histograms: $627 \dots 3.71e^{+07}$)

JPDF of specific vorticity in $x-y$ plane for Zone 1 is similar to the previous cases (§ 5.1 and 5.2), while for Zone 2, as a confirmation of what seen in Fig. 5.74, a certain number

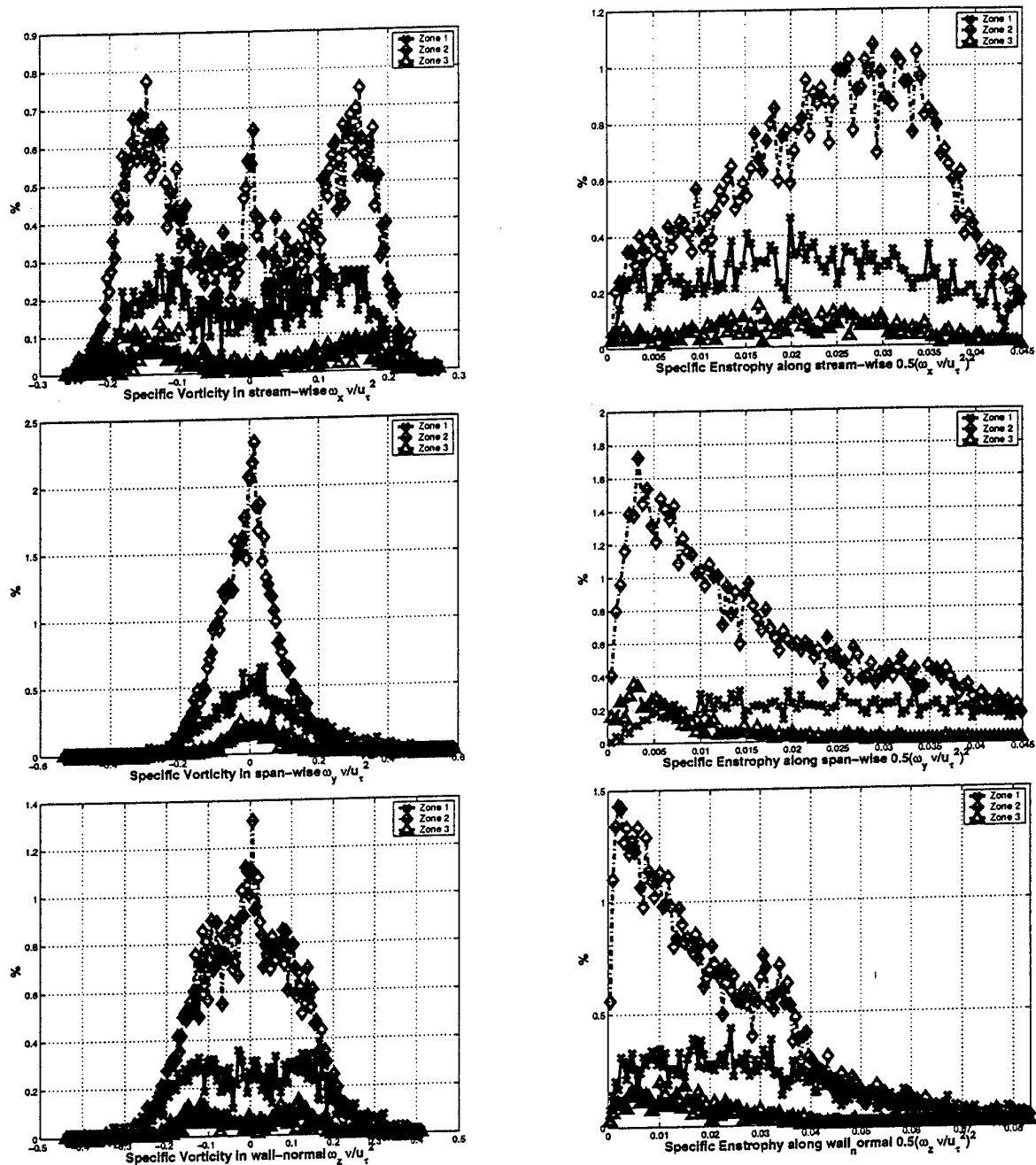


Fig. 5.74: Structures statistics: Specific Vorticity (left) and enstrophy (right) for x (top), y (middle) and z (bottom). $Re_\tau = 180$ (Case III). (Number of bins: 200; limits of histograms (from top to bottom), vorticity: $-0.26 \dots 0.27$, $-0.56 \dots 0.58$, $-0.44 \dots 0.41$; enstrophy: $0 \dots 0.08$, $0 \dots 0.38$, $0 \dots 0.21$)

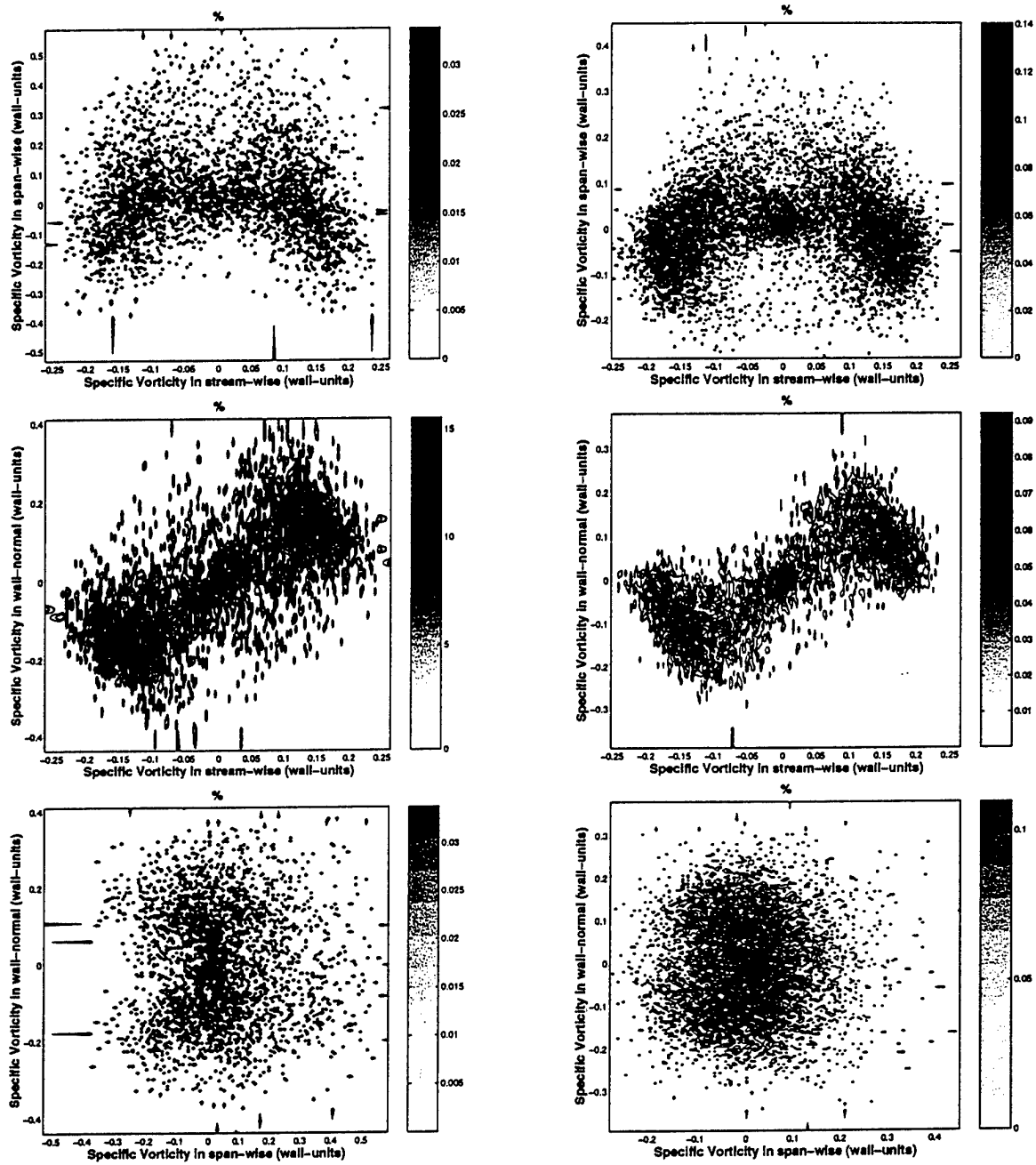


Fig. 5.75: Structures statistics, lower half-channel: JPDF for structures vorticity. Left Zone 1, right Zone 2, xy -top, xz -middle and yz -bottom. $Re_\tau = 180$ (Case III)

of structures having no rotation in the $x - y$ plane are visible. Values of specific vorticity associated to most probable region are however similar for the D and Q defined structures, giving credit to the hypothesis that the structures clustered around (0,0) for top (and middle) right of Fig. 5.75 are in reality more distinct structures merged together.

Considering JPDF of specific vorticity in the $x - z$ plane for Zones 1 and 2, it can be again remarked that distribution and value for most probable cases are similar to ones found applying Q criterion, with the exclusion of the already mentioned structures clustered around $(0,0)$; for the case of rotating structures, range of possible values is similar to the ones yielded by Q criterion, as for specific vorticity in the $y - z$ plane.

In conclusion, application of Q and D criteria underlines the difference between the two approaches, already discussed in § 4 and previous analysis (Rambaud, 2000) and, notably, the detection, by D , of a larger population of no-rotating structures. Present results, however, do not allow to definitively recommend one criterion over another.

In the opinion of present authors, one main drawback of D criterion lies with the uncertainty concerning the selection of proper trigger level, while consistent results for Q criterion can always be obtained applying the procedure proposed in § 4, as shown in present Chapter and as it will be confirmed in chapter 6.

Furthermore, at same grid size and similar percentage in volume occupied by the structures, D criterion seems more likely to define abnormal structures of very big sizes, which are consequence of interaction of the mathematics of the criterion and present algorithm, at risk of skewing the conclusions of the analysis.

However, it has to be stressed that analysis based upon inertial moments of the distribution yields, however, similar sizes for typical structure, while discrepancy of global statistics is in order of 5% and JPDF results show satisfactory agreement concerning values and main trends.

This level of agreement being acceptable for present investigation, lower CPU requirement and more reliable choice of trigger level lead to retain Q criterion for the remaining of the investigation, while it is confirmed that inertial moments approach represents the most reliable method to define size and orientation of typical structures for this flow topology.

5.4 Effect of precision of LES numerical algorithm

As discussed in § 3, numerical precision of LES can be increased, and quality of results improved, applying a formal 4th order accurate discretization in space; importance of this choice on the simulation of coherent structures will now be tested. As the present purpose is only to evaluate the sensibility of the simulation, only grid 1 (see § 5.1) is tested⁵, keeping in mind that previous conclusions on effect of grid refining (§ 5.2) will also apply to this case. The simulation is performed applying the value $C_s = 0.1$ for Smagorinsky coefficient, the same used in § 5.1 which was then found to yield the best agreement with DNS data. In Annex C, the eulerian statistics for this same case computed for $C_s = 0.065$ are presented to allow to appreciate the influence of the Smagorinsky coefficient on the low and high order eulerian statistics.

Q criterion is applied and a trigger level $Tr = 88$ is found for this case, showing an acceptable agreement with value found for test on 2nd order discretization (§ 5.1).

Deviation for the global quantities for the entire flow field is shown Tab. 5.14.

Table 5.14: Plane channel at equilibrium at $Re_\tau = 180$ (Case IV). Total, turbulent kinetic energy, vorticity and enstrophy in present non-dimensional units. Comparison between 2nd and 4th order discretization

Grid 1	2 nd	4 th	Deviation	
<i>TKE</i>	115.25 %	105.93 %	4.2	%
<i>VorticityModulus</i>	1457.0 %	1471.6 %	0.5	%
<i>Enstrophy</i>	63603.0 %	67477. %	1.0	%

Global statistics of organized turbulence for the two simulations are compared in Tab. 5.15.

Table 5.15: Plane channel at equilibrium at $Re_\tau = 180$ (Case IV). Volume, turbulent kinetic energy, module of vorticity and enstrophy within structures versus corresponding quantities within the full computational field. Comparison between 2nd and 4th order discretization

Grid 1	2 nd	4 th	Deviation	
<i>Volume</i>	9.661 %	7.582 %	12.1	%
<i>TKE</i>	14.075 %	11.472 %	10.2	%
<i>VorticityModulus</i>	19.893 %	16.248 %	10.1	%
<i>Enstrophy</i>	25.058 %	20.000 %	11.2	%
<i>NumberOfStructures</i>	247	210	8.1	%

Tab. 5.14 puts in evidence a good agreement of the two simulations.

⁵Details of present LES can be seen in Annex B where improved agreement with DNS data can be noted.

On the contrary, Tab. 5.15 shows a 10% deviation for the quantities associated with the structures, as it could have expected, keeping in mind that all the detection criteria are based on calculations of gradient of velocity gradients and, therefore, potentially sensible to the effect of numerical accuracy.

However the main characteristics of the population are similar to the ones remarked in § 5.1, as shown in Annex B: in particular JPDF for L_x , L_y and L_z show values and distribution similar to the ones yielded by 2nd order simulation (§ 5.1). Similar agreement is also found for JPDF of components of specific vorticity.

It could be concluded that numerical accuracy of LES is not of primary importance, compared with the effect of grid refinement and detection criterion and the extra cost of this refined calculation would be justified only when very precise estimation of quantities associates with the structures was necessary for design purpose.

5.5 Effect of choice of SGS model

As discussed in § 2, SGS modeling is the corner stone of LES, and its effects on simulation of the structures must, therefore, be assessed⁶. In order to investigate this point, a comparison is performed on grid 1 (§ 5.1), where SGS model can be expected to have a detectable effect on the resolved field; an advantage of being able to evaluate the TKE budget (see § 2 and § 4) lies with the possibility of evaluating, in quantitative way, the effect of the SGS model in the simulation: knowing that in any case the flow field is deeply influenced from the choice of the model (this effect being visible in the resolved terms of the TKE budget), the SGS dissipation (ek_{SGS} in Fig. 5.4 or Fig. A.3) is a good indicator of the influence of the SGS model. For the simulation considered (§ 5.1), the Smagorinsky model apparently plays a small role (Fig. 5.4), the dissipation that it provides being quite small compared to the viscous dissipation, which is the case for a wall resolved LES computation⁷, however, it will be shown how the change of the SGS model alters the statistics.

Apart the already applied Smagorinsky model ('SMA'), filtered structure function ('FSF') model (Compte et al., 1994) and mixed ('SS') model (self-similar model S3+Smagorinsky dissipation, Louda (2001)) are tested together with un-resolved DNS ('NO-SGS') approach.

Results for the resolved field for these simulations are presented in Annex D for FSF, E for NO-SGS and F for SS. First of all, it must be remarked that, since the self similar model is not an eddy viscosity model, a different version of the TKE budget has to be used; however, even if developed, it has not been sufficiently tested and so it is not presented in Annex F.

It can be seen that all the SGS models are able provide an acceptable reproduction of DNS data, the biggest scattering can be found in the statistics in the cross-flow direction, starting from low order statistics like the velocity rms. Some interesting remarks can be extracted from the comparison of the TKE presented in § 5.1 and Annex E (NO-SGS): there is a over-prediction of rms associated to span-wise and wall normal direction, as well of turbulent kinetic energy production and in turn dissipation: the eddy viscosity model is well suited for this kind of flow. In Fig. E.3 it is possible to observe how the unresolved LES is still very close to the DNS behavior, at least in term of shape for the different TKE terms.

Now, for an interesting remark about the difference between two SGS models, consider first Fig. E.2 and 5.2: apparently for the FSF model, fluctuations are more damped, in particular in span-wise and wall normal directions, while the turbulent shear stress has, apparently, a better behavior; apparently this SGS model is more dissipative than the Smagorinsky, and this is clearly visible in Fig. E.3 and 5.4, where the SGS dissipation (ek_{SGS}) is now almost

⁶Besides the choice of model, the tuning of the empirical constants involved should furthermore taken into account, see § 5.4 and difference between Annex B and C

⁷This observation could provide a nice and obvious way of classifying LES computations, according from the relative magnitude of the viscous dissipation vs SGS dissipation

comparable to the viscous one (ϵk). On the other side, the SGS contribution of Smagorinsky to the total stress is negligible (Fig. 5.3), while FSF has a decisive influence on the shear stress (Fig. E.1).

Like stated above, all the SGS models are able provide an acceptable reproduction of DNS data, but an important scattering exists for the results. Total values for global quantities are presented in Tab. 5.16.

Table 5.16: Plane channel at equilibrium at $Re_\tau = 180$ (case V). Global quantities: turbulent kinetic energy, vorticity and enstrophy in present non-dimensional units. Comparison between NO-SGS, SMA, FSF and SS

TOTAL	NO-SGS	SMA	FSF	SS
<i>TKE</i>	119.79	115.25	110.64	95.16
<i>VorticityModulus</i>	1558.0	1457.0	1286.9	1279.8
<i>Enstrophy</i>	73131.0	63603.0	48161.0	48060.0
DEVIATION	NO-SGS	SMA	FSF	SS
<i>TKE</i>	8.7 %	4.6 %	0.4 %	13.7 %
<i>VorticityModulus</i>	11.7 %	4.5 %	7.8 %	8.3 %
<i>Enstrophy</i>	25.6 %	9.2 %	17.3 %	17.5 %

A typical deviation in the order of 10% for turbulent kinetic energy and vorticity is clear from Tab. 5.16.

In comparison, percentages of contribution of organized field show much smaller deviation, as shown by Tab. 5.17.

Detailed comparison is presented in Annex G and shows a similar agreement in what concerns the statistical behavior of the population.

It can be concluded at the current stage, that the search algorithm is always able to isolate the active part of this field and the choice of SGS model must be based on quality of reproduction of global resolved turbulence or/and the cost/effectiveness of the actual calculation.

Table 5.17: Plane channel at equilibrium at $Re_\tau = 180$. Volume, turbulent kinetic energy, vorticity and enstrophy in present non-dimensional units. Comparison between NO-SGS, SMA, FSF and SS

	NO-SGS	SMA	FSF	SS
<i>VOLUME</i>	8.066 %	9.661 %	9.350 %	8.655 %
<i>TKE</i>	12.357 %	14.075 %	12.651 %	13.189 %
<i>VorticityModulus</i>	17.666 %	19.893 %	18.32 %	18.929 %
<i>Enstrophy</i>	23.32 %	25.06 %	21.217 %	23.86 %
<i>Num.Structures</i>	280	247	210	231
DEVIATION	NO-SGS	SMA	FSF	SS
Volume	9.7 %	8.1 %	4.7 %	3.1 %
TKE	5.4 %	7.7 %	3.2 %	3.8 %
Vorticity Modulus	5.5 %	6.4 %	2.0 %	1.2 %
Enstrophy	16.0 %	2.0 %	13.0 %	4.5 %

5.6 Conclusions

Present results have demonstrated capability of LES to reproduce the behavior of organized turbulence and ability of present algorithms to detect and classify the recognized entities embedded in the flow-field.

Structures population statistics and their relative importance with respect to the total turbulent field can be put into evidence.

Global statistics of the field of coherent structures were found to be relatively insensible to different simulation parameters tested, with the exception of what concerns shape and size of individual structures, which is critically dependent on grid size and detection criterion.

This last result had to be expected, in view of the fact this element is, necessarily, strongly dependent of the numerical detail of the implementation.

As this point is not of paramount importance for the understanding of the physical behavior of the overall phenomenon it is decided, and is recommended for future investigations, on ground of cost-effectiveness, to prosecute the study applying:

- Smagorinsky model as SGS model
- 2nd order accuracy of space discretization
- Q criterion of detection of structures

6. INVESTIGATION OF COHERENT STRUCTURES AT DIFFERENT REYNOLDS NUMBERS

In previous chapters, phenomenology of organized turbulence was studied for the case of channel flow at $Re_\tau = 180$, in order to limit the computational effort involved with the assessment of performances of present algorithm and its sensibility to different parameters of simulation.

Regardless from the data until now gathered, results and conclusions reached cannot be considered fully representative of behavior and characteristics of coherent structures in fully developed turbulence, since the Reynolds number adopted was low enough for flow to be affected by viscous effects.

In order to remove this deficiency and complete the present study, flow at $Re_\tau = 395$ and 590, where turbulent behavior can be considered fully established (AGARD, 1998), are simulated.

6.1 Test conditions and global results

Available computer power made it impossible to achieve a level of resolution corresponding to the one of Case II (see Tab. 5.1); grids applied in present context (See Tab. 6.1) have resolution roughly equivalent to Case I (see Tab. 5.7).

It was found that at higher grid resolution, results might put in evidence the presence of structures more numerous and smaller than the ones to be found by the current grid; however, results of § 5.2 compared to the ones of § 5.1, show that the global information on organized turbulence is well captured at present grid resolution; therefore it can be assumed that effect of Reynolds number can be reliably studied within this frame.

Table 6.1: Reynolds effect study: Relevant parameters for computational field and grid sizes. Grid stretched in wall-normal direction with coefficient 1.08

Geometry & Grid	L_x	L_y	L_z	N_x	N_y	N_z	Δx^+	Δy^+	Δz^+
$Re_\tau = 180$	$\frac{5}{2}\pi$	$\frac{4}{3}\pi$	2	64	96	64	22	7.85	1.5 ... 16
$Re_\tau = 395$	$\frac{9}{5}\pi$	$\frac{1}{6}\pi$	2	96	128	96	23.27	6.47	0.8 ... 30
$Re_\tau = 590$	$\frac{6}{5}\pi$	$\frac{9}{20}\pi$	2	96	128	96	23.25	6.51	1.2 ... 44

It has to be noticed that, even if the computational field is reduced of size with increasing Re , it remains bigger, by one order of magnitude, than the longitudinal macro-scale in the inertial layer, as yielded by DNS results (AGARD, 1998); therefore, the corresponding results can be considered to be a representative sample of the true flow.

Detailed results of LES and structures distribution are presented in Annex H, while present discussion focus on the differences among different Re 's.

Following the conclusions of Chapter 5, Q criterion is applied to the detection of structures; trigger level for different cases is found applying the criterion for decrease of PDF by a decade (see § 4.3) and the corresponding values are resumed in Tab. 6.2.

Table 6.2: Reynolds effect study: Trigger level for different Re_τ

Reynolds number	Trigger level
$Re_\tau = 180$	72
$Re_\tau = 395$	185
$Re_\tau = 590$	271

Global values for the two populations of structures are compared in Tab. 6.3.

Table 6.3: Reynolds effect study: Volume, turbulent kinetic energy, module of vorticity and enstrophy within structures versus corresponding quantity within the full computational field

Re_τ	Volume	TKE	Vor.Mod.	Ens.	Num. Structures
$Re_\tau = 180$	9.661 %	14.075 %	19.893 %	25.058 %	247
$Re_\tau = 395$	10.926 %	16.429 %	25.014 %	30.707 %	323
$Re_\tau = 590$	11.479 %	17.413 %	26.924 %	36.854 %	280

These results point out to a fundamental similarity of behavior of organized turbulence at all Reynolds numbers, leading to the conclusion that what said in Chapter 5 might be considered valid for this entire class of flows. It can be remarked that contributions of organized turbulence in global quantities and for the procedure here applied gradually increases with Re , see at example the field TKE in Tab. 6.3.

Further analysis will be performed, for the two new Reynolds number to be considered, to put in evidence the possible effects of Reynolds number. It must be noticed that, in Tab. 6.3, the average number of structures detected within the computational field is given, together with information concerning global quantities (expressed in percentage) of organized turbulence; this information is not consistent with the others, since it has not been normalized, and it cannot be used in order to make comparisons, for example the domain size is different case by case.

However, this number is given to offer an indication of the sample size to be considered. It must be kept in mind that this number is an averaged value, obtained averaging data from,

typically, around 50 – 60 flow fields when possible and in any case no lower than 36, in order to bring statistics to a satisfactory convergence (see § 5.1).

On the other hand, it must be reminded that most of the relevant features of the population behavior (such as the distinguished peak in the stream-wise vorticity) are already discernible even over an handful of gathered flow-fields (Giammanco, 2000), due to the high number of structures present in one single flow realization.

Statistics gathered on one single snap-shot are equivalent to an ensemble averaging over a small population.

6.2 Analysis of coherent structures at $Re_\tau = 395$

$Re_\tau = 395$ corresponds to a *bulk* Reynolds number of 6875, high enough to ensure it should not anymore affected by the viscous effects, present in $Re_\tau = 180$. This case has been investigated in deep and compared with reference DNS data to evaluate the quality of the simulation, as shown in Annex H.

Overall view of vortex structures is presented in Fig. 6.1 and 6.2.

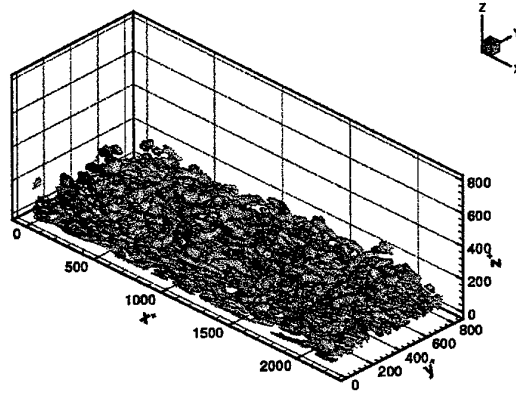


Fig. 6.1: 3-D overview of the field of detected structures of plane channel at $Re_\tau = 395$

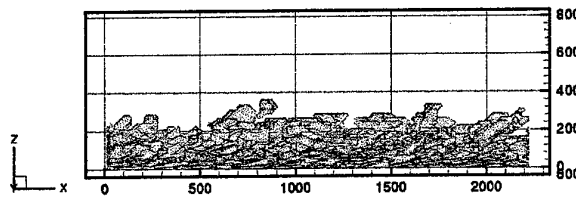


Fig. 6.2: Lateral overview of the field of detected structures of plane channel at $Re_\tau = 395$

Comparison with corresponding views for $Re_\tau = 180$ (Fig. 5.10 and 5.8) presents more complex distribution of structures (Fig. 6.1) and increase of thickness of layer affected by this mechanism (Fig. 6.2). However the overall features of the field are similar.

The average population is in the order of 323 structures (Fig. 6.3) for an average value $Vol_{mean} = 4.95e^{+05}$ wall units. Comparison with corresponding result at $Re_\tau = 180$ ($Vol_{mean} = 1.48e^{+05}$ wall units) could be considered an indication of increase of typical sizes

with Re . It must be remarked that, as discussed in § 5.3, this value has to be considered only as first crude indication of overall trend, while reliable estimation of size of typical structure has to be obtained by inertial moments of the population.

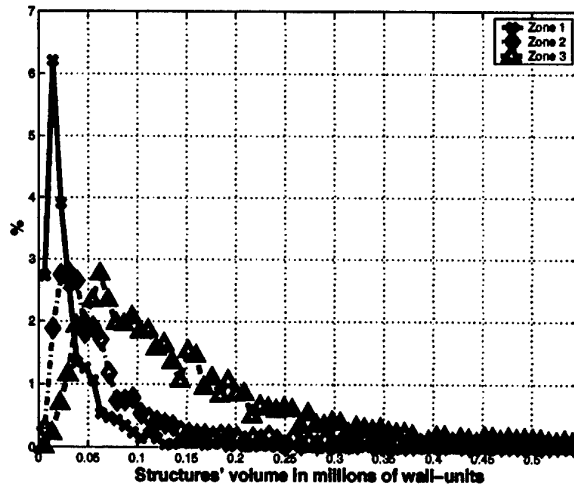


Fig. 6.3: Structures Volume of plane channel at $Re_\tau = 395$ with usual Zone distinction. (Number of bins: 8000; limits of histogram: $1.23e+03 \dots 6.49e+07$)

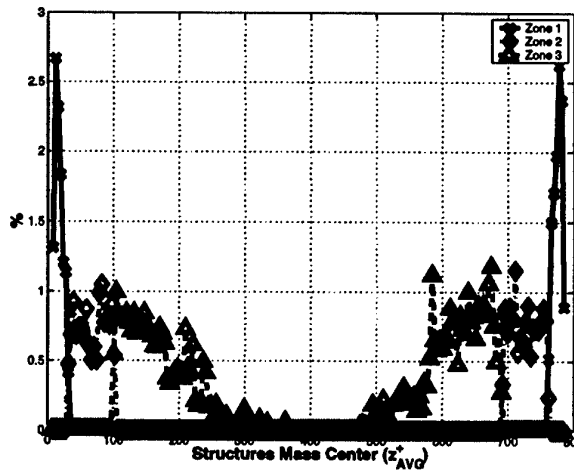


Fig. 6.4: Structures mass center of plane channel at $Re_\tau = 395$ with usual zone distinction. (Number of bins 200; limits of histogram: $4.7147 \dots 790$)

The distribution of structures mass center across the height of the channel (Fig. 6.4) shows a nearly uniform distribution for $z^+ < 200$, indicating that the active layer is, now, much wider than one found for previous case and contribution of Zone 3 could no more be neglected in the analysis to be carried out on the present flow: indeed, 57 % of the structures are now found in Zone 3, while Zone 2 now only hosts 22% of the structures found.

Advection velocity of mass center (Fig. 6.5) confirms the structures follow the average advection of overall flow.

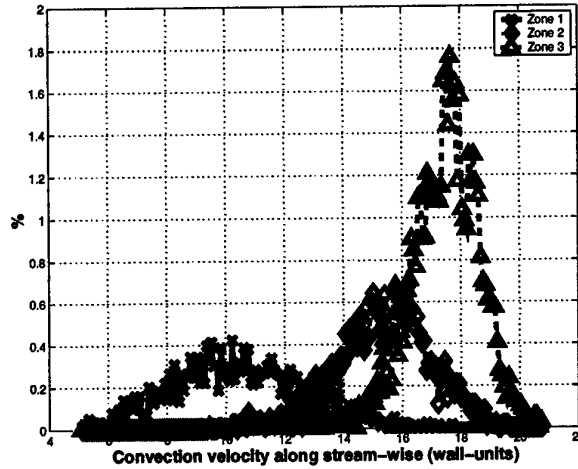


Fig. 6.5: Stream-wise advection of structures center of mass of plane channel at $Re_\tau = 395$. (Number of bins: 200; limits of histogram: 5.03 ... 20.77)

Projection of structures on x , y , z axis (Fig. 6.6) shows sizes similar to ones found at $Re_\tau = 180$ (Fig. 5.15).

It can be remarked that most probable value for L_x is nearly constant for all the 3 zones (Fig. 6.6) at $L_x \cong 100$, while L_y and L_z increase with the distance from the wall.

A more complete information can be obtained from corresponding joint probability function (JPDF) $L_x - L_y$, $L_y - L_z$ and $L_x - L_z$. Distributions for the 3 pairing are presented in Fig. 6.7 and Fig. 6.8.

The similar behaviors of Zone 2 and Zone 3 confirms the conclusion that presence of organized structures covers the entire inertial region and corresponding entities belong to a same phenomenology.

As discussed in Chapter 5, the most reliable estimation of size and orientation of the structures is the one obtained by the analysis of their inertial moments, which are presented in Fig. 6.9 and Fig. 6.10.

Present results show patterns similar to ones discussed in § 5.1 and 5.2: in Zone 1 most of structures are oriented along x direction (Fig. 6.9 left column); in Zone 2 (Fig. 6.9 right column), turning of structures away from $x - y$ plane increases, as well the dispersion of structures in different orientations; this trend further increases (Fig. 6.10) in Zone 3, making it difficult to detect a preferred orientation.

It must be remarked that, since higher Reynolds number strongly increases the percent-

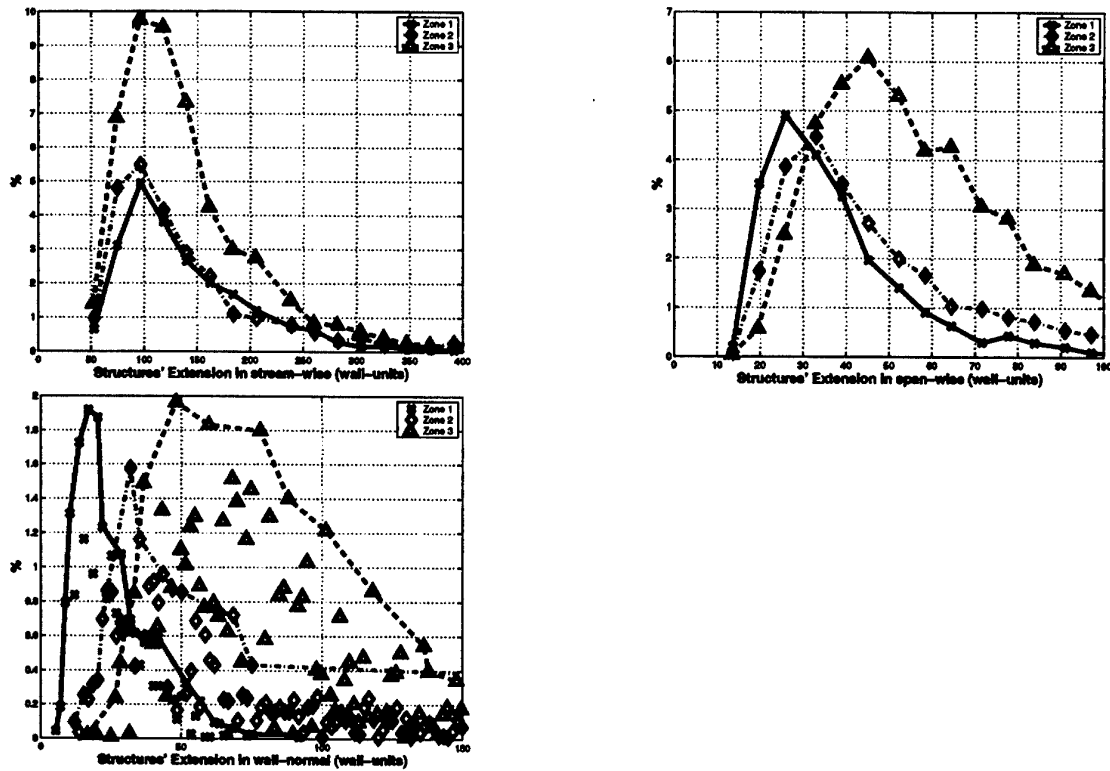


Fig. 6.6: Structures statistics at $Re_\tau = 395$: length in wall units. (From top left to bottom right: number of bins: 200, 800, 200; limits of histograms: $46.53 \dots 2.23e^{+03}$, $12.92 \dots 827.28$, $4.22 \dots 336.4058$)

age presence of Zone 3 respect to Zone 2 and Zone 1, being the procedure used to produce Fig. 6.10 and Fig. 6.9 the same than the one used to produce similar figures in the previous chapters, the number of structures present in the Fig. 6.10 appears extremely high compared to Fig. 5.42, but this is consistent with the relative presence of structures noted above.

Extracting tilt and incidence angle for from these data yields the results presented in Fig. 6.11 to Fig. 6.14, where the global normalization and the local normalization for the angles proposed in § 5.2 is applied.

Fig. 6.11 and 6.13 confirm that there is no preferred tilt angle; distribution of data is very similar for Zones 1 and 2, while variance of the distribution increases in Zone 3, showing that structures tend to turn away from x axis with increasing distance from wall; it can be noted that distribution for Zone 2 is similar to the corresponding one at $Re_\tau = 180$ but not to such an extent to possibly conclude of an universal behavior for inertial layer; for the local normalization (conf. Fig. 5.45 and Fig. 6.13) the PDF hints to a bigger dispersion for the lower Reynolds.

Existence of an average incidence angle (Fig. 6.12 and Fig. 6.13) shows the tendency of

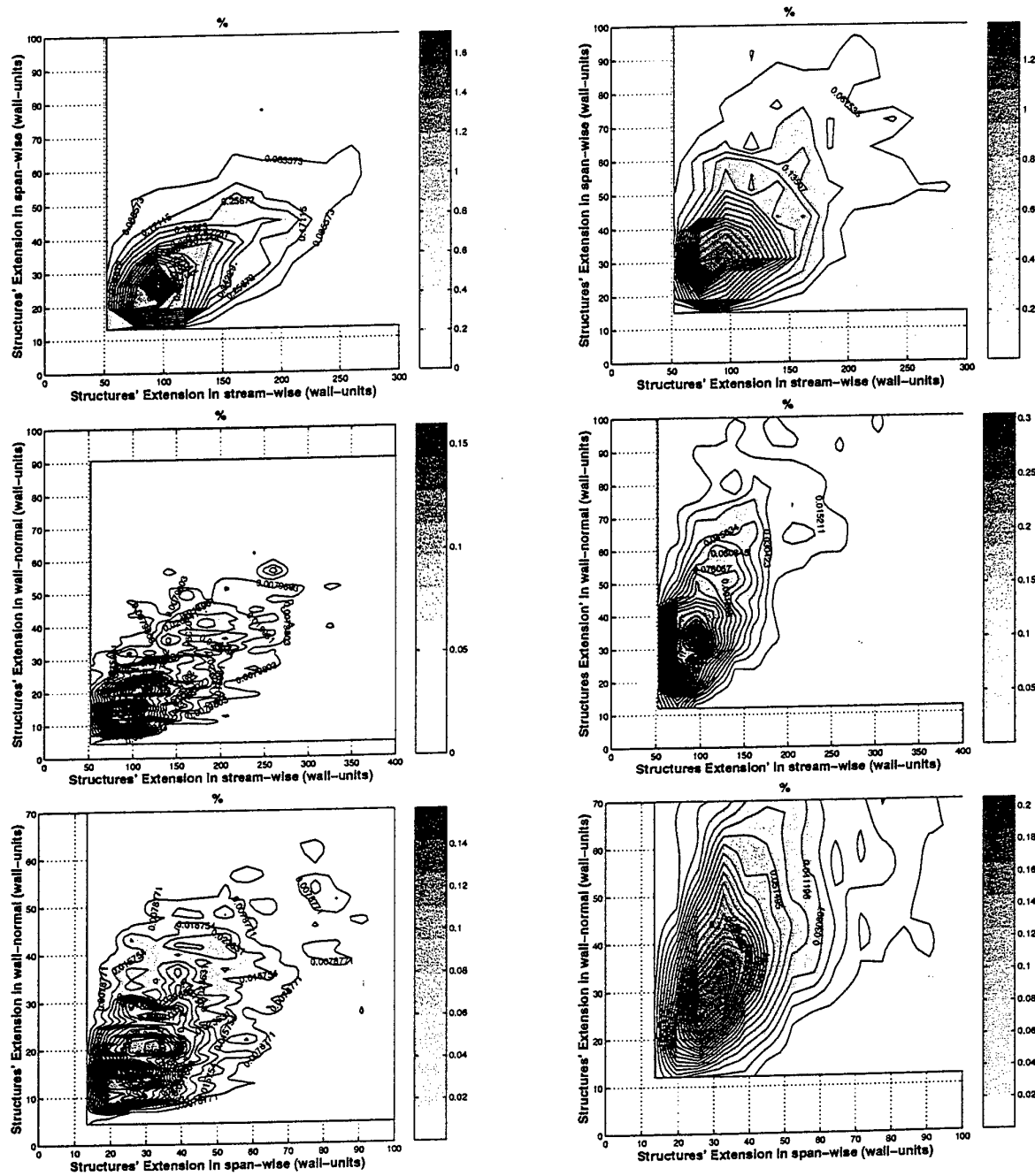


Fig. 6.7: Structures statistics: JPDF for structures extension. $Re_\tau = 395$. Left column Zone 1, right column Zone 2, xy -top, xz -middle and yz -bottom.

structures to rotate away from the $x - y$ plane: incidence angle increases from Zone 1 to 3 to reach a most probable state of $\alpha \cong 14$ degrees for the intermediate zone; again, it has to be remarked that the incidence angle for Zone 2, here found, is comparable to the one found at $Re_\tau = 180$ both in § 5.1 and § 5.2.

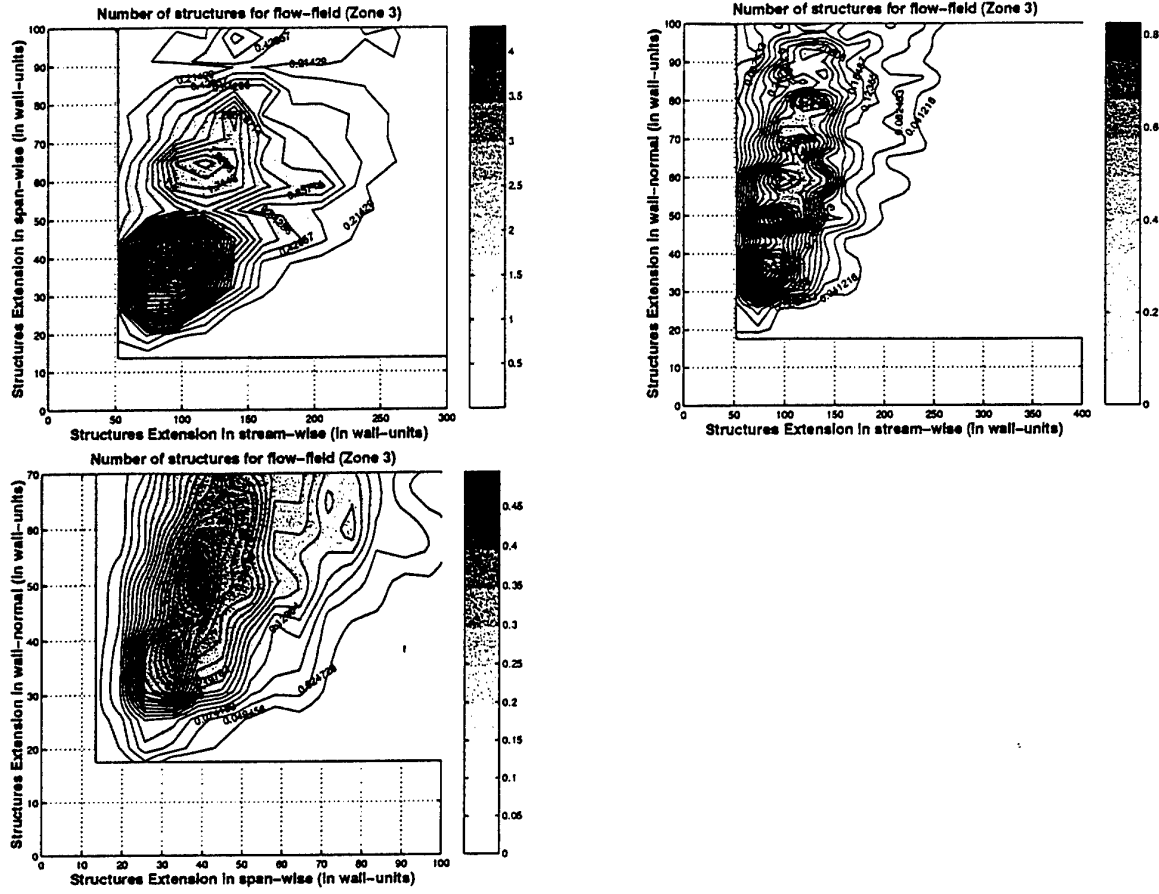


Fig. 6.8: Structures statistics: JPDF for structures extension. $Re_\tau = 395$. Zone 3, xy -top left, xz -top right and yz -bottom.

Following conclusions reached in § 5.1, the typical shape of the structure is assumed to be an ellipsoid of volume $\frac{4}{3}\pi abc$, where $a \geq b \geq c$ are the semi-length on the 3 axis, whose values are presented in Fig. 6.15 to Fig. 6.17. It is possible to compare the volume of the ellipsoid with the volume of the corresponding structure, being able finally to retrieve Fig. 6.18.

According to Fig. 6.15 to 6.17, the most probable state, for Zone 2, would be an ellipsoid having $a \cong 37.3$, $b \cong 15.9$ and $c \cong 11.4$ wall units.

Values comparable to the ones found in § 5.1. It is to be remarked that the values $2 \times a$, $2 \times b$ are reasonable close to the most probable state yielded by the JPDF $L_x - L_z = 75 - 35$, for Zone 2 (Fig. 6.7); this result confirms the capability of present approach to identify the dimensions of the representative structure.

Significantly higher values are found for Zone 3: $a \cong 57.2$, $b \cong 25$ and $c \cong 16.4$; structures found in Zone 3, or in the middle of the channel, are convected from the walls, as confirmed by the study of the velocity of structures mass center. The fact that the structures

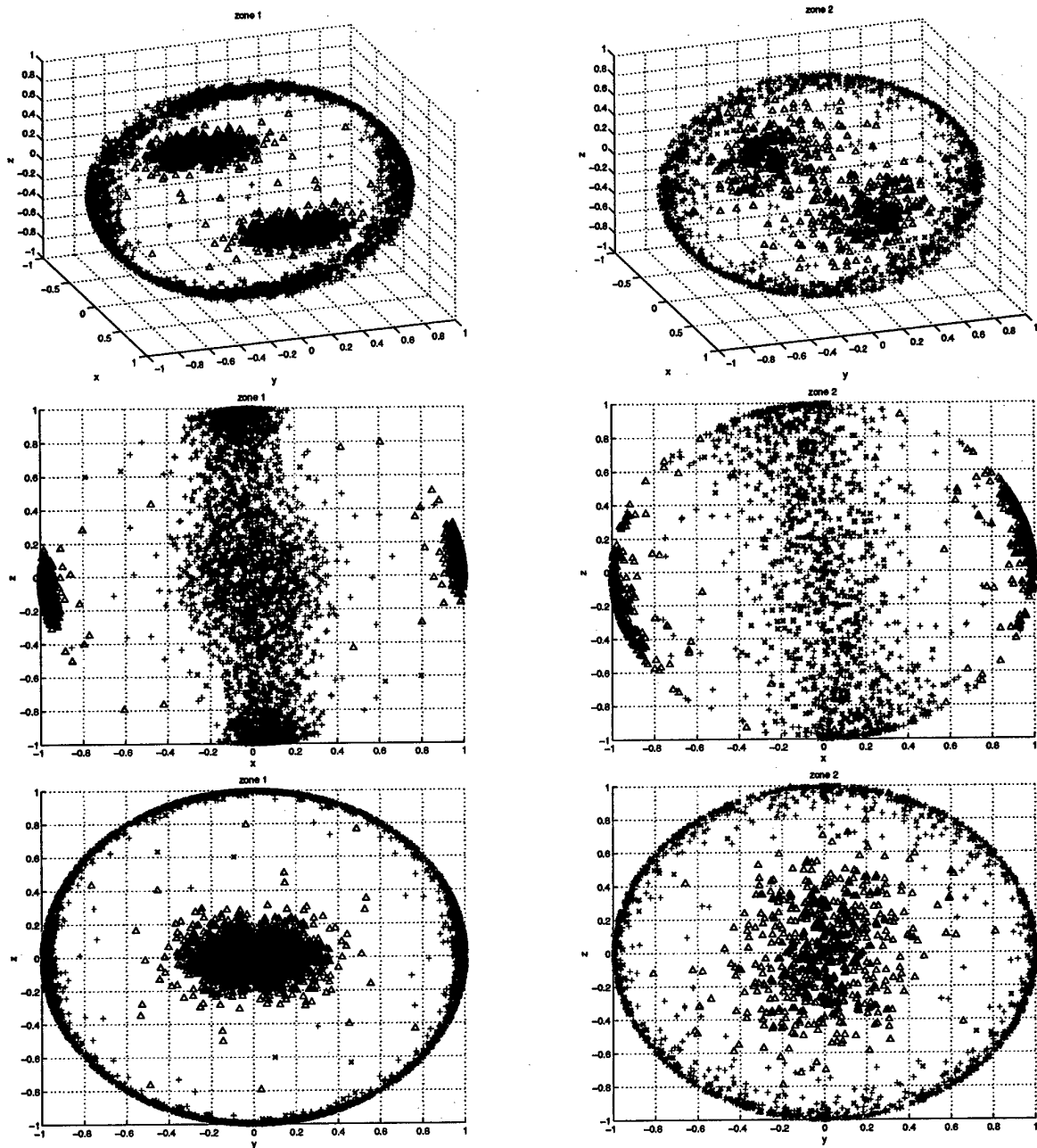


Fig. 6.9: Structures statistics, $Re_\tau = 395$: spatial alignment, different pov. \triangle Structure mean alignment. Zone 1 left column, Zone 2 right column

are different in size could hint to a extremely rapid growth process, but another possibility, already addressed in § 5.3, is that, close to the wall, the structures are so close to each other that the algorithm merges some of them in some very big structures with very low probability, removing structures that could possibly modify in a significantly way the overall statistics.

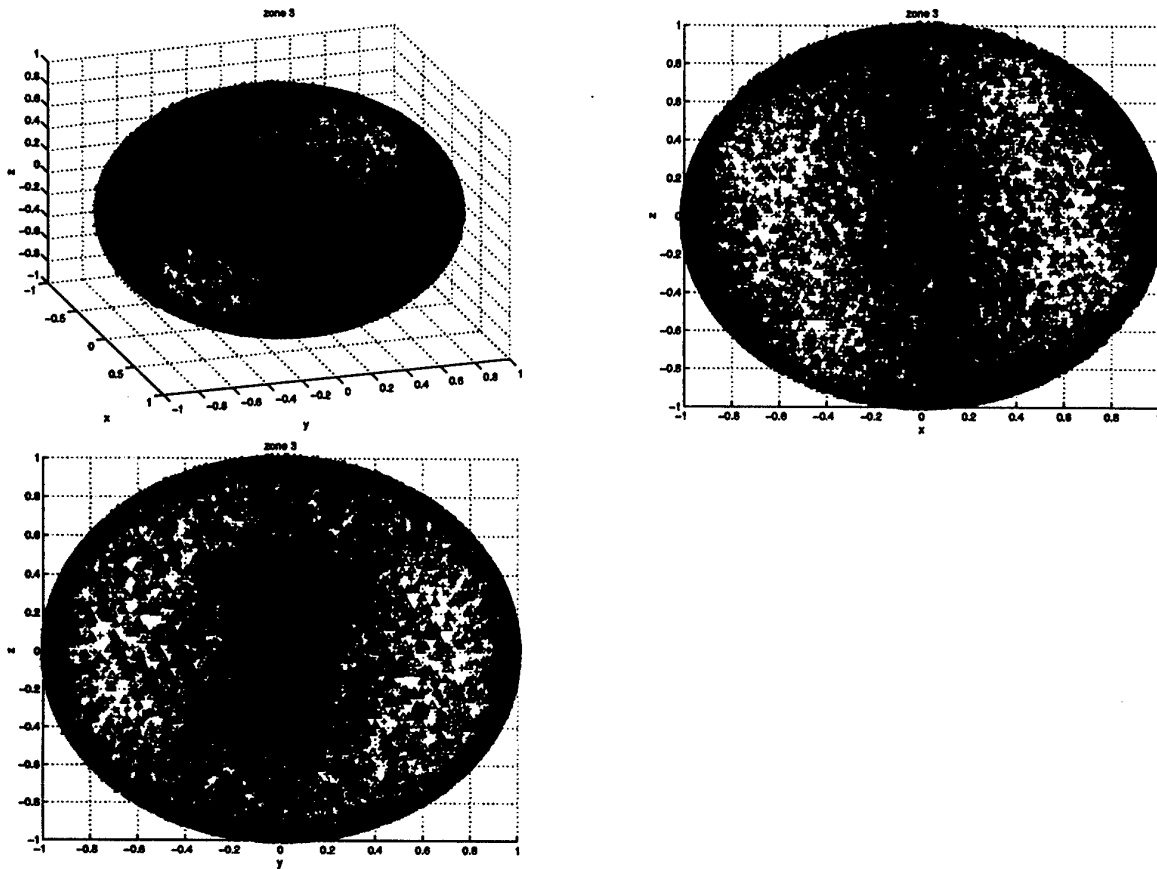


Fig. 6.10: Structures statistics, $Re_\tau = 395$: spatial alignment, different pov. Δ Structure mean alignment. Zone 3

This fact alone should be considered worth of further studies.

Dynamic of organized vorticity can be assessed in Fig. 6.19, where specific vorticity is presented component per component.

Predominant clockwise and counter-clockwise rotation around x axis can be noted in the aforementioned figure (top left), being most evident for Zone 3; this pattern of behavior confirms that all structures present in the inertial region belong to a same family; different behavior of Zone 3 with respect to $Re_\tau = 180$ case shows the enlarging of the active region and the passage to fully developed turbulent flow.

Corresponding behavior is visible for wall-normal specific vorticity (bottom left). Gaussian like behavior of specific vorticity in span-wise direction (middle left) puts in evidence absence of tilt in $x - y$ axis, always for average in the whole channel.

The JPFD of specific vorticity (Fig. 6.20 and Fig. 6.21) offer a more complete understanding of the organization of vorticity field; on the basis of the experience accumulated

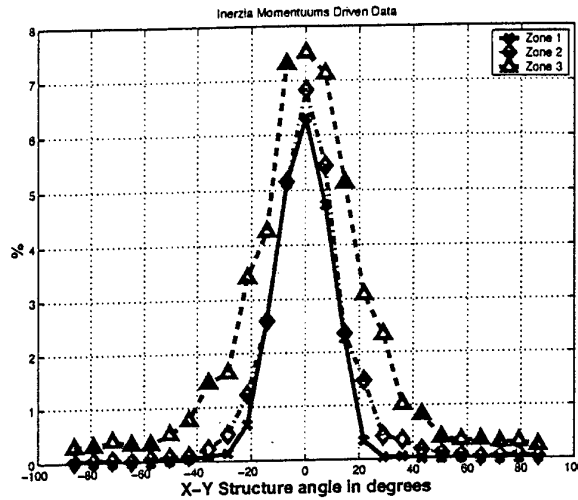


Fig. 6.11: Structures statistics $Re_\tau = 395$: Tilting angle extracted from inertial tensor. (Number of bins: 25; limits of histogram: $-90 \dots 90$)

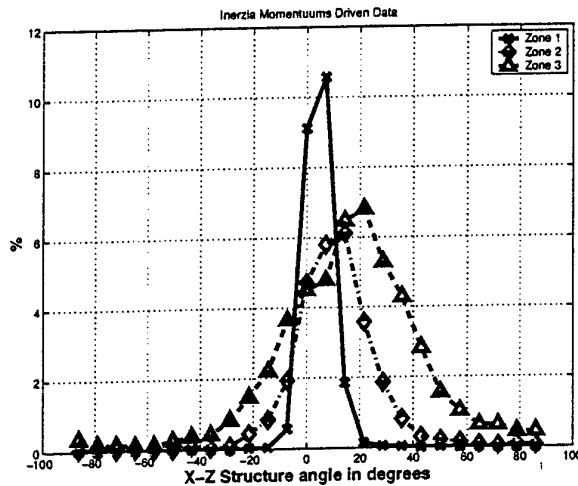


Fig. 6.12: Structures statistics $Re_\tau = 395$: Incidence angle extracted from inertial tensor. (Number of bins: 25; limits of histogram: $-90 \dots 90$)

previous tests (see § 5) while for the previous cases, only the behavior of the lower half channel are presented here, for clarity sake, as the joint PDF for the whole channel might hide possible information.

The JPFD of specific vorticity in x and y direction for all three zones (Fig. 6.20 and Fig. 6.21) show similar pattern: the overwhelming majority of present structures have a rotation along x ; separation of clock-wise and counter-clock-wise rotation can be well remarked in Zones 2 and 3 and is more clear-cut than one found for $Re_\tau = 180$. Values of stream-wise

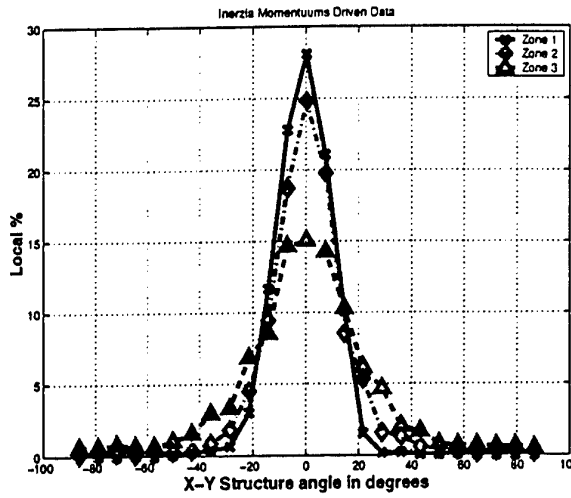


Fig. 6.13: Structures statistics $Re_\tau = 395$: Tilting angle extracted from inertial tensor. (Number of bins: 25. Limits of histograms $-90 \dots 90$)

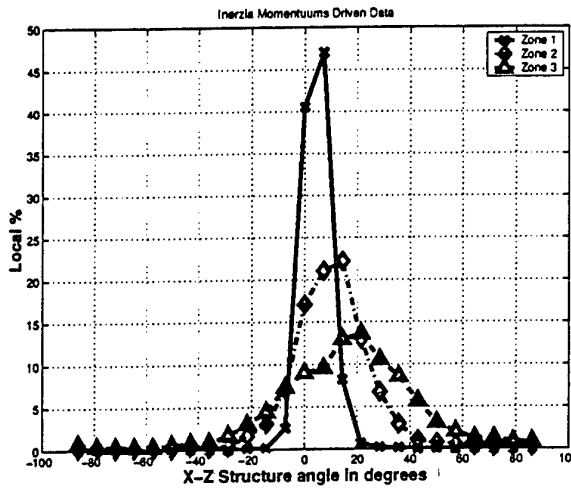


Fig. 6.14: Structures statistics $Re_\tau = 395$: Incidence angle extracted from inertial tensor. (Number of bins: 25. Limits of histograms $-90 \dots 90$)

vorticity are clustered around ± 0.10 for Zone 2 and ± 0.08 for Zone 3; values for span-wise vorticity are typically twice smaller, which is further indicating that stream-wise rotation is dominant, even if it should not be forgotten that the mean vorticity has been subtracted.

Similar behavior is evident for JPDF of specific vorticity in x and z direction ; it has to be remarked that, in Zone 3, Fig. 6.21, wall-normal specific vorticity is in the same order of magnitude as the one in stream-wise direction, further confirming the tendency of the structures to turn away from $x - y$ plane.

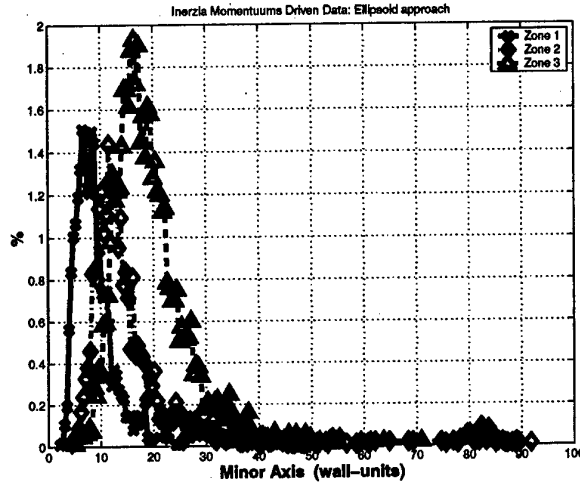


Fig. 6.15: Structures statistics $Re_\tau = 395$: Equivalent ellipsoid minor semi-axis.

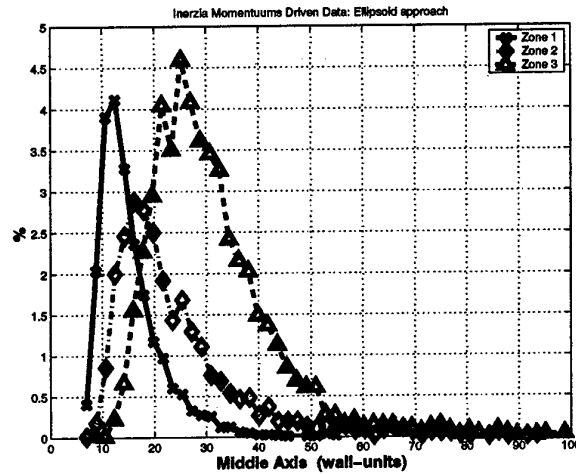


Fig. 6.16: Structures statistics $Re_\tau = 395$: Equivalent ellipsoid middle semi-axis.

JPDF of specific vorticity in y and z direction shows the absence of preferred state in cross-flow plane.

6.2.1 Conclusion

It can be concluded that main findings for case of $Re_\tau = 180$ are confirmed:

- Applying present proposal for the choice of the trigger level to case $Re_\tau = 395$ yields comparable values for main physical parameters for organized turbulence.

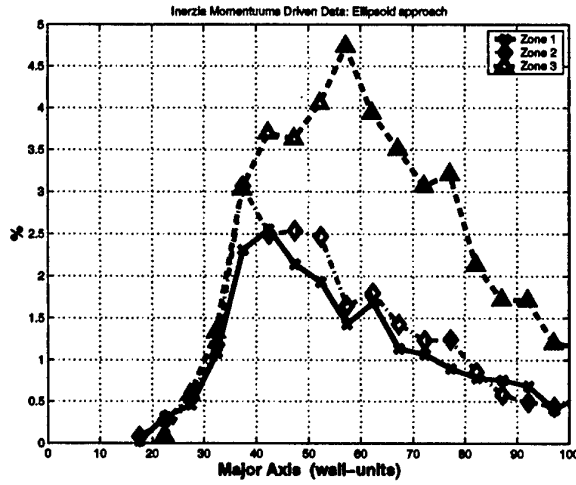


Fig. 6.17: Structures statistics $Re_\tau = 395$: Equivalent ellipsoid major semi-axis.

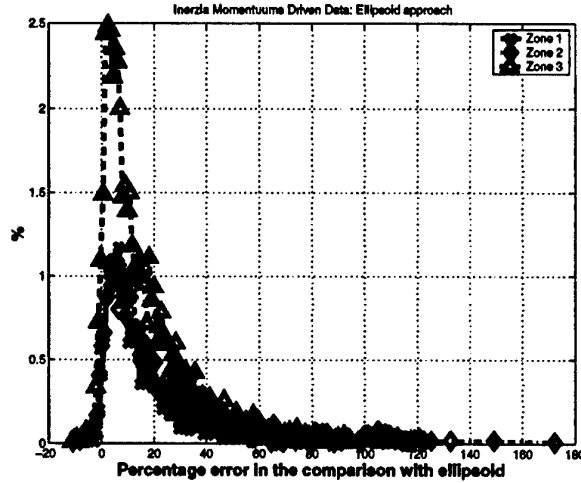


Fig. 6.18: Structures statistics $Re_\tau = 395$: Equivalent ellipsoid volume deviation.

- Most of individual structures detected by the search algorithm have size smaller than longitudinal macro-scale, even if a minority of structures exists whose length is comparable or bigger than this value.
- Close to the wall (Zone 1) structures are oriented along the x axis; moving away from the wall, turning away from $x - y$ plane is observed.
- Results at $Re_\tau = 395$ are consistent with corresponding ones at $Re_\tau = 180$ for same resolution.

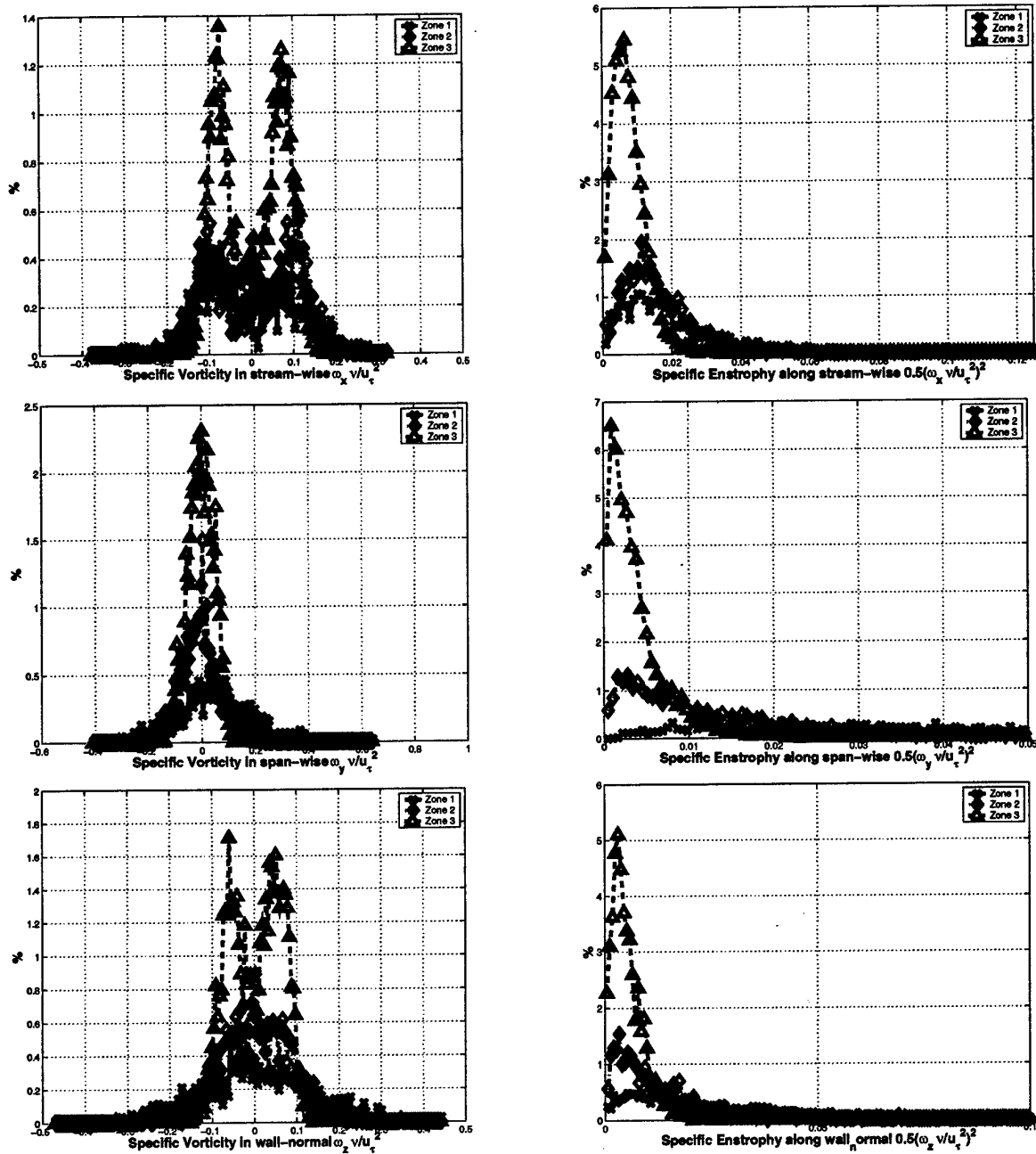


Fig. 6.19: Structure statistics: Specific Vorticity (left) and enstrophy(right) for x (top), y (middle) and z (bottom). $Re_\tau = 395$. (Number of bins: 200; limits of histograms (from top to bottom), vorticity: $-0.38 \dots 0.32$, $-0.46 \dots 0.64$, $-0.47 \dots 0.37$; enstrophy: $0 \dots 0.23$, $0 \dots 0.46$, $0 \dots 0.26$)

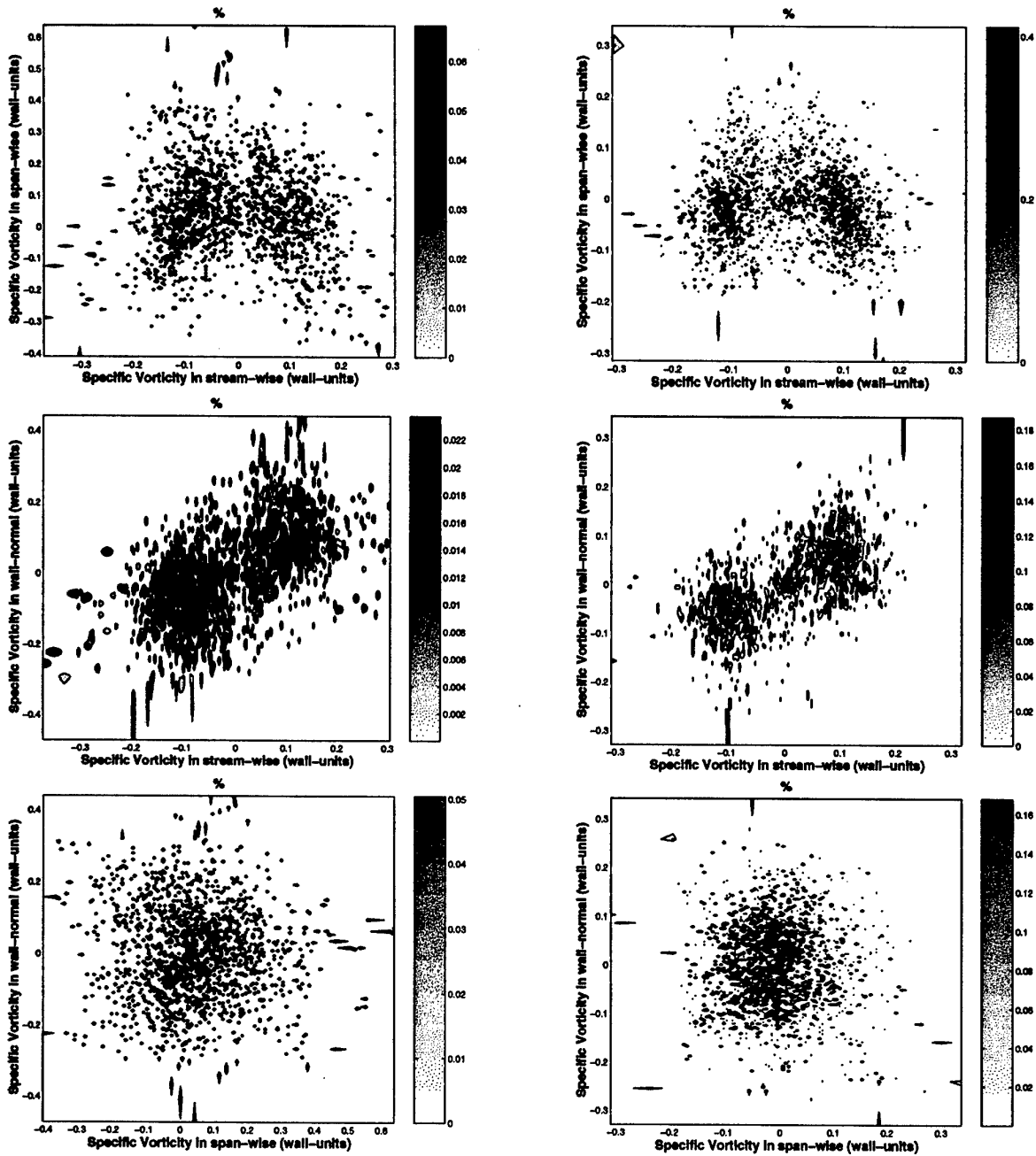


Fig. 6.20: Structures statistics lower half-channel: JPDF for structures vorticity, lower half channel. Left Zone 1, right Zone 2, xy -top, xz -middle and yz -bottom. $Re_\tau = 395$

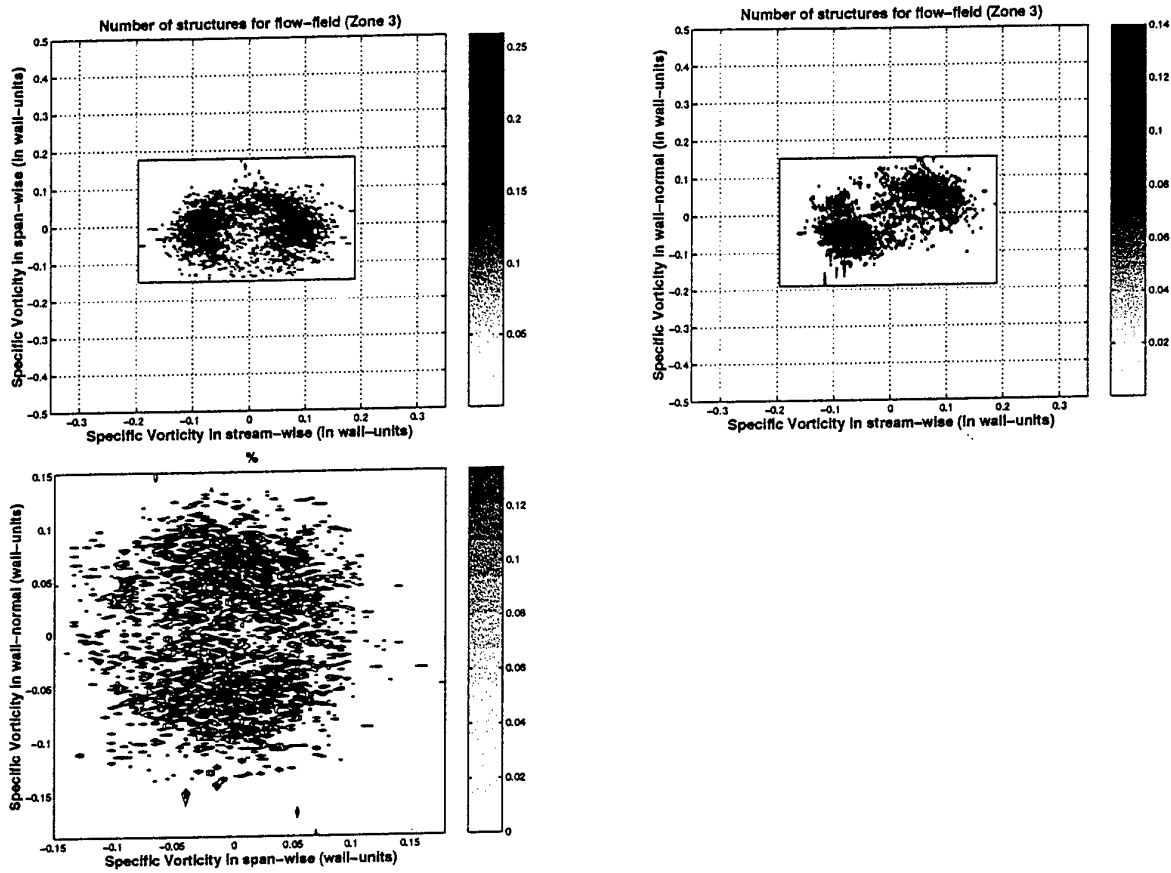


Fig. 6.21: Structures statistics lower half-channel: JPDF for structures vorticity, lower half channel. Zone 3, xy -top left, xz -top right and yz -bottom. $Re_\tau = 395$

6.3 Analysis of coherent structures at $Re_\tau = 590$

Complete results for LES of eulerian field and organized structures are presented in Annex I, while most relevant finding and differences with results at lower Re_s are reviewed below.

Overall view of vortex structures are presented in Fig. 6.22 and 6.23.

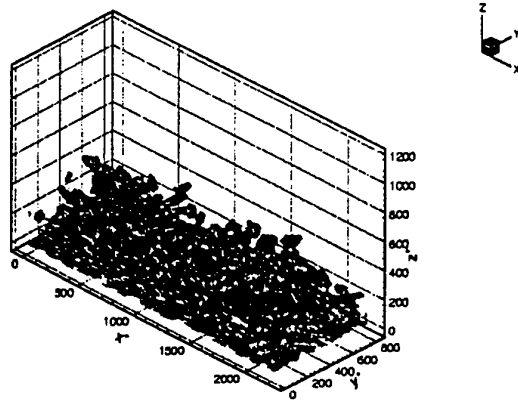


Fig. 6.22: 3-D overview of the field of detected structures of plane channel at $Re_\tau = 590$

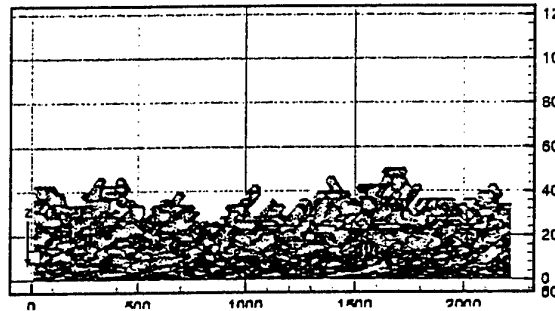


Fig. 6.23: Lateral overview of the field of detected structures of plane channel at $Re_\tau = 590$

Comparison with corresponding Fig. 6.1 and Fig. 6.2 shows a remarkable similarity, which is a first indication the region of self-similar behavior of turbulence is attained; further enlargement of the layer affected by the process can be remarked.

The average population is in the order of 276 structures (Fig. 6.24) for an average value $Vol_{mean} = 9.07e^{+05}$ wall units, in line with the tendency for volume of average structure increases with Re , although this value must be considered as rough indication of overall trend, as it was already remarked discussing results for $Re_\tau = 180$ and $Re_\tau = 395$.

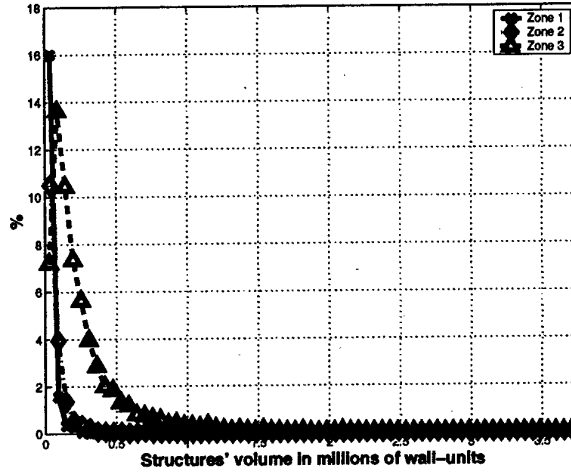


Fig. 6.24: Structures Volume of plane channel at $Re_\tau = 590$ with usual Zone distinction. (Number of bins: 2000; limits of histogram: $1.05e^{+03} \dots 1.11e^{+08}$)

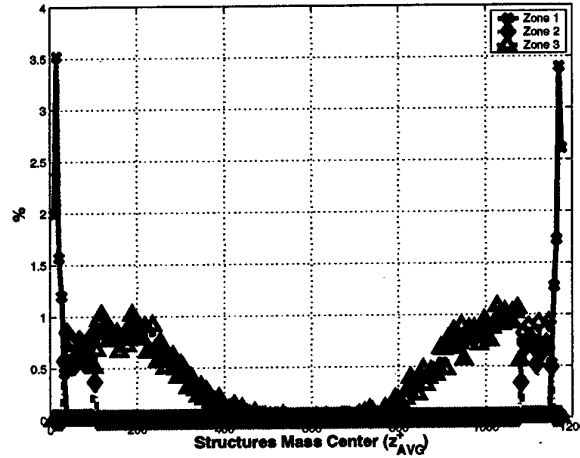


Fig. 6.25: Structures mass center of plane channel at $Re_\tau = 590$ with usual Zone distinction. (Number of bins: 200; limits of histogram: $3.8 \dots 1176$)

The distribution of center of mass of the structures across the height of the channel (Fig. 6.25) shows most of population is now located in region for $z^+ < 300$, confirming that the active increases with Re_τ . The distribution appears nearly uniform over $20 < z^+ < 300$, indicating all these structures are part of single phenomenology. It has to be remarked that, now only 18 % of structures belong to Zone 2, while the percentage of presence of structures in Zone 3 is now as high as 64 %.

Advection velocity of mass of the structures (Fig. 6.26) for different zones is in the same order of magnitude as the corresponding average advection of overall flow, without visible

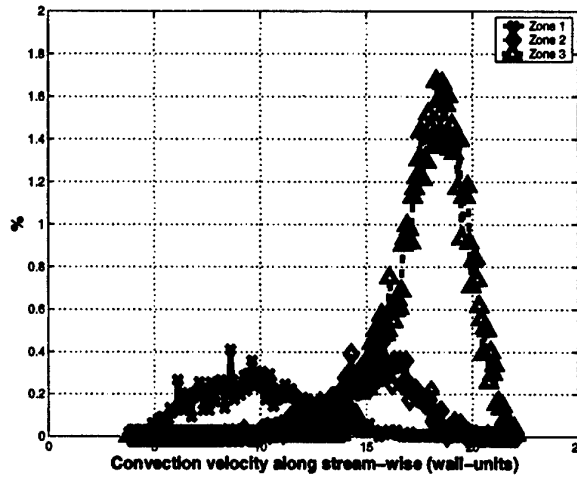


Fig. 6.26: Stream-wise advection of structures center of mass of plane channel at $Re_\tau = 590$. Number of bins 200, limits 3.71 ... 22.11.

lag.

Projection of structures on x , y and z axis (Fig. 6.27) shows slightly bigger sizes than the ones found at lower Re_s .

It can be remarked that most probable value for L_x is nearly constant for all the 3 zones at $L_x \cong 100$, while L_y and L_z increase with the distance from the wall, to reach $L_y \cong 50$; $L_z \cong 80$ in Zone 3. This trend further confirms the tendency of structures to turn away from x axis.

A more complete information can be obtained from corresponding joint probability function (JPDF) $L_x - L_y$; $L_y - L_z$ and $L_x - L_z$. Distributions for the 3 pairing are presented in Fig. 6.28 and Fig. 6.29.

Present results are consistent with trends visible at lower Re_s , the most probable state being: $L_x - L_z = 100 - 40$ for Zone 2 and $L_x - L_z = 100 - 55$ for Zone 3, which is another indication of turning away $x - y$ plane by the structures.

As already stated, (§ 5), estimation of size and orientation of the structures must be obtained by the analysis of their inertial moments of present population, which are presented in Fig. 6.30 and 6.31.

Present results show trends similar to ones observed for $Re_\tau = 395$ case: in Zone 1 most of structures are oriented along x direction (Fig. 6.30 left column); in Zone 2, turning of structures away from $x - y$ plane increases together with existence of structures with different orientations (Fig. 6.30 right column); Fig. 6.31 shows how most of structures lie within Zone 3; dispersion of data further increases, making it difficult to recognize a preferred orientation.

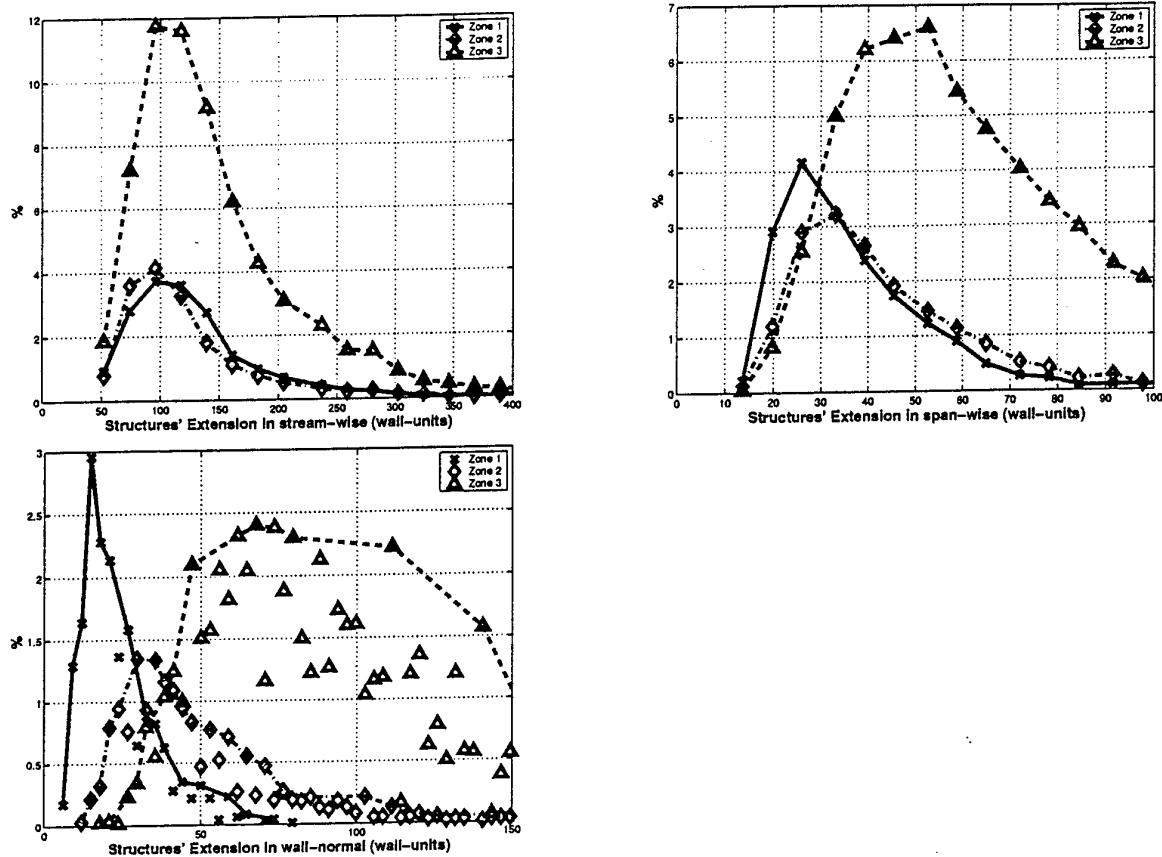


Fig. 6.27: Structures statistics at $Re_\tau = 590$: length in wall units. (From top left to bottom right, number of bins: 200, 800, 200; limits of histograms, $46.53 \dots 2.224e^{+03}$, $13.03 \dots 834.09$, $4.55 \dots 590$)

Extracting tilt and incidence angle for from these data yields the results presented in Fig. 6.32 to Fig. 6.35.

Following the procedure introduced in § 5.2, global normalization and local normalization for the angles are given as separate figures.

Fig. 6.32 confirms that there is no preferred tilt angle; distribution of data is very similar for Zones 2 and 3, variance of distribution being in the same order of magnitude as the corresponding one at $Re_\tau = 395$. Evolution of average incidence angle from Zone 1 to 3 shows the tendency of structures to rotate away from the $x - y$ plane: incidence angle increases from Zone 1 to 3 to reach a most probable state of $\alpha \cong 21$ degrees in Zone 3; while only 7 for Zone 2. Again, the incidence angle for Zone 2 is comparable to the one found at $Re_\tau = 180$ and 395, remembering conclusions of § 5.2.

The typical shape of the structure is assumed to be an ellipsoid of volume $\frac{4}{3}\pi abc$, where $a \geq b \geq c$ are the semi-length on the 3 axis, whose values are presented in Fig. 6.36 to

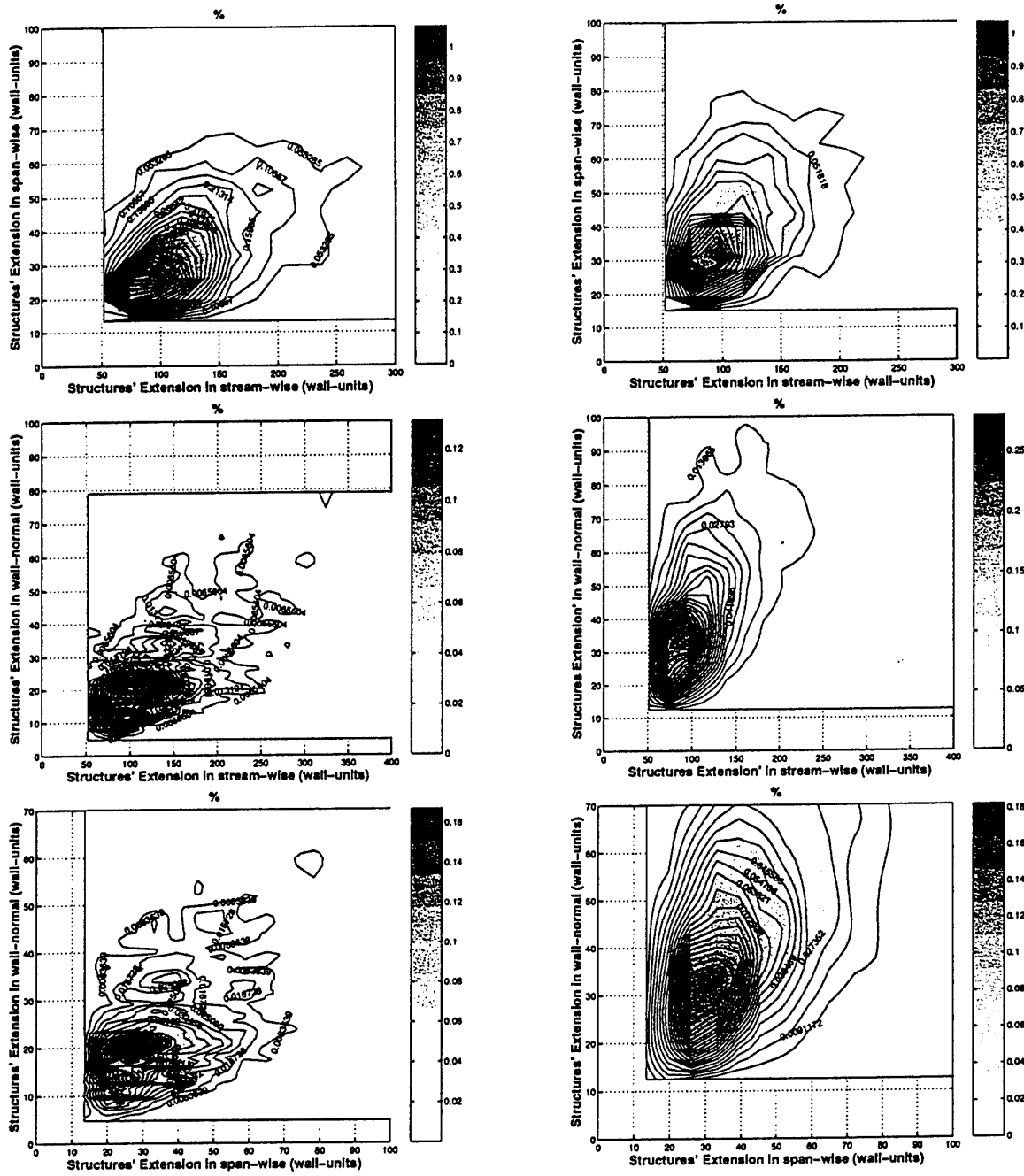


Fig. 6.28: Structures statistics: JPDF for structures extension. $Re_\tau = 590$. Left column Zone 1, right column Zone 2, xy -top, xz -middle and yz -bottom.

Fig. 6.38. Corresponding deviation is presented in Fig. 6.39.

Most probable values for the three half-axis, for zones 3 are $a \cong 54.54$; $b \cong 30.58$; $c \cong 17.74$. The values are comparable to ones found for Zone 3 at $Re_\tau = 395$, suggesting an

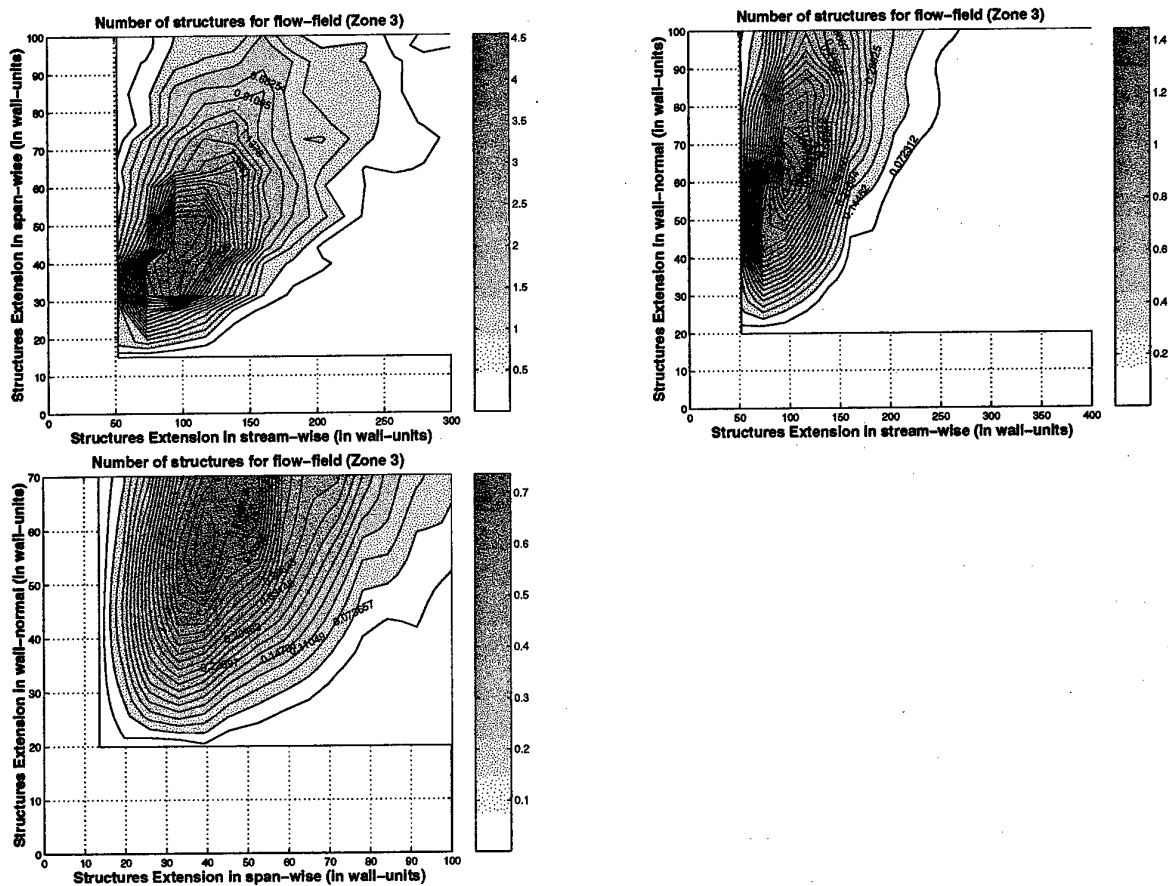


Fig. 6.29: Structures statistics: JPDF for structures extension. $Re_\tau = 590$. Zone 3, xy -top left, xz -top right and yz -bottom.

universal phenomenology for structures in zones at high local Re_τ .

Dynamic of organized vorticity can be assessed in Fig. 6.40, where specific vorticity (see § 4) is presented component per component.

Present trends are very similar to ones remarked at $Re_\tau = 395$: predominant clockwise and counter-clockwise rotation around x axis can be noted in the afore mentioned figure (top left) and is most evident for Zone 3; this pattern of behavior confirms that all structures present in inertial region belong to a same family. Corresponding behavior is visible for wall-normal specific vorticity (bottom left). Gaussian like behavior of specific vorticity in span-wise direction (middle left) puts in evidence the lack of preferential orientation around y axis, for whole channel averaging.

JPDF of specific vorticity in x and y direction for three zones (Fig. 6.41 and Fig. 6.42) shows increasing organization moving away from the wall: majority of present structures has a rotation along x ; separation of clock-wise and counter-clock-wise rotation progresses from

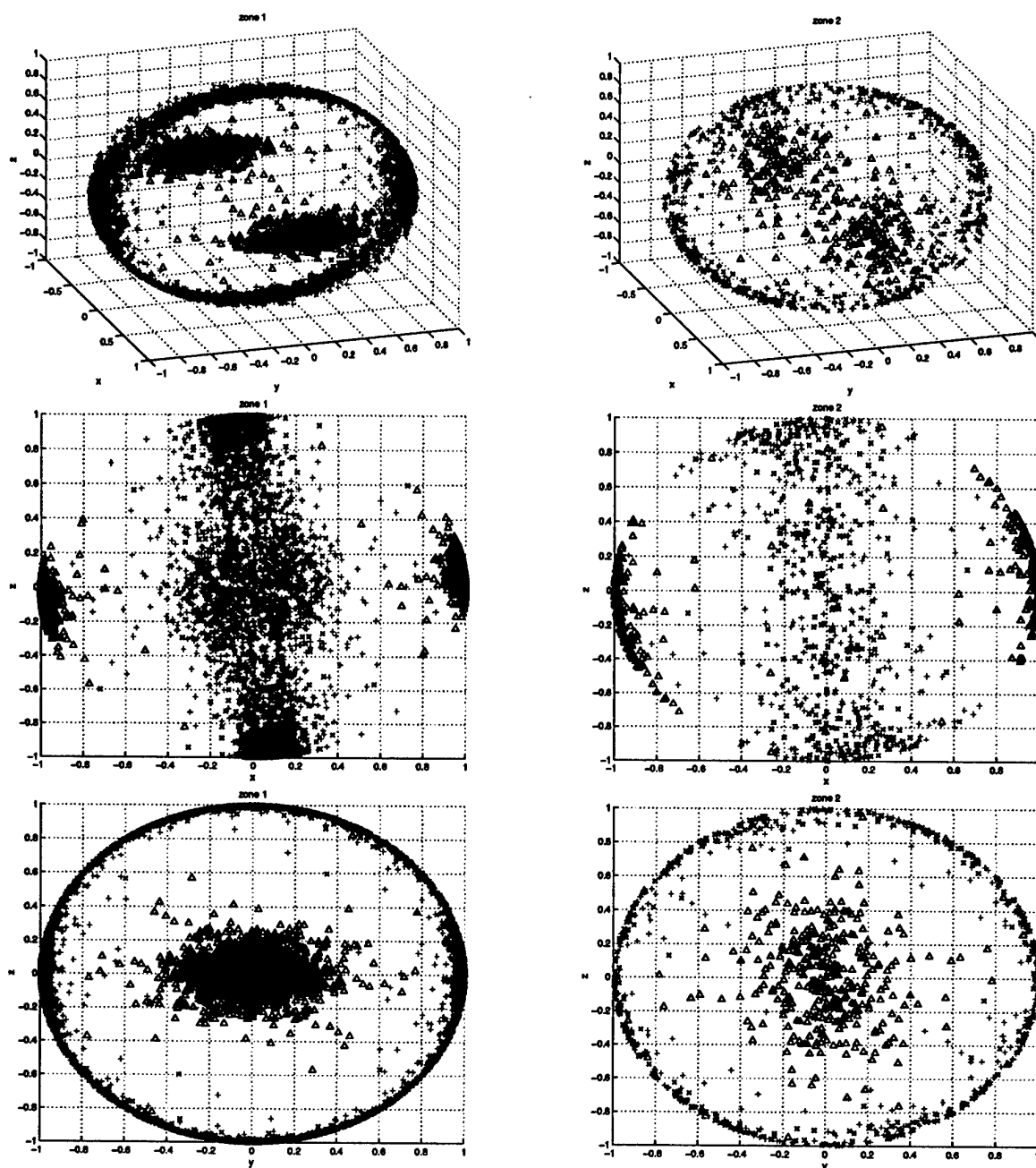


Fig. 6.30: Structures statistics, $Re_\tau = 590$: spatial alignment, different pov. Δ Structure mean alignment. Zone 1 left column, Zone 2 right column

Zone 2 to Zone 3 toward a well defined preferred state: values of stream-wise vorticity are clustered around ± 0.10 for Zone 2 and ± 0.08 for Zone 3; values for span-wise vorticity are typically twice smaller; all values are very close to the ones found at $Re_\tau = 395$.

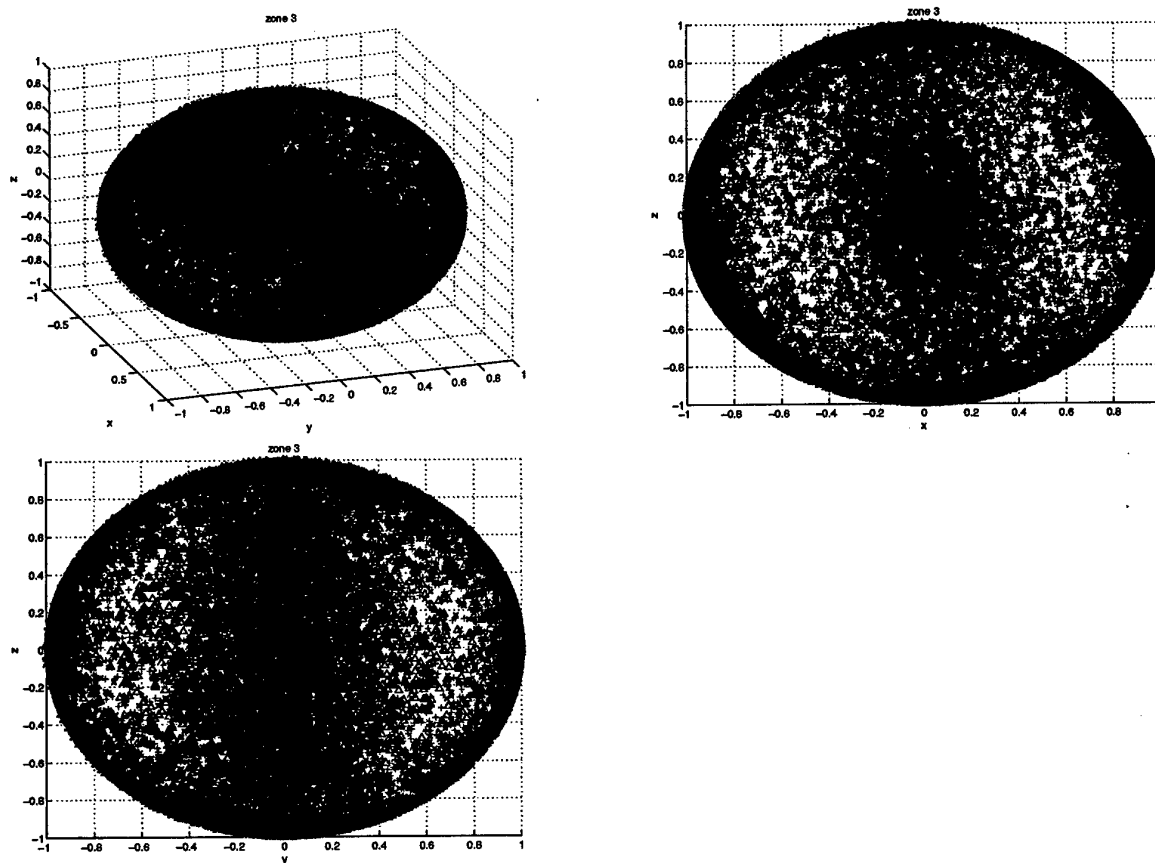


Fig. 6.31: Structures statistics, $Re_\tau = 590$: spatial alignment, different pov. Δ Structure mean alignment. Zone 3

Similar behavior is evident for JPDF of specific vorticity in x and z direction; it has to be remarked that, in Zone 3, Fig. 6.42, the wall-normal specific vorticity is in the same order of magnitude as stream-wise one, further confirming the tendency of the structures to turn away from $x - y$ plane.

JPDF of specific vorticity in y and z direction shows the absence of preferred state in cross-flow plane.

6.4 Conclusion

Overall, present results confirm the trends remarked for $Re_\tau = 180$ and $Re_\tau = 395$, and allow to conclude that, in all three cases, organized turbulence partakes the same phenomenology.

It can be concluded that the typical size of structures and width of layer affected by the

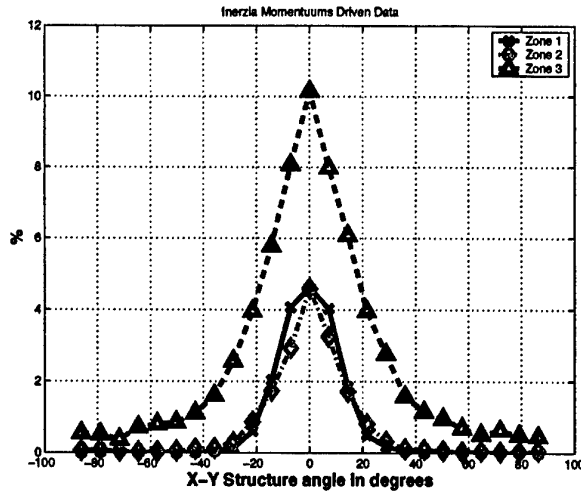


Fig. 6.32: Structures statistics $Re_\tau = 590$: Tilting angle extracted from inertial tensor. (Number of bins:25. Limits of histograms $-90 \dots 90$)

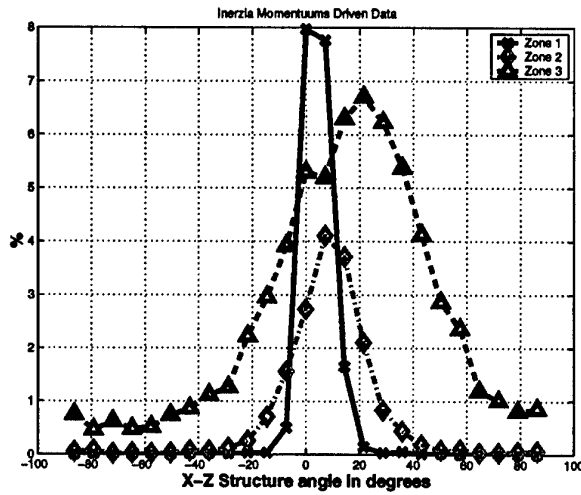


Fig. 6.33: Structures statistics $Re_\tau = 590$: Incidence angle extracted from inertial tensor. (Number of bins:25. Limits of histograms $-90 \dots 90$)

phenomenon seems to TO-CHECK slightly increase with Re_τ ; pattern and values of specific vorticity indicated universal behavior of the structures defined by present criterion.

Results so obtained are consistent and detailed and, therefore, allow some general conclusions which will be presented in § 7.

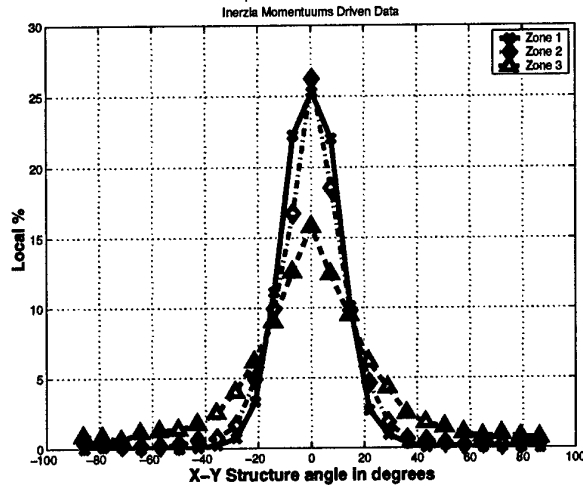


Fig. 6.34: Structures statistics $Re_\tau = 590$ (Case I): Tilting angle extracted from inertial tensor.(Number of bins:25. Limits of histograms $-90 \dots 90$)

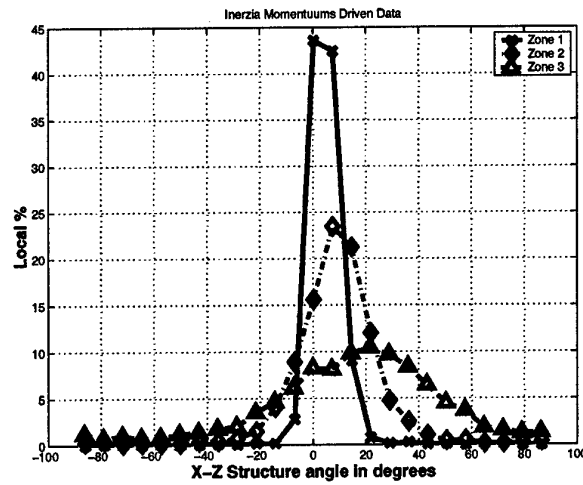


Fig. 6.35: Structures statistics $Re_\tau = 590$: Incidence angle extracted from inertial tensor.(Number of bins:25. Limits of histograms $-90 \dots 90$)

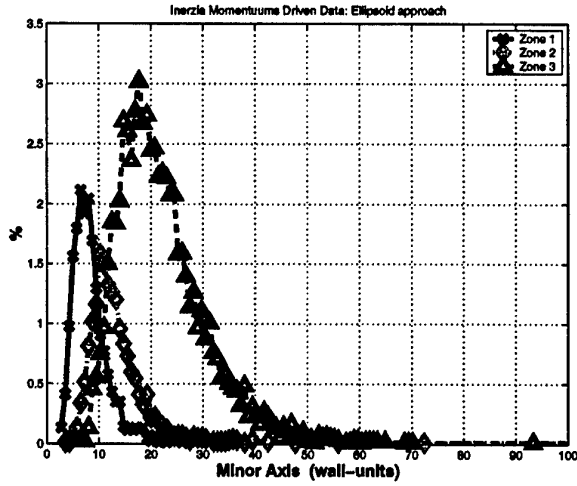


Fig. 6.36: Structures statistics $Re_\tau = 590$: Equivalent ellipsoid minor semi-axis.

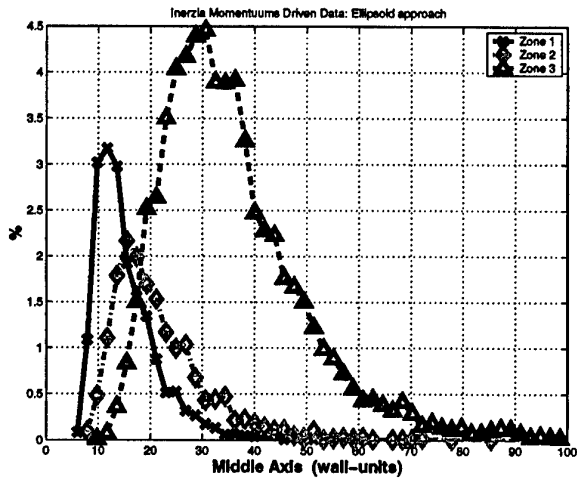


Fig. 6.37: Structures statistics $Re_\tau = 590$: Equivalent ellipsoid middle semi-axis.

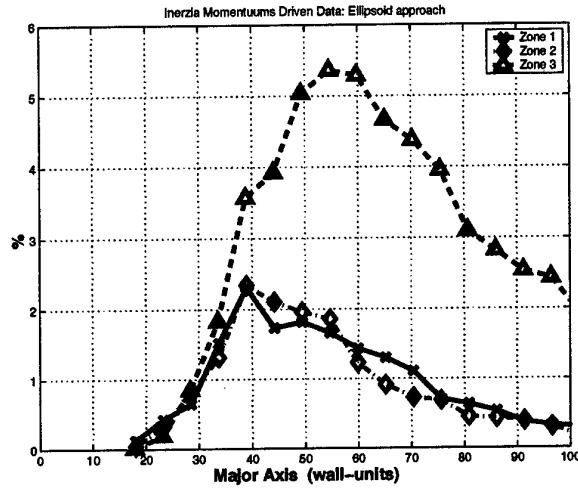


Fig. 6.38: Structures statistics $Re_\tau = 590$: Equivalent ellipsoid major semi-axis.

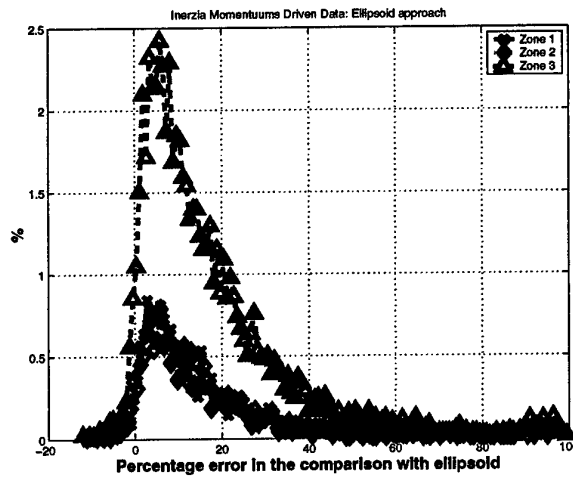


Fig. 6.39: Structures statistics $Re_\tau = 590$: Equivalent ellipsoid volume deviation.

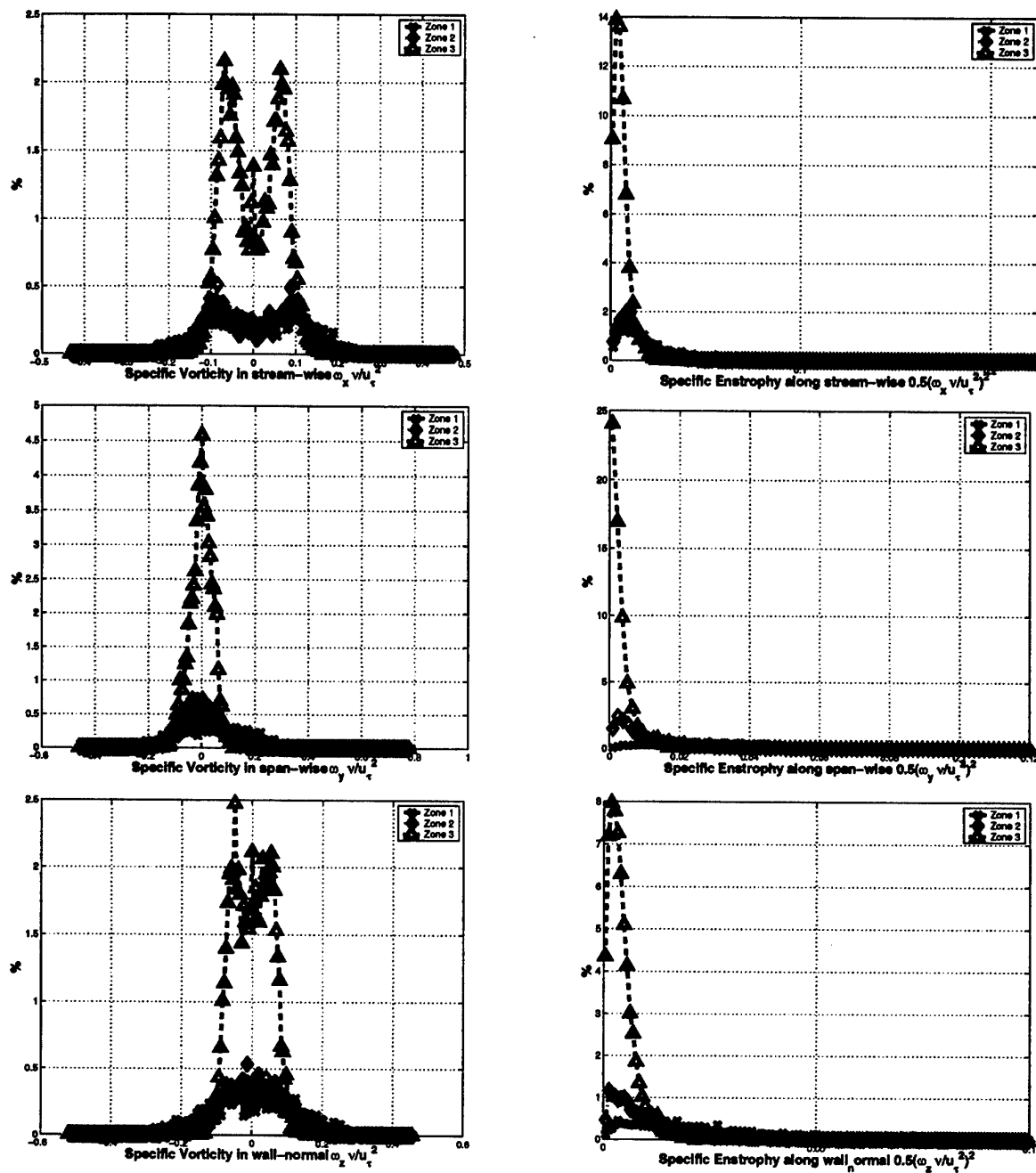


Fig. 6.40: Structure statistics: Specific Vorticity (left) and enstrophy(right) for x (top), y (middle) and z (bottom). $Re_\tau = 590$. (Number of bins: 200; limits of histograms (from top to bottom), vorticity: $-0.43 \cdots 0.47$, $-0.78 \cdots 0.62$, $-0.49 \cdots 0.52$; enstrophy: $0 \cdots 0.3588$, $0 \cdots 1.16$, $0 \cdots 0.29$.)

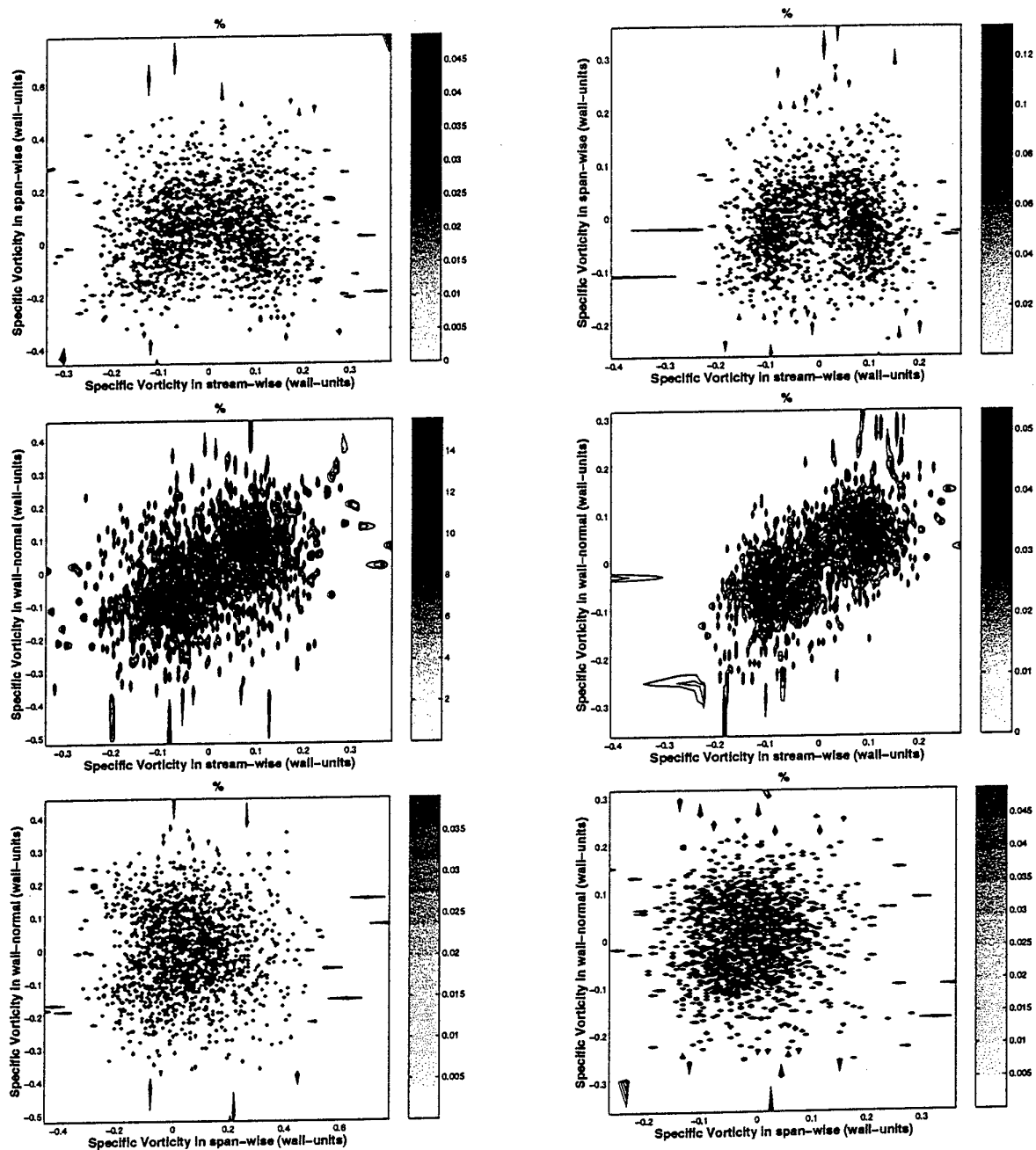


Fig. 6.41: Structures statistics lower half-channel: JPDF for structures vorticity, lower half channel. Left Zone 1, right Zone 2, xy -top, xz -middle and yz -bottom. $Re_\tau = 590$

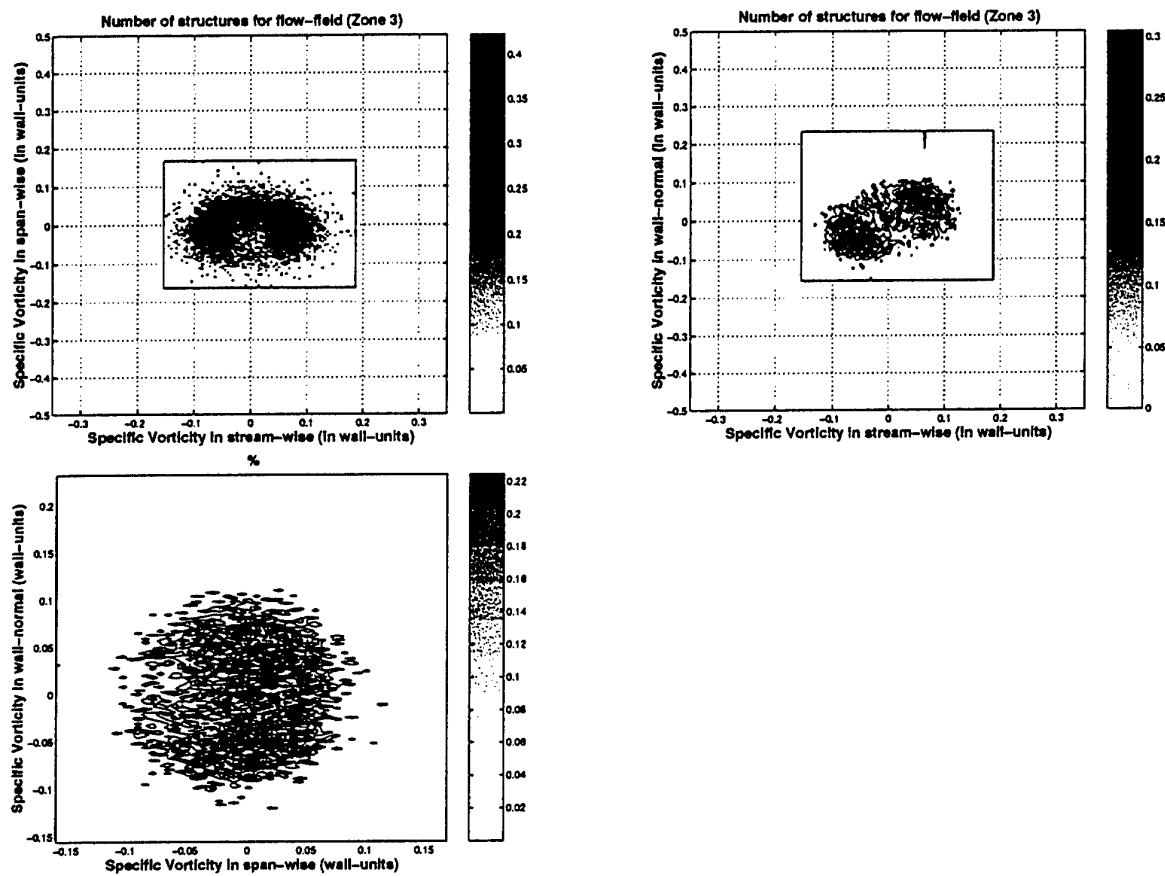


Fig. 6.42: Structures statistics lower half-channel: JPDF for structures vorticity, lower half channel. Zone 3, xy -top left, xz -top right and yz -bottom. $Re_\tau = 590$

7. CONCLUSIONS

A search and detection procedure has been developed, which allows to detect, define and classify all structures of organized vorticity/turbulence in 3D flow-fields, as well to extract the corresponding relevant statistics. The present code is compatible with all detection criteria proposed by the current literature (see § 4). Reliability and easiness to application lead to the choice of Q criterion for most present simulation and to recommend its application for future application.

It has to be remarked that present procedure has been developed and tested for LES application, but is compatible and is recommended for DNS.

Concerning the study of physics of coherent structures, present simulations of plane channel at equilibrium for 3 Reynolds numbers allow to conclude that, in all three cases, organized turbulence presents the same similar behavior and has comparable weight with respect to the overall turbulent field. Therefore, it can be suggested that structures here identified are typical for attached wall layers.

Application of present detection and identification algorithm allows to conclude that:

- The procedure proposed for the choice of trigger level yields consistent values for main physical parameters for organized turbulence and can, therefore, be applied as general rule to further investigations.
- Most of individual structures detected by the search algorithm have sizes smaller than the macro-scales of the flow, even if a minority of structures comparable or bigger than this scale can be found. It can be remarked that volume of structure, expressed in wall units, slightly increases with Re , and while the possibility that present wall-unit adimensionalization might not be the most suited one for present task has been addressed, at the moment it is sufficient to compare in a meaningful way different Reynolds.
- Close to the wall (Zone 1) structures are aligned along x axis; moving away from the wall, a turning motion in $x - y$ plane and away from $x - y$ plane is observed; typical inclination with respect $x - y$ plane was found to be in order of 20 degrees.

It is found that, refining the grid, global results for the entire population remain nearly constant, indicating that LES is adequate to recognize and assess the contribution of organized structures to turbulence; however, it is also found that, with increasing grid refinement, results indicated more and numerous and smaller structures, for similar volume occupied by the entire population; therefore it is suggested that complete definition of geometry and sizes of whole population would be possible only applying DNS resolution.

Bibliography

- AGARD (1998). A selection of test cases for the validation of large-eddy simulations of turbulent flows. Agard Advisory Report 345, North Atlantic Treaty Organization, 7 Rue Ancelle, 92200 Neuilly-Sur-Seine, France.
- Akselvoll, K. and Moin, P. (1995). Large eddy simulation of turbulent confined coannular jets and turbulent flow over a backward facing step. TF 63, Stanford University.
- Arakawa, A. (1966). Computational design for long-term numerical integration of the equations of fluid motion: Two-dimensional incompressible flow. part 1. J. Comp. Phys., 1:119.
- Baggett, J. S., Jimenez, J., and Kravchenko, A. G. (1997). Resolution requirements in large-eddy simulations of shear flows. Annual Research Briefs 51, Center for turbulence research, Stanford University.
- Balaras, E. (1995). Large Eddy Simulation of High Reynolds Number Wall Bounded Flows. PhD thesis, von Karman Institute for Fluid Dynamics.
- Bardina, J., Ferziger, J. H., and W.C, R. (1984). Improved turbulent models based on les of homogeneous incompressible turbulent flows. TF 19, Stanford University.
- Blackburn, H. M., Mansour, N. N., and Cantwell, B. J. (1996). Topology of fine-scale motions in turbulent channel flow. J. Fluid. Mech., 310:269.
- Brown, G. L. and Roshko, A. (1975). On density effects and large structures in turbulent mixing layer. J. Fluid. Mech., 64:775.
- Cabot, W., Jimenez, J., and Baggett, J. S. (1999). On wakes and near-wall behavior in coarse large-eddy simulation of channel flow with wall models and second-order finite-difference methods. Annual Research Briefs 343, Center for turbulence research, Stanford University.
- Cantwell, B. J. (1992). Exact solution of a restricted euler equation for the velocity gradient tensor. Phys. of Fluids, A 4(4):782.
- Chacin, J. M. and Cantwell, B. J. (2000). Dynamic of a low reynolds number turbulent boundary layer. J. Fluid. Mech., 404:87.
- Chong, M. S., Soria, J., Perry, A., Chacin, J., Cantwell, B. J., and Na, Y. (1998). Turbulent structures of wall-bounded shear flows found using dns data. J. Fluid. Mech., 357:225.
- Chorin, A. (1968). Numerical solution of the navier-stokes equations. J. Fluid. Mech., 22:742.
- Compte, P., Ducros, F., Silvestrini, J., David, E., Lamballais, E., Metais, O., and Lesieur, M. (1994). Simulation de grandes échelles d'écoulements transitionnels. In AGARD, editor, AGARD 74th FDP Symposium, AGARD SERIES.

- Compte, P. and Lesieur, M. (1998). Large-eddy simulations of compressible turbulent flows. VKI Lecture Series 5, von Karman Institute for Fluid Dynamics, Chaussée de Waterloo 72,B - 1640 Rhode Saint Genèse - Belgium.
- Domaradzki, A. and C., L. K. (1999). The subgrid-scale estimation model in the physical space representation. Phys. of Fluids, 11(8):2330.
- Domaradzki, A. and Saiki, E. M. (1997). A subgrid-scale model based on the estimation of unresolved scales of turbulence. Phys. of Fluids, 9(7):2148.
- Farge, M., Kevlahan, N., Perrier, V., and Goirand, E. (1996). Wavelets and turbulence. In IEEE 84, page 639.
- Ferziger, J. H. (1997). Physics and simulation of turbulence. VKI Lecture Series 3, von Karman Institute for Fluid Dynamics, Chaussée de Waterloo 72,B - 1640 Rhode Saint Genèse - Belgium.
- Ferziger, J. H. and Peric, M. (1997). Computational Methods for Fluid Dynamics. Springer.
- Germano, M. (1986). A proposal for a redefinition of the turbulent stresses in the filtered navier-stokes equations. Phys. of Fluids, 29(7):2323.
- Germano, M. (1992). Turbulence: The filtering approach. J. Fluid Mech., 238:325.
- Germano, M., Piomelli, U., Moin, P., and Cabot, W. H. (1991). A dynamic subgrid-scale eddy viscosity model. Phys. of Fluids, 3(7):1760.
- Ghosal, S. (1995). Analysis of discretization errors in les. Annual research briefs, Center for turbulence research, Stanford University.
- Ghosal, S. and Moin, P. (1995). The basic equations for the large eddy simulation of turbulent flows in complex geometry. J. Comp. Phys., 118:24.
- Giammanco, R. (2000). Identification of coherent structures in les flow field. Dc report, von Karman Institute for Fluid Dynamics.
- Giammanco, R., Simons, E., Manna, M., and Benocci, C. (2001). Large eddy simulation of turbulent flows over a cylinder of square cross section. In DNS-LES Workshop-IV. University of Twente, Kluwert.
- Härtel, C. and Kleiser, L. (1994). Subgrid-scale energy transfer in the near-wall region of turbulent flows. Phys. of Fluids, 6(9):313.
- Härtel, C. and Kleiser, L. (1998). Analysis and modeling of subgrid-scale motion in near-wall region of turbulence. J. Fluid. Mech., 356:327.

- Hirsh, C. (1990). Numerical computation of internal and external flows. Vol. 1 : Fundamentals of numerical discretization. Wiley.
- Hoffman, G. (1996). Engineering Application of Large Eddy Simulation to Turbulent Free and Wall-Bounded Flows. PhD thesis, von Karman Institute for Fluid Dynamics.
- Hunt, J. C. R., Way, A., and Moin, P. (1988). Eddies, stream, and convergence zones in turbulent flows. Center for Turbulence Research Report CTR-S88, Center for turbulence research, Stanford University.
- Hussain, F. (1983). Coherent structures-reality and myth. Phys. of Fluids, 26(10):2816-2847.
- Hussain, F. (1986). Coherent structures and turbulence. J. Fluid. Mech., 173:303-356.
- Hussain, F. and Hayakawa, M. (1987). Eduction of large scale organized structures in a turbulent plane wake. J. Fluid. Mech., 180:191.
- Jeong, J., Hussain, F., Schoppa, W., and Kim, J. (1997). Coherent structures near the wall. J. Fluid. Mech., 332:185.
- Kawamura, T., Takami, H., and Kuwahara, K. (1984). Lecture Notes in Physics, volume 218, chapter New higher upwind schemes for incompressible Navier-Stokes equations. Springer Verlag.
- Laskowski, G. M. (1999). Wall resolved large eddy simulation (les): a first step towards direct numerical simulation. DC Report VKI PR 1999-19, von Karman Institute for Fluid Dynamics.
- Lesieur, M. (1987). Turbulence in Fluids. Martinus Nijhoff Publishers.
- Louda, P. (2001). Investigation of self-similar subgrid models for les. DC Report VKI PR 2001-20, von Karman Institute for Fluid Dynamics.
- Lyn, D. A., Einav, S., Rodi, W., and Park, J. H. (1995). A laser-doppler velocimetry study of ensemble-averaged characteristics of the turbulent near wake of square cylinder. J. Fluid. Mech., 304:285.
- Meneveau, C. and Katz, J. (2000). A laser-doppler velocimetry study of ensemble-averaged characteristics of the turbulent near wake of square cylinder. Annu. Rev. Fluid. Mech., 32:1.
- Moin, P. and Mahesh, K. (1998). Direct numerical simulation: A tool in turbulence research. Annu. Rev. Fluid. Mech., 32:539.
- Piomelli, U. (1997). Large-eddy and direct simulation of turbulent flows. VKI Lecture Series 3, von Karman Institute for Fluid Dynamics, Chaussée de Waterloo 72,B - 1640 Rhode Saint Genèse - Belgium.

- Ramnaud, P. (2000). Contribution à l'étude du comportement de particules solides en écoulements turbulent confiné par simulation numérique directe. PhD thesis, von Karman Institute for Fluid Dynamics.
- Ramnaud, P. (2001). Vki private communication. DNS CHANNEL.
- Robinson, S. K., Kline, S. J., and Spalart, P. R. (1990). Near-Wall Turbulence, chapter Quasi-coherent structures in the turbulent boundary layer: Part II. Verification and new information from a numerically simulated flat-plate layer, page 218. Hemisphere Publishing Corp.
- Rodi, W., Ferziger, J., Breuer, M., and Pourquié, M. (1997). Status of large eddy simulation: Results of a workshop. J. Fluids Eng., 119:248.
- Scarano, F., Benocci, C., and Riethmuller, M. (1999). Pattern recognition analysis of turbulent flow past a backward facing step. Phys. of Fluids, 11(12):3808.
- Schmidt, H., Schumann, U., and Volkert, H. (1984). Three-dimensional, direct and vectorized elliptic solvers for various boundary conditions. Mitteilung DFVLR-Mitt. 84-15, DFVLR Institut für Physik der Atmosphäre, Oberpfaffenhofen.
- Shah, K. B. and Ferziger, J. H. (1995). A new non-eddy viscosity subgrid-scale model and its application to channel flow. Annual Research Briefs 73, Center for turbulence research, Stanford University.
- Simons, E. (2000). An efficient multi-domain approach to large-eddy simulation of incompressible turbulent flows in complex geometries. PhD thesis, von Karman Institute for Fluid Dynamics.
- Simons, E., Manna, M., and C., B. (2001). Parallel multi-domain large-eddy simulation of the flow over a backward-facing step at $re=5100$. In EUROMECH COLLOQUIUM 412. Kluwer Academic Publishers.
- Smagorinsky, J. (1963). General circulation experiments with the primitive equations, i) the basic experiments. Monthly Weather Review, 91:99.
- Spalart, P. (1988). Direct simulation of turbulent boundary layer up to $re_\theta = 1410$. J. Fluid. Mech., 187.
- Tennekes, H. and Lumley, J. L. (1983). A First Course in Turbulence. MIT Press, Cambridge, MA.
- Verstappen, R. W. C. P. and Veldman, A. E. P. (1997). Direct numerical simulation of turbulence at lower costs. J. Engineering Mathematics, 32:143.

APPENDIX

A. $Re_\tau = 180$ -CASE II

This appendix presents plots and information thought not necessary for the main analysis in § 5.2.

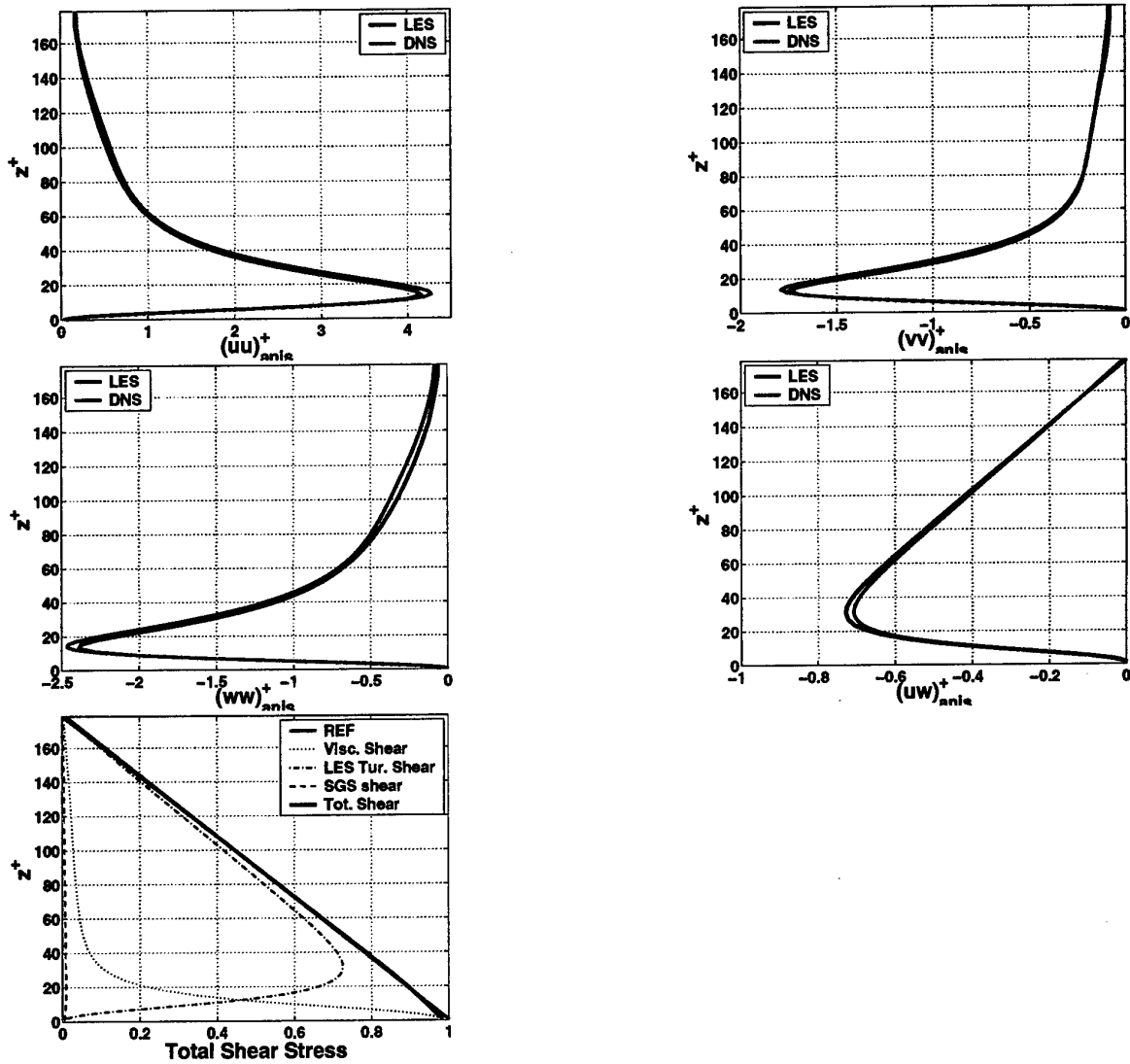


Fig. A.1: Anisotropic part of the resolved Reynolds stress tensor of plane channel at $Re_\tau = 180$ (Case II: refined grid) and total shear stress

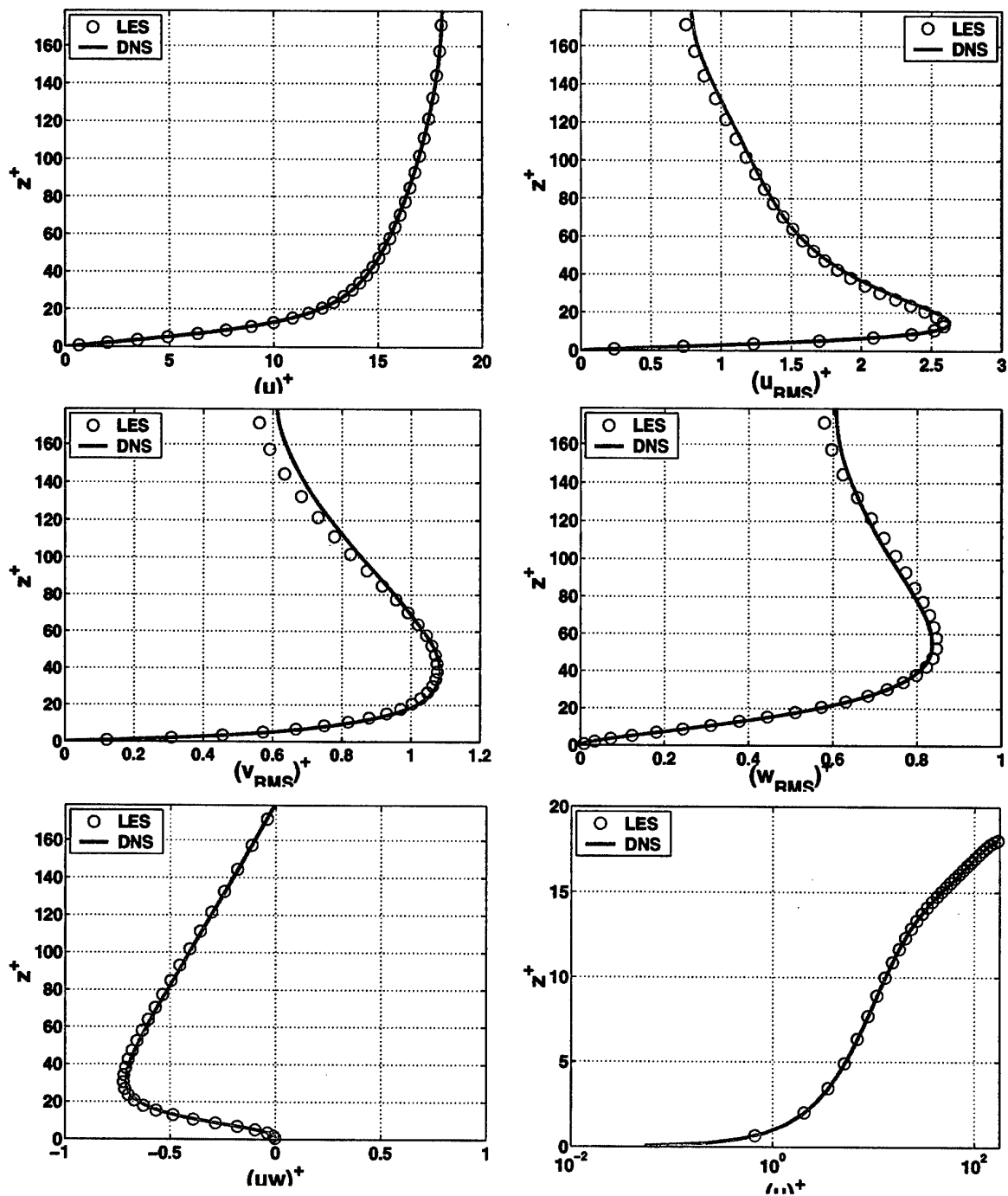


Fig. A.2: Mean stream-wise velocity and rms of resolved turbulence of plane channel at $Re_\tau = 180$ (Case II: refined grid)

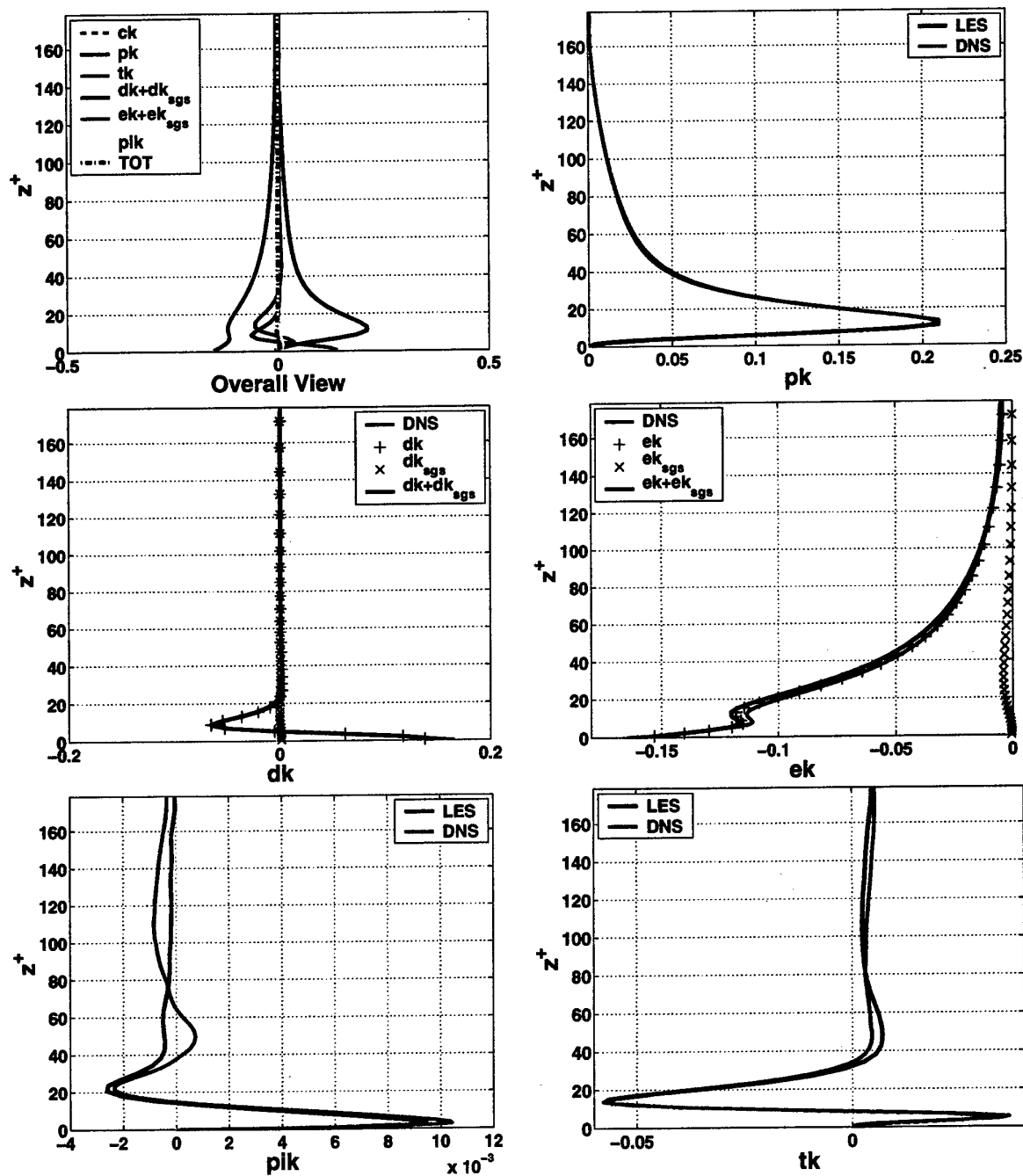


Fig. A.3: Budget of resolved turbulent kinetic energy of plane channel at $Re_\tau = 180$ (Case II: refined grid)

B. $Re_\tau = 180$ -CASE IV

This appendix presents plots and information thought not necessary for the main analysis in § 5.4.

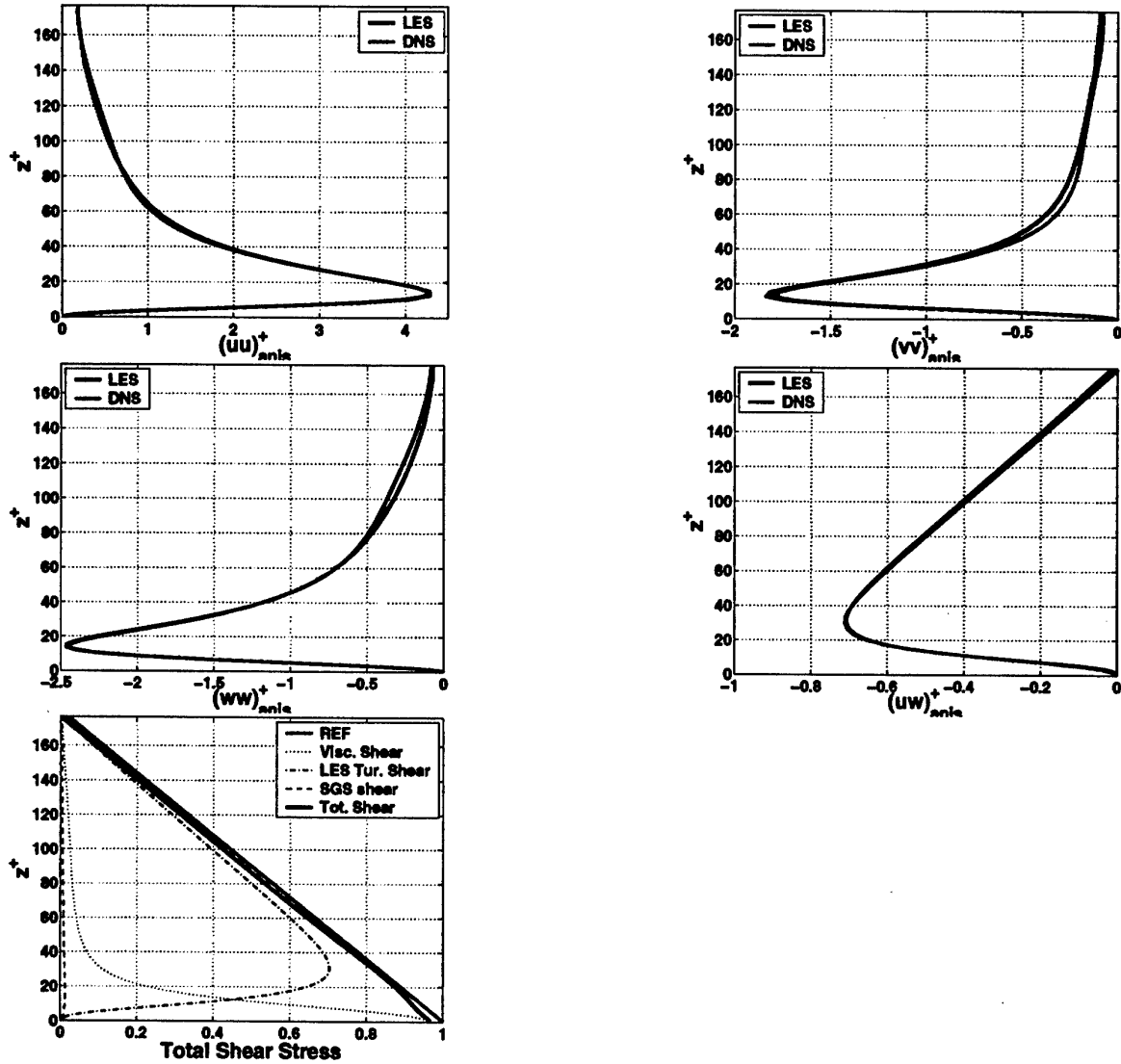


Fig. B.1: Anisotropic part of the resolved Reynolds stress tensor of plane channel at $Re_\tau = 180$ (Case IV: 4th order) and total shear stress

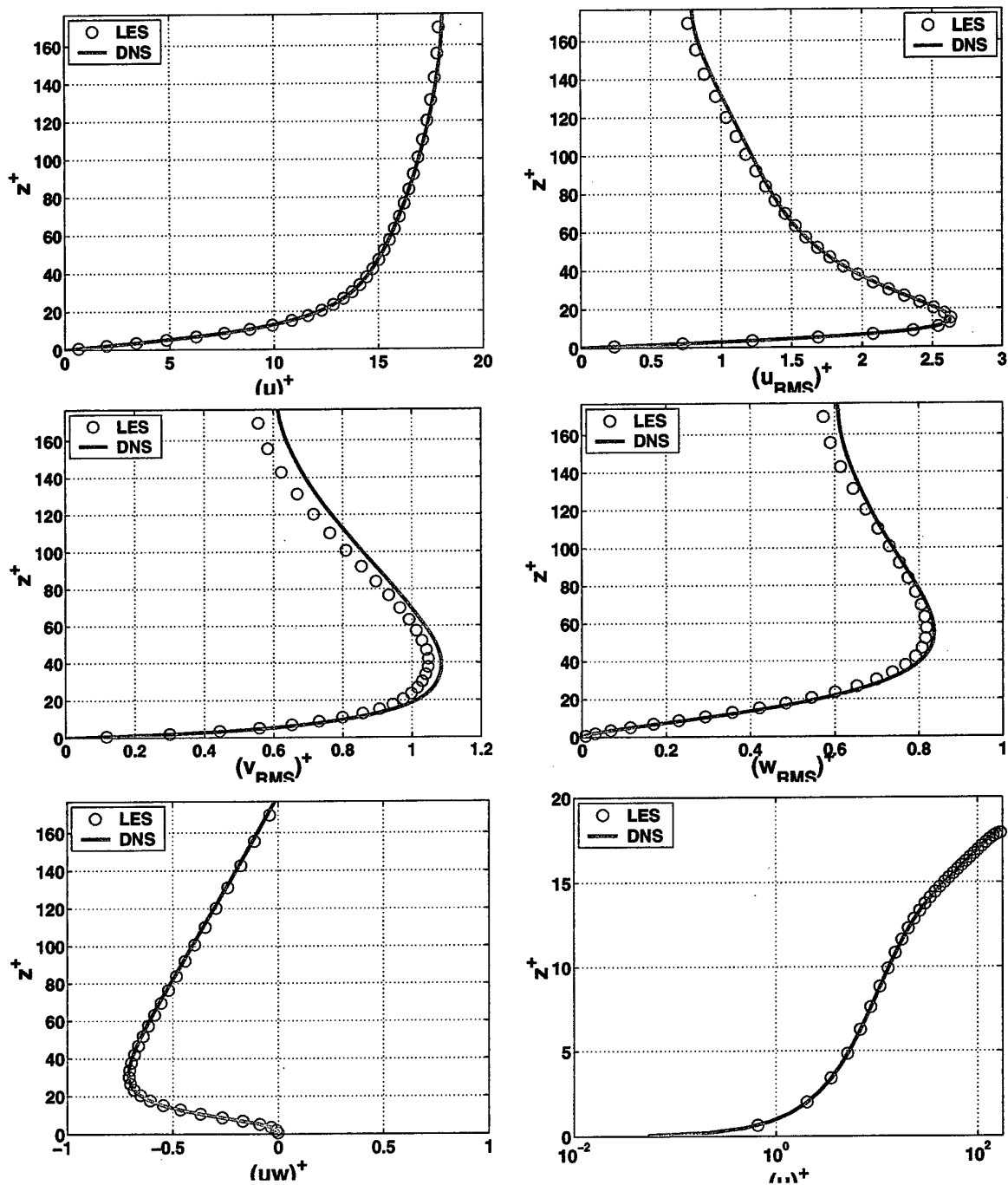


Fig. B.2: Mean stream-wise velocity and rms of resolved turbulence of plane channel at $Re_\tau = 180$ (Case IV: 4th order)

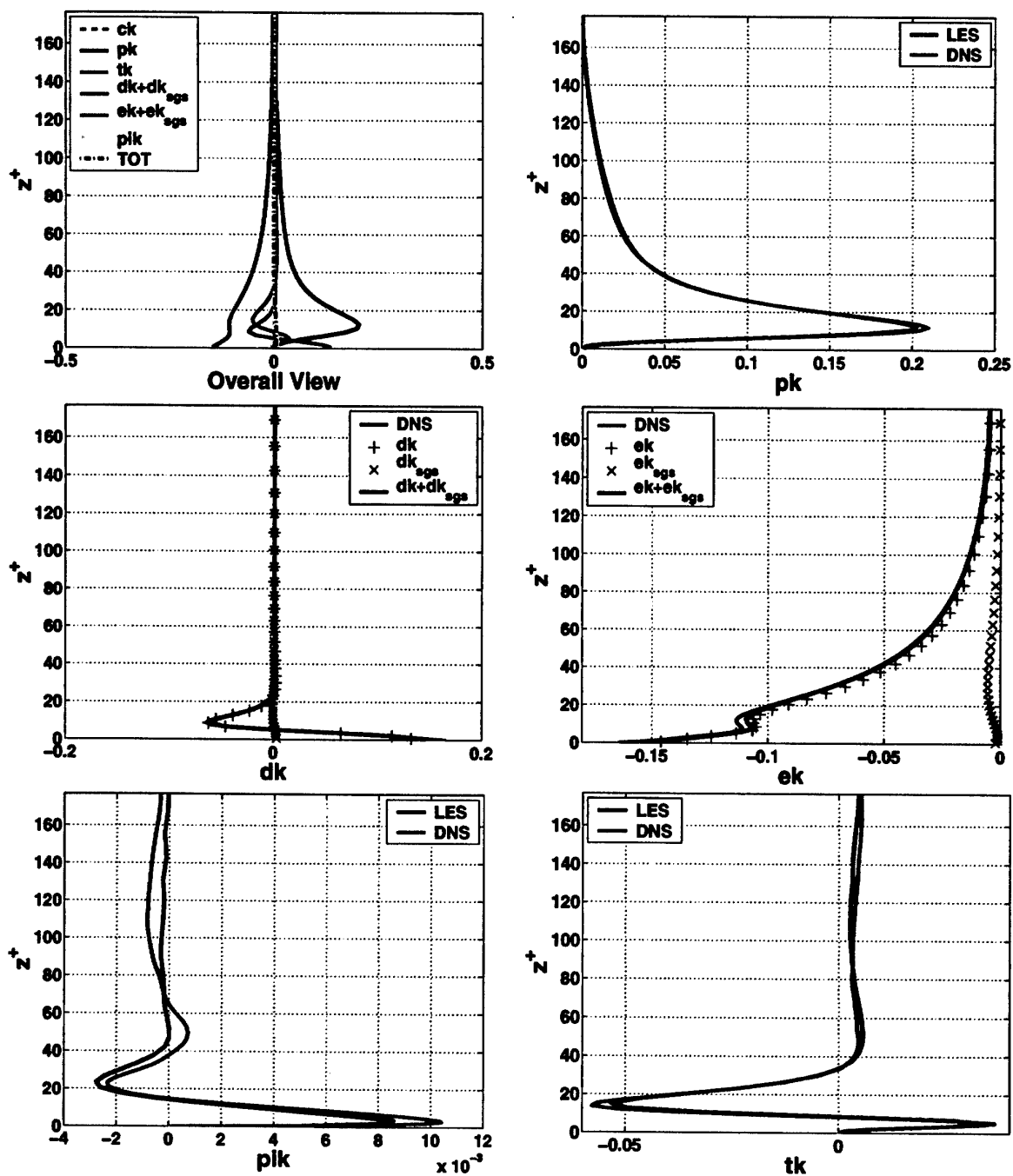


Fig. B.3: Budget of resolved turbulent kinetic energy of plane channel at $Re_\tau = 180$ (Case IV: 4th order)

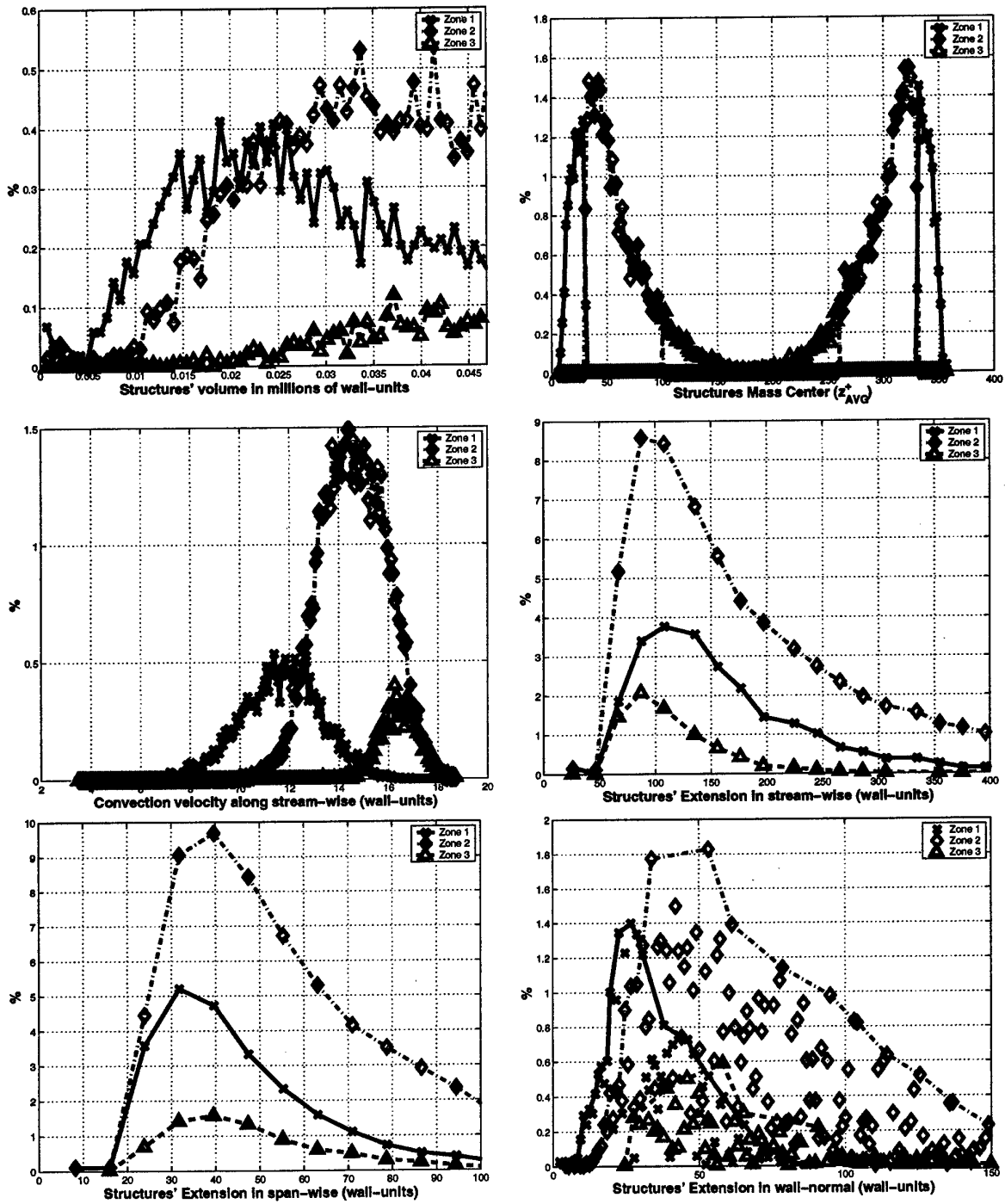


Fig. B.4: $Re_\tau = 180$ (Case IV: 4th order), various plots

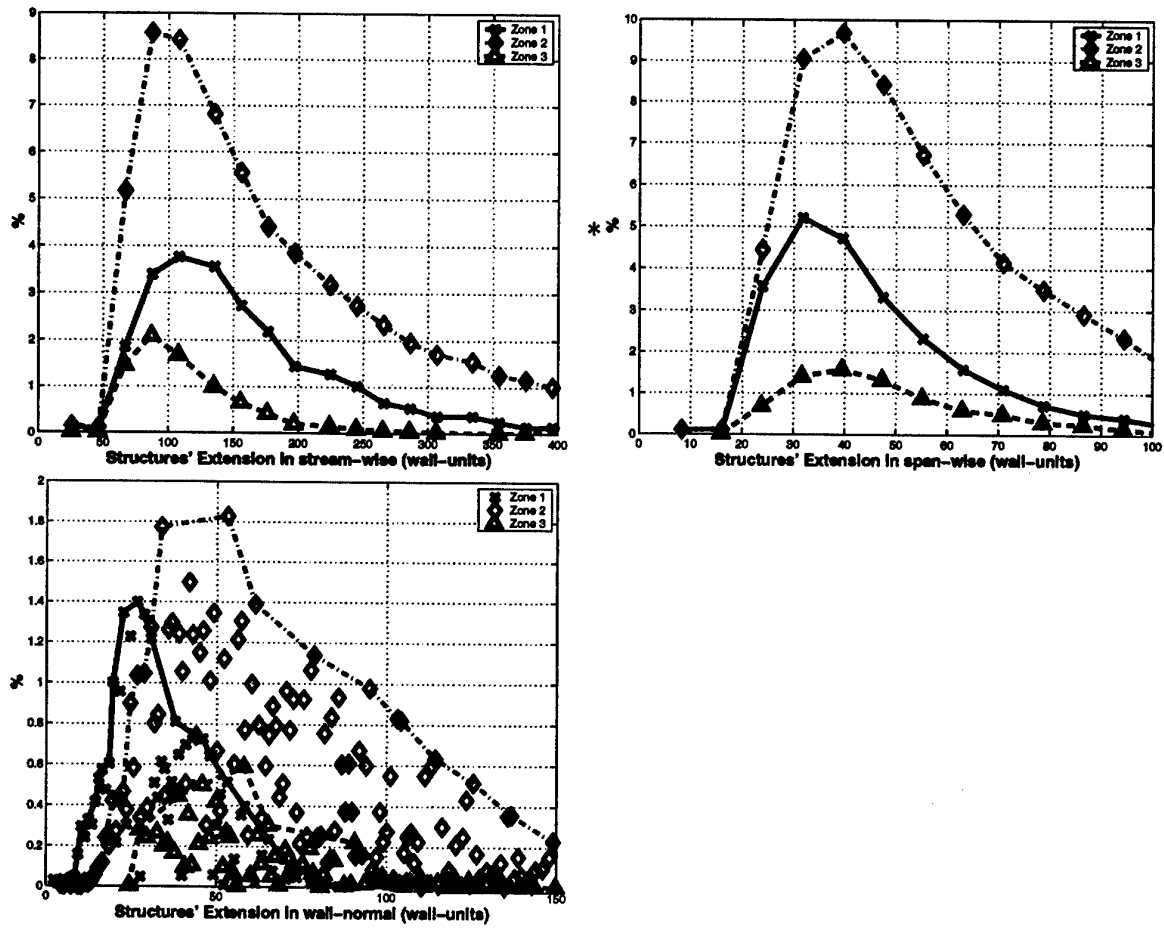


Fig. B.5: Structures statistics at $Re_\tau = 180$ (Case IV: 4th order): length in wall units.

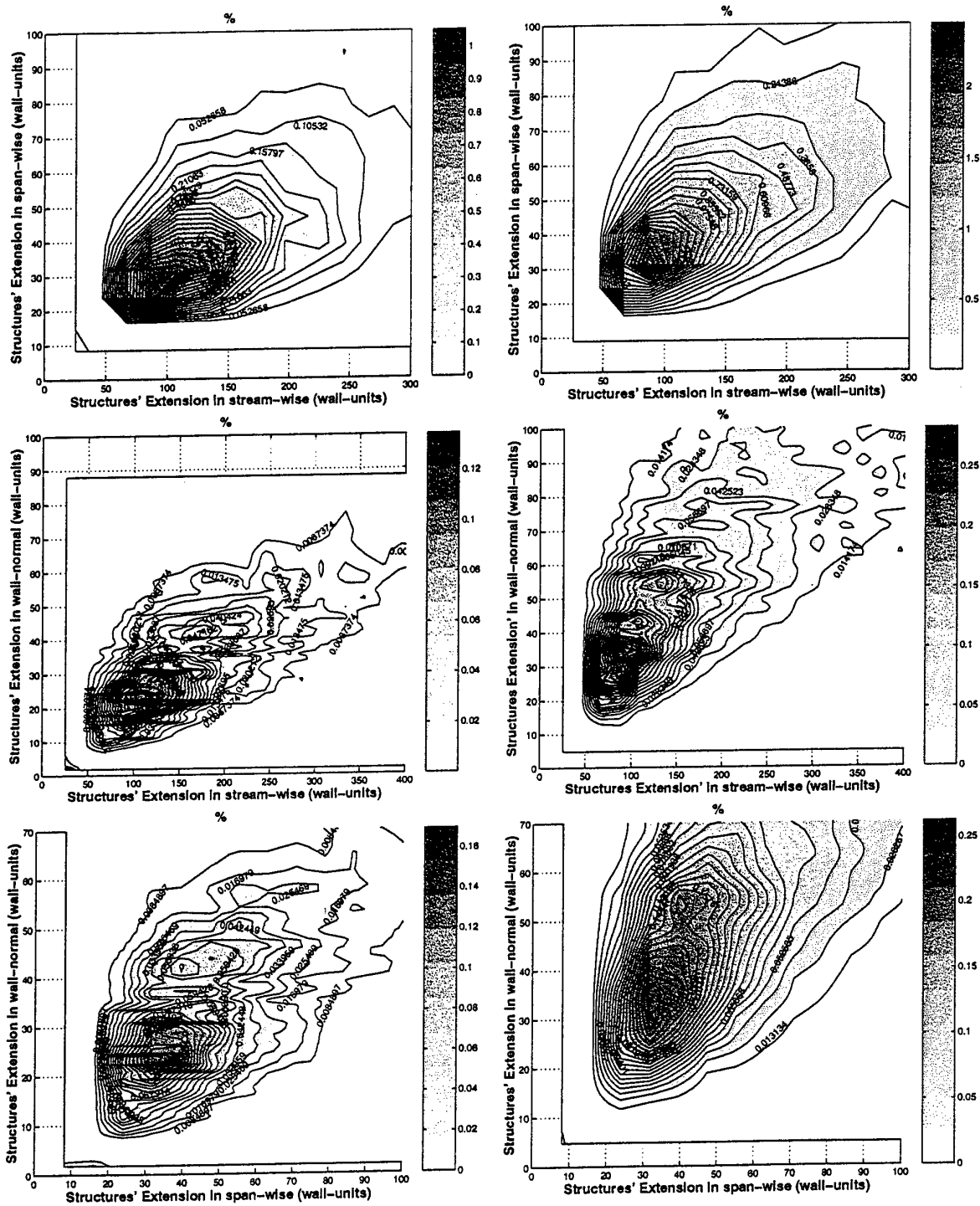


Fig. B.6: Structures statistics: JPDF for structures extension. $Re_\tau = 180$ (Case IV: 4th order). Left column zone 1, right column zone 2, xy -top, xz -middle and yz -bottom.

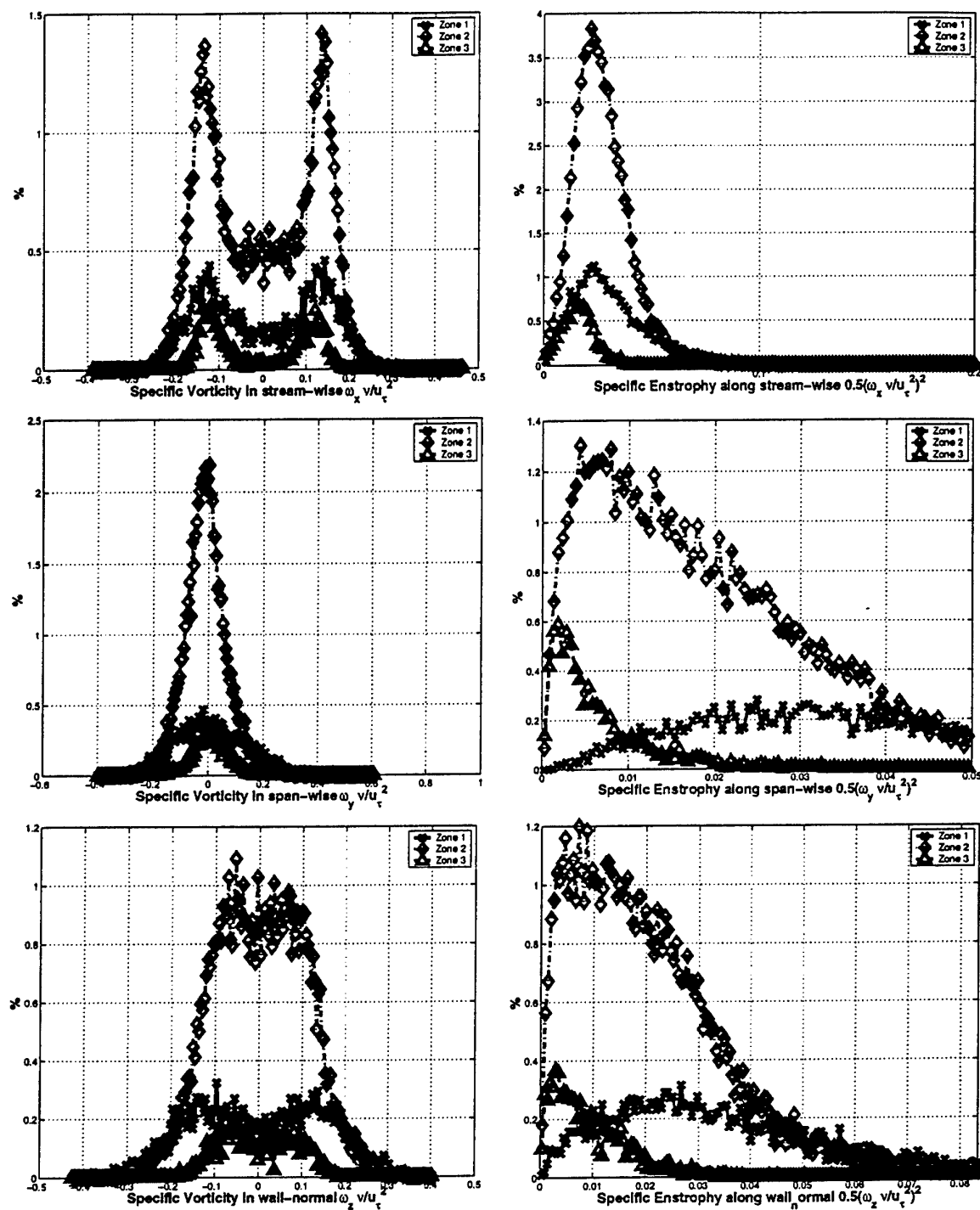


Fig. B.7: Structure statistics: Specific Vorticity (left) and enstrophy(right) for x (top), y (middle) and z (bottom). $Re_\tau = 180$ (Case IV: 4th order).

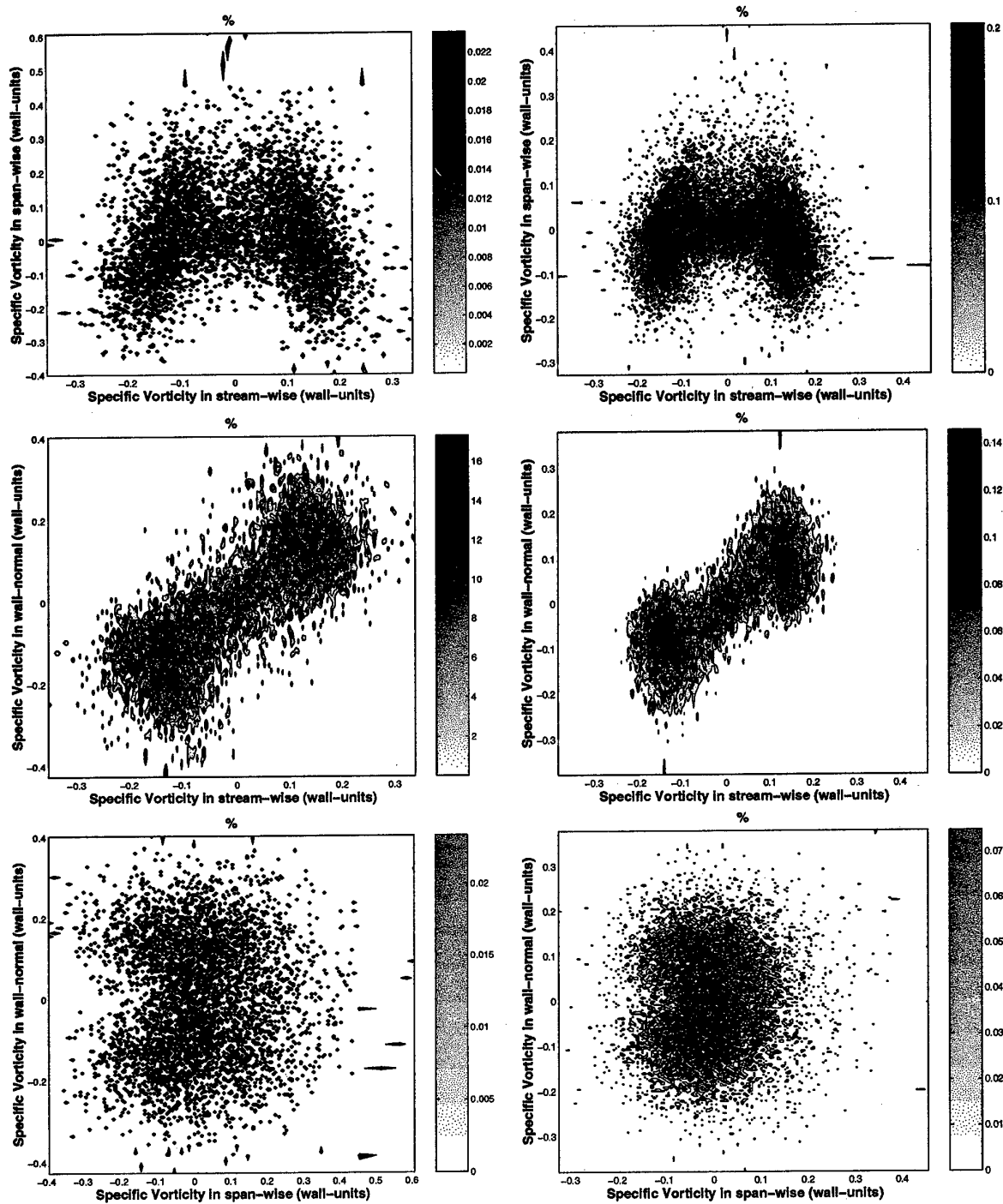


Fig. B.8: Structures statistics, lower half-channel: JPDF for structures vorticity. Left zone 1, right zone 2, xy -top, xz -middle and yz -bottom. $Re_\tau = 180$ (Case IV: 4th order)

C. $Re_\tau = 180$ -CASE IV-B

This appendix presents plots and information thought not necessary for the main analysis in § 5.4.

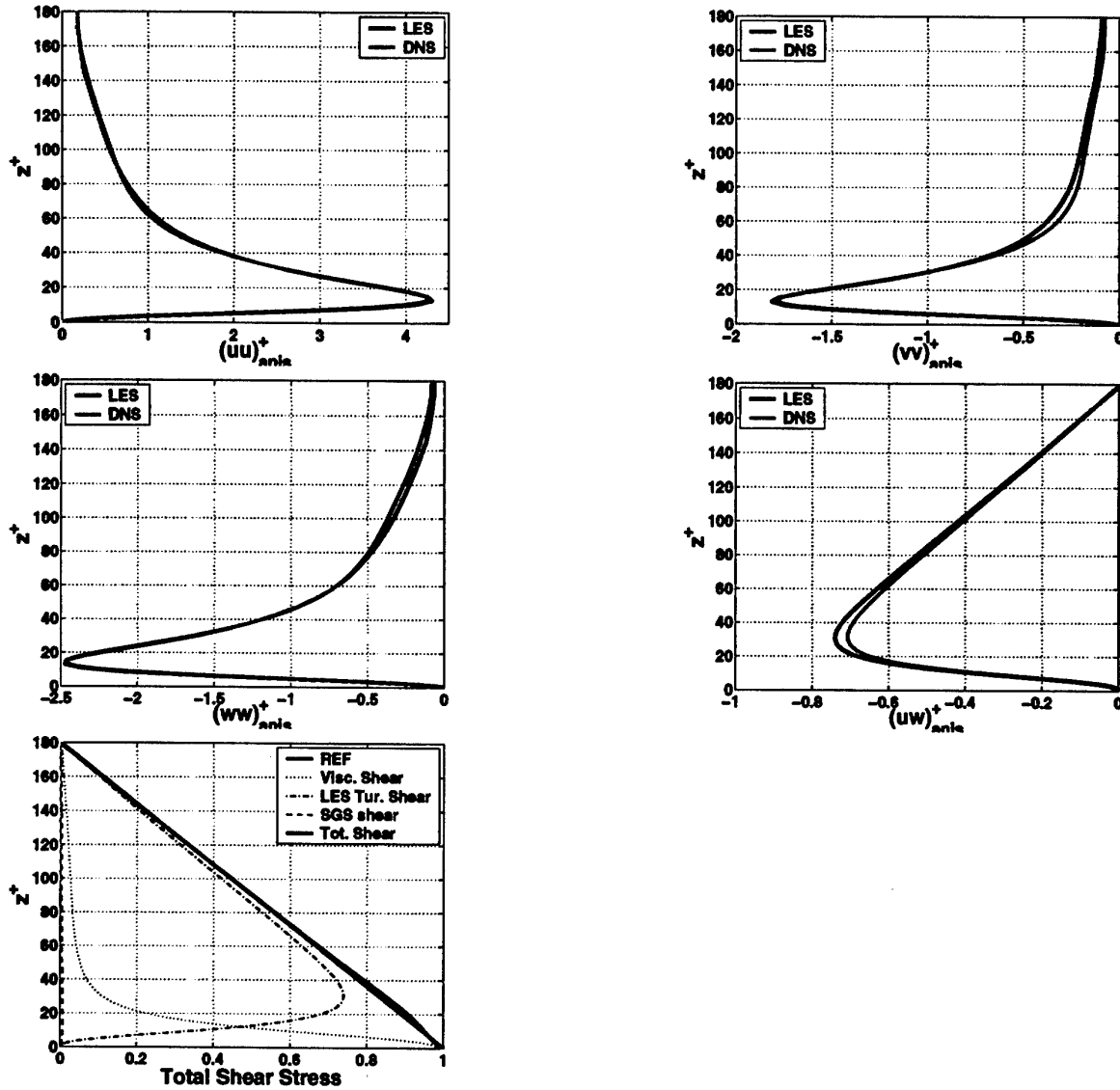


Fig. C.1: Anisotropic part of the resolved Reynolds stress tensor of plane channel at $Re_\tau = 180$ (Case IV-B: 4th order, $C_{ss} = 0.065$) and total shear stress

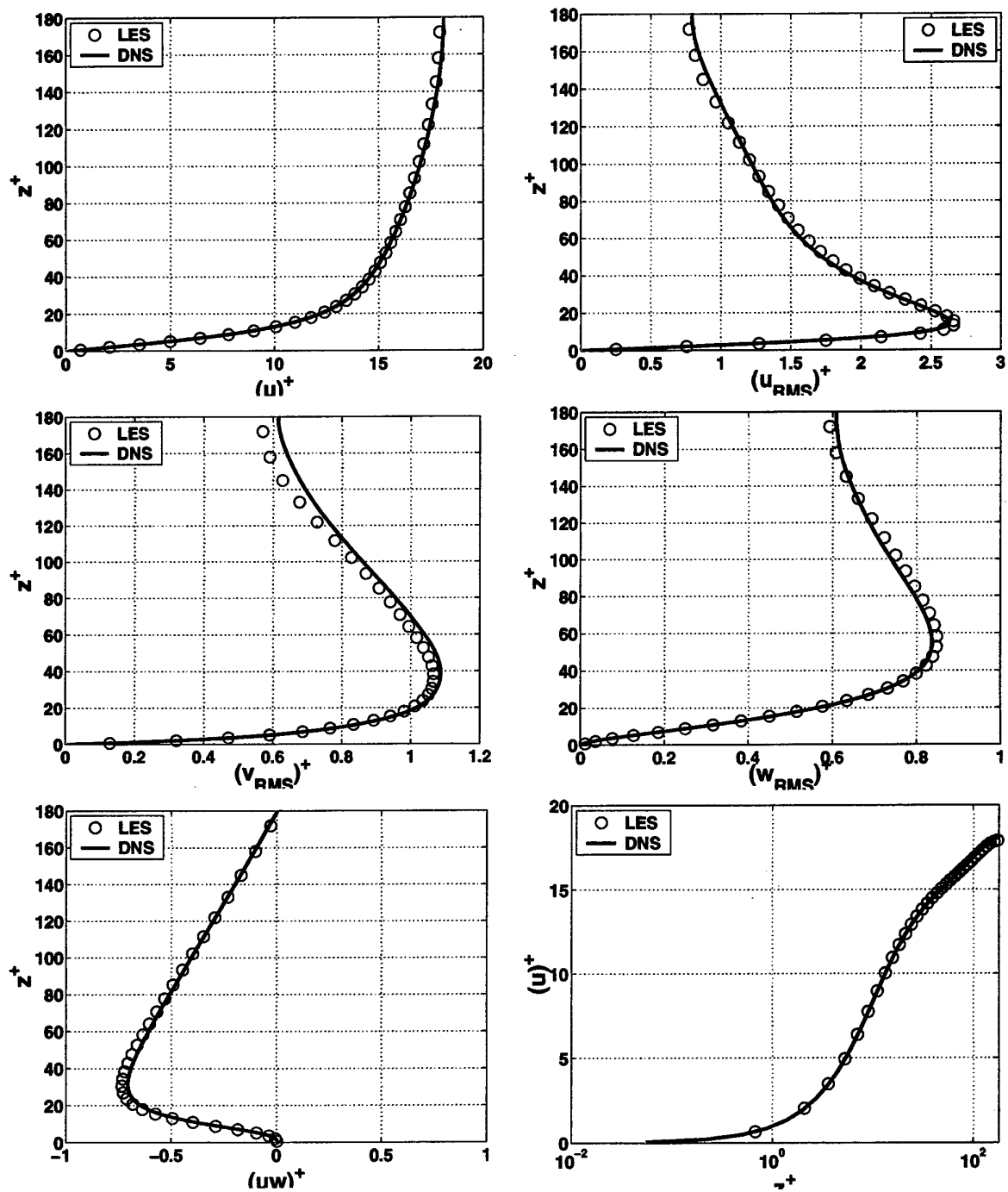


Fig. C.2: Mean stream-wise velocity and rms of resolved turbulence of plane channel at $Re_\tau = 180$ (Case IV-B: 4th order, $C_{ss} = 0.065$)

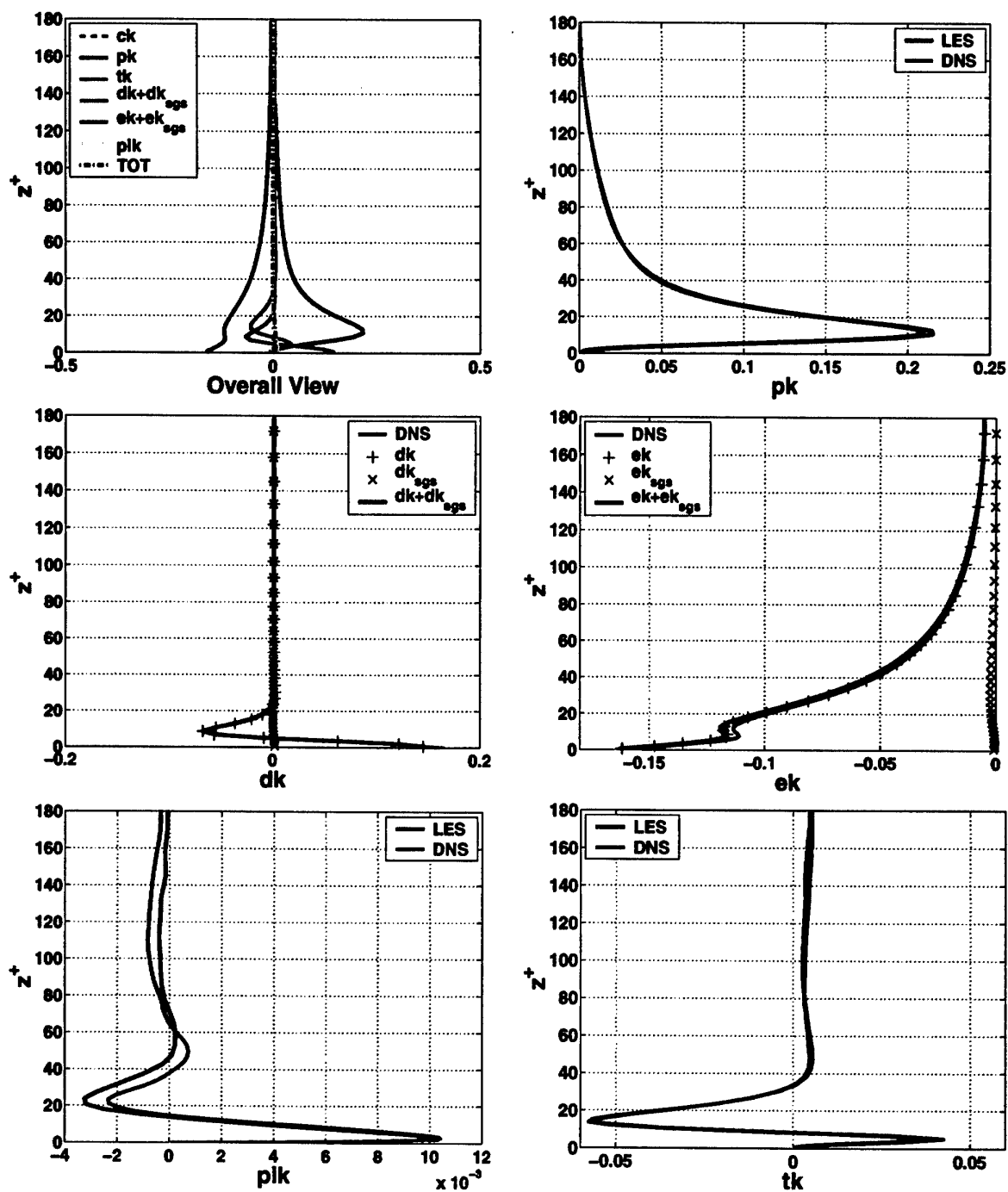


Fig. C.3: Budget of resolved turbulent kinetic energy of plane channel at $Re_\tau = 180$ (Case IV-B: 4th order, $C_{ss} = 0.065$)

D. $Re_\tau = 180$ -CASE V-A

This appendix presents plots and information about the FSF SGS model thought not necessary for the main analysis in § 5.5.

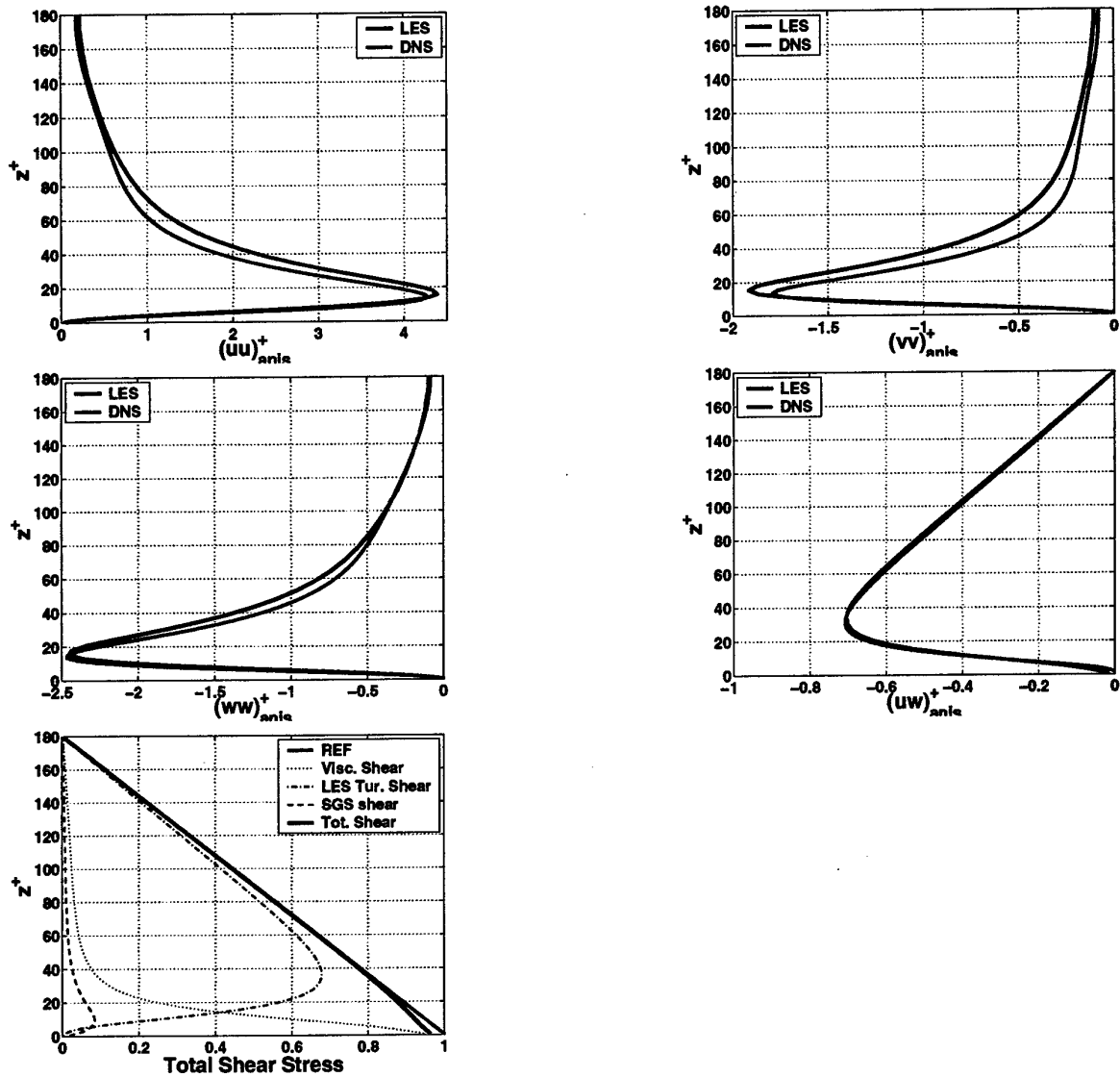


Fig. D.1: Anisotropic part of the resolved Reynolds stress tensor of plane channel at $Re_\tau = 180$ (Case V-A: FSF) and total shear stress

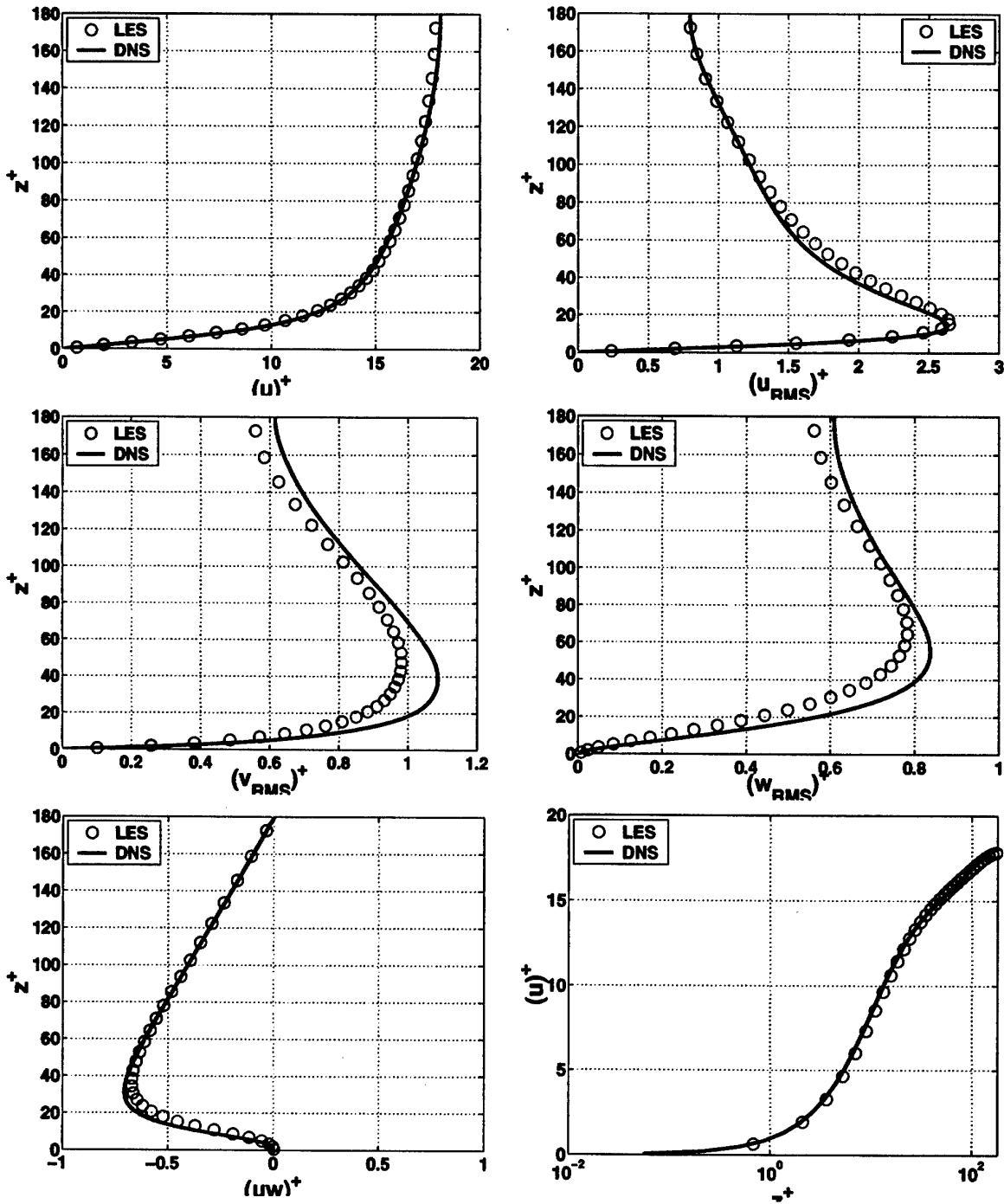


Fig. D.2: Mean stream-wise velocity and rms of resolved turbulence of plane channel at $Re_\tau = 180$ (Case V-A: FSF)

E. $Re_\tau = 180$ -CASE V-B

This appendix presents plots and information about the absence of SGS model thought not necessary for the main analysis in § 5.5.

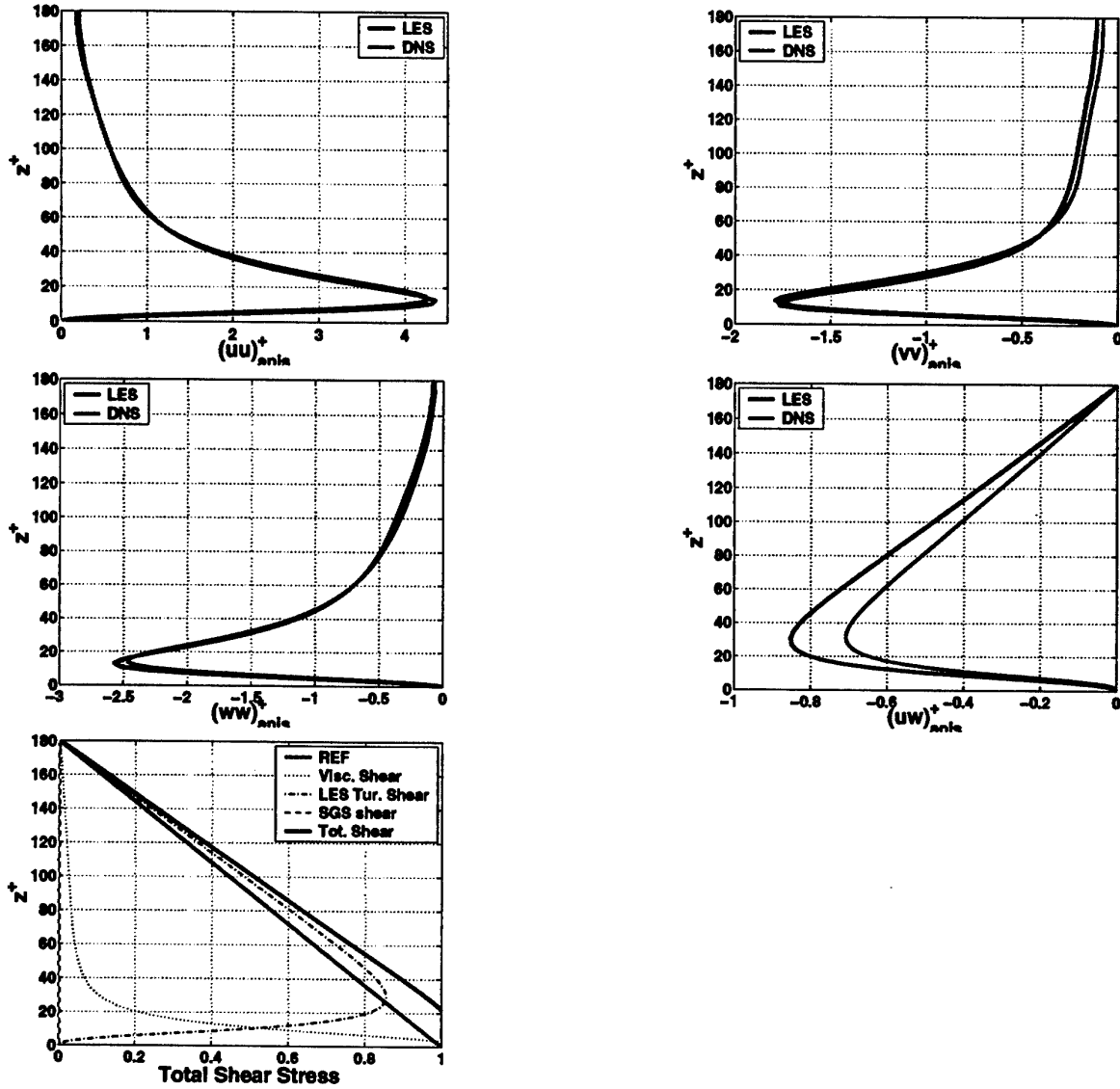


Fig. E.1: Anisotropic part of the resolved Reynolds stress tensor of plane channel at $Re_\tau = 180$ (Case V-A: NO) and total shear stress

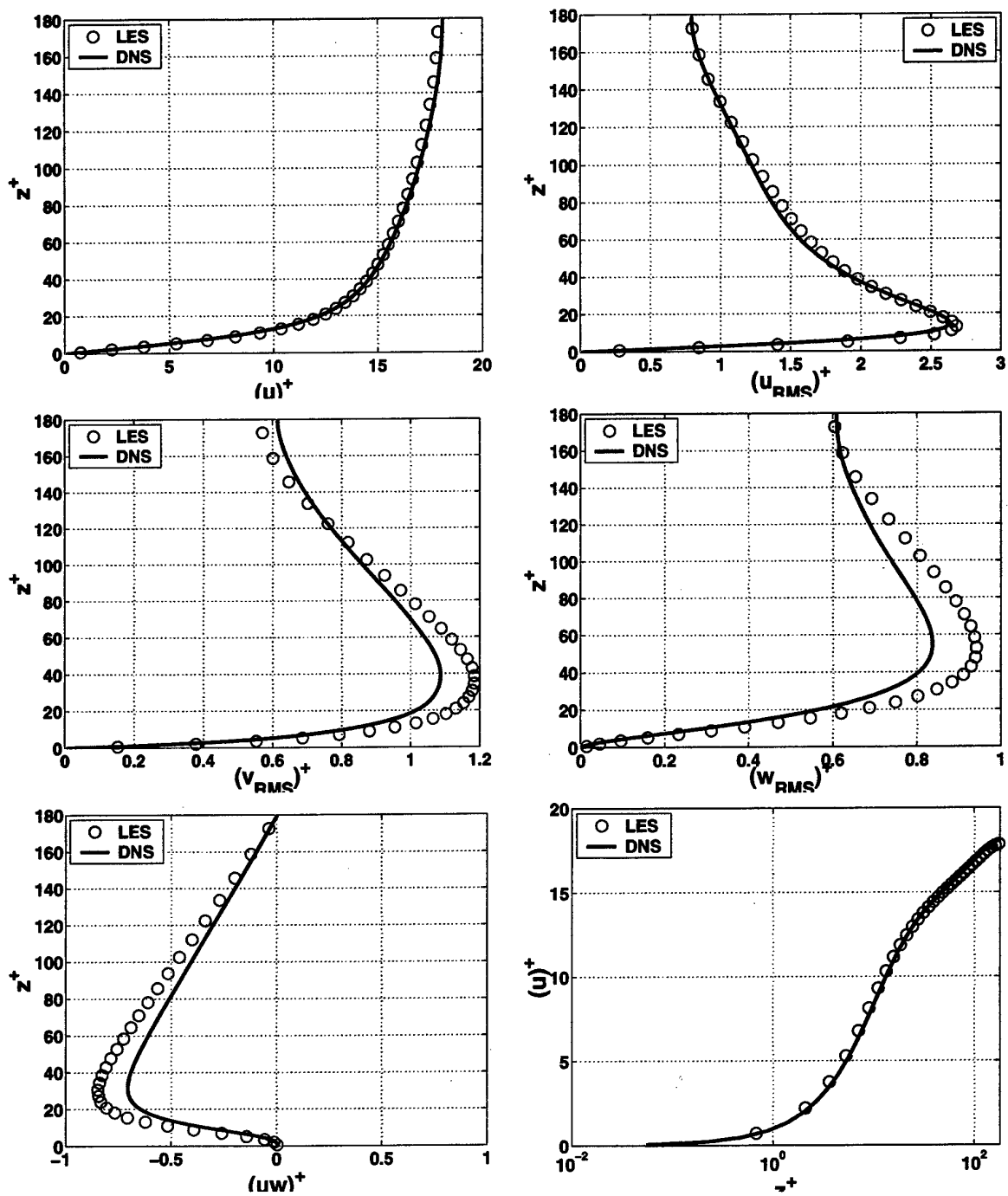


Fig. E.2: Mean stream-wise velocity and rms of resolved turbulence of plane channel at $Re_\tau = 180$ (Case V-A: NO)

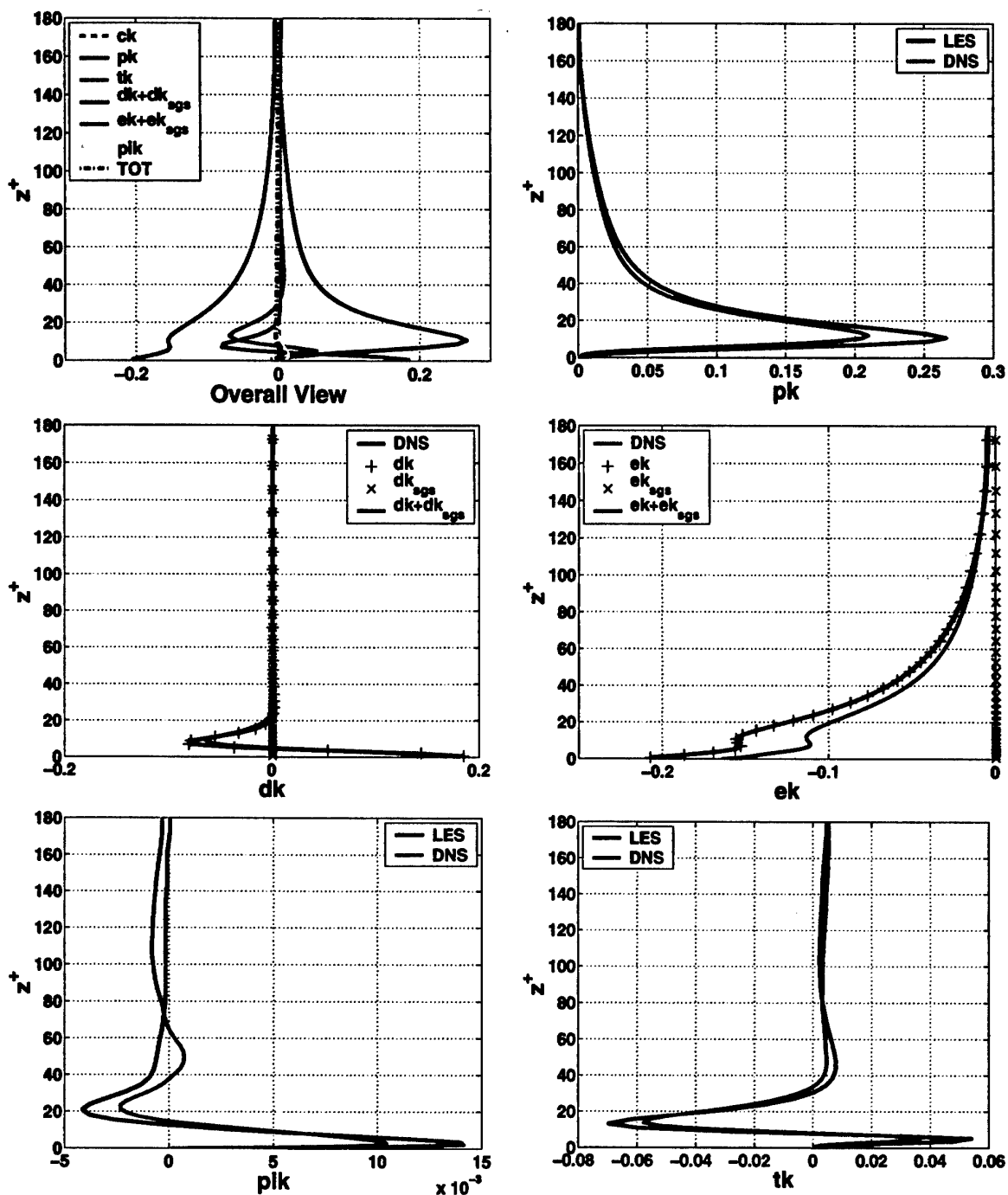


Fig. E.3: Budget of resolved turbulent kinetic energy of plane channel at $Re_\tau = 180$ (Case V-A: NO)

F. $Re_\tau = 180$ -CASE V-C

This appendix presents plots and information about the SS model thought not necessary for the main analysis in § 5.5; here the usual TKE budget is not presented since the self similar model requires a different derivation that has not been validated.

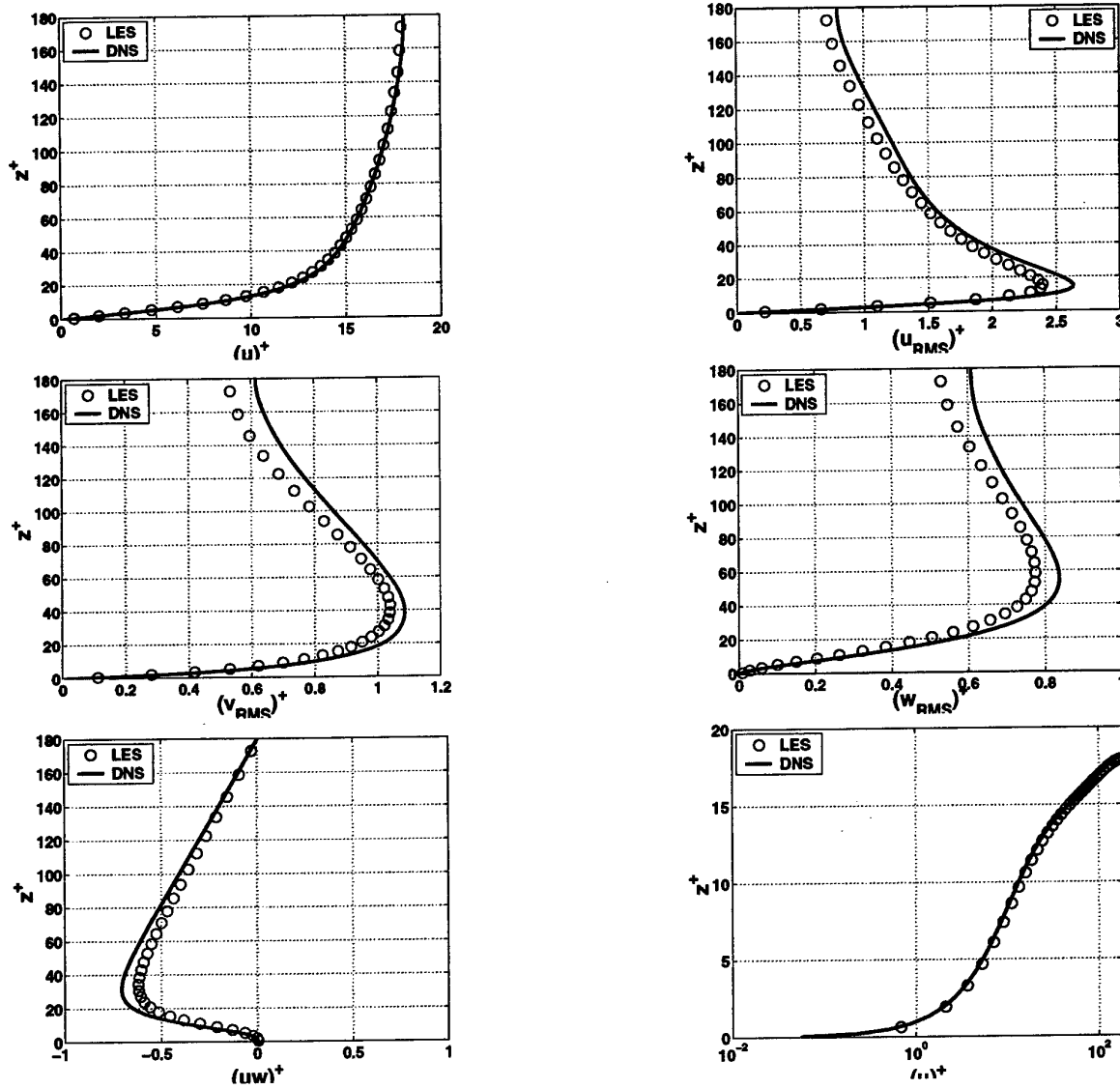


Fig. F.1: Mean stream-wise velocity and rms of resolved turbulence of plane channel at $Re_\tau = 180$ (Case V-A: NO)

G. $RE_\tau = 180$ -CASE V

This appendix presents plots and informations are relative to the comparison between the simulation discussed in § 5.5, between SMA, FSF, SS and NO-SGS models.

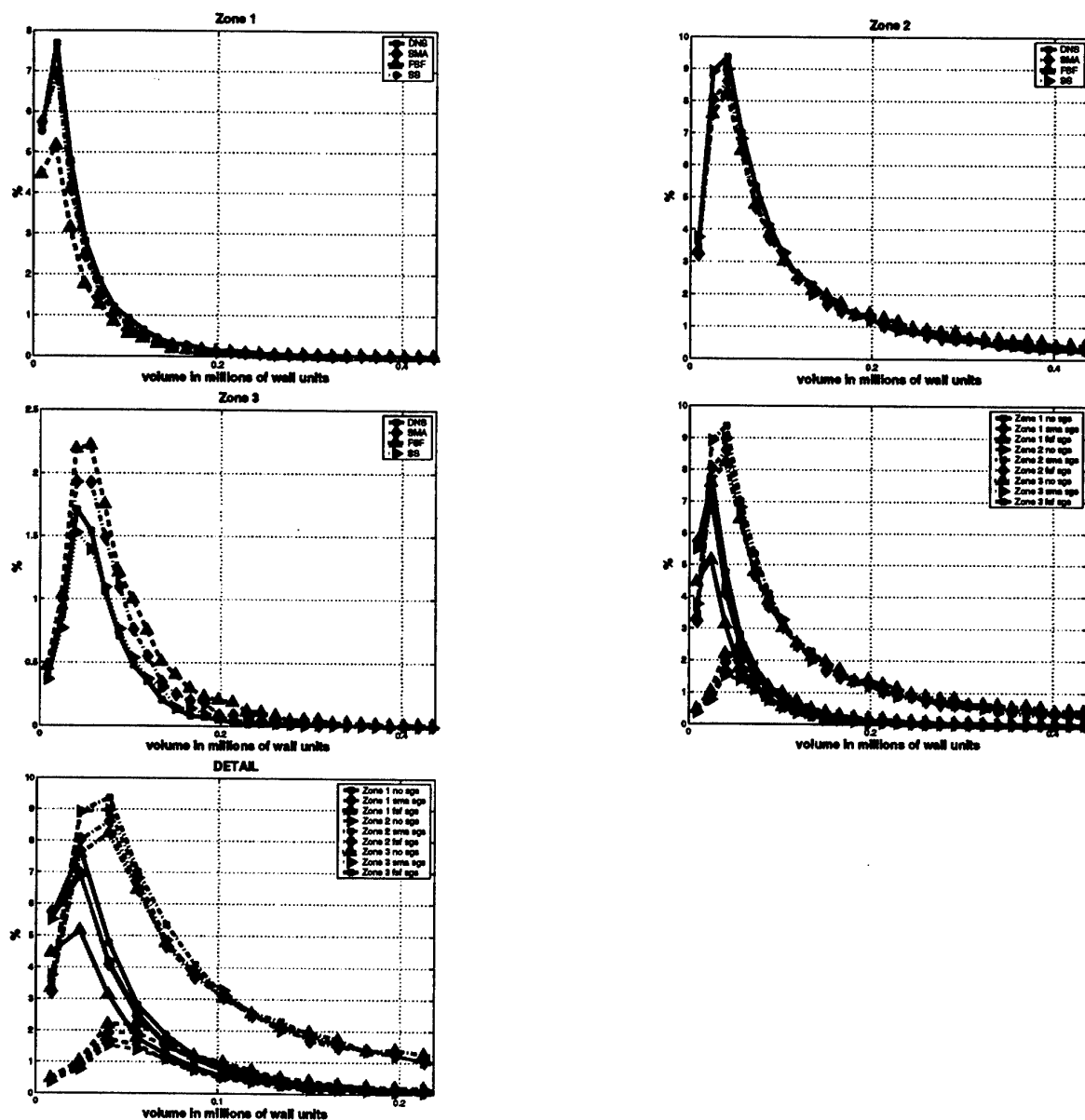


Fig. G.1: Volume comparison between SGS models

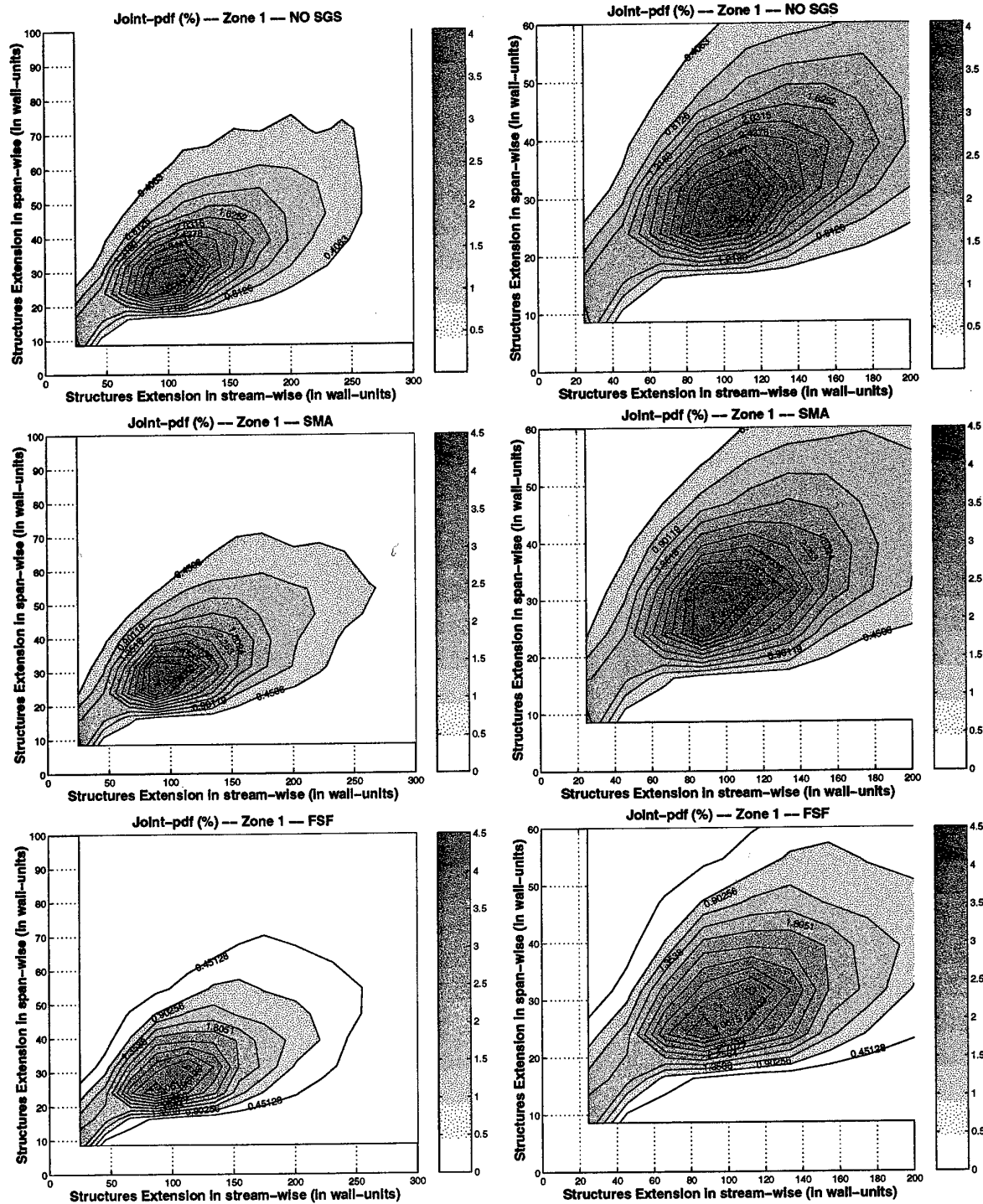


Fig. G.2: JPF for structure extensions between SGS models: Zone 1, $L_x - L_y$ -I-

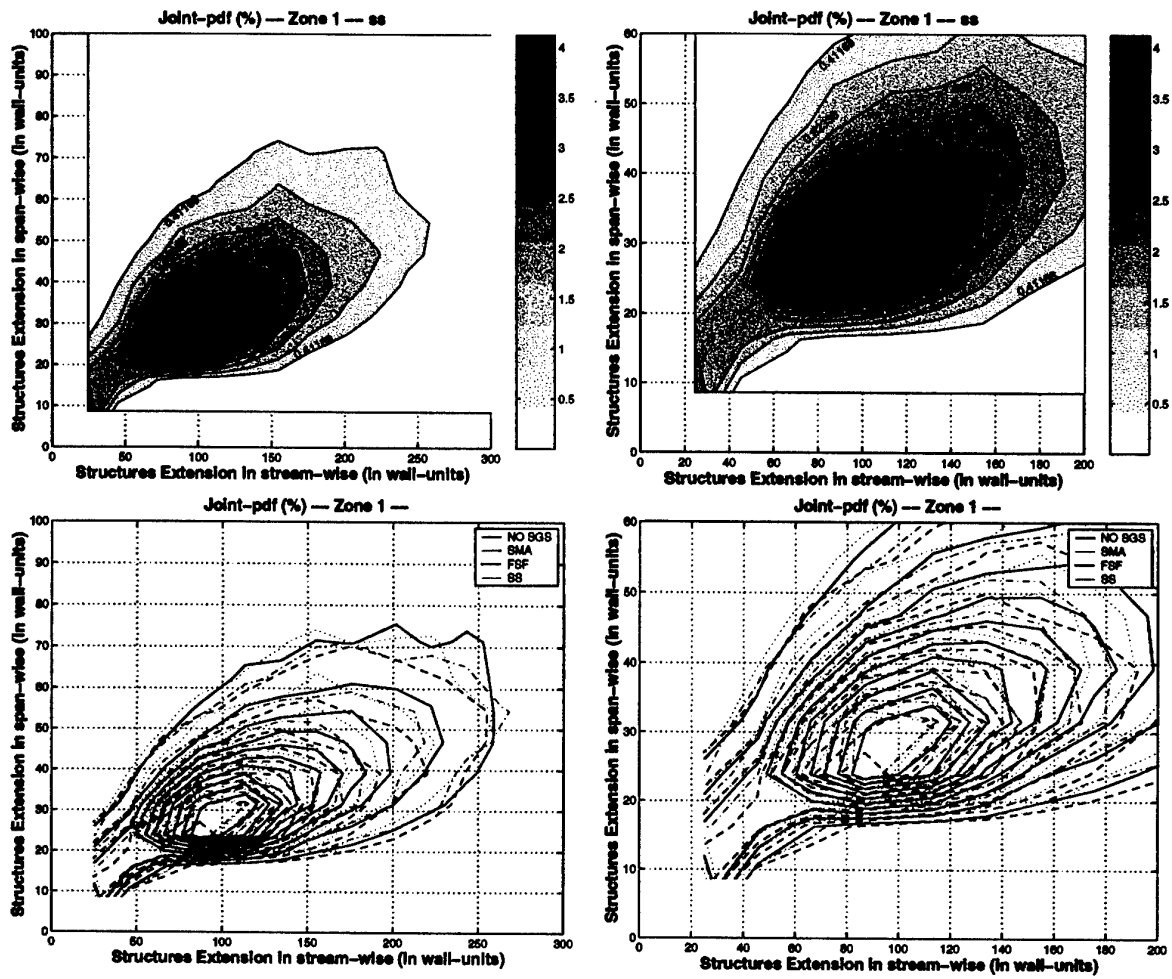


Fig. G.3: JPF for structure extensions between SGS models: Zone 1, $L_x - L_y$ -II-

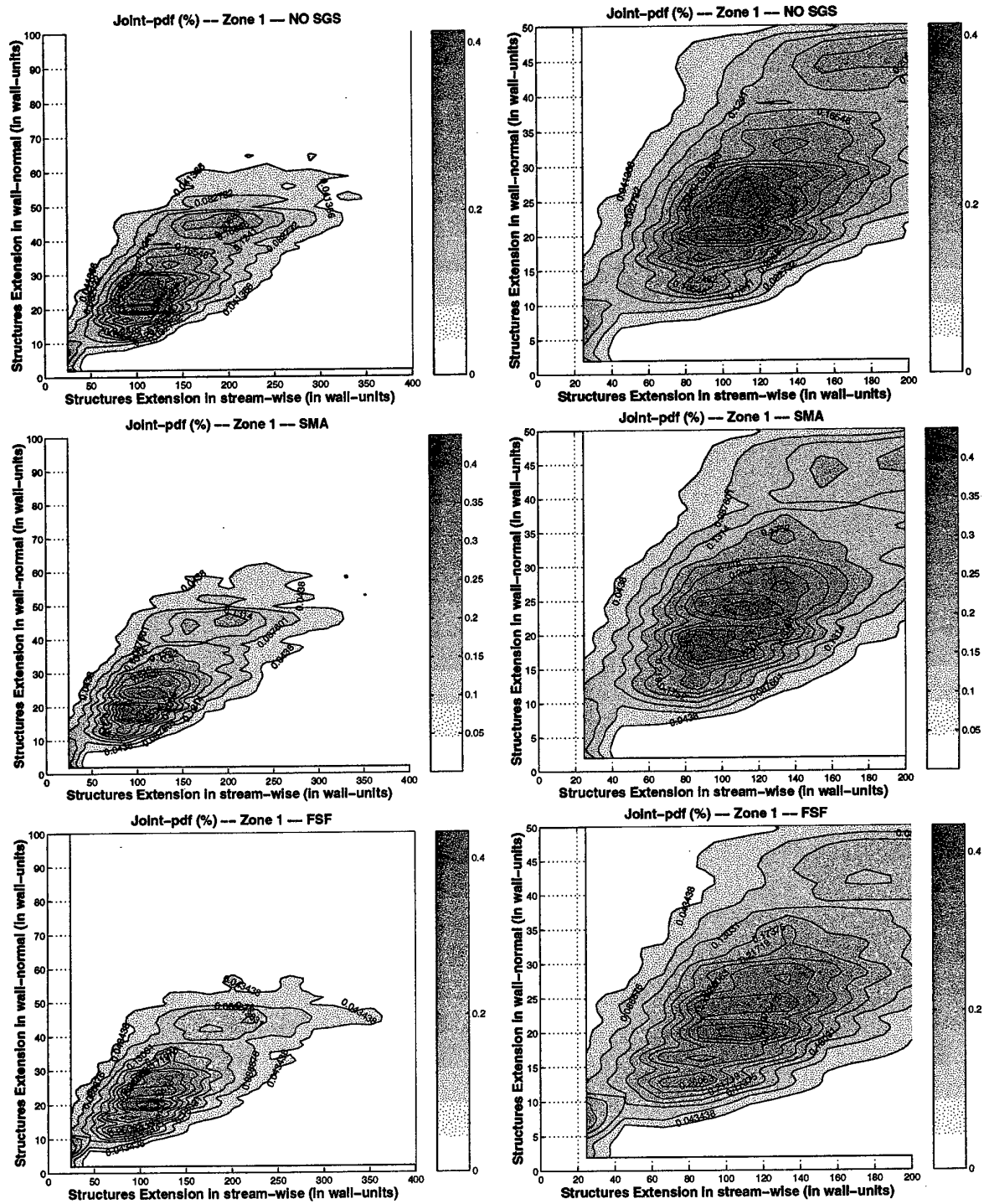


Fig. G.4: JPF for structure extensions between SGS models: Zone 1, $L_x - L_z$ -I-

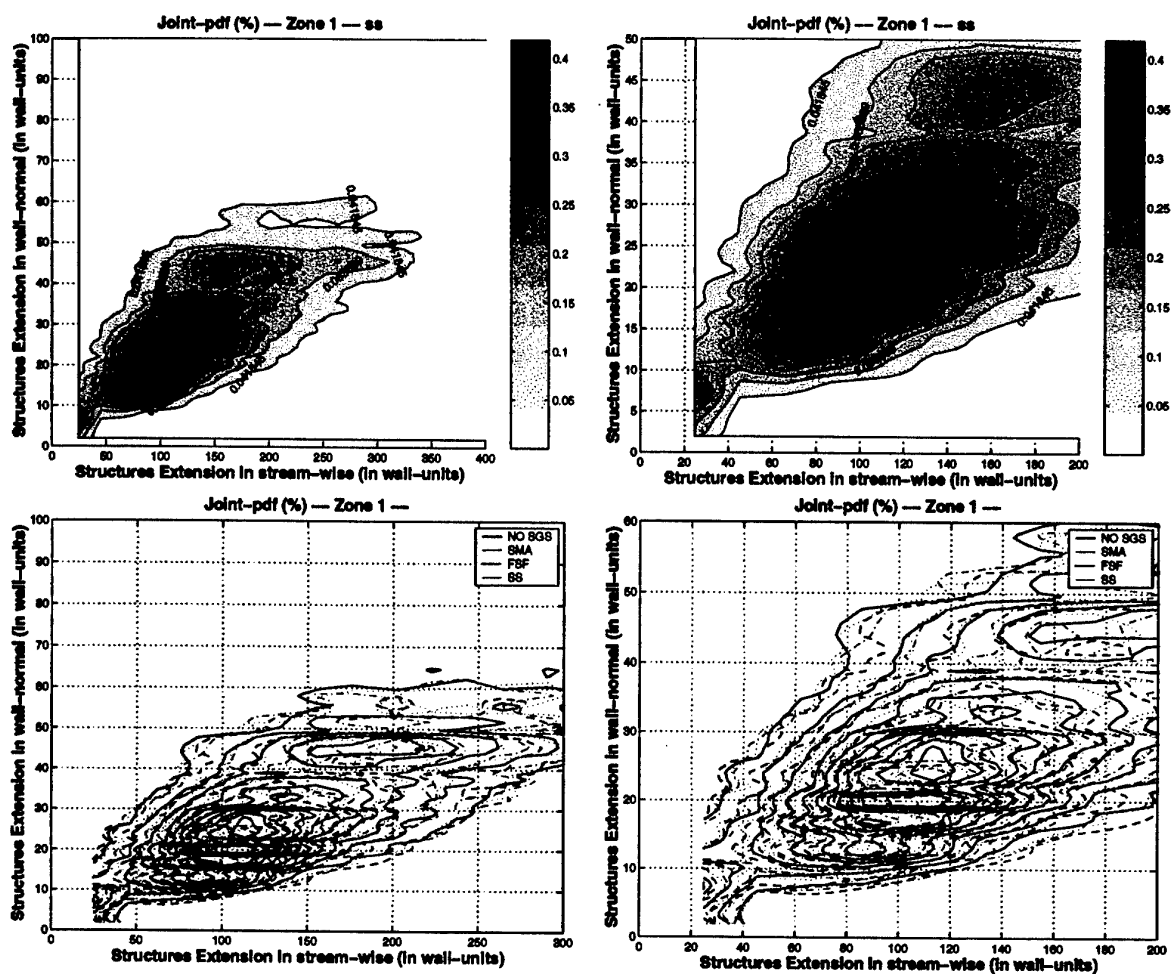


Fig. G.5: JPF for structure extensions between SGS models: Zone 1, $L_x - L_z$ -II-

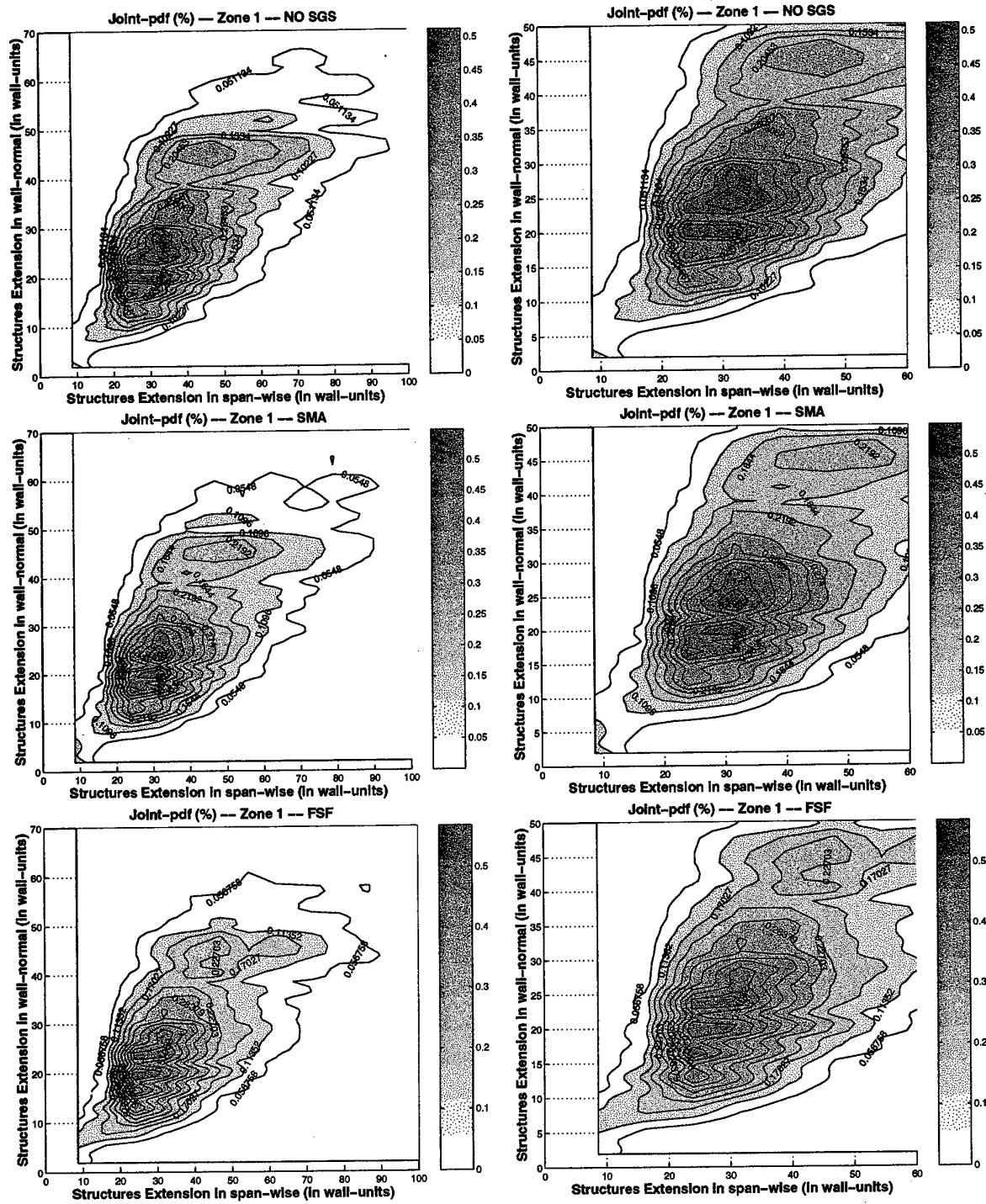


Fig. G.6: JPF for structure extensions between SGS models: Zone 1, $L_y - L_z$ -I-

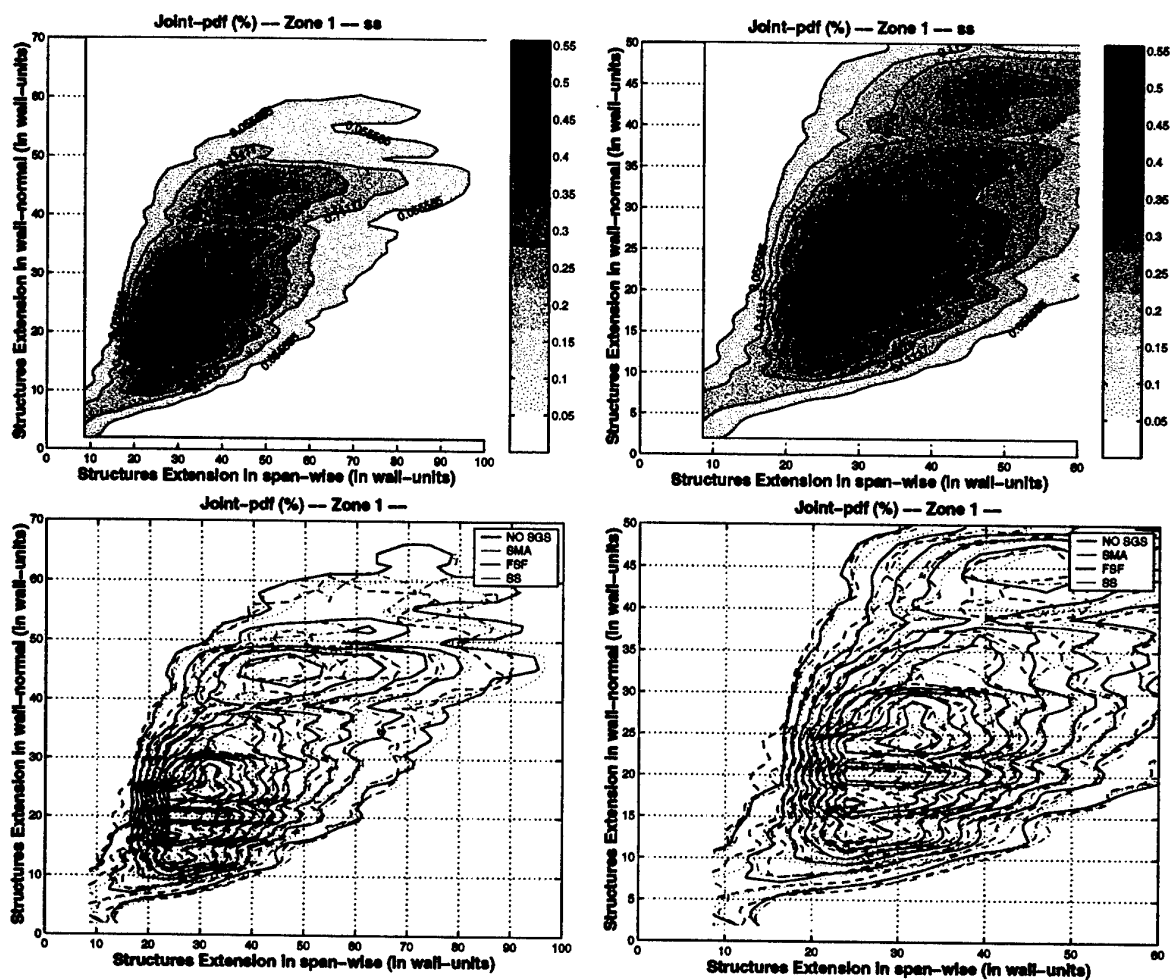


Fig. G.7: JPF for structure extensions between SGS models: Zone 1, $L_y - L_z$ -II-

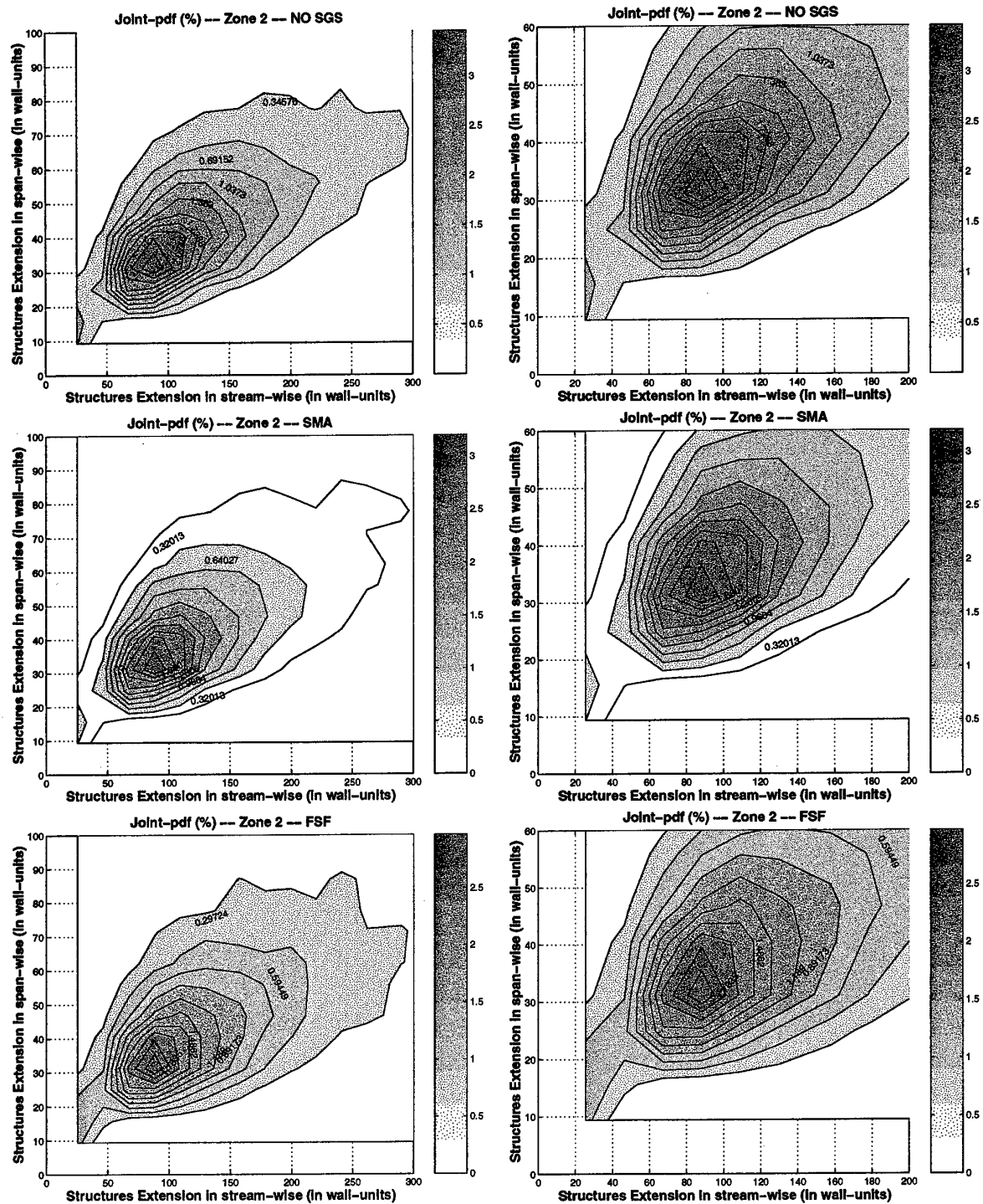


Fig. G.8: JPF for structure extensions between SGS models: Zone 2, $L_x - L_y$ -I-

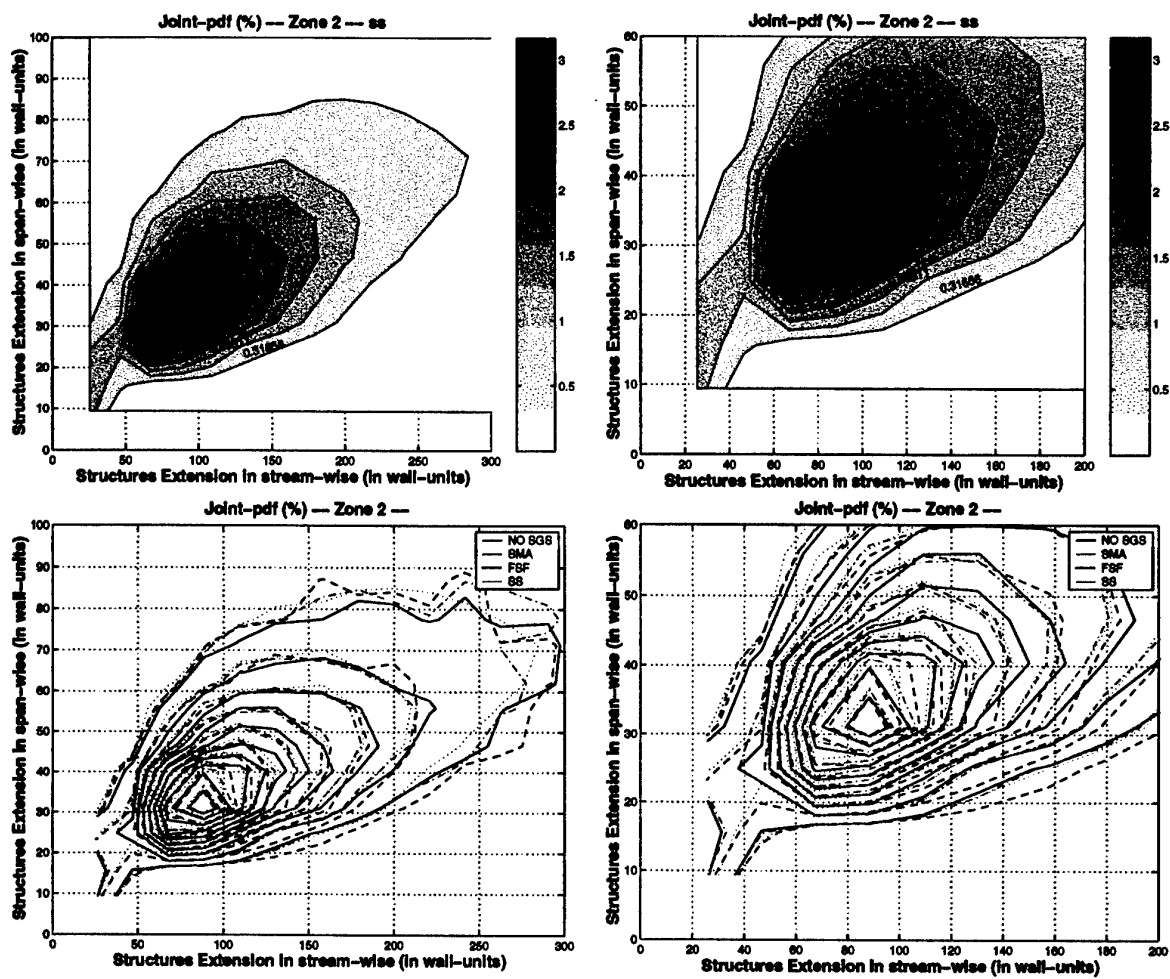


Fig. G.9: JPF for structure extensions between SGS models: Zone 2, $L_x - L_y$ -II-

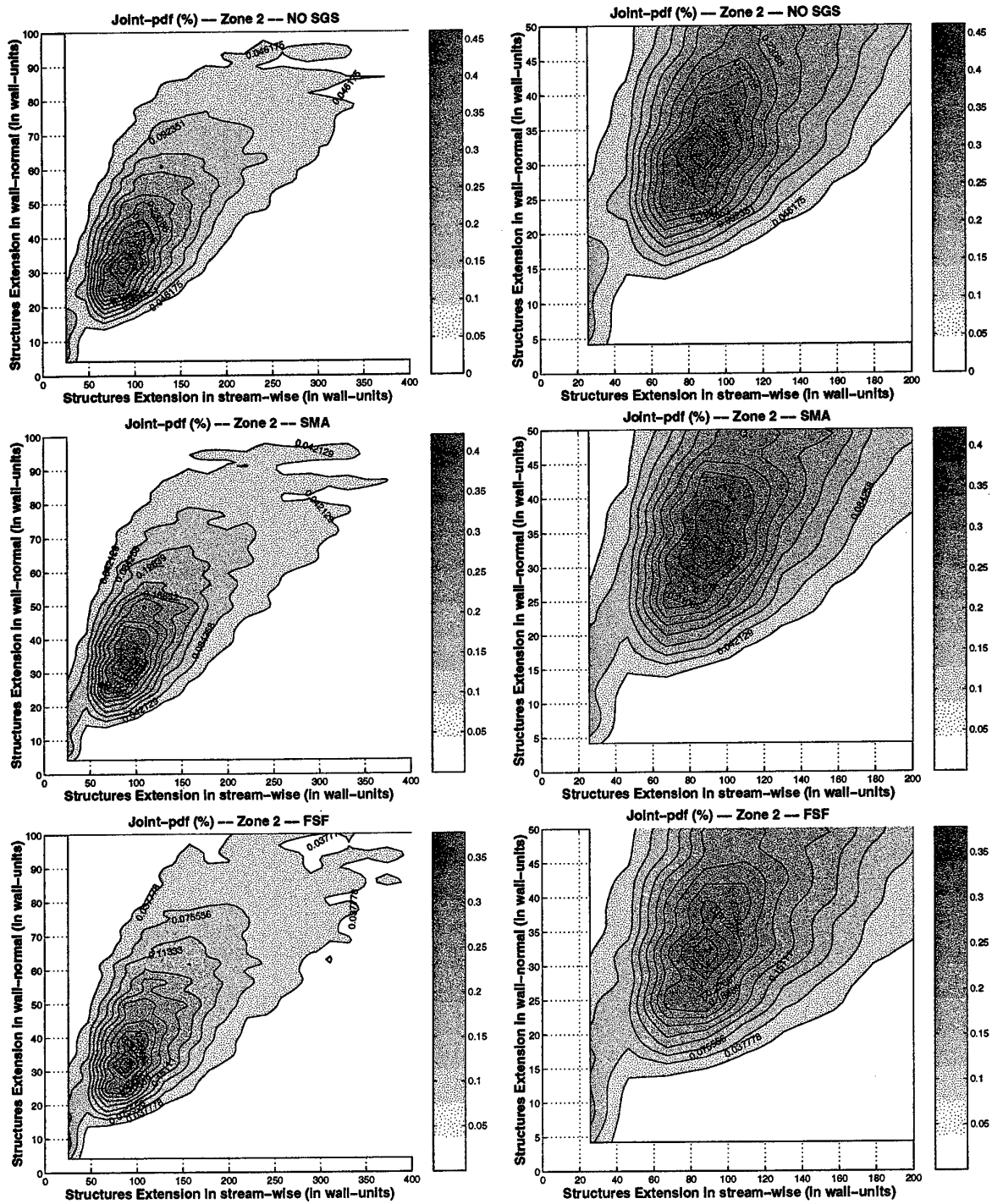


Fig. G.10: JPF for structure extensions between SGS models: Zone 2, $L_x - L_z$ -I-

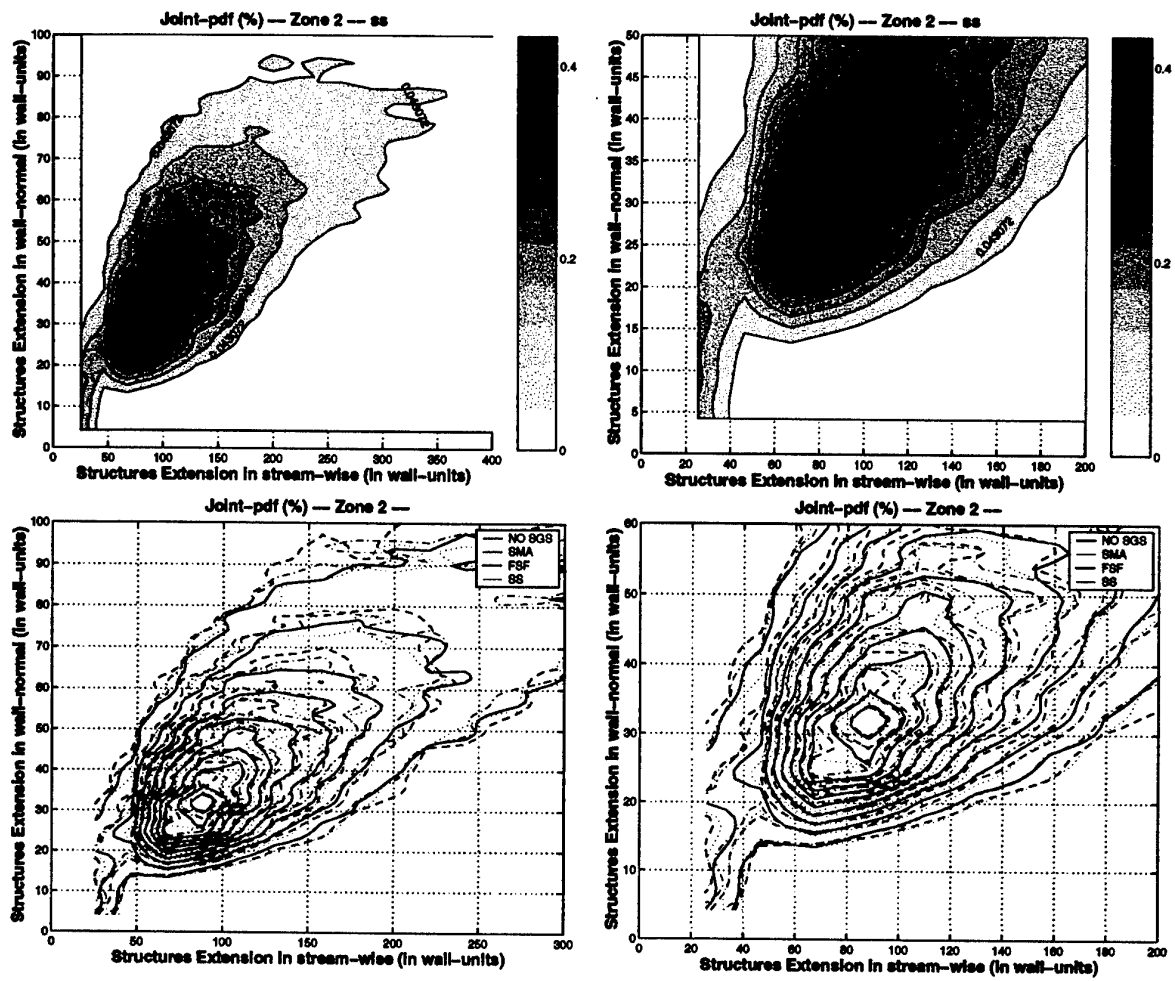


Fig. G.11: JPF for structure extensions between SGS models: Zone 2, $L_x - L_z$ -II-

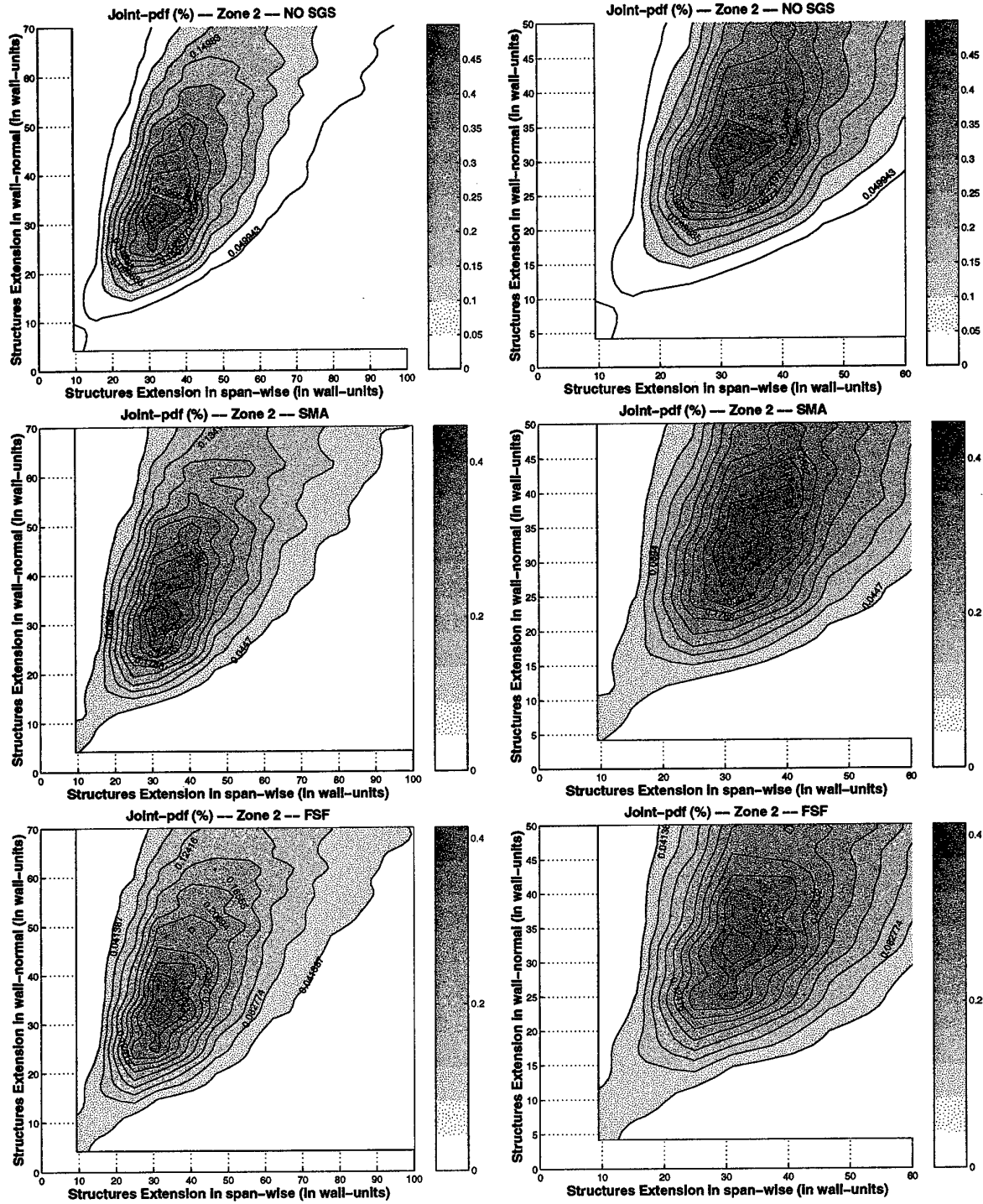


Fig. G.12: JPF for structure extensions between SGS models: Zone 2, $L_y - L_z$ -I-

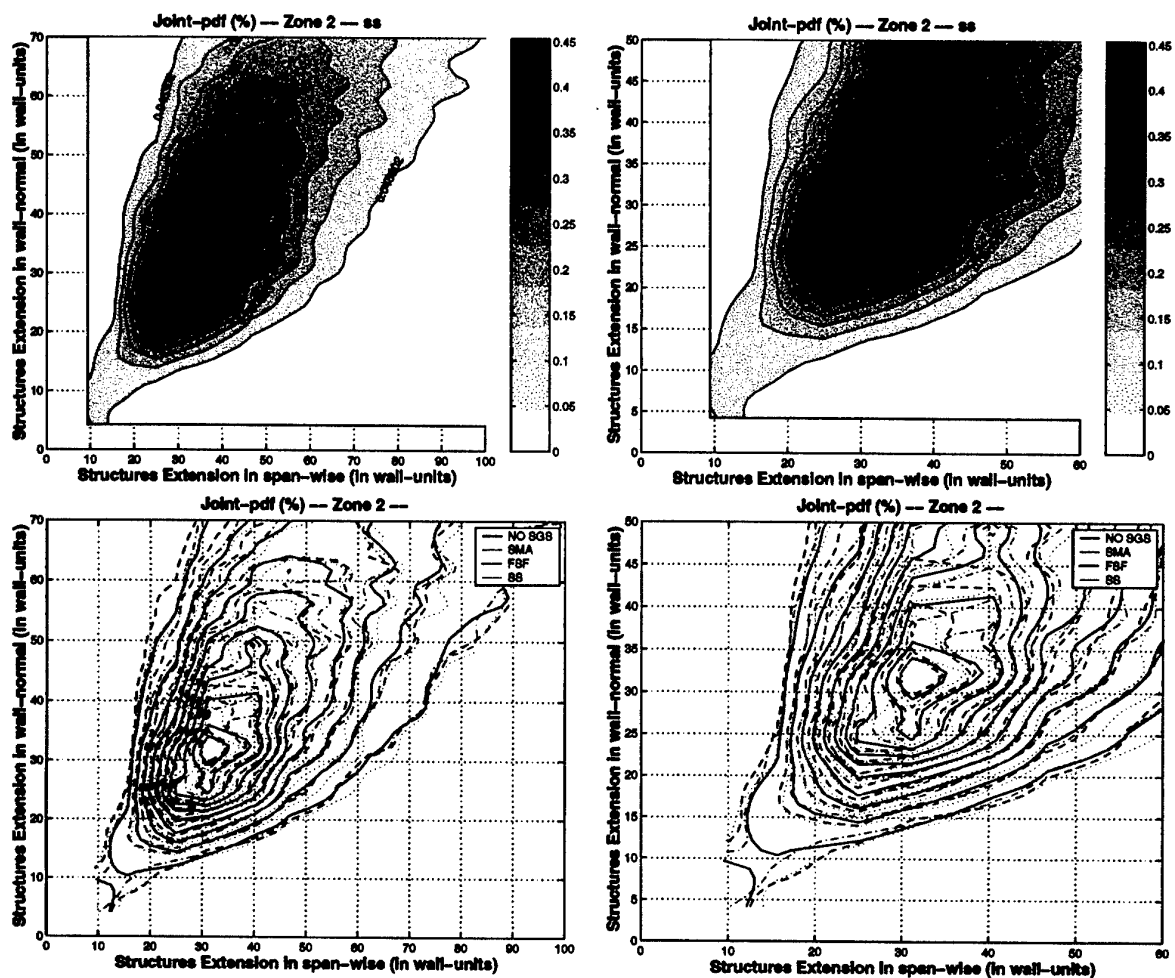


Fig. G.13: JPF for structure extensions between SGS models: Zone 2, $L_y - L_z$ -II-

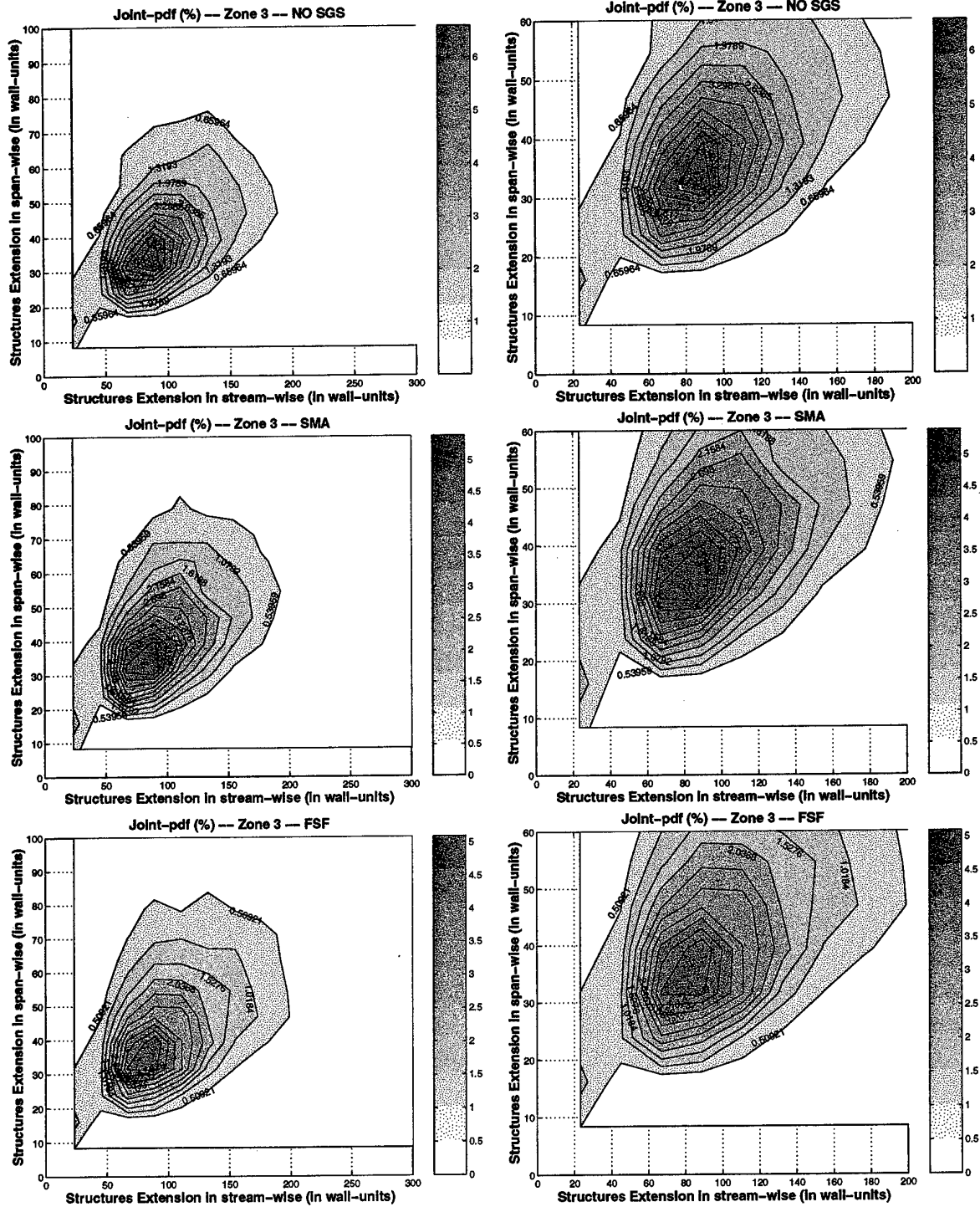


Fig. G.14: JPF for structure extensions between SGS models: Zone 3, $L_x - L_y$ -I-

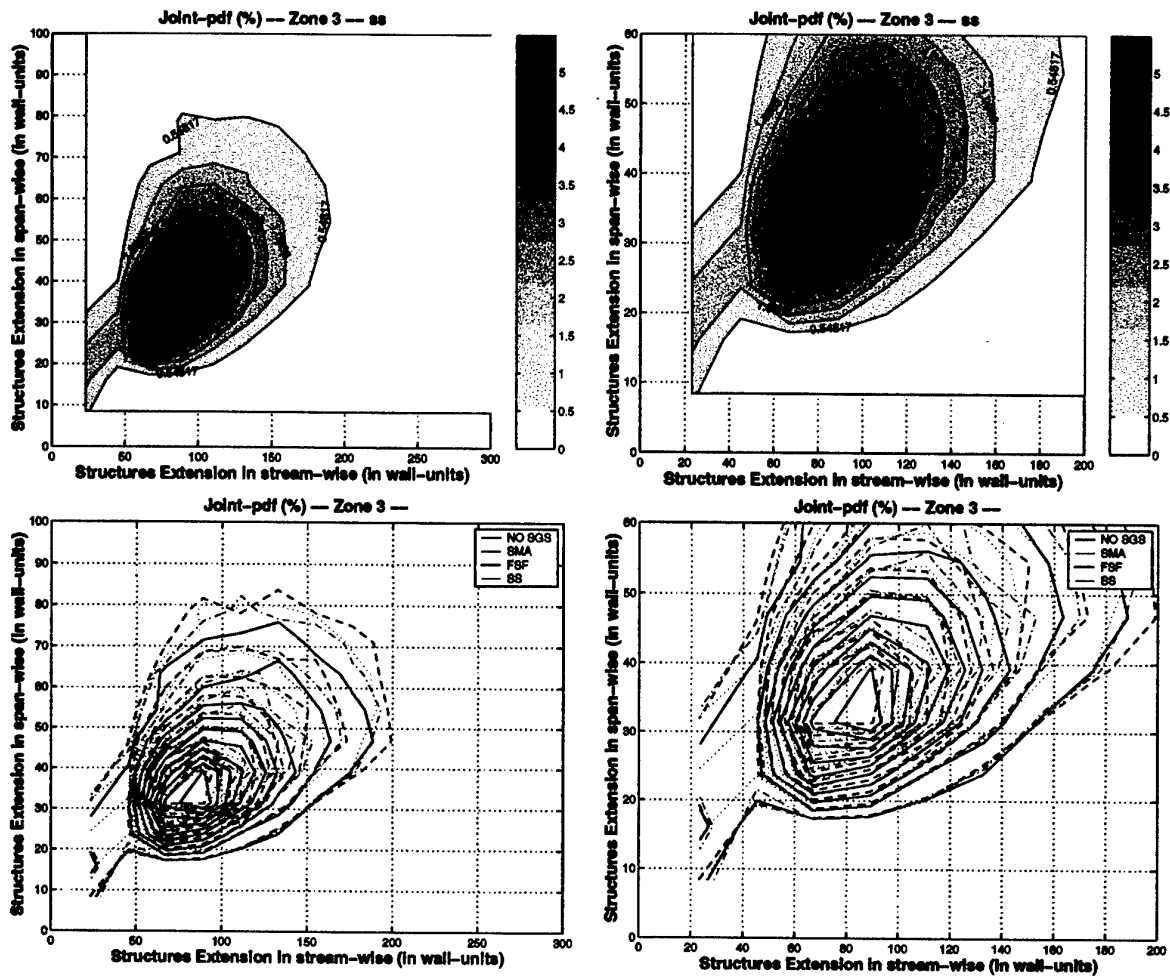


Fig. G.15: JPF for structure extensions between SGS models: Zone 3, $L_x - L_y$ -II-

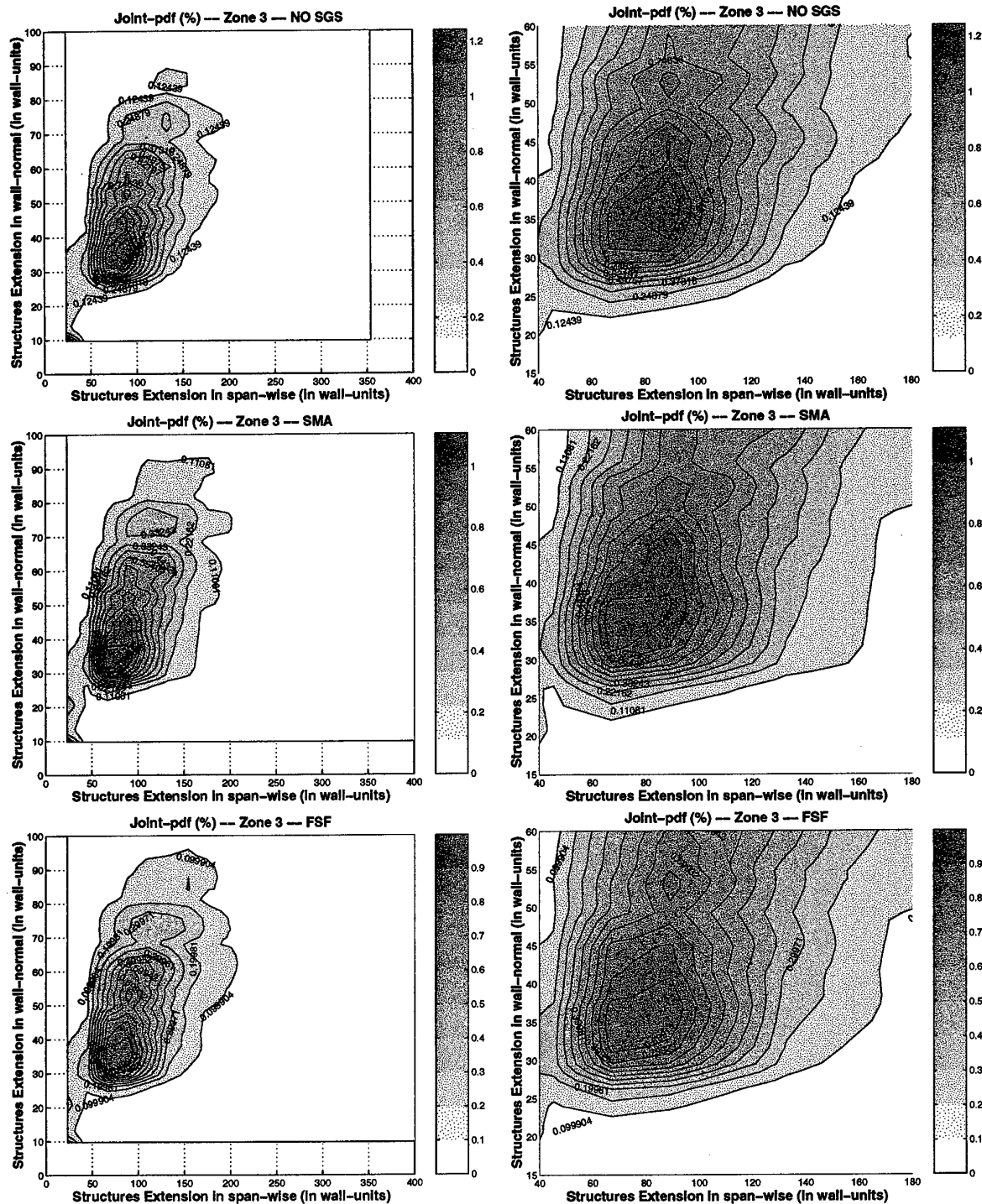


Fig. G.16: JPF for structure extensions between SGS models: Zone 3, $L_x - L_z$ -I-

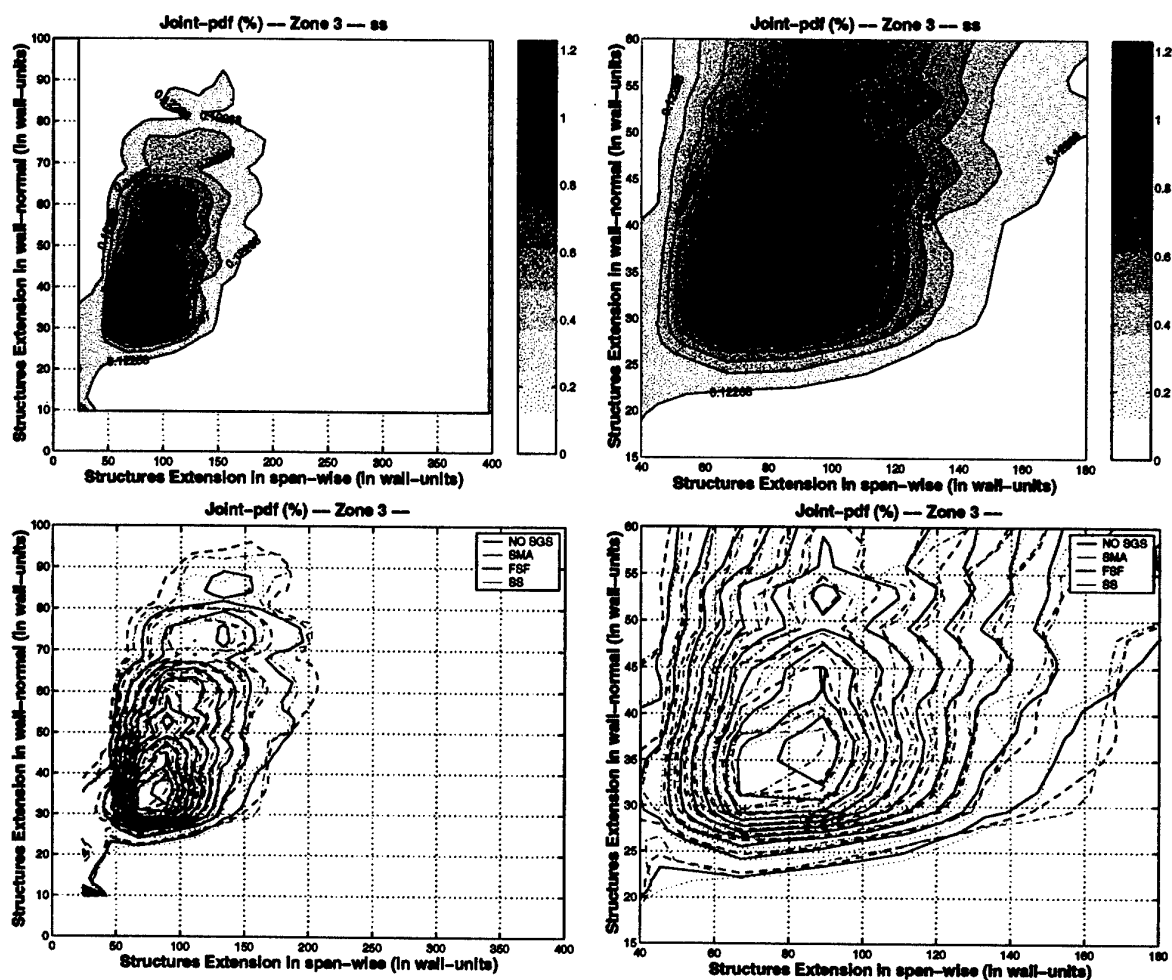


Fig. G.17: JPF for structure extensions between SGS models: Zone 3, $L_x - L_z$ -II-

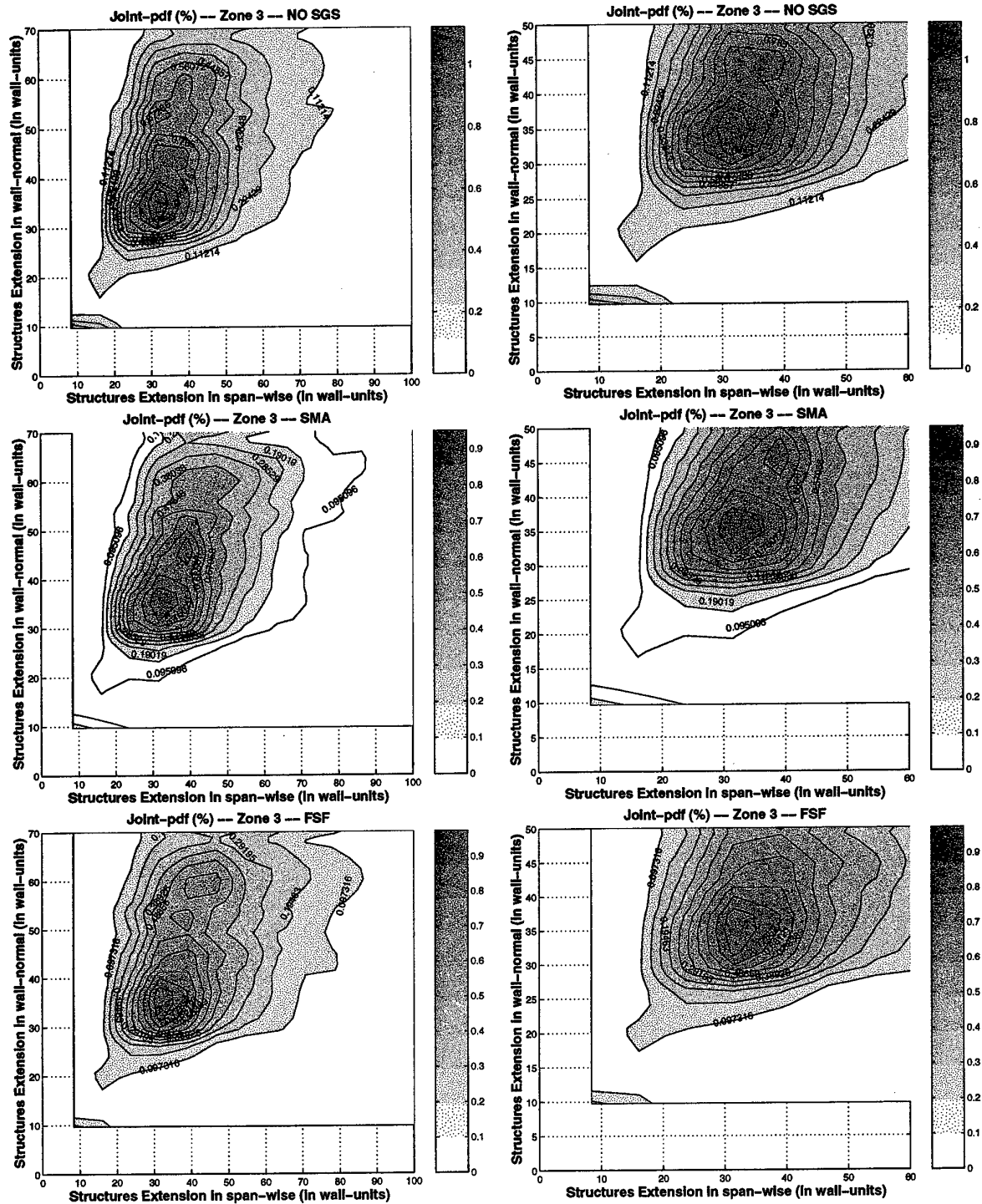


Fig. G.18: JPF for structure extensions between SGS models: Zone 3, $L_y - L_z$ -I-

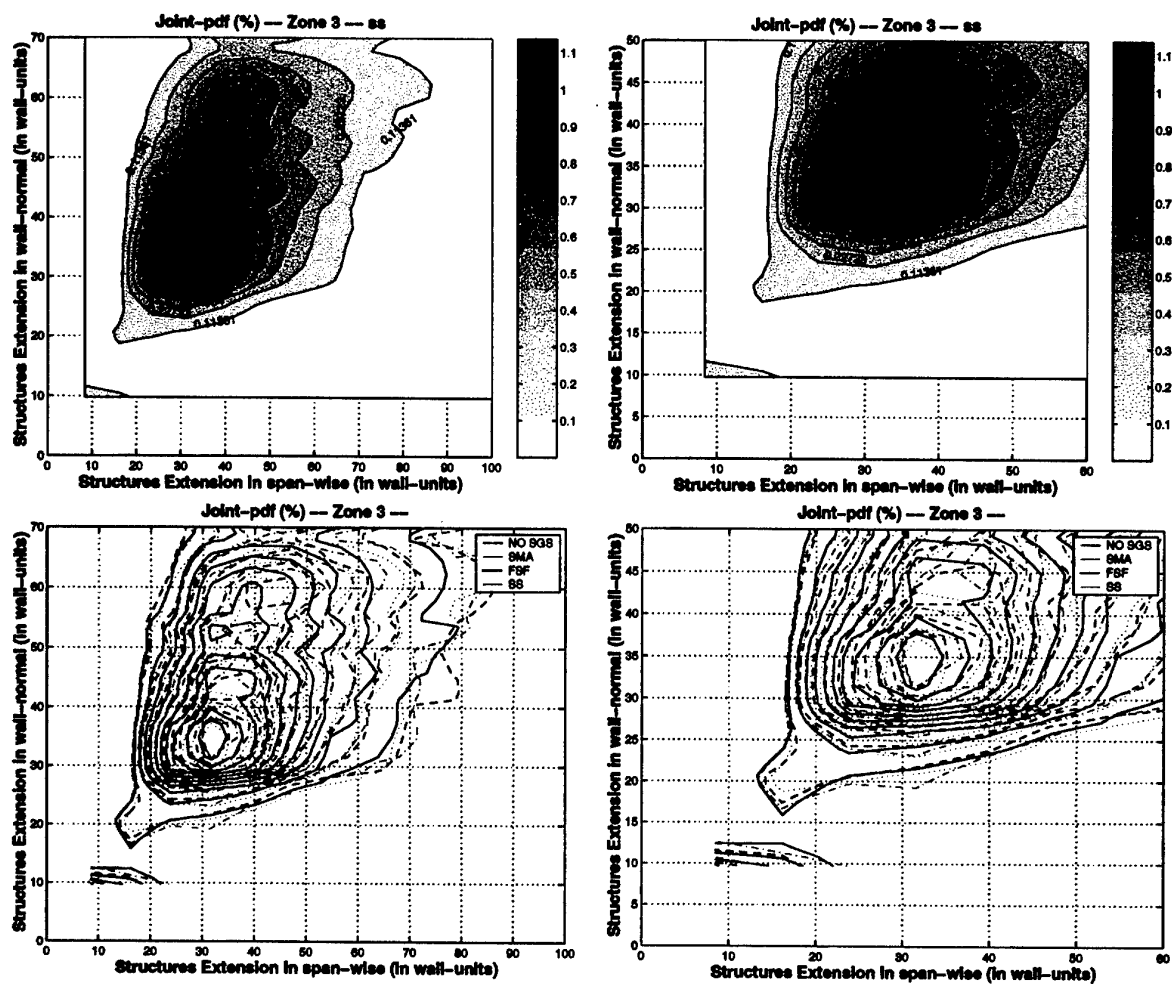


Fig. G.19: JPF for structure extensions between SGS models: Zone 3, $L_y - L_z$ -II-

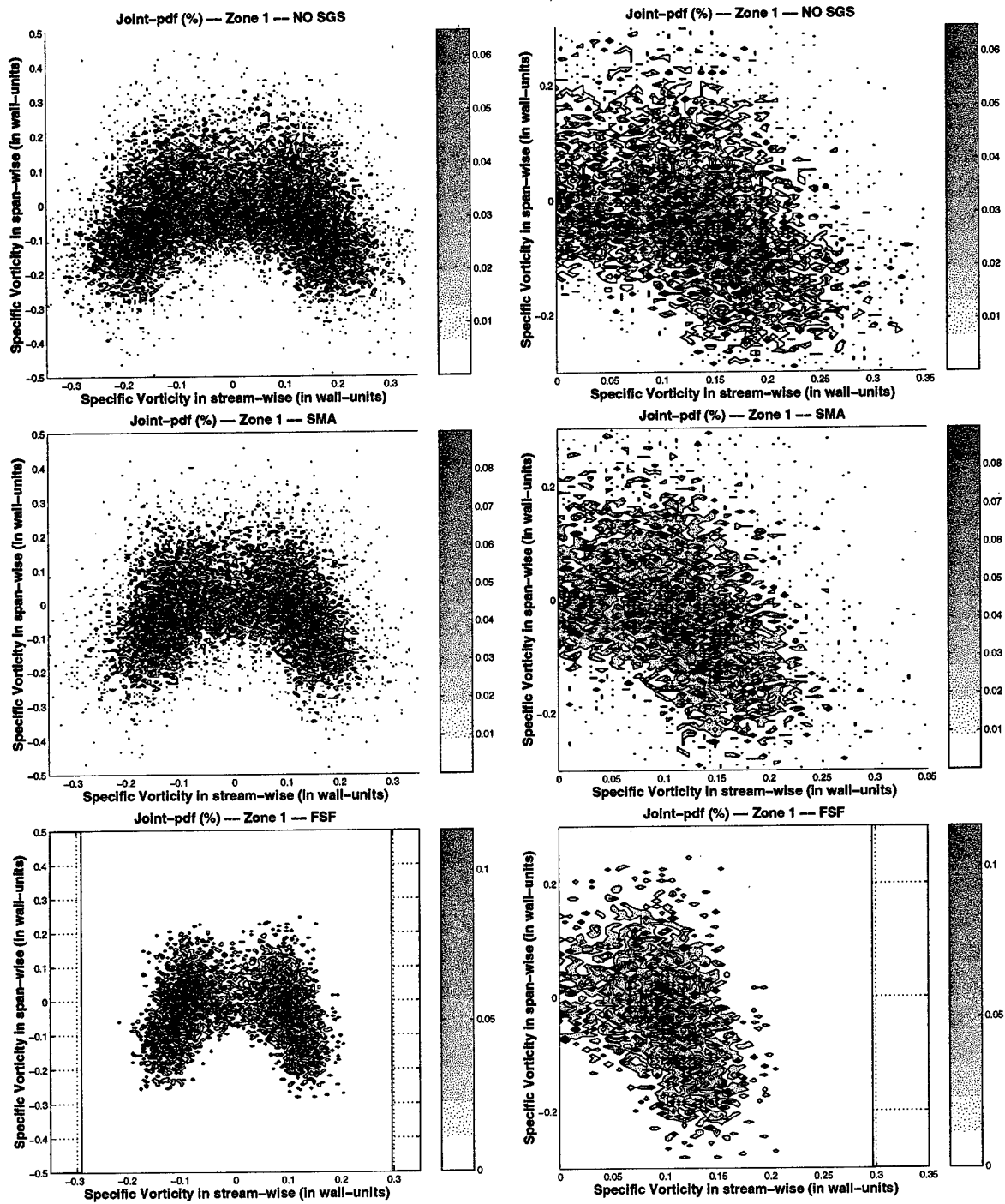


Fig. G.20: JPF for vorticity components between SGS models: Zone 1, $\omega_x - \omega_y$ -I-

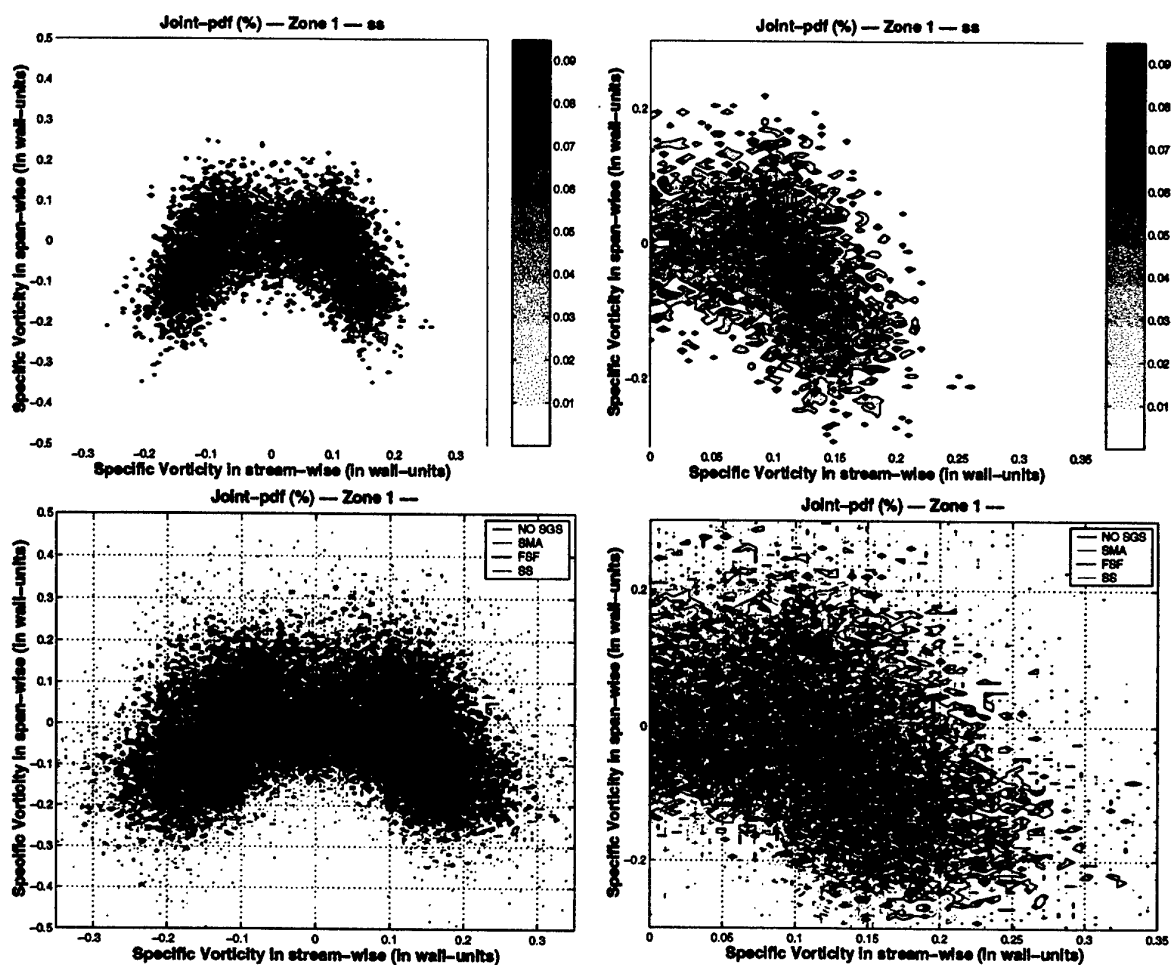


Fig. G.21: JPF for vorticity components between SGS models: Zone 1, $\omega_x - \omega_y$ -II-

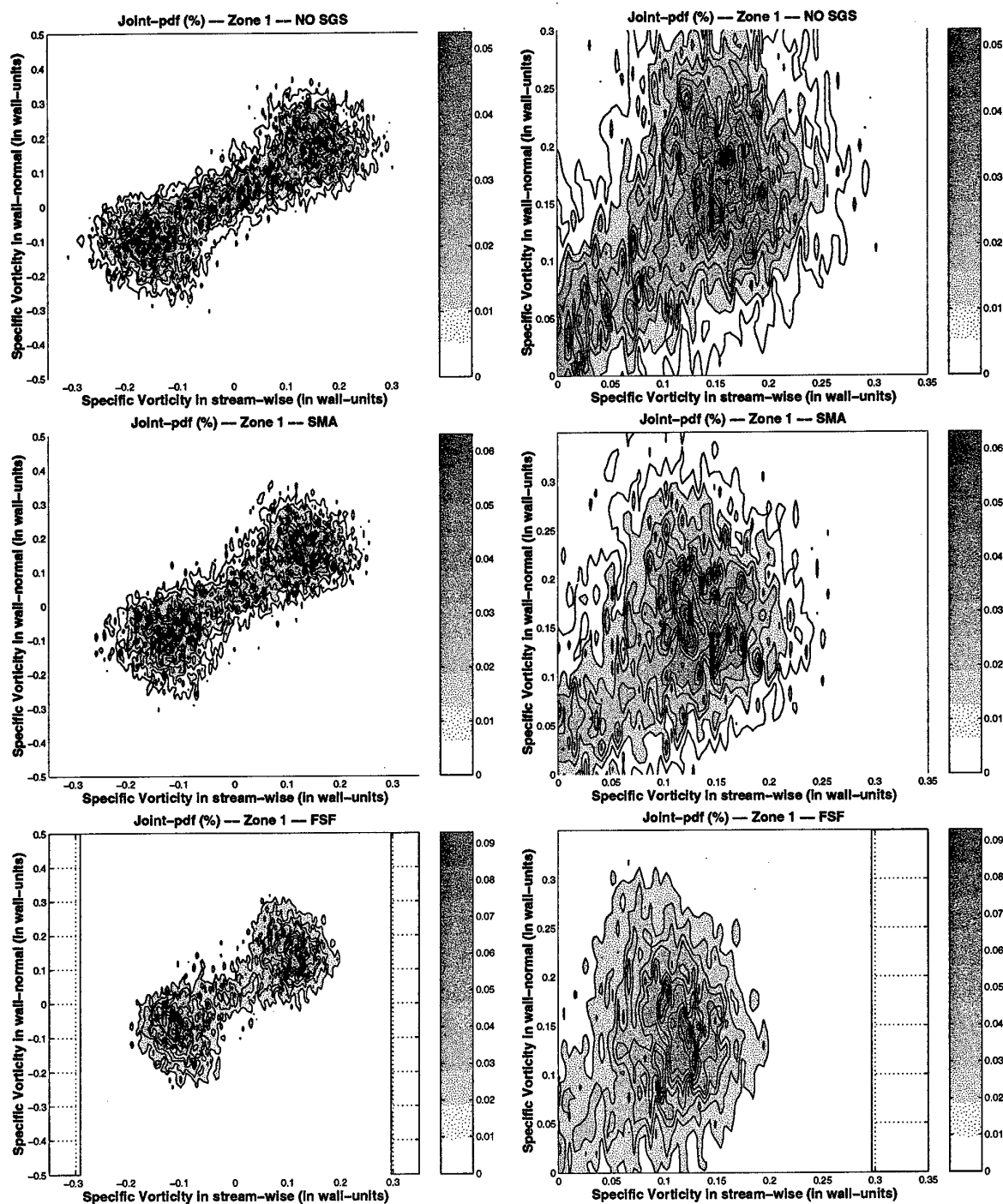


Fig. G.22: JPF for vorticity components between SGS models: Zone 1, $\omega_x - \omega_z$ -I-

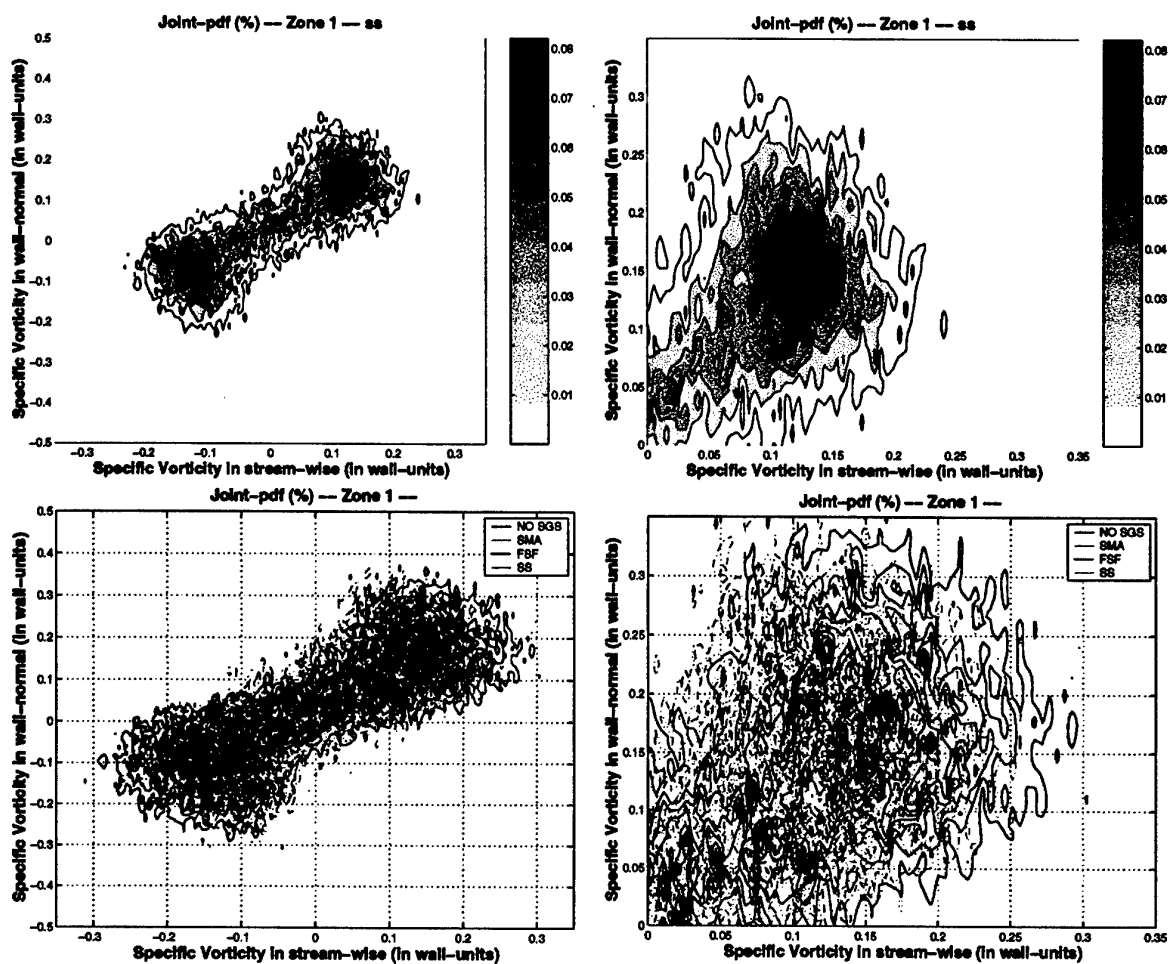


Fig. G.23: JPF for vorticity components between SGS models: Zone 1, $\omega_x - \omega_z$ -II-

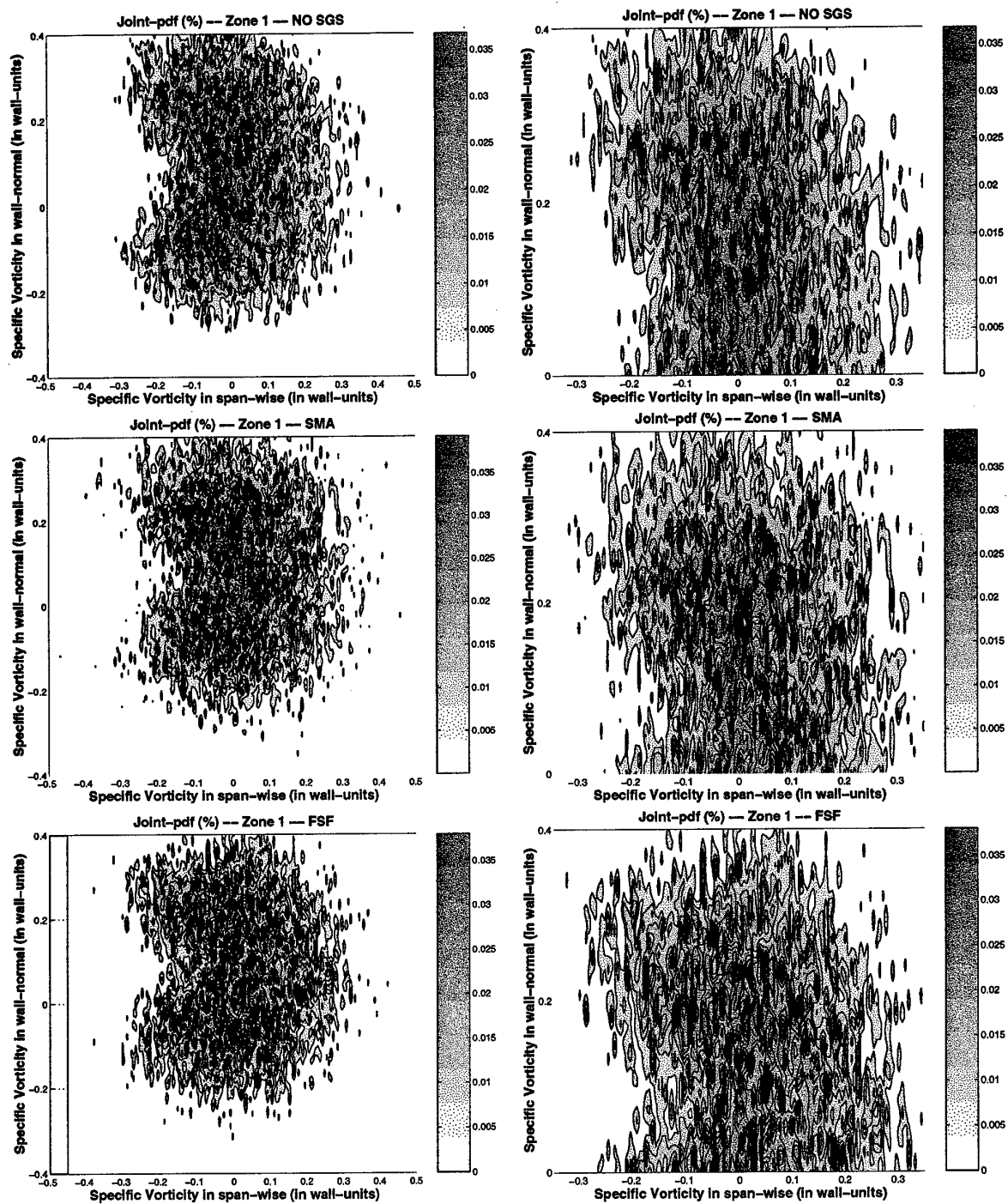


Fig. G.24: JPF for vorticity components between SGS models: Zone 1, $\omega_y - \omega_z$ -I-

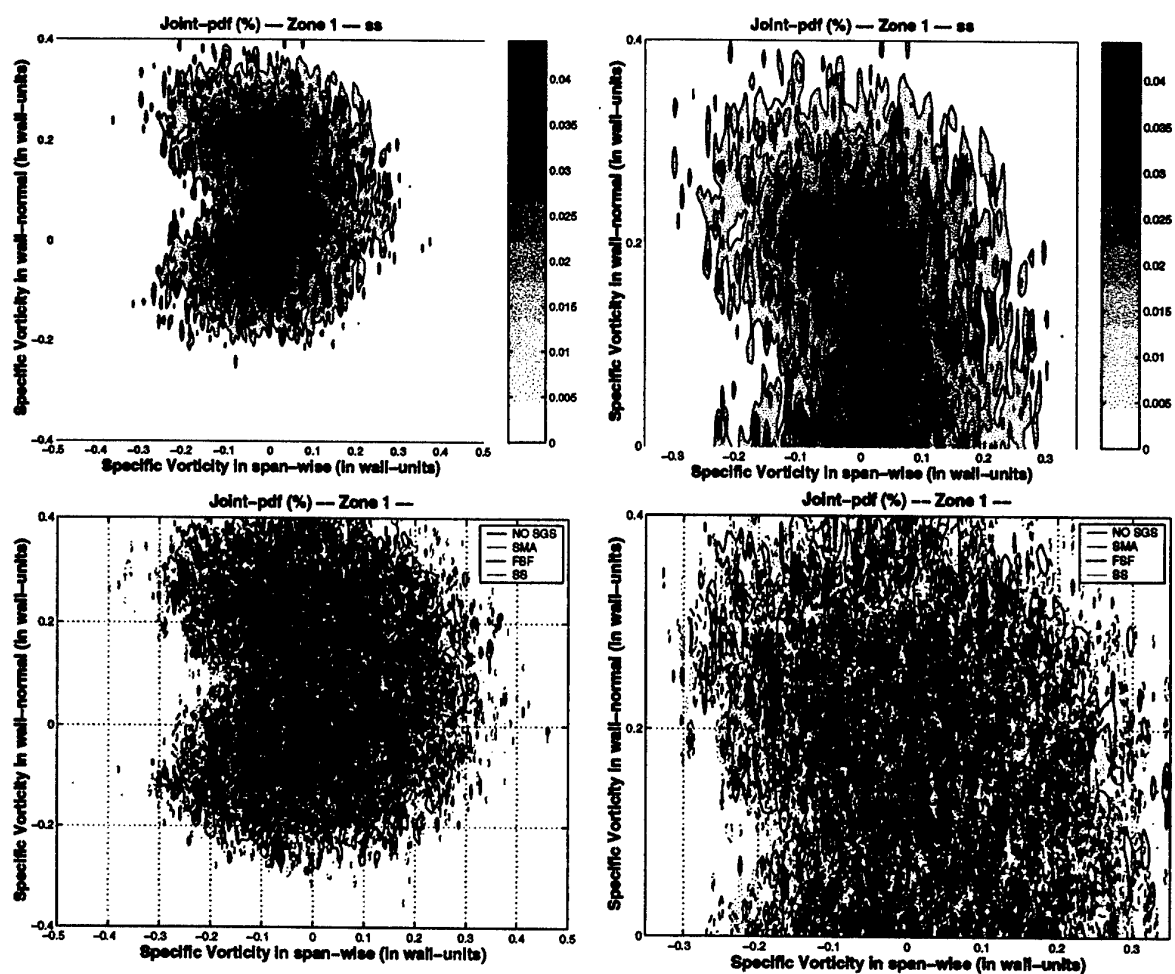


Fig. G.25: JPF for vorticity components between SGS models: Zone 1, $\omega_y - \omega_z$ -II-

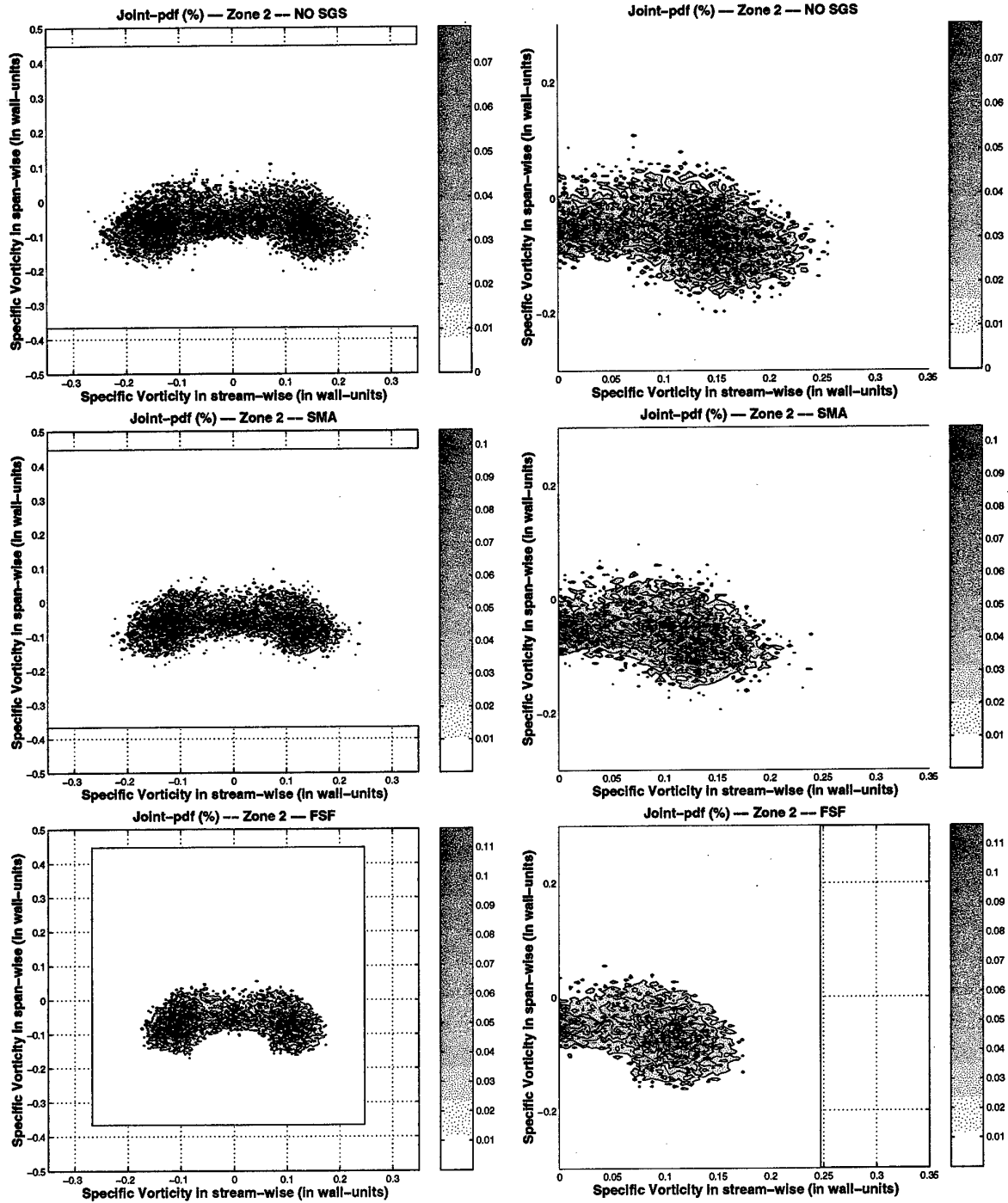


Fig. G.26: JPF for vorticity components between SGS models: Zone 2, $\omega_x - \omega_y$ -I-

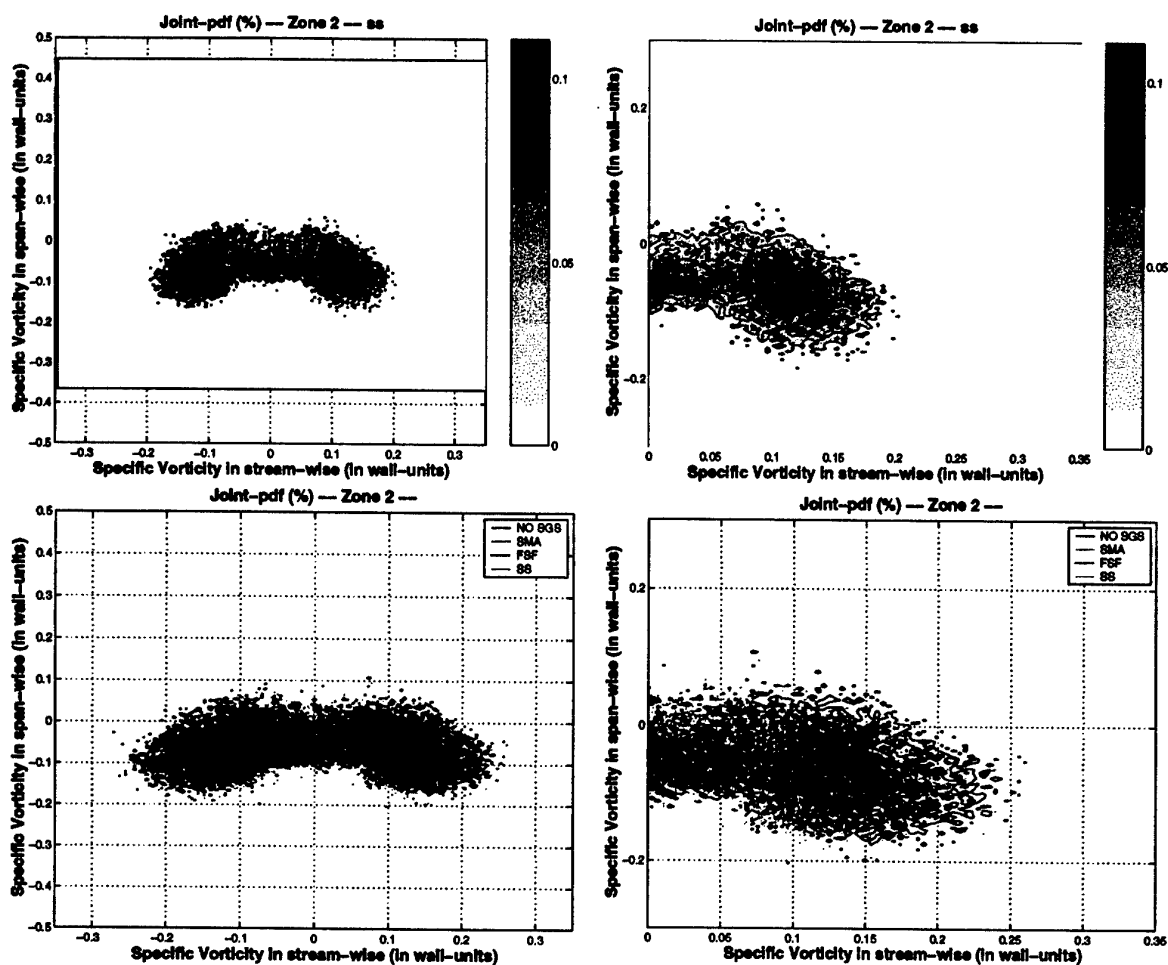


Fig. G.27: JPF for vorticity components between SGS models: Zone 2, $\omega_x - \omega_y$ -II-

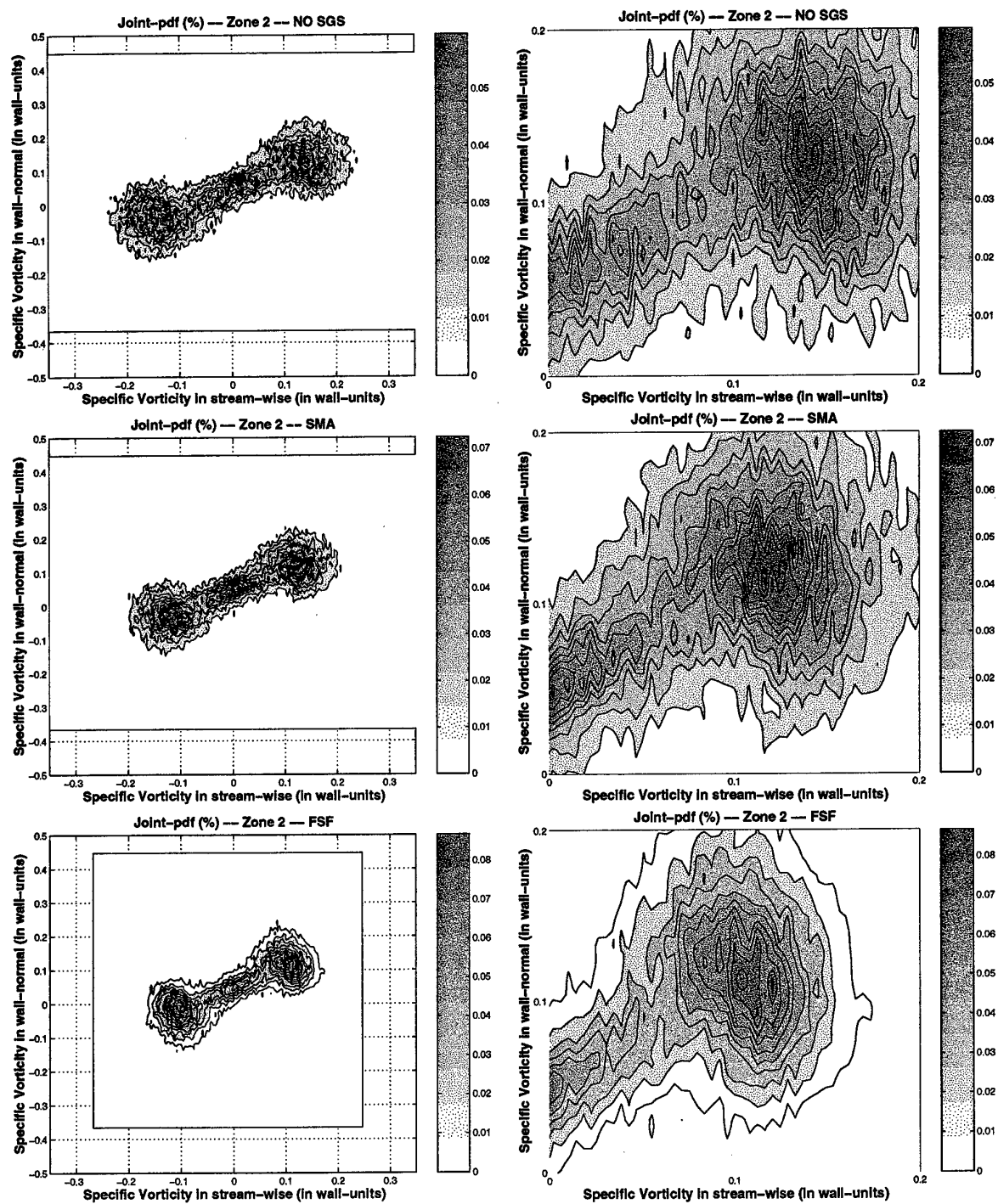


Fig. G.28: JPF for vorticity components between SGS models: Zone 2, $\omega_x - \omega_z$ -I-

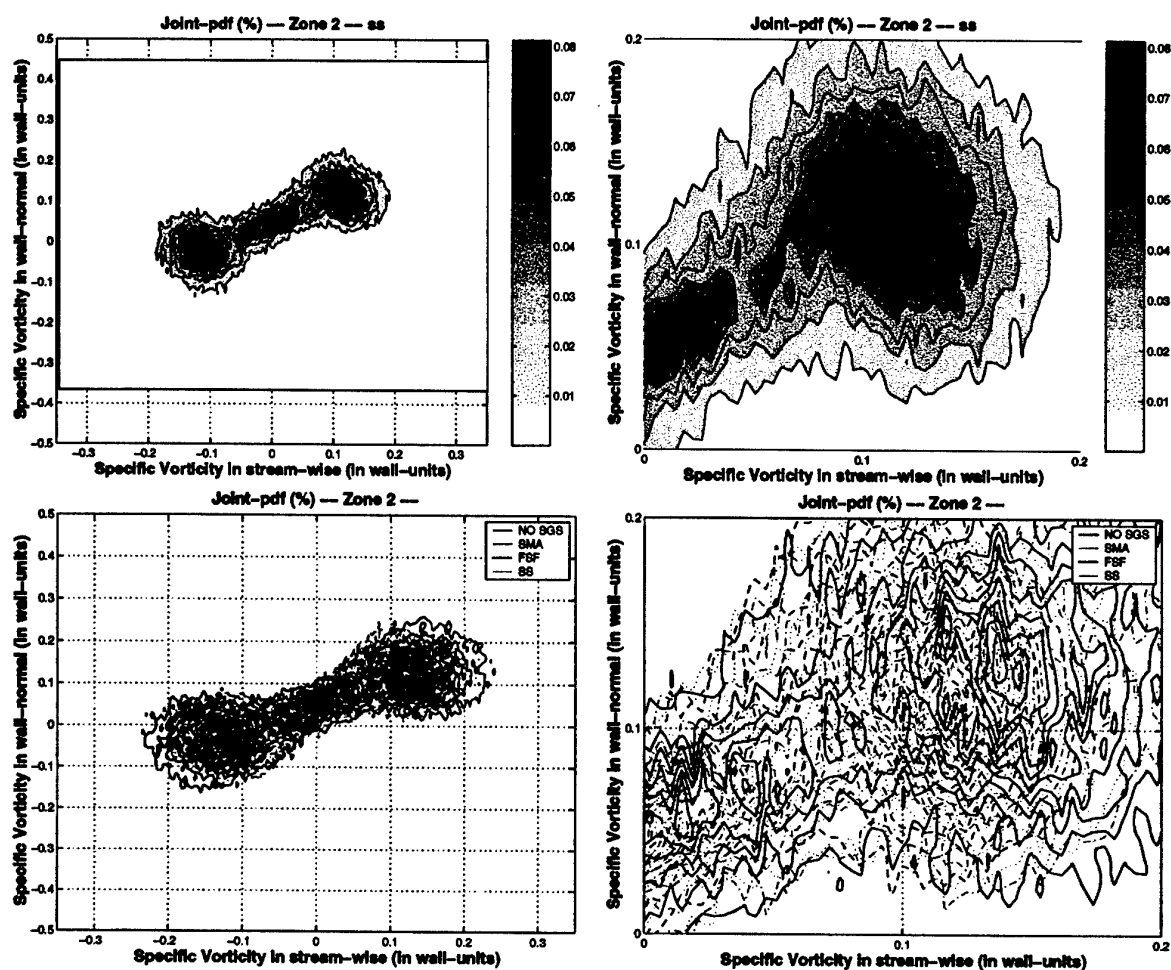


Fig. G.29: JPF for vorticity components between SGS models: Zone 2, $\omega_x - \omega_z$ -II-

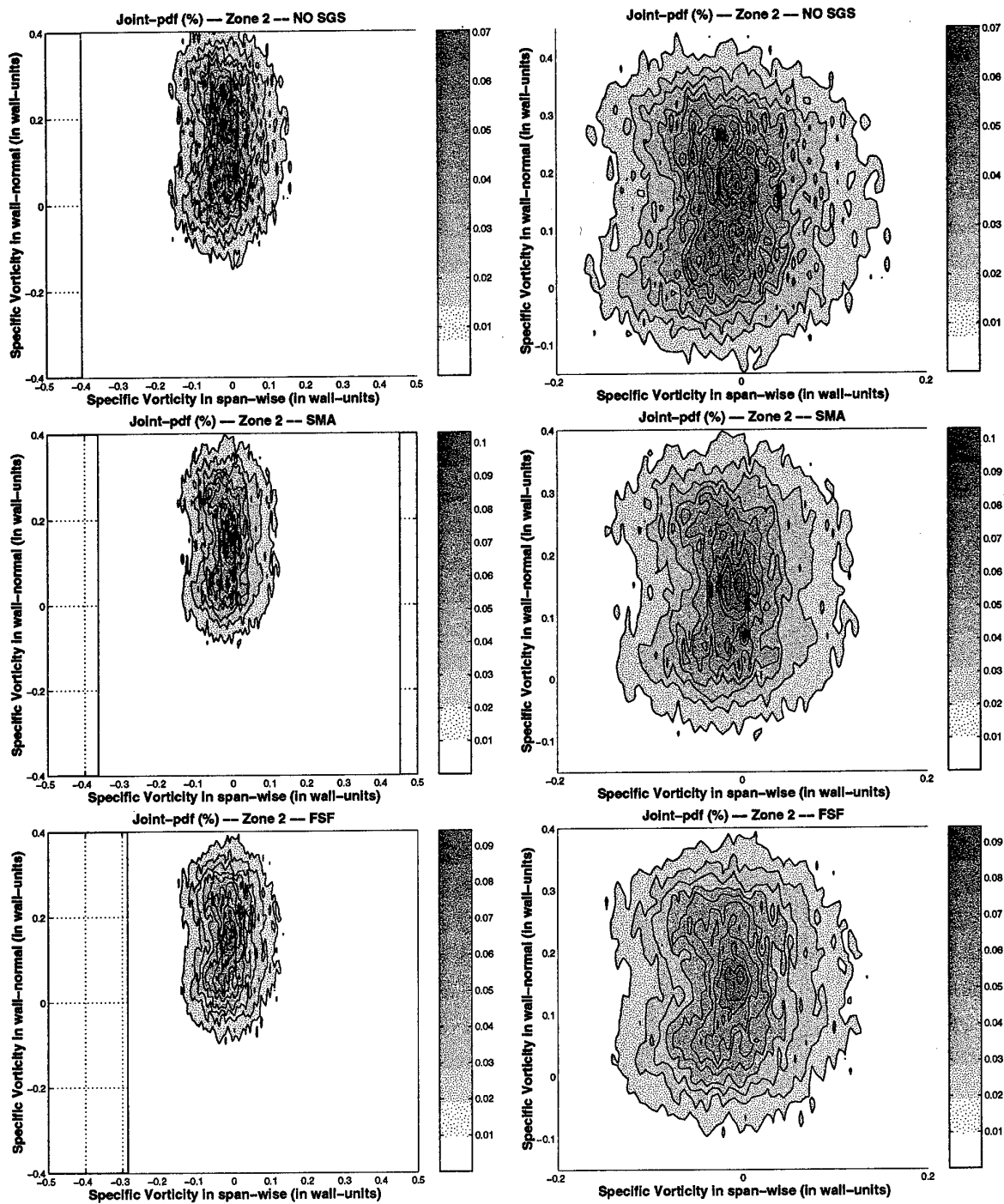


Fig. G.30: JPF for vorticity components between SGS models: Zone 2, $\omega_y - \omega_z$ -I-

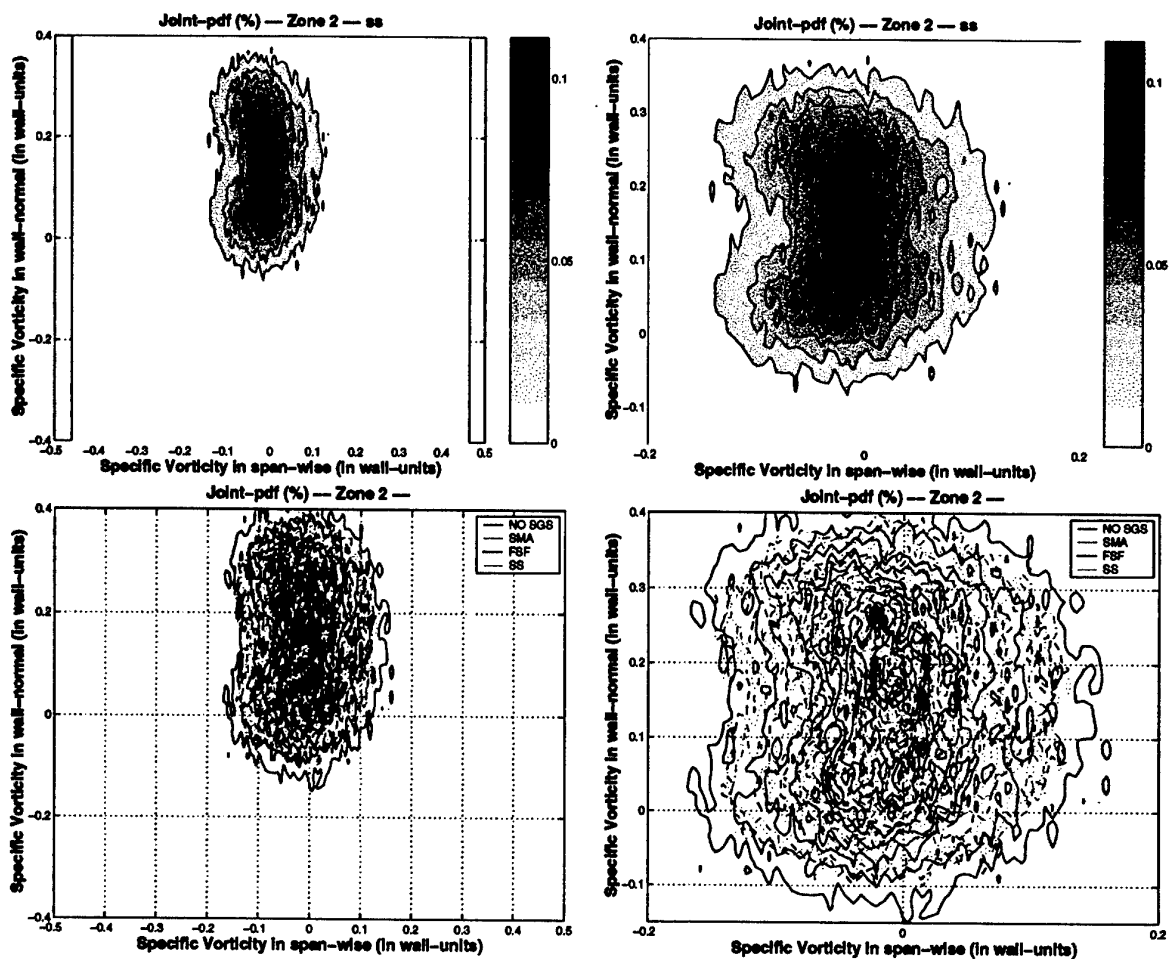


Fig. G.31: JPF for vorticity components between SGS models: Zone 2, $\omega_y - \omega_z$ -II-

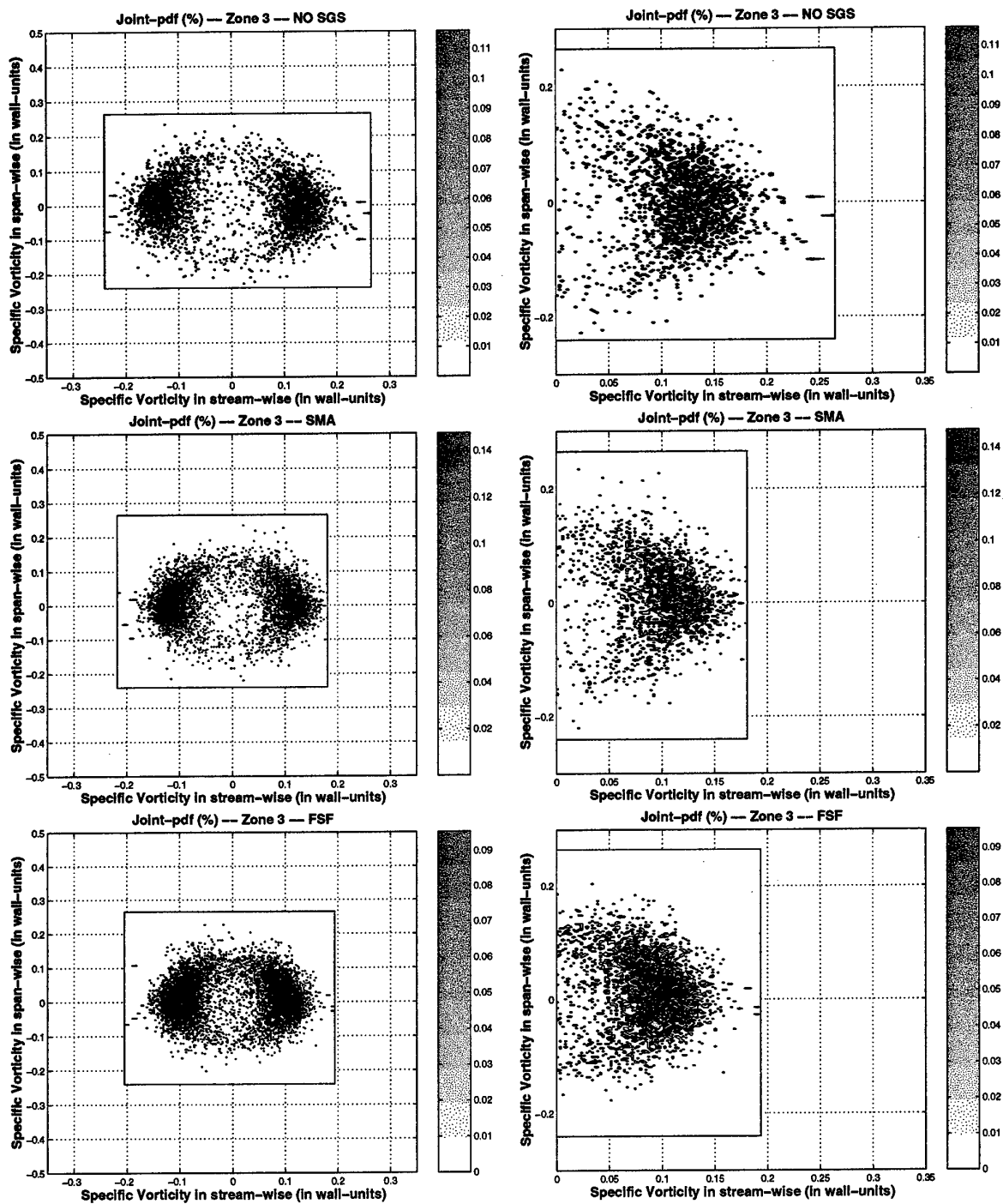


Fig. G.32: JPF for vorticity components between SGS models: Zone 3, $\omega_x - \omega_y$ -I-

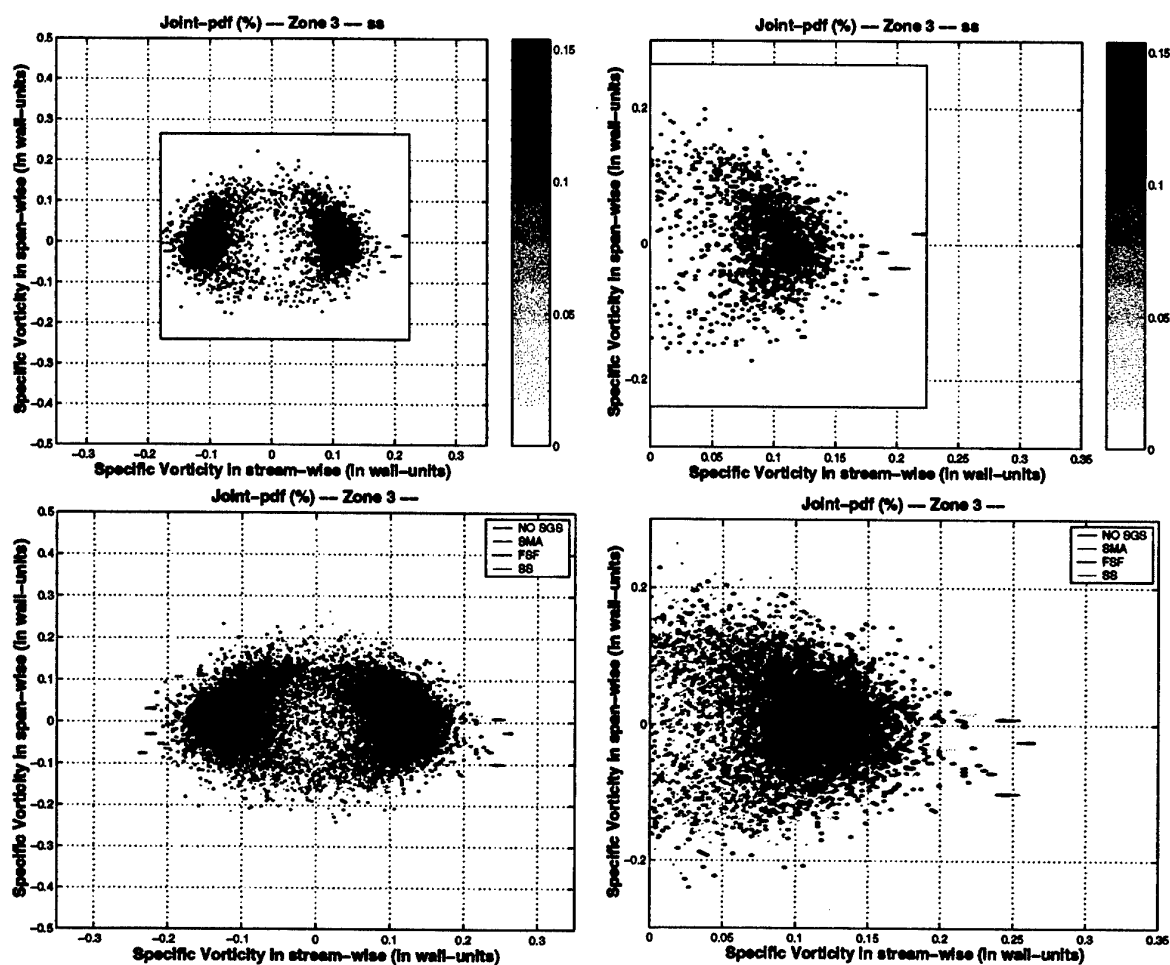


Fig. G.33: JPF for vorticity components between SGS models: Zone 3, $\omega_x - \omega_y$ -II-

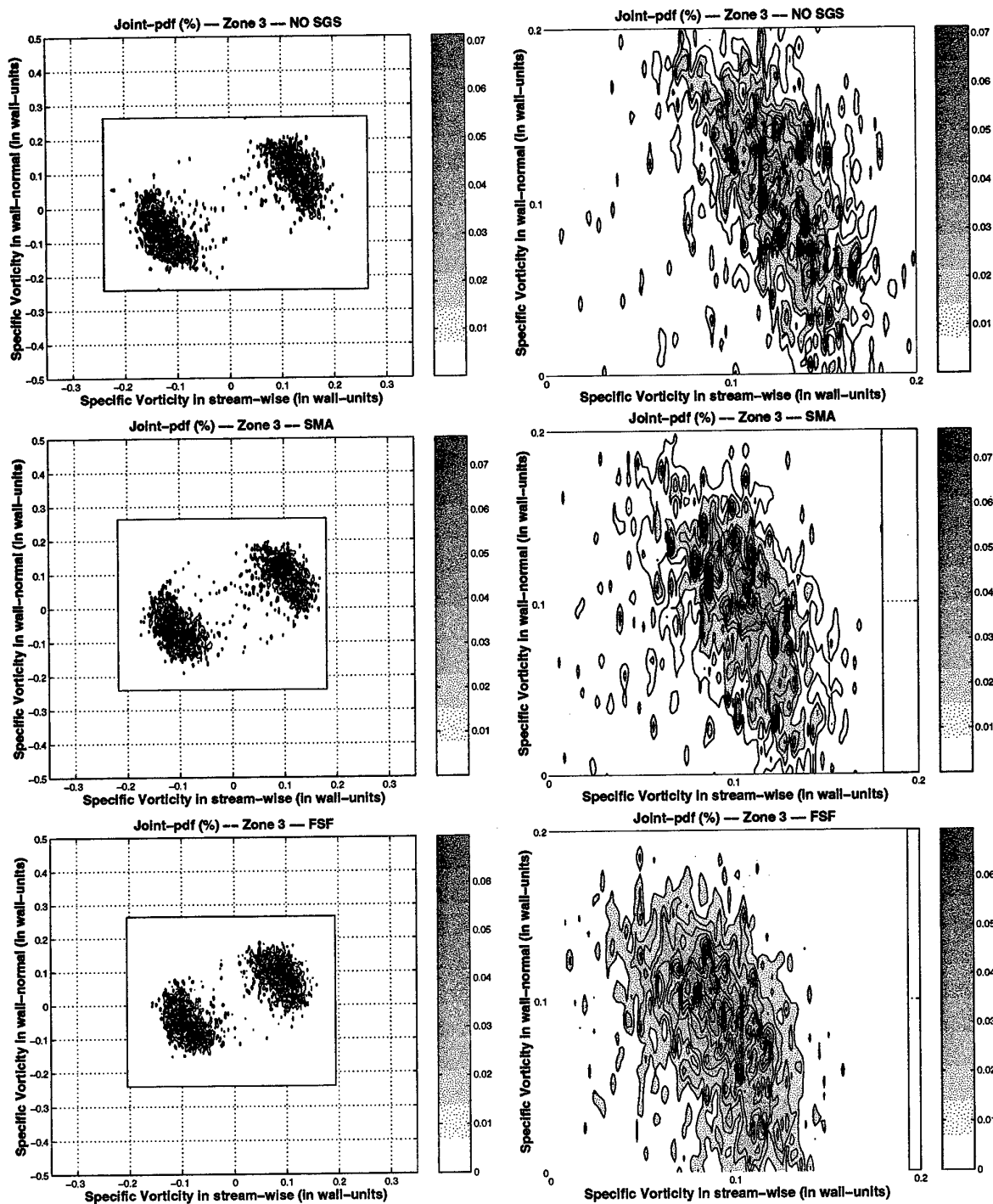


Fig. G.34: JPF for vorticity components between SGS models: Zone 3, $\omega_x - \omega_z$ -I-

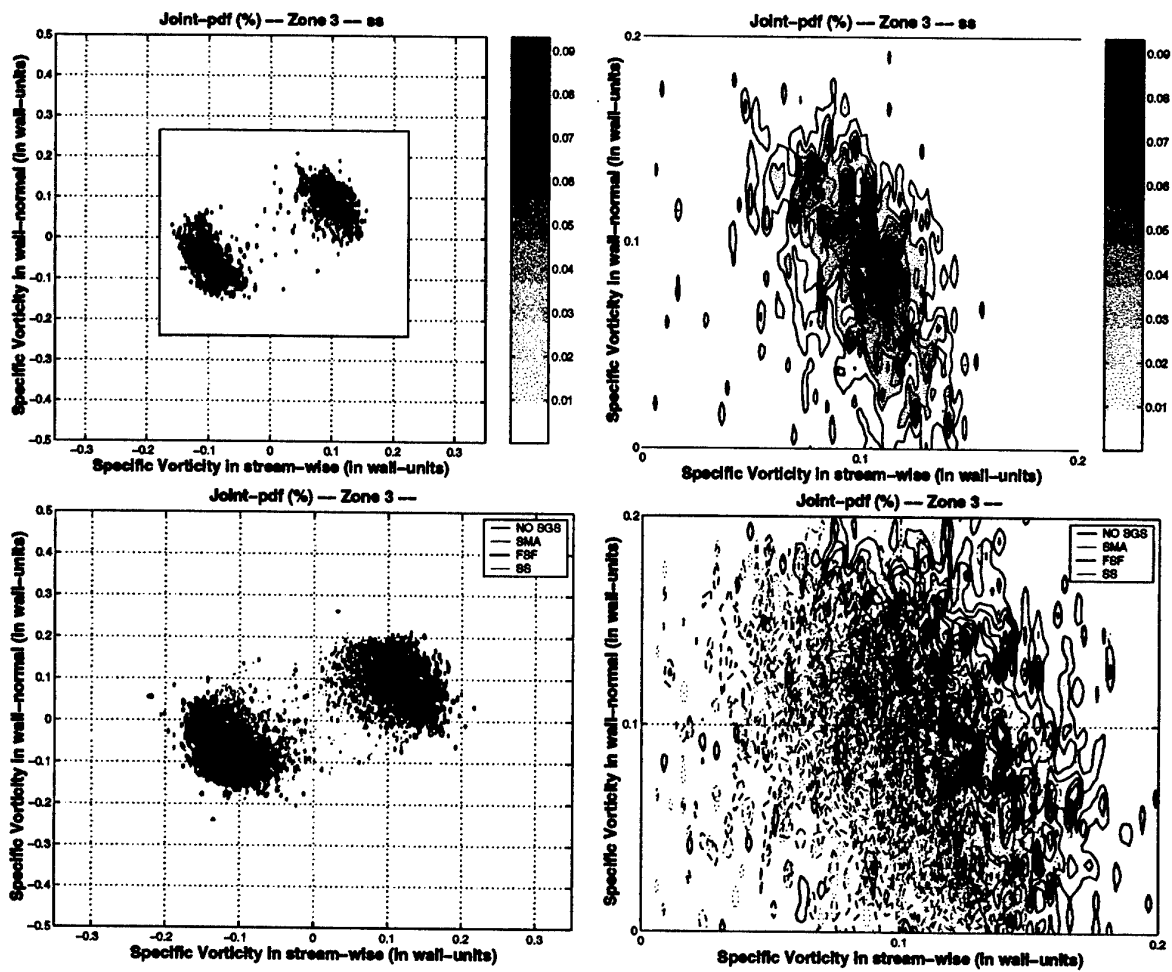


Fig. G.35: JPF for vorticity components between SGS models: Zone 3, $\omega_x - \omega_z$ -II-

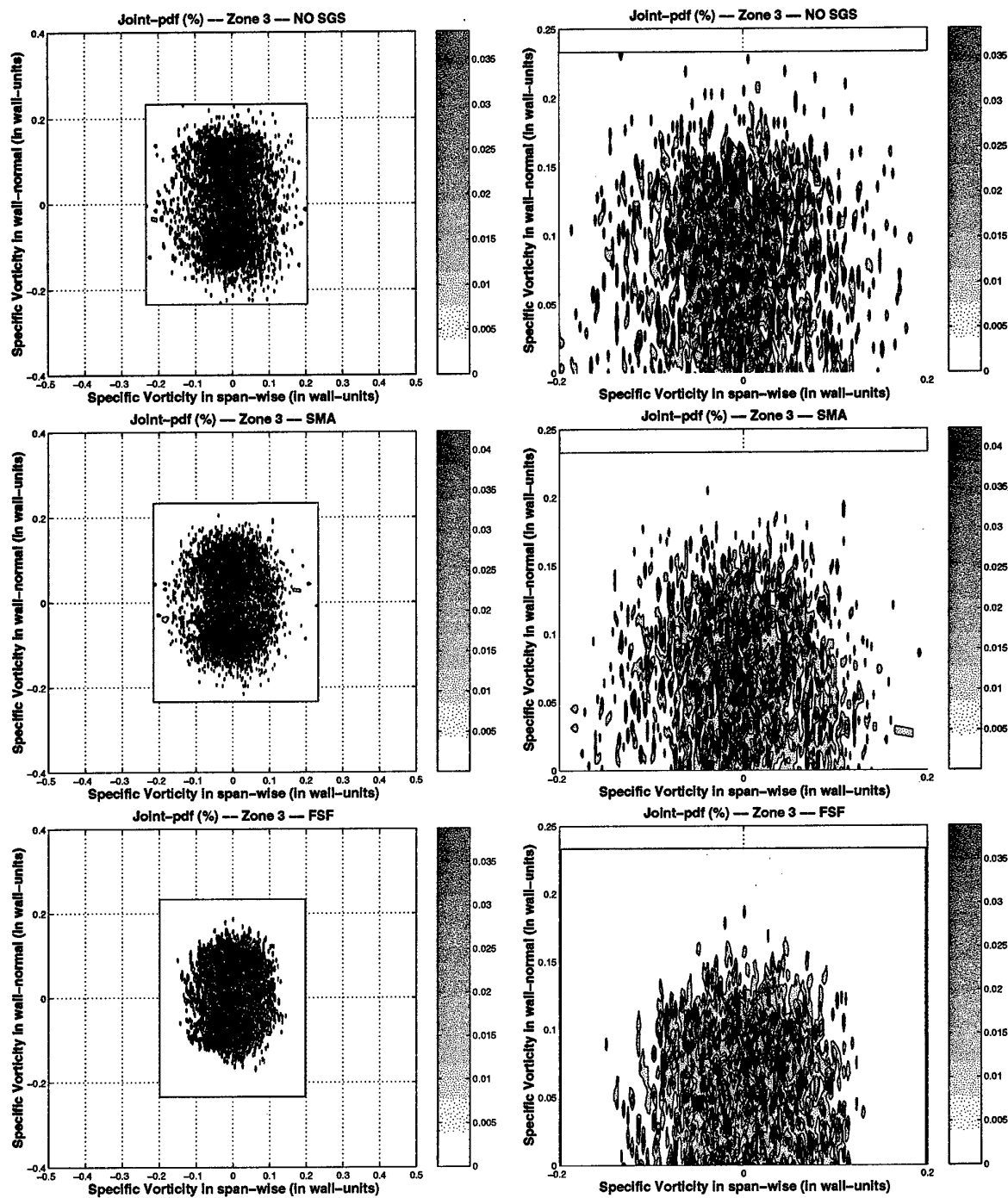


Fig. G.36: JPF for vorticity components between SGS models: Zone 3, $\omega_y - \omega_z$ -I-

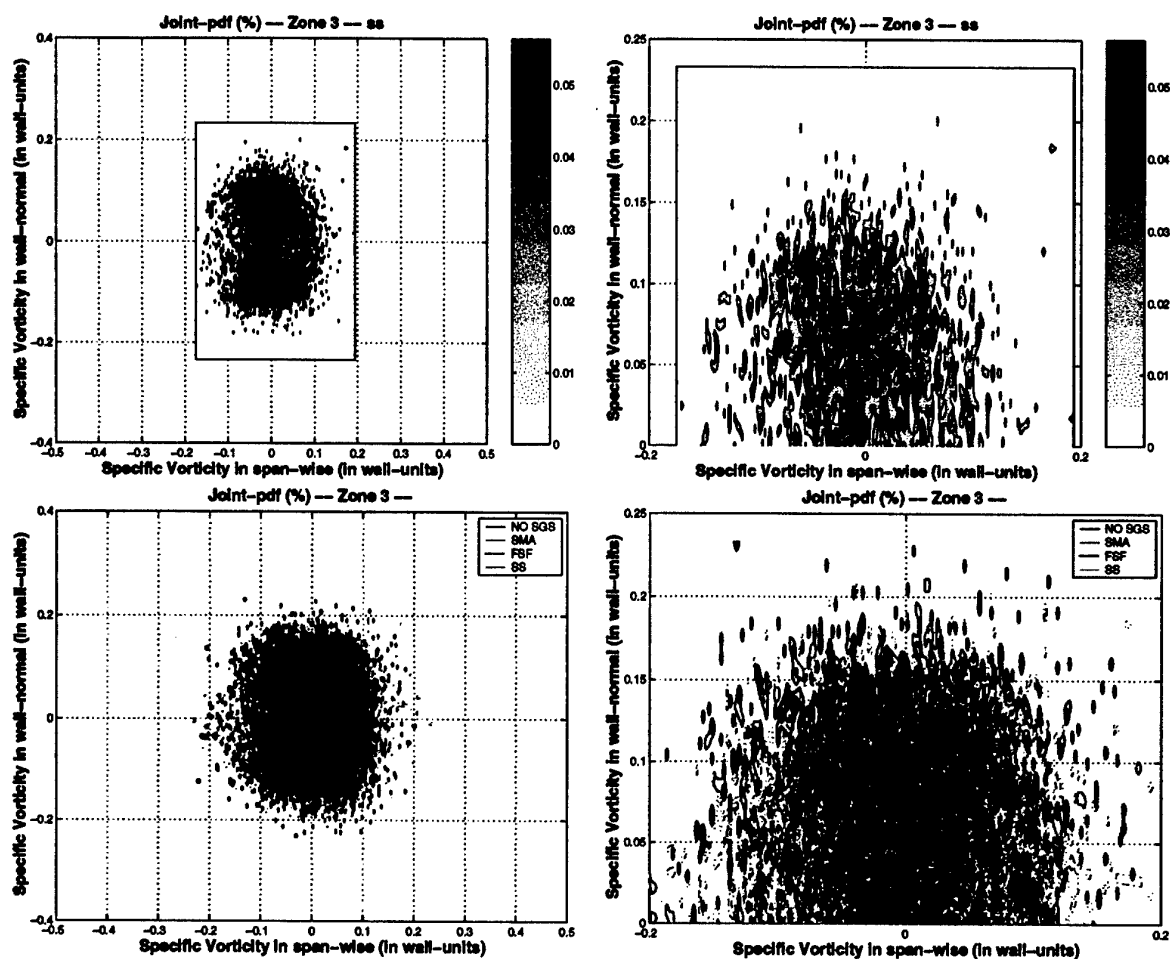


Fig. G.37: JPF for vorticity components between SGS models: Zone 3, $\omega_y - \omega_z$ -II-

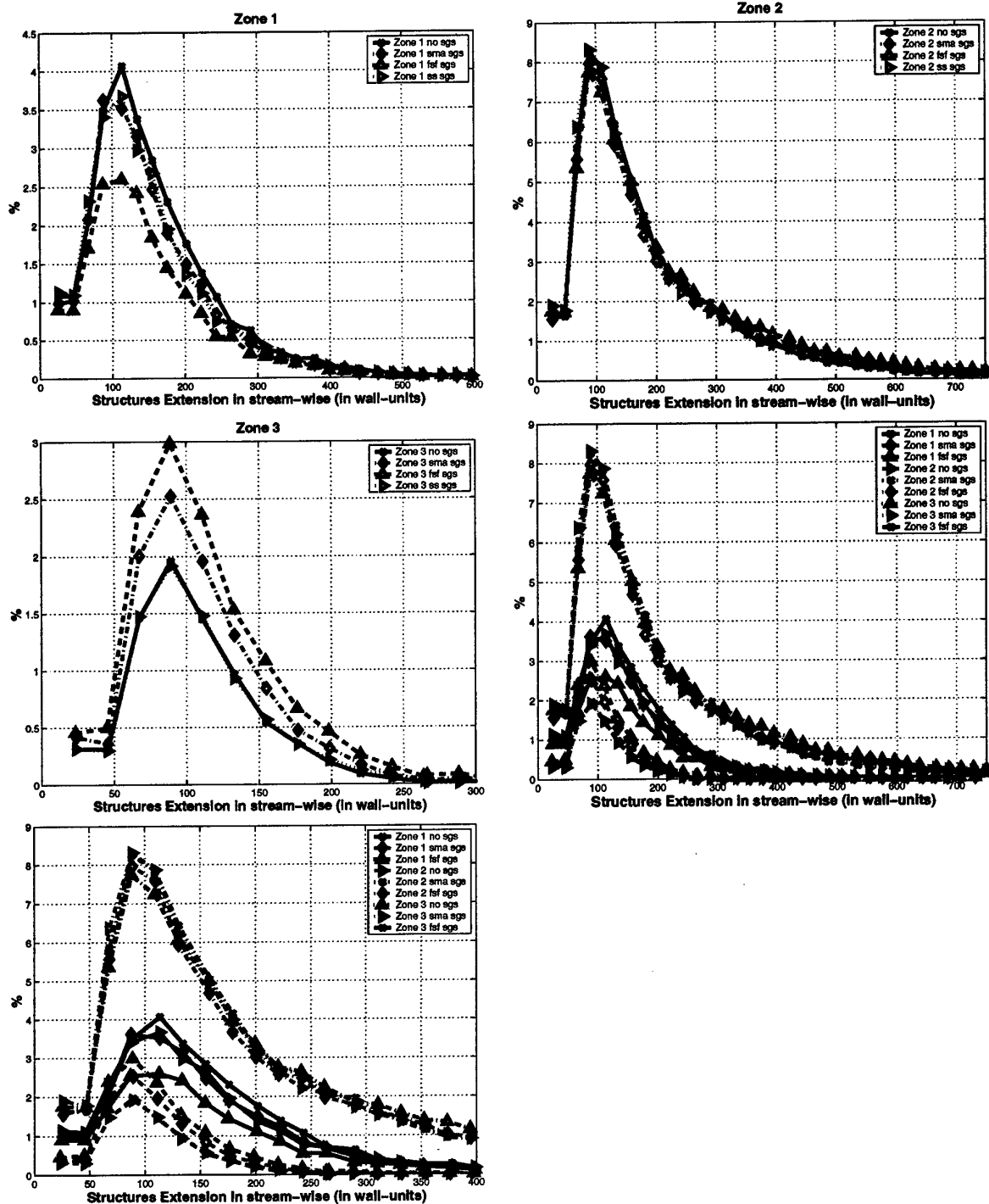


Fig. G.38: Comparison for structures length in stream-wise between SGS models

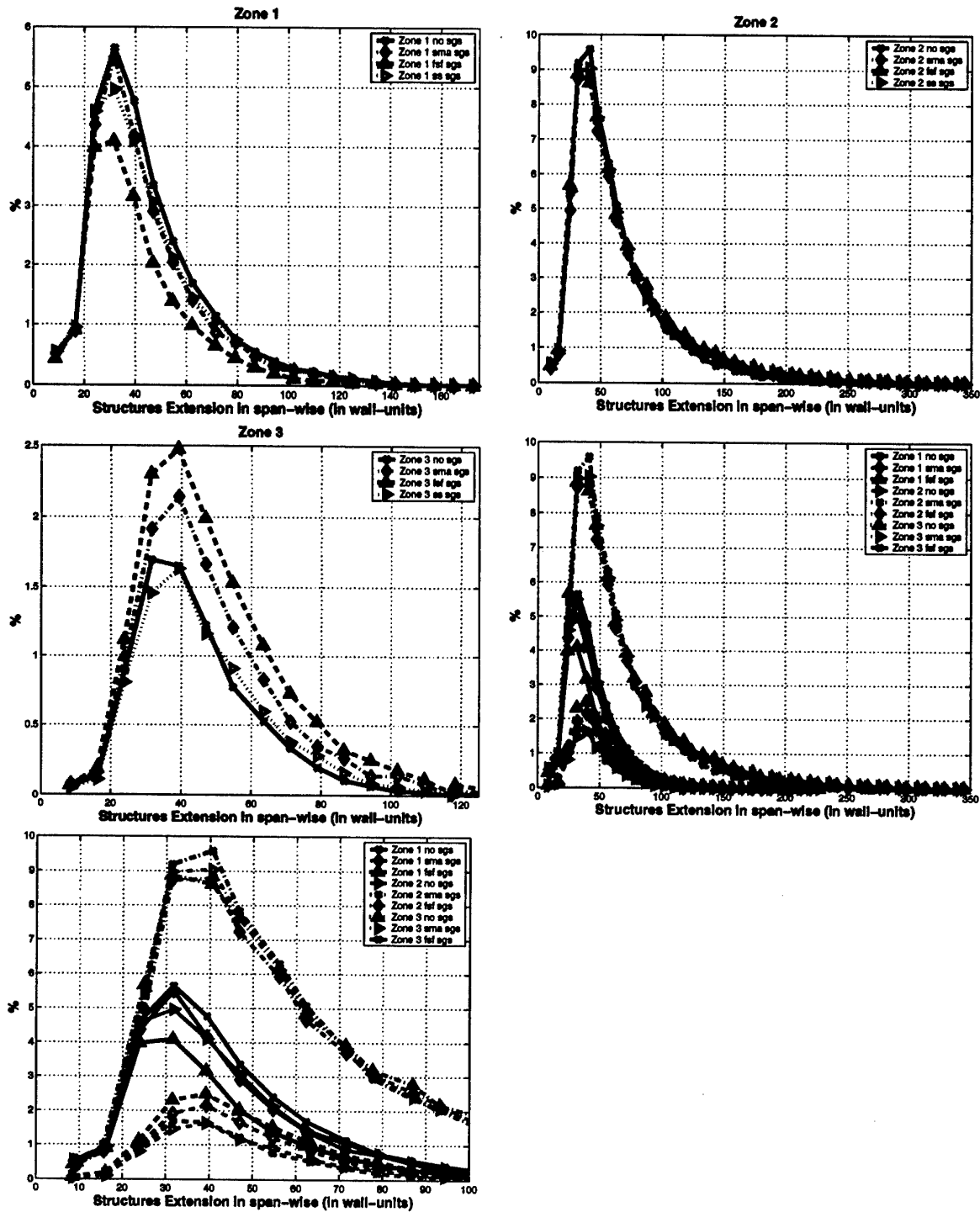


Fig. G.39: Comparison for structures length in span-wise between SGS models

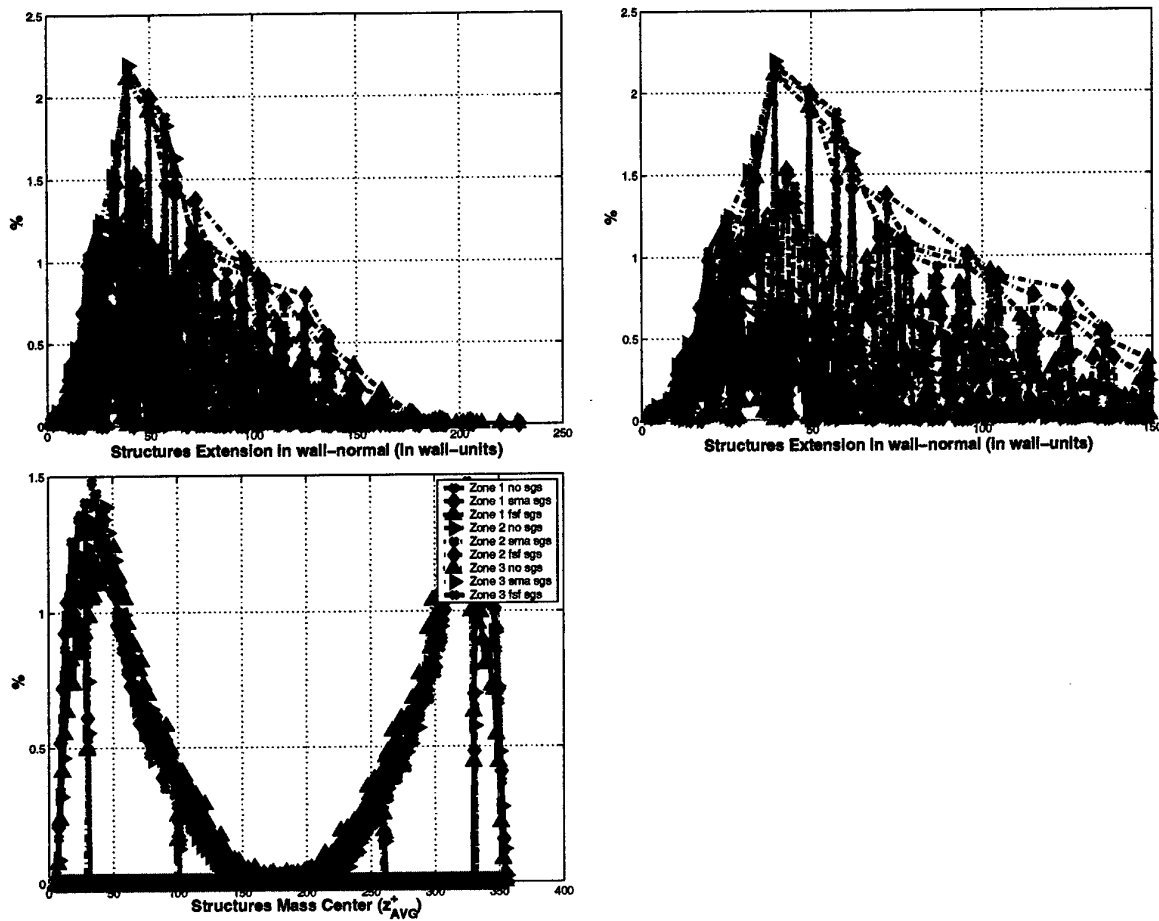


Fig. G.40: Comparison for structures length in wall-normal between SGS models plus position of mass center in wall-normal direction

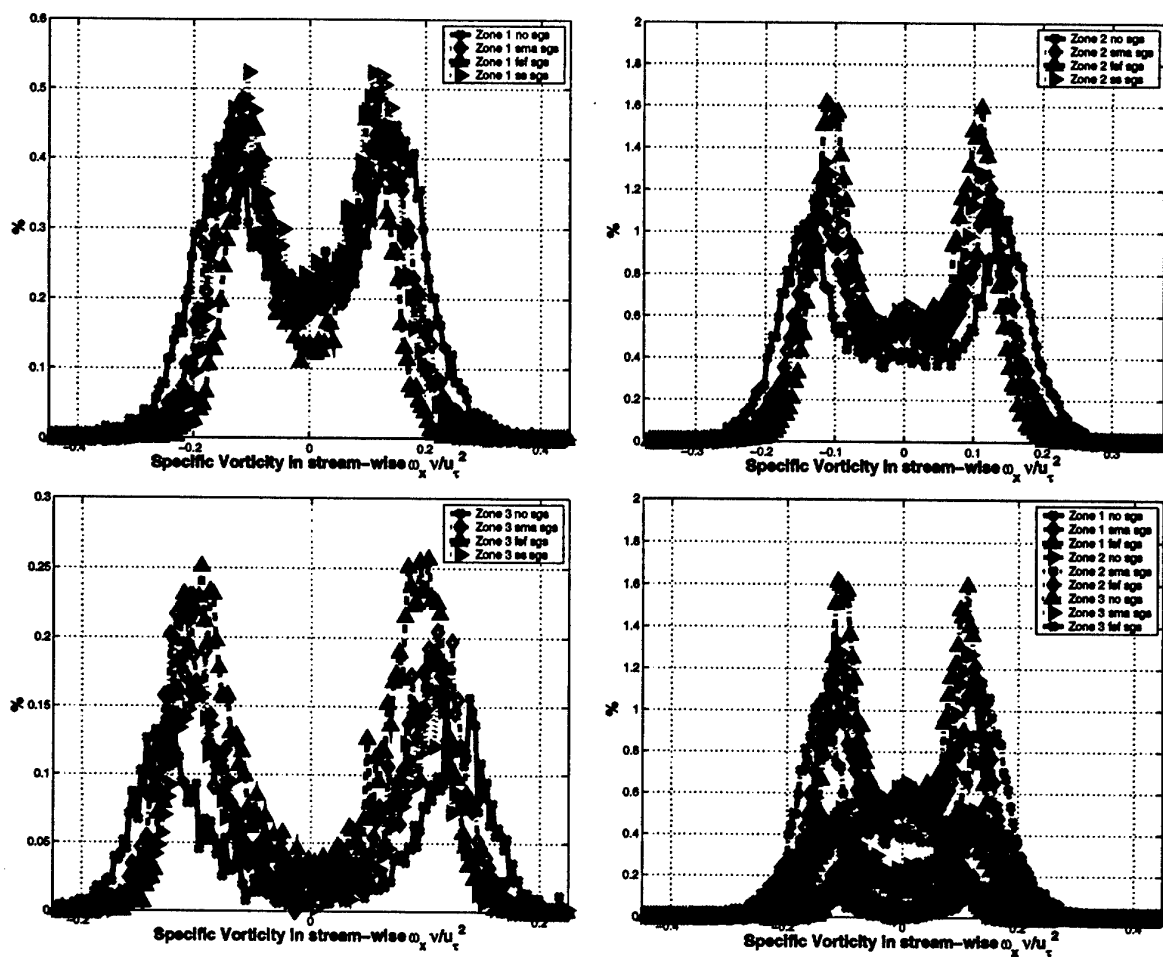


Fig. G.41: Comparison for structures vorticity in stream-wise direction between SGS models

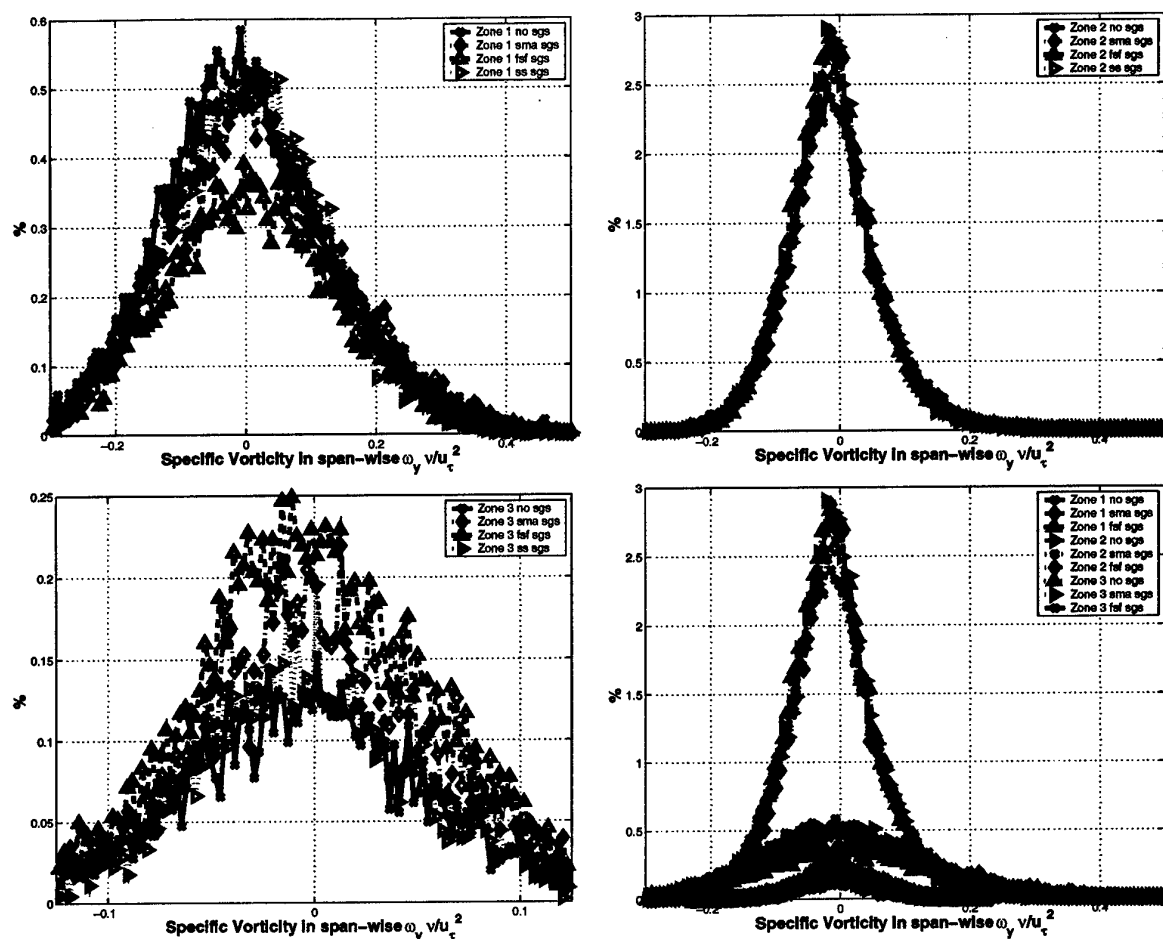


Fig. G.42: Comparison for structures vorticity in span-wise direction between SGS models

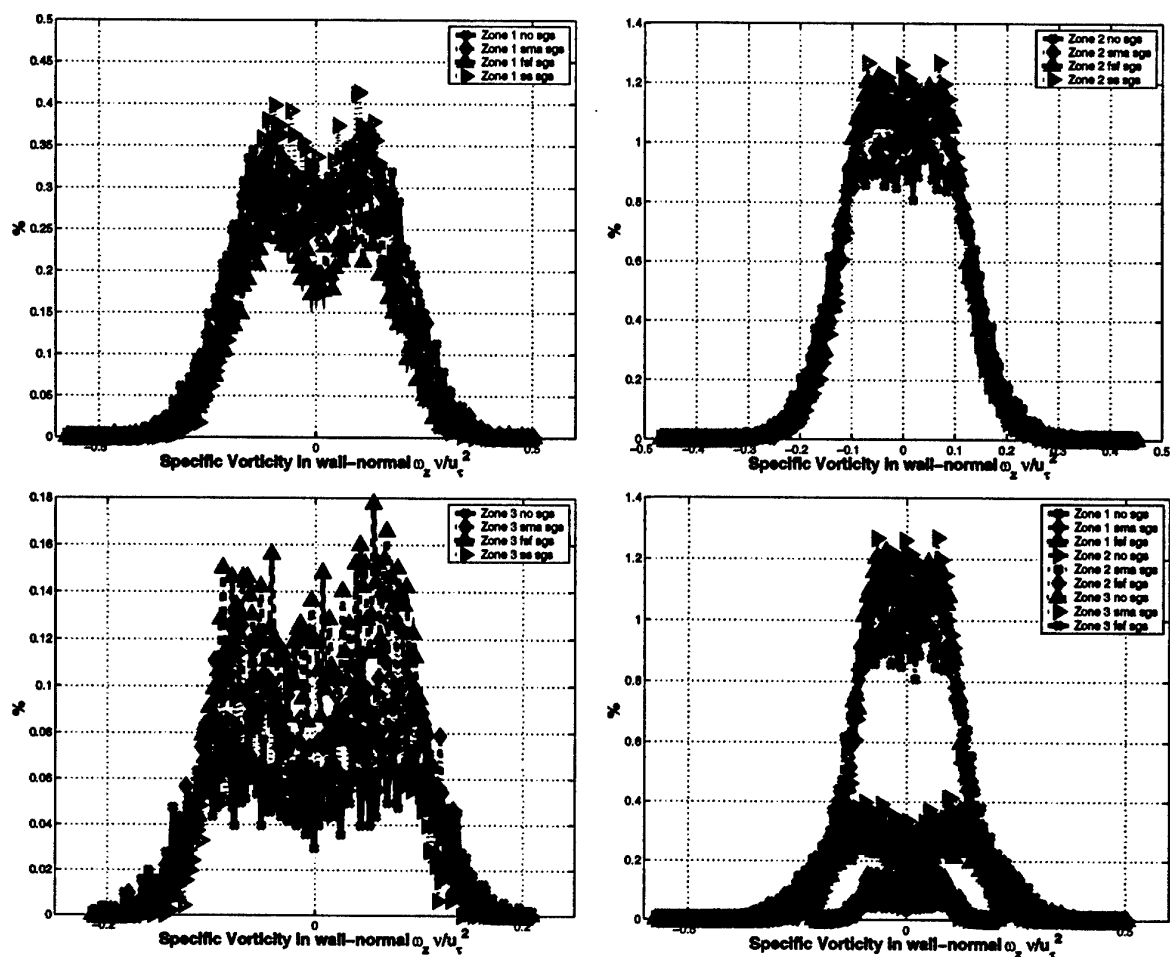


Fig. G.43: Comparison for structures vorticity in wall-normal direction between SGS models

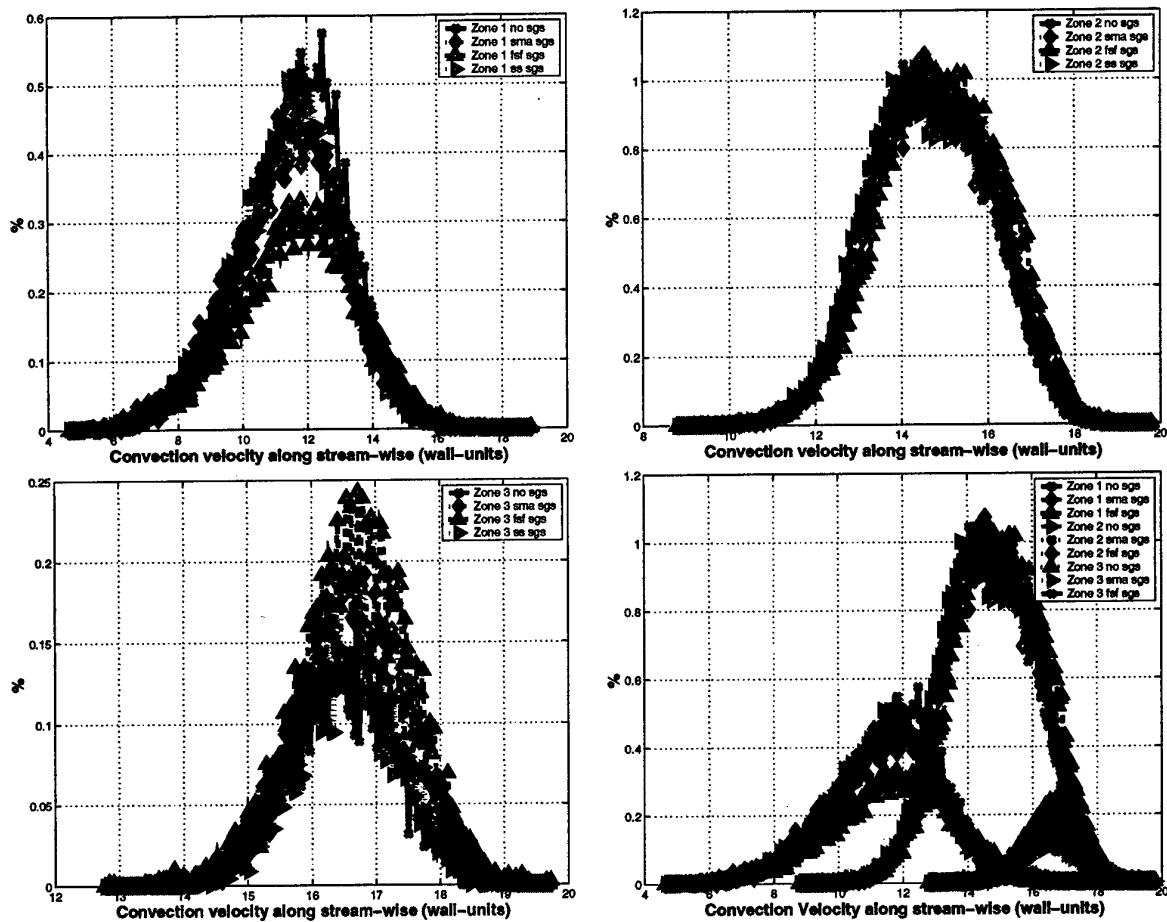


Fig. G.44: Comparison for structures convection velocity in stream-wise direction between SGS models

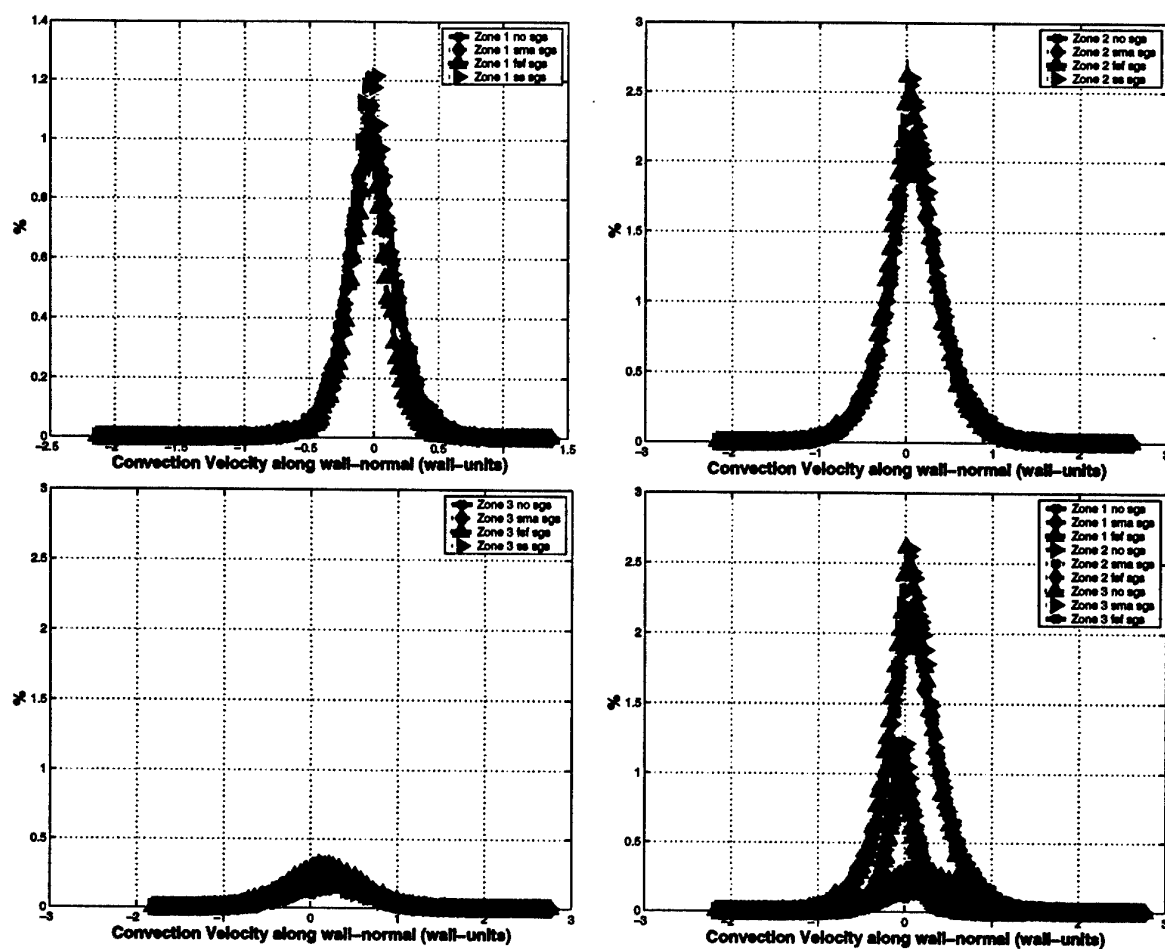


Fig. G.45: Comparison for structures convection velocity in wall-normal direction between SGS models

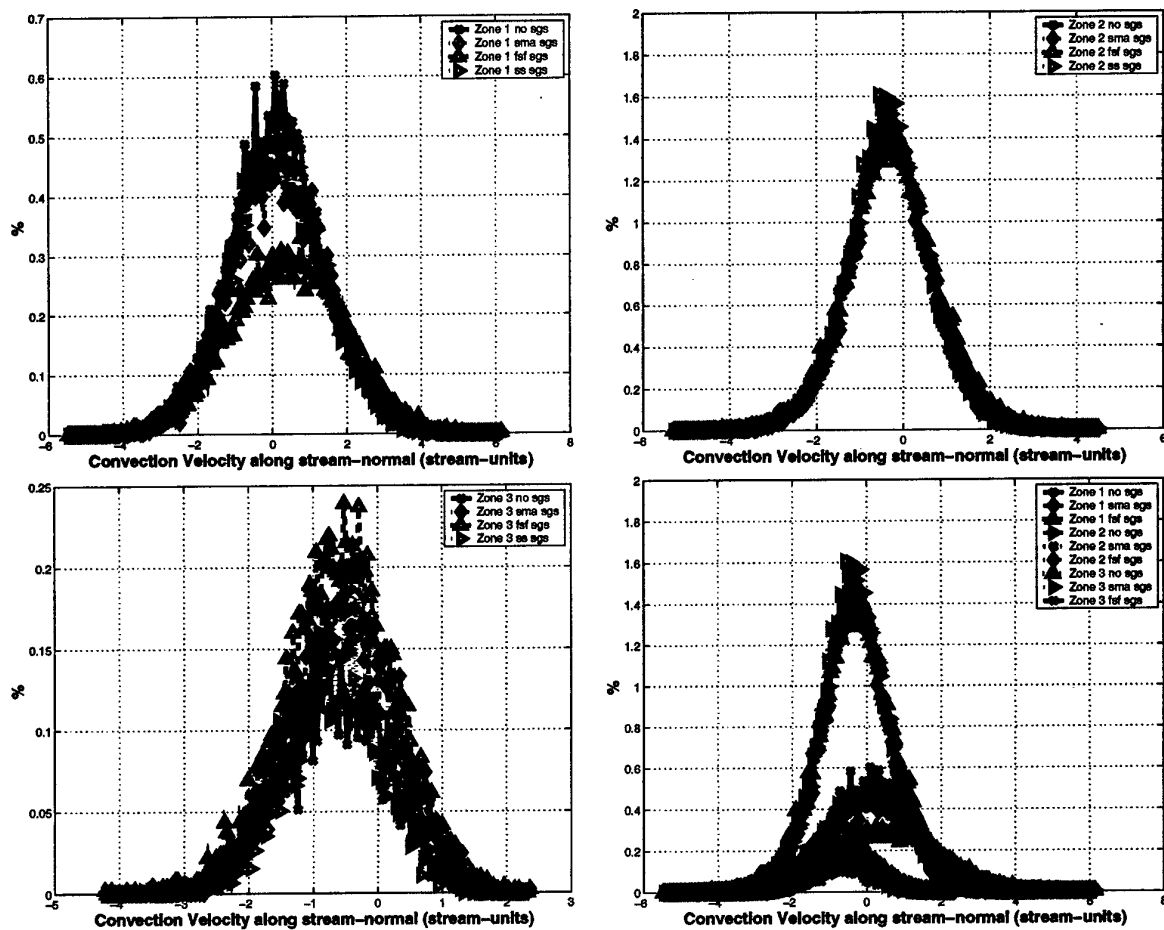


Fig. G.46: Comparison for structures ΔV in stream-wise direction between SGS models

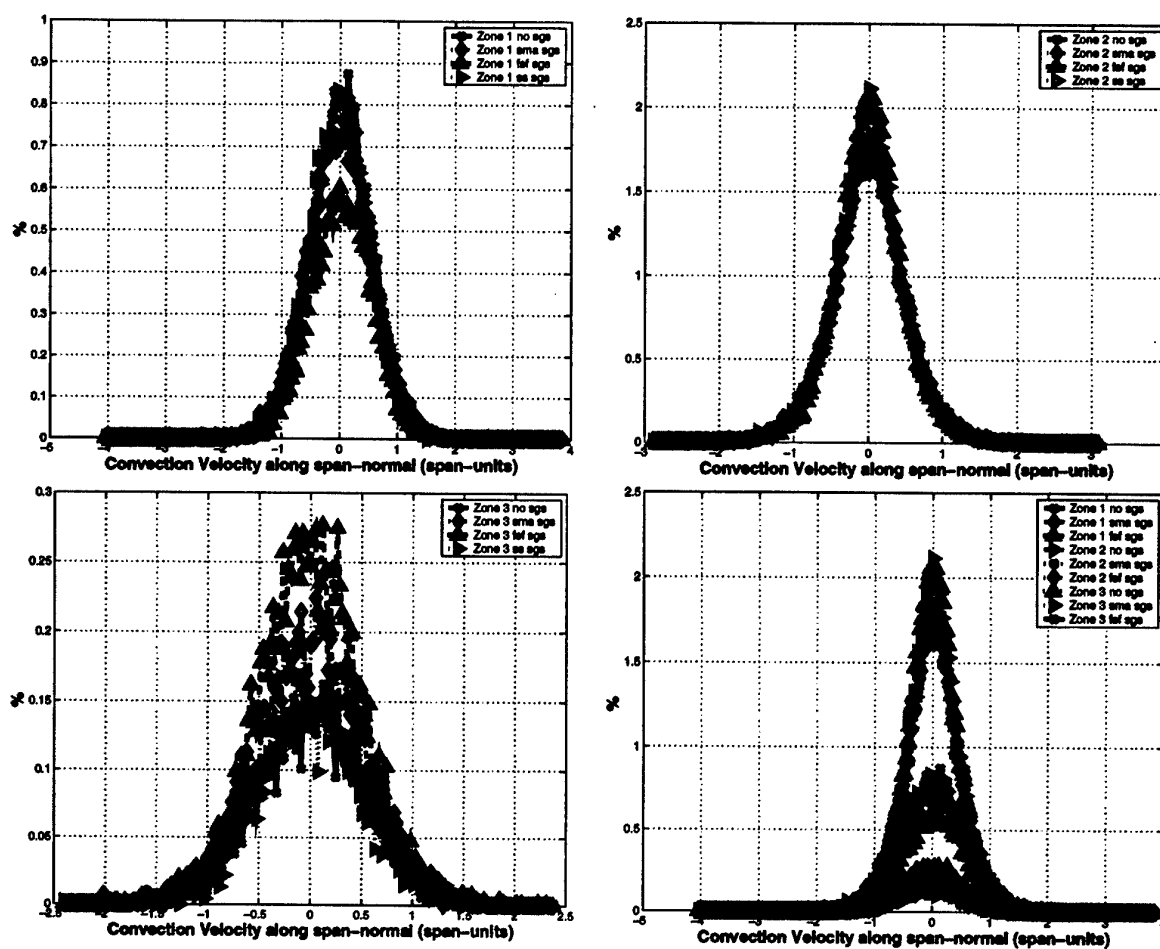


Fig. G.47: Comparison for structures ΔV in span-wise direction between SGS models

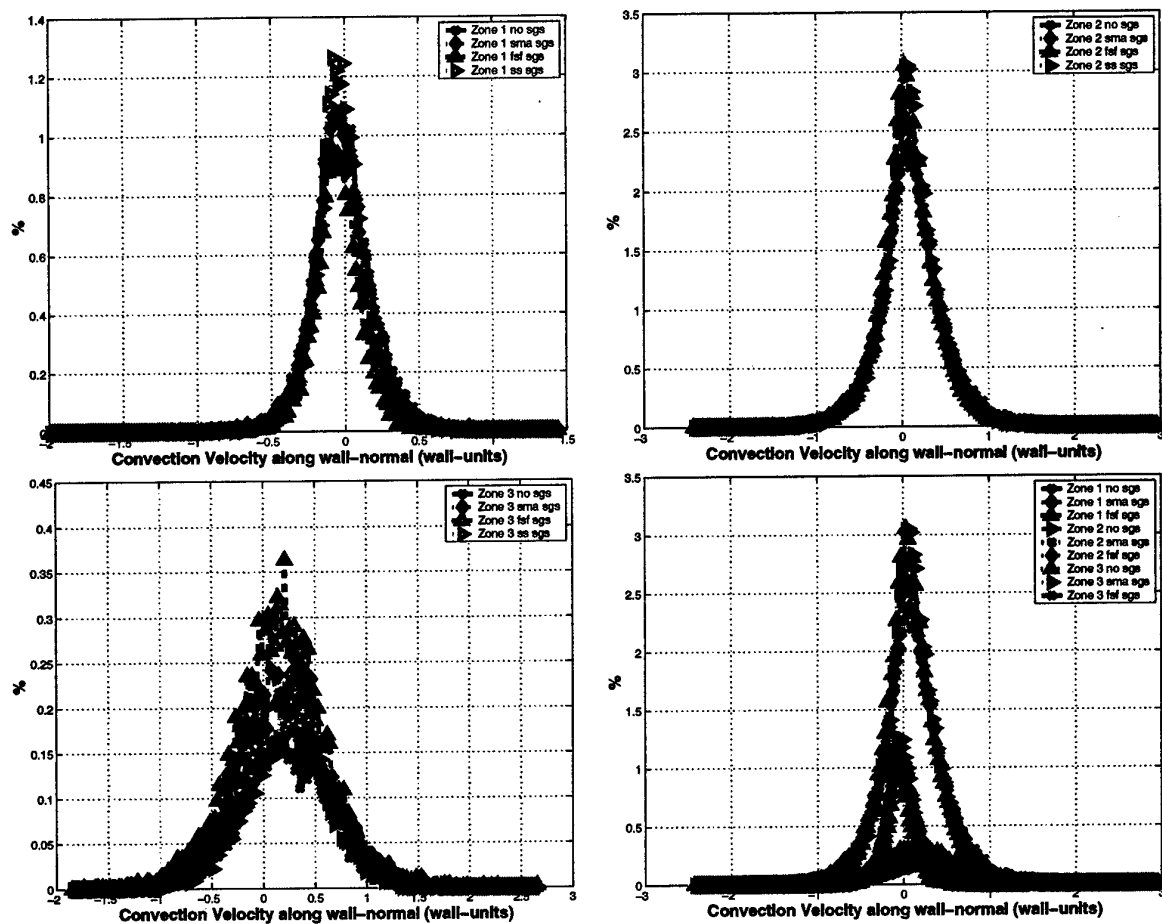


Fig. G.48: Comparison for structures ΔV in wall-normal direction between SGS models

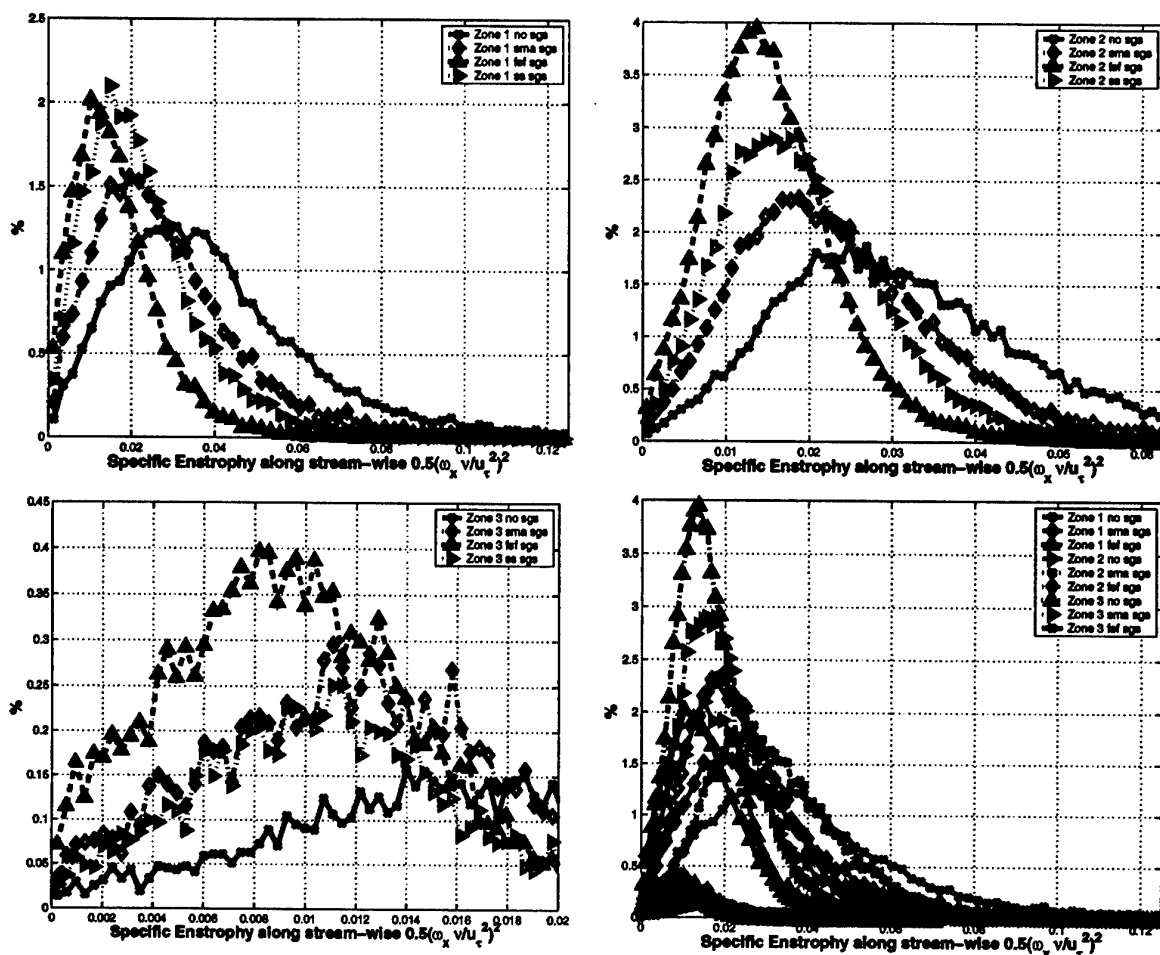


Fig. G.49: Comparison for structures entrophy in stream-wise direction between SGS models

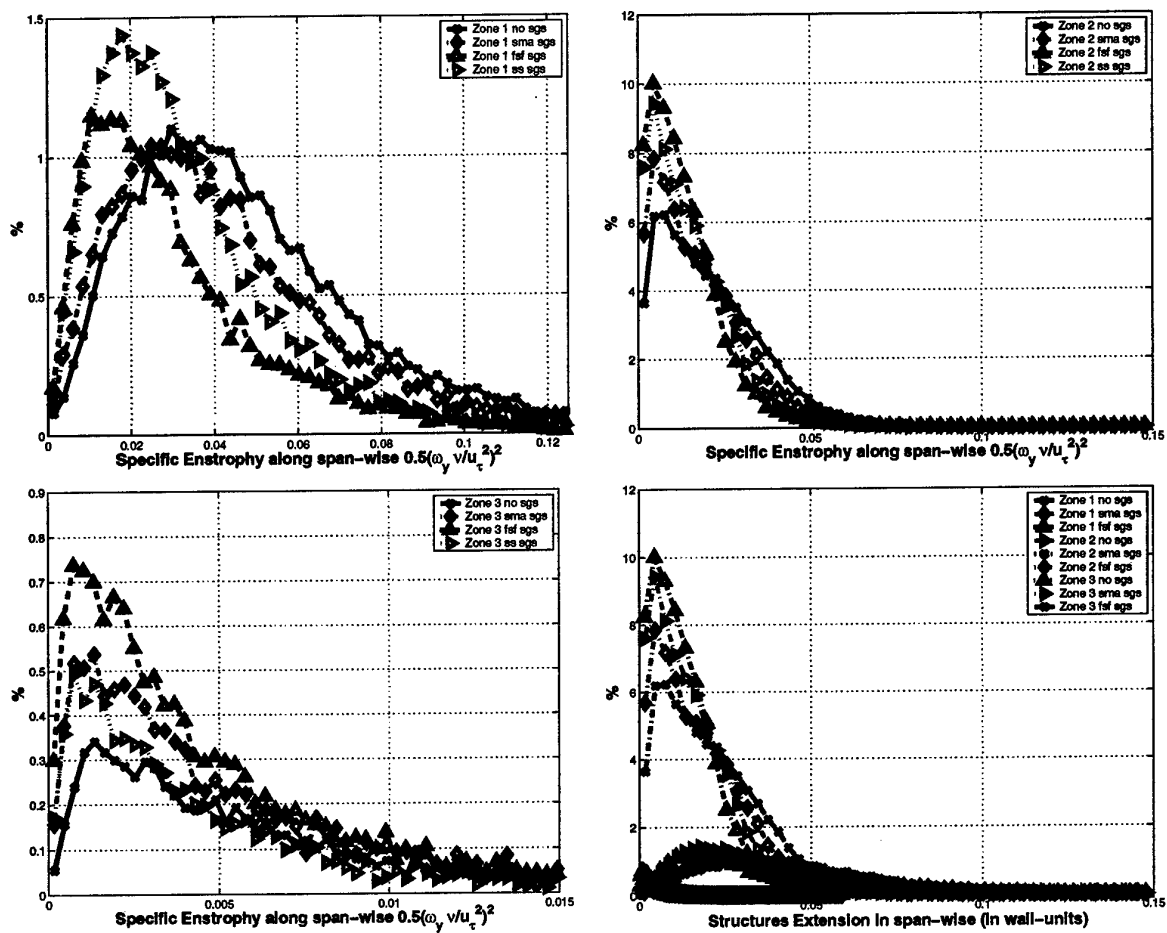


Fig. G.50: Comparison for structures enstrophy in span-wise direction between SGS models

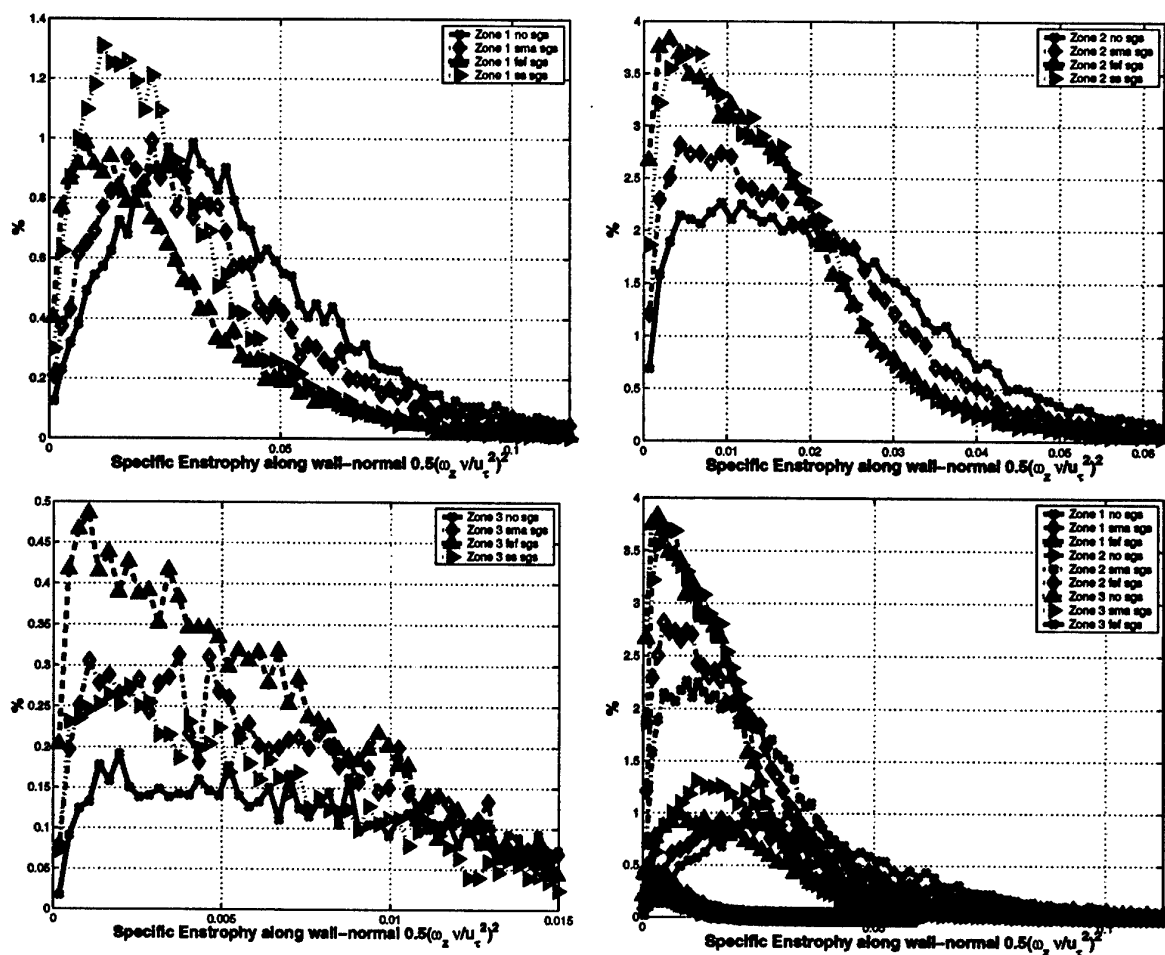


Fig. G.51: Comparison for structures enstrophy in wall-normal direction between SGS models

H. $Re_\tau = 395$

This appendix presents plots and information thought not necessary for the main analysis in § 6.2.

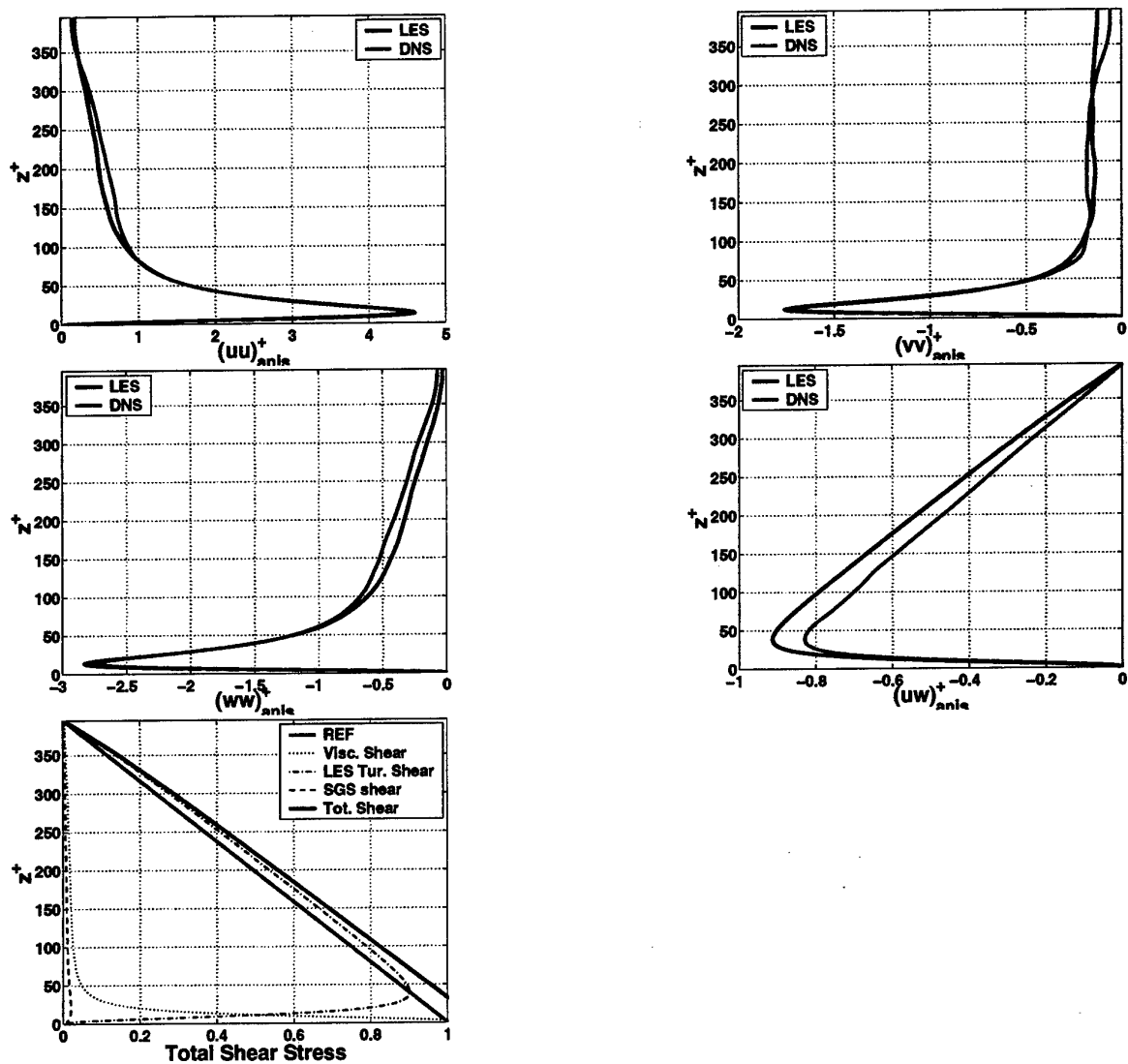


Fig. H.1: Anisotropic part of the resolved Reynolds stress tensor of plane channel at $Re_\tau = 395$ and total shear stress

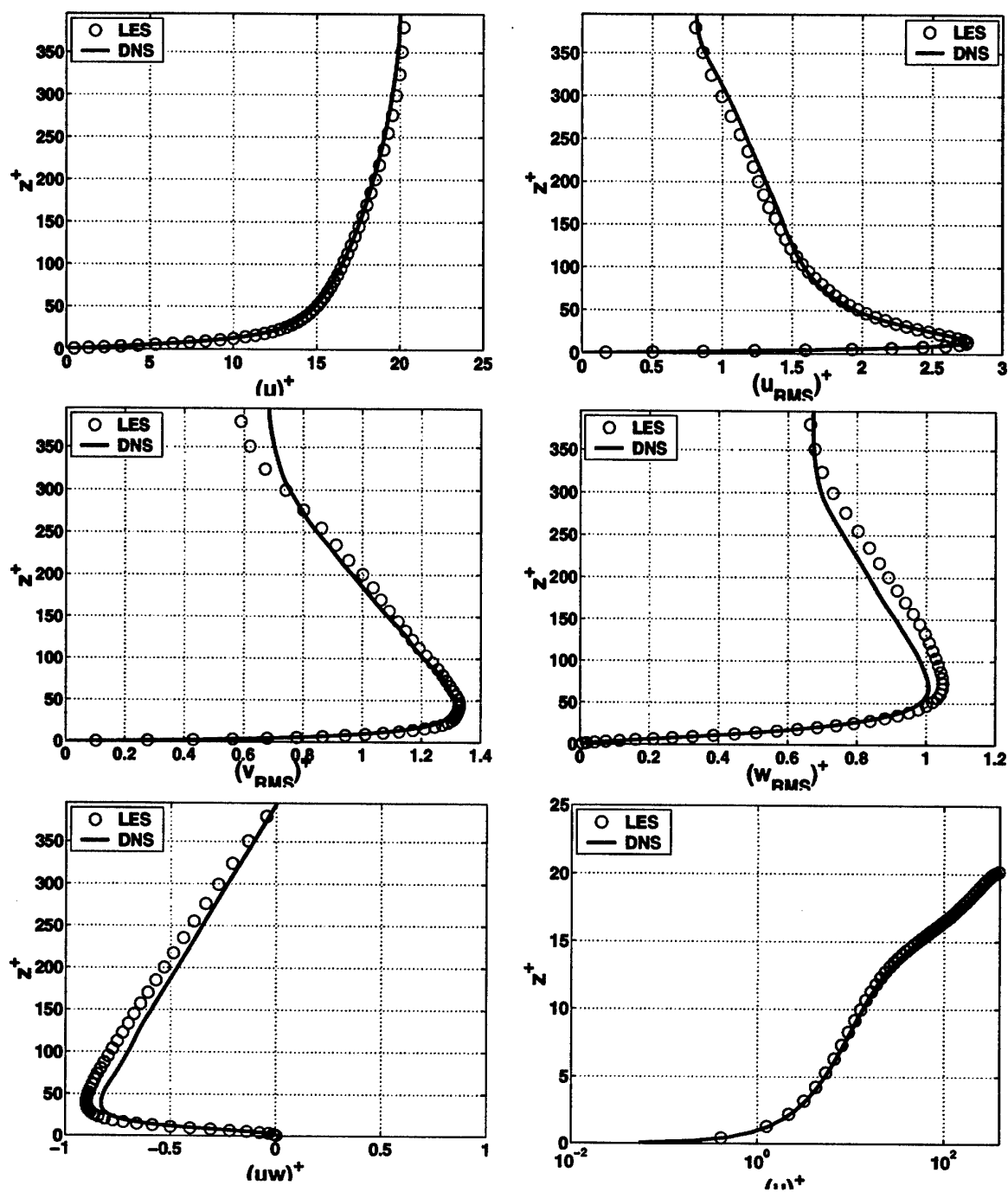


Fig. H.2: Mean stream-wise velocity and rms of resolved turbulence of plane channel at $Re_\tau = 395$

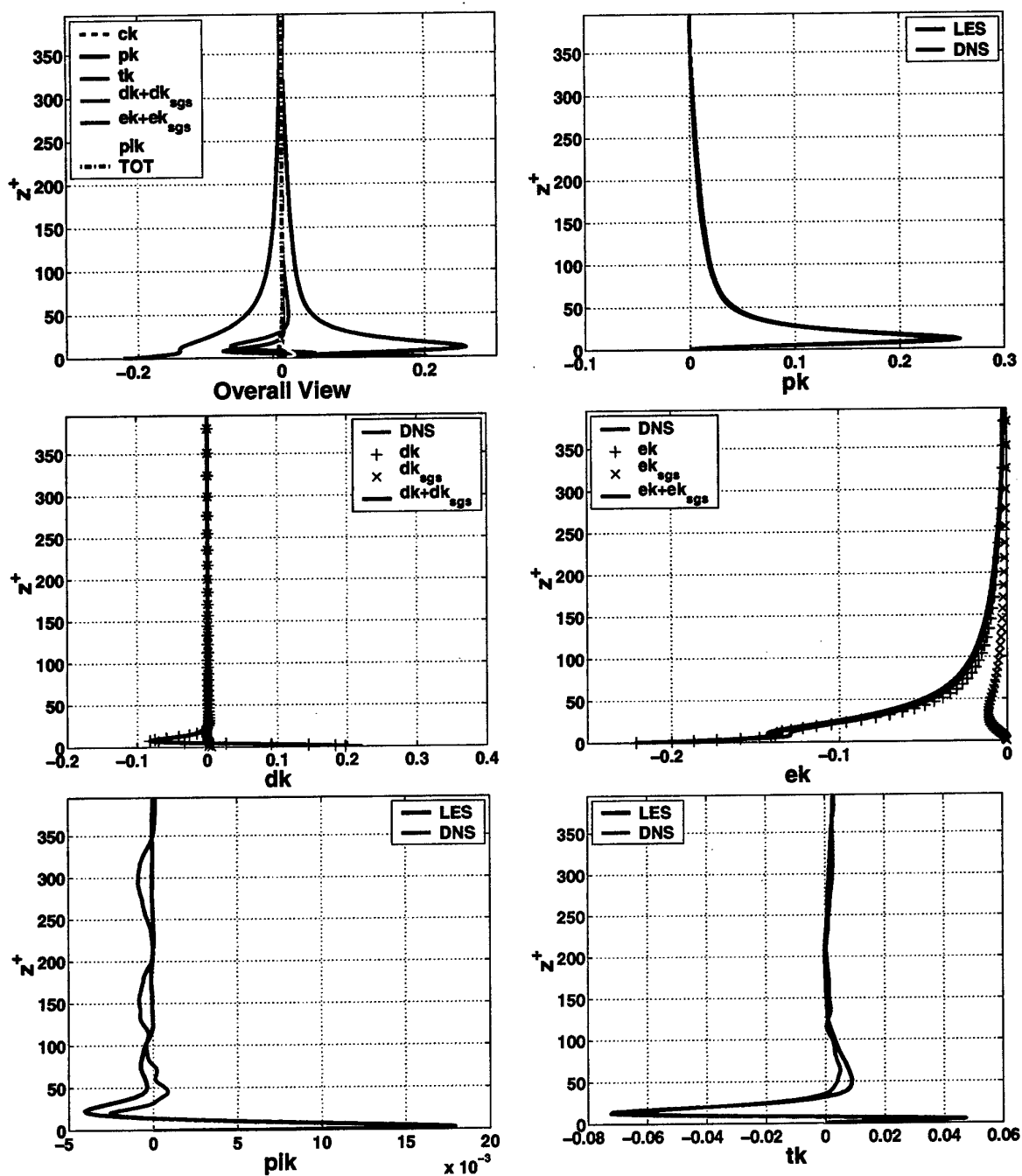


Fig. H.3: Budget of resolved turbulent kinetic energy of plane channel at $Re_\tau = 395$

I. $Re_\tau = 590$

This appendix presents plots and information thought not necessary for the main analysis in § 6.3.

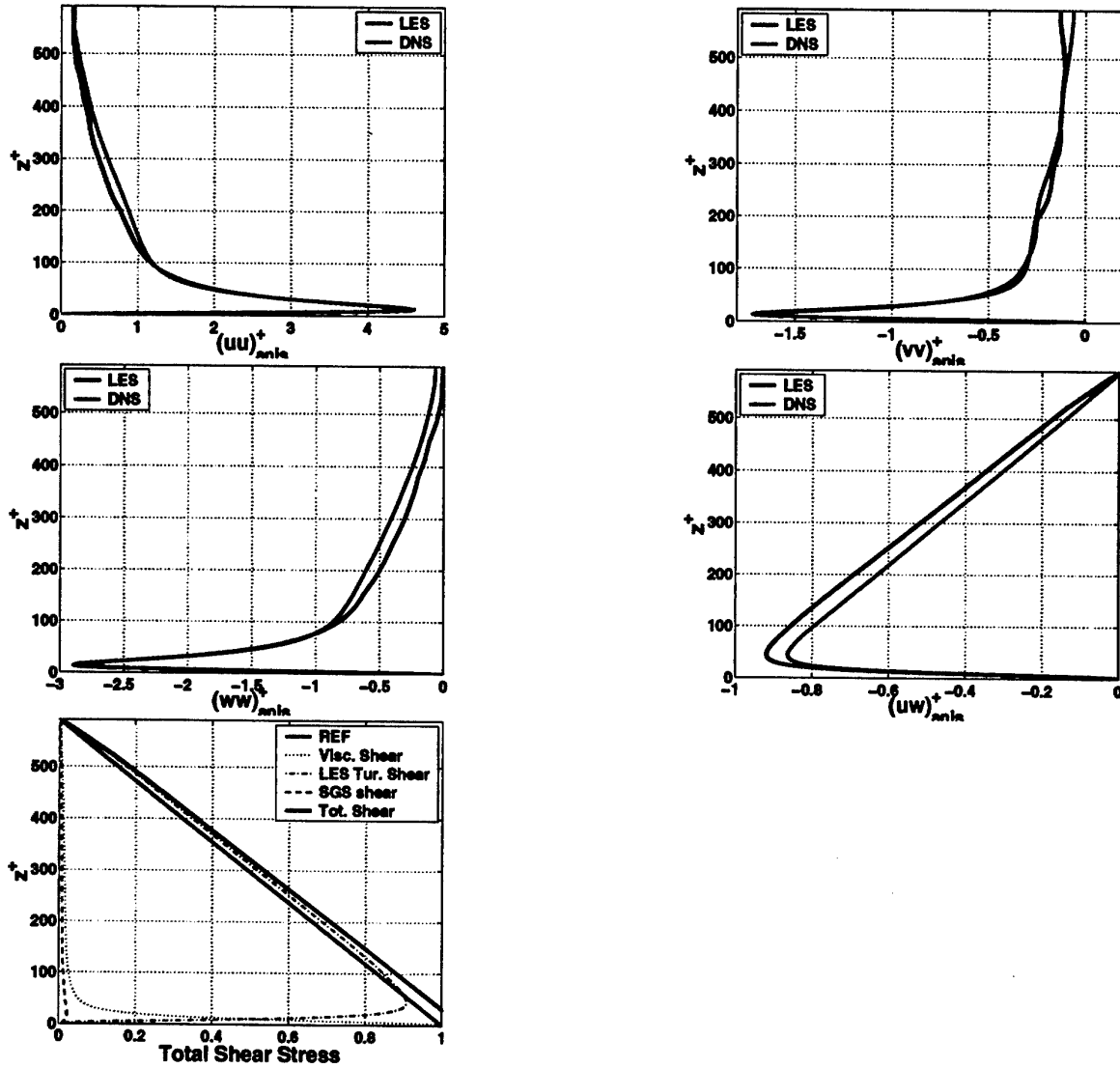


Fig. I.1: Anisotropic part of the resolved Reynolds stress tensor of plane channel at $Re_\tau = 590$ and total shear stress

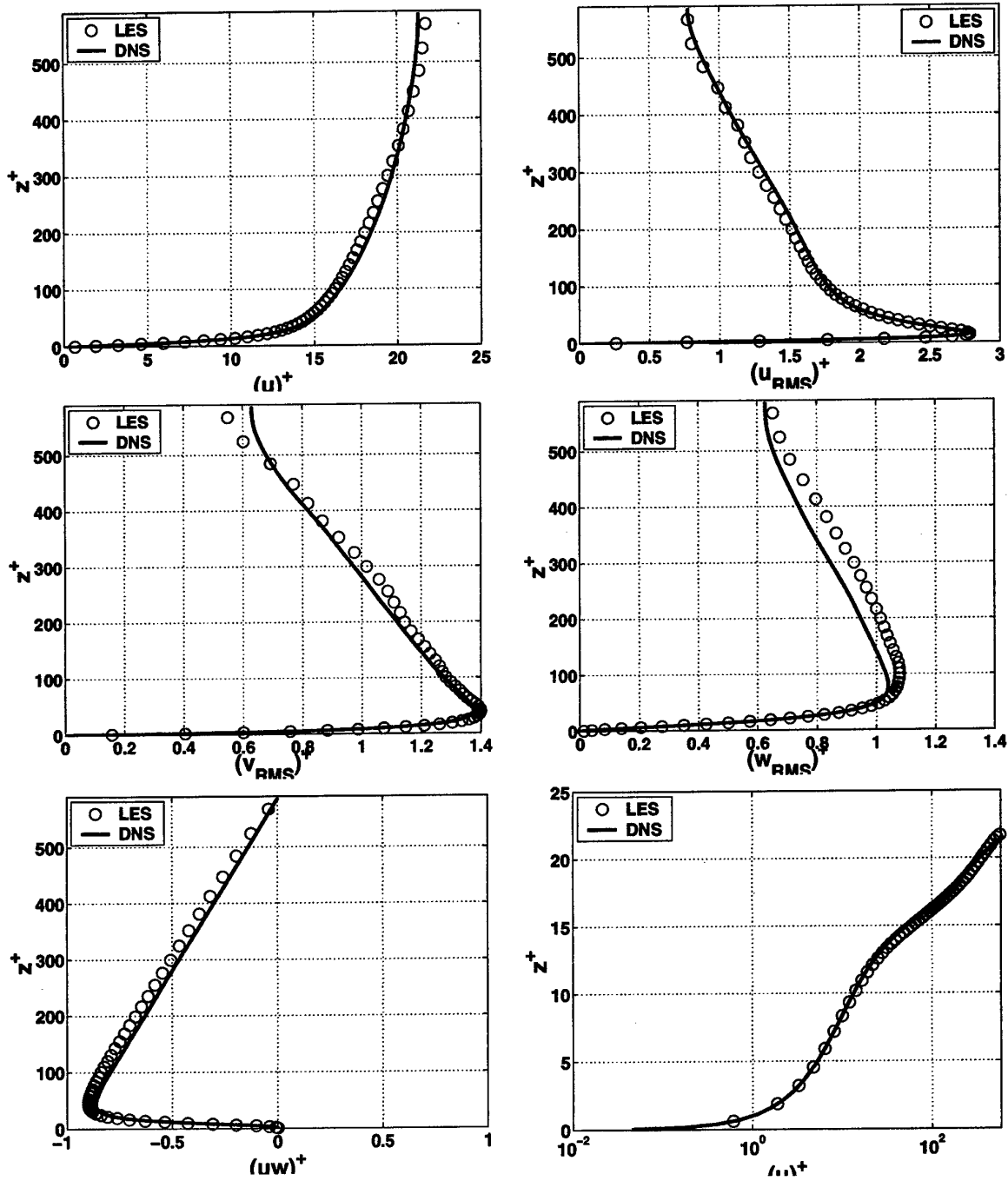


Fig. I.2: Mean stream-wise velocity and rms of resolved turbulence of plane channel at $Re_\tau = 590$

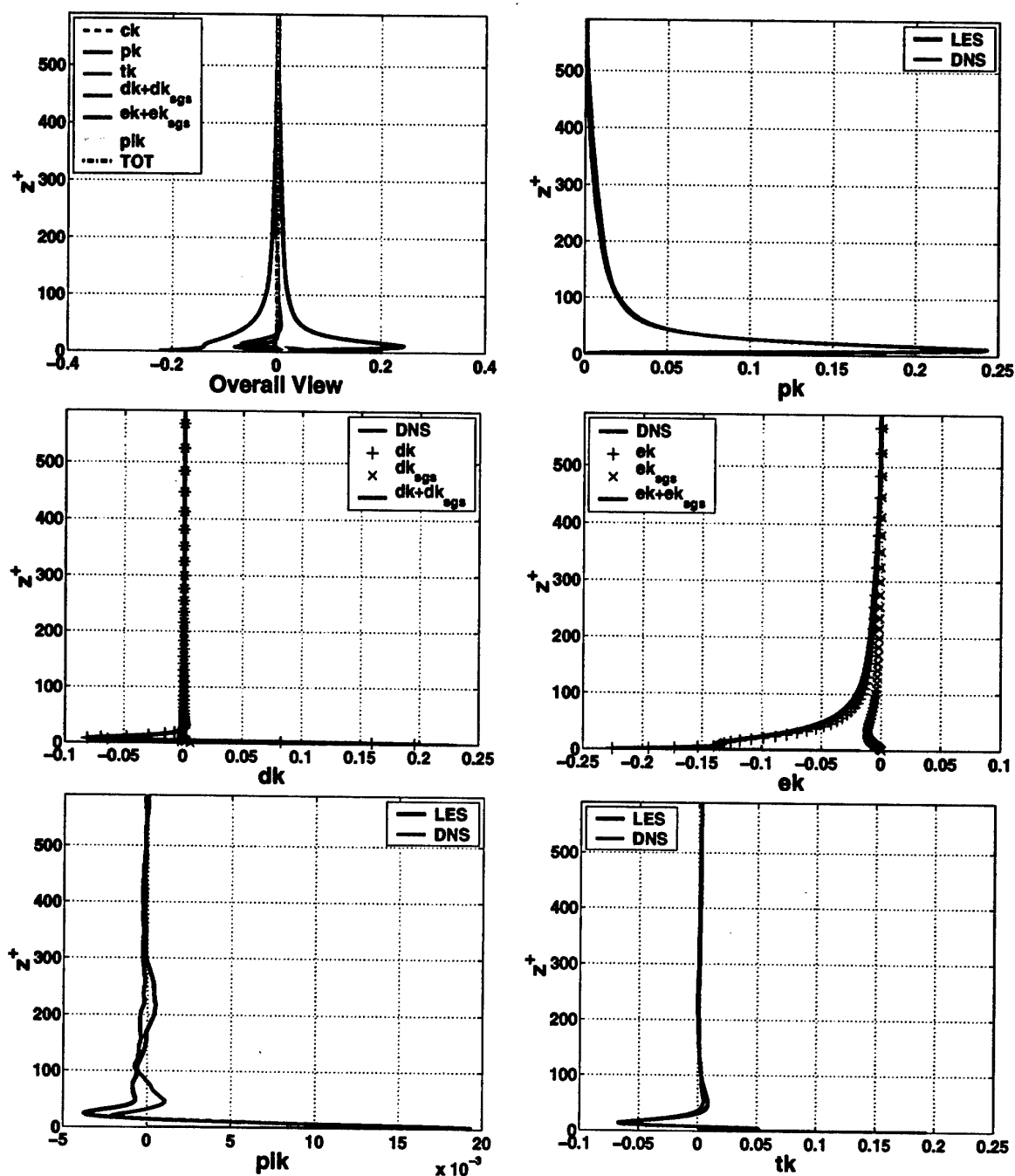


Fig. I.3: Budget of resolved turbulent kinetic energy of plane channel at $Re_\tau = 590$

REPORT DOCUMENTATION PAGE

Form Approved OMB No. 0704-0188

Public reporting burden for this collection of information is estimated to average 1 hour per response, including the time for reviewing instructions, searching existing data sources, gathering and maintaining the data needed, and completing and reviewing the collection of information. Send comments regarding this burden estimate or any other aspect of this collection of information, including suggestions for reducing this burden to Washington Headquarters Services, Directorate for Information Operations and Reports, 1215 Jefferson Davis Highway, Suite 1204, Arlington, VA 22202-4302, and to the Office of Management and Budget, Paperwork Reduction Project (0704-0188), Washington, DC 20503.

1. AGENCY USE ONLY (Leave blank)

2. REPORT DATE

December 2002

3. REPORT TYPE AND DATES COVERED

Final Technical Report

4. TITLE AND SUBTITLE

LES investigation of coherent structures in boundary layers and wakes
Volume I: Investigation of coherent structure in an attached shear layer

5. FUNDING NUMBERS

Grant No. N0014-99-1-0834

6. AUTHOR(S)

R. Giammanco & C. Benocci

7. PERFORMING ORGANIZATION NAME(S) AND ADDRESS(ES)

Institut von Karman de Dynamique des Fluides (Von Karman Institute for Fluid Dynamics)
Chaussee de Waterloo, 72
1640 Rhode-Saint-Genese, BELGIUM

8. Performing Organization Report Number

Grant No. : N00014-99-1-0834

9. SPONSORING/MONITORING AGENCY NAME(S) AND ADDRESS(ES)

Office of Naval Research, Ballston Centre Tower, 800 North Quincy Street Arlington, VA 22217-5660

10. SPONSORING/MONITORING
AGENCY REPORT NUMBER
EAR9944

11. SUPPLEMENTARY NOTES

This research was sponsored by the Office of Naval Research (ONR Grant Number: N00014-99-1-0834; Contract Report 2003-08). Reproduction in whole or in part is permitted for any purpose of the United States Government. Part of a three volume set -- LES investigation of coherent structures in boundary layers and wakes -- **Volume I: Investigation of coherent structure in an attached shear layer (240 pages);** Volume II: Wake Around Square Cylinder (164 pages); Volume III: Development of a Parallel Unstructured Grid LES Code (173 pages).

12a. DISTRIBUTION/AVAILABILITY STATEMENT

Approved for public release; distribution is unlimited.

12b. DISTRIBUTION CODE

A

ABSTRACT (Maximum 200 words)

Purpose of the present investigation was to assess the feasibility of simulating and studying coherent structures in turbulent shear layers, making use of Large Eddy Simulations (LES). The current investigation has been performed across a rather wide range of simulated flows and LES implementations, starting from an established and validated structured LES code based on finite differences and cartesian grids ending to an unstructured LES code under development. The use of the unstructured approach was considered necessary whenever complex geometries have to be analyzed, which cannot be handled by the structured code, regardless its advanced features (like multi-domain approach). The unstructured LES code was developed in the frame of current GRANT, and it has undergone validation. The structured LES code, which had already validated over a wide range of flow configurations, was used to analyze the wake behind an obstacle, attempt which was not made before. Extensive studies were needed in the attempt to validate to code for this case.

Given the wide scope of present report and the mass of data available from different LES codes, flows and structures, the work has been spit between two work groups, the one devoted to the structured LES and the one devoted to the unstructured LES. In this frame it was found more practical to sub-divide the full report in three volumes: Volume I -- Investigation of Coherent Structures in an Attached Shear Layer; Volume II -- Wake around square Cylinder; Volume III -- Unstructured LES.

The different volumes are not completely independent: Volume I, for example, in the description of the structured LES code, introduces concepts and algorithms which will be applied in computations that will be presented only in Volume II. The subdivision of present report in different volumes was, indeed, adopted to simplify the organize and present the collected data, and also to take into account the fact that different groups worked on different aspects of the grant, and their respective work should be easily recognizable. Volume I of present report has described the general background, the main development and the results obtained for wall bounded turbulent flow, particularly, for the case of turbulent plane channel flow at equilibrium. Volume II is devoted to the study of the flow around an obstacle, specifically, a cylinder with square cross section and infinite length in span-wise direction. This test case belongs to a completely different class of flows, respect to the one analyzed in Volume I, and it is a severe test case; for the LES code.

Most of the advanced features of the code were exploited to achieve this task, different simulations were performed, in order to collect, whenever possible, sufficient data to draw conclusions and remarks. Differently from the case of channel flow, where the code has been extensively validated and analyzed in detail, down to the level of turbulent kinetic energy budget, the present flow constitutes a still active area of basic research. The higher complexity of the flow, the absence of a second direction of homogeneity, beside the span-wise direction, the existence of a dominant frequency in the flow, the necessity of employing upwinding discretization for advection terms and other numerical difficulties have led to such complexities of execution that only the very basic set of statistics (statistical moments of first and second order) were obtained. At the same time, limits and draw-backs for current LES code implementation have been outlined. Most of the efforts were devoted to reach a sufficient similarity in behavior between LES simulation and reference experimental data; this attempt has led to build grids not perfectly suited to analyze structures applying the criteria introduced in Volume I, which are based on operators working on the tensor of gradient of velocity.

This fact, together with intrinsic difficulty of dealing with the presence of a wide range of structures of different sizes and shapes, has limited the possibility to obtain a thorough and complete description of vortical behavior for this class of flow. However, it was possible to find useful global statistics for organized turbulence and to show that a very important part of the entire turbulent field lies within very active structures, which cover a very small part of the entire flow field. It can be moreover suggested that these characteristics of these structures are the ones which define and control the wake behavior, and their identification could be key of understand and possibly identify and recognize specific wakes.

Possible avenues for future investigations starting from present study are also suggested.

14. SUBJECT TERMS

ONR, Belgium, Large-Eddy simulations, SGS models, LES equations, Coherent structure concept, Wall shear layer

15. NUMBER OF PAGES

16. PRICE CODE

17. SECURITY CLASSIFICATION
OF REPORT

UNCLASSIFIED

18. SECURITY CLASSIFICATION
OF THIS PAGE

UNCLASSIFIED

19. SECURITY CLASSIFICATION
OF ABSTRACT

UNCLASSIFIED

20. LIMITATION OF ABSTRACT

UL

2980NR20Feb03



von KARMAN INSTITUTE FOR FLUID DYNAMICS INPA

INSTITUT von KARMAN DE DYNAMIQUE DES FLUIDES AISBL

von KARMAN INSTITUUT VOOR STROMINGSDYNAMICA IVZW

REF.

Dr. Patrick Purtell
Office Naval Research
Ballston Center Tower One,
800 North Quincy Street
Arlington VA 22217-5660
U.S.A.

Administrative Office
Office of Naval Research Regional Office Boston
495 Summer Street Room 627
Boston MA 02210-2109
U.S.A

Defense Technical Information Center
8725 John J. Kingman Road Ste 0994
Fort Belvoir VA 22060-6218
U.S.A.

Office of Naval Research
ATTN: ONR 363
Ballston Center Tower One,
800 North Quincy Street
Arlington VA 22217-5660
U.S.A.

Patent Office
Office of Naval Research
ATTN: ONR 00CC
Ballston Center Tower One,
800 North Quincy Street
Arlington VA 22217-5660
U.S.A.



von KARMAN INSTITUTE FOR FLUID DYNAMICS INPA

INSTITUT von KARMAN DE DYNAMIQUE DES FLUIDES AISBL

von KARMAN INSTITUUT VOOR STROMINGSDYNAMICA IVZW

REF.

AGA0000/MC/GM/803
8 January 2003

Defense Technical Information Center
8725 John J. Kingman Road Ste 0994
Fort Belvoir VA 22060-6218
USA

Ref: GRANT NO: N00014-99-1-0834
"LES investigation of coherent structures in boundary layers and wakes"

Dear Madam, Dear Sir,

Please, find enclosed a copy of the Final Technical Report (Part 1, 2 and 3) for :

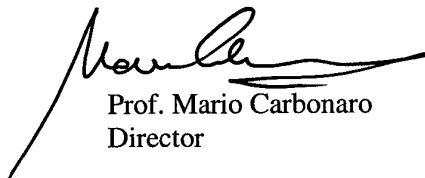
Grant No: N00014-99-1-0834,
"LES investigation of coherent structures in boundary layers and wakes"

The preparation and distribution of the Performance/Technical report is experiencing a slight delay, but it will be available in short time.

The final financial document covering the expenses of the von Karman Institute is being sent to the grant administrator.

We remain, of course, to your full disposal for any further information you might require.

Sincerely yours,



Prof. Mario Carbonaro
Director

Copies sent to : see next page